University of Kent

Faculty of Sciences

School of Physical Sciences (SPS)

Design and synthesis of novel amphiphilic calixarenes, amphiphilic urea sulfonate salts and fluorescent anion receptors.

By

Faith Rebecca Taylor

Thesis for the Masters of Science by Research

Supervisor: Dr. Jennifer Hiscock

Abstract

Antimicrobial resistance has become a growing threat over the last decade to the health and safety of the human populous, with the task of developing new antimicrobials having become the responsibility of academic researchers. Current antimicrobials are largely based on those that interact with specific proteins, but these are becoming increasingly less and less effective as microbials develop resistance to the antimicrobials currently in circulation. Work published by Hiscock *et al*. has developed a novel class of amphiphilic antimicrobials that target the phospholipid membrane rather than common protein targets. Building on the past work within the Hiscock group and extending this research is the basis for the work described herein. Amphiphilic antimicrobial calix[4]arene derived compounds have been synthesised and amphiphilic urea-sulfonate salts have been designed, the properties of which have been studied in the solid, liquid and gas states.

The study of the urea-sulfonate salts in the solid state showed that the compound tends to form extended structures with several different binding modes. In the gas phase, low level complexes are visible which indicate the bonds formed between the structures are strong as they survive the experimental conditions. Studies in the solution state show that the compounds form larger structures in DMSO, whilst one compound formed larger structures in an H_2O: EtOH 19:1 solution. The results obtained thus far prove the compounds to be amphiphilic, but do not indicate antimicrobial activity, so, further study is required.

The detection of anions in the environment is an ever-growing concern in modern society as the world becomes more aware of the impact that anionic pollutants are having upon the Earth. Anionic receptors are molecules designed to detect, respond to, and recognise species carrying a negative charge. The application of anionic receptors to modern day science is varied and includes organocatalysts which may be catalysed through hydrogen bond formation, in the separation of anionic mixtures in industrial or radioactive waste as well as applications in biology, for the treatment of ion channel based diseases such as cystic fibrosis.[1] Novel fluorescent anionic receptors

have been designed and synthesised based on works published by Hiscock *et al.*, with properties studied in the solid, liquid and gas state also.

Studies in the solid state showed the formation of intramolecular bonds with two of the compounds synthesised, along with the formation of intermolecular bonds between one compound and water that is used to stabilise the extended crystal structure. In the gas phase, one compound showed the presence of low-level complexes. In the solution state all the receptors detected the presence of anions and showed selectivity to specific anions also, where the order of selectivity showed an inverse in the Hofmeister series.

Acknowledgements

I would like to thank Dr Jennifer Hiscock for her continued support in aiding me to complete this thesis. Well, lets face it, this work would not have been possible without her, so, thank you Dr Jen. I would like to take a moment to thank the Hiscock group as a whole, but most of all I want to thank Kendrick and Rebecca. You were my friends through all of this and you both mean a lot to me; I will never forget the support you have showed me.

To my two best friends, Diana and Vassi. How could I have completed this monstrous task without you two? You have become my family this last year and I treasure you both so much. I hope you are in my life forever and thank you for always giving me someone to moan to about how terrible thesis life can be sometimes. I love you both very much. You mean more to me than words can describe, I will always be there for you both, as you have been for me.

I would like to thank my mim, Karen and my sister, Emerald. Thank you for picking me up when I was down and thank you for helping me to stand when I could only kneel. If it weren't for you both, I would not have been able to make it through the past few years as gracefully and as well as I have. Though we may be apart sometimes, I always feel your love and support. I have a lot of family that I love sincerely and who have supported me not only through this, but throughout my life, thank you all.

Finally, to my wonderful and amazing boyfriend Sam. Words cannot express how completely and utterly vital you have been to me this last year. When times became unbearable, you somehow made them better. You raise me to be the best version of myself, beyond where I could ever have imagined I could be. Thank you so much, not only for your help and support, but most importantly for your love and adoration. Here's to spending our lives together, may we continue now as we have begun. Happy, in love and full of hope for the future. I love you.

Although I love you all so much, I dedicate this thesis to my mim. You're the best, I love you. I would also like to dedicate this thesis to my dad, who sadly passed away after I submitted. I miss you so much, thank you for all of your encouragement. I love you more than you know.

Contents

Abbreviations

Carbon (NMR)	^{13}C
Acetone	Ace
Acetonitrile	ACN
Association constant	K_a
Broad doublet (NMR)	br d
Cooperative equal K	CoEK
Copper catalysed azide-alkine cycloaddition	CuAAC
Coupling constant (NMR)	J
Critical micelle concentration	CMC
Deuterated DMSO	DMSO-$_{d6}$
Deuterated water	D_2O
Dichloromethane	DCM
Diffusion-ordered spectroscopy	DOSY
Dimethylformamide	DMF
Dimethylsulfoxide	DMSO
Doublet (NMR)	d
Dynamic light scattering	DLS
Electronegativity	E_{min}
Electropositivity	E_{max}
Electrospray ionisation mass spectroscopy	ESI-MS
Electrostatic potential maps	ESMPs
Equal K	EK
Escherichia coli	*E.coli*

Ethanol	EtOH
Ethyl acetate	EtOAc
Hydrodynamic diameter	d_H
Hydrogen bond acceptor	HBA
Hydrogen bond donor	HBD
Infra-red	IR
Inner filter effect	IFE
Mass to charge ratio	m/z
Methanol	MeOH
Methicillin-resistant Staphylococcus aureus	*MRSA*
Minimum inhibitory concentration	MIC_{50}
Multiplet (NMR)	m
Nitric acid	HNO_2
Nuclear magnetic resonance spectroscopy	NMR
Palladium on carbon	Pd/C
Potassium carbonate	K_2CO_3
Proton	^1H
Quartet (NMR)	q
Silicon dioxide	SiO_2
Single crystal X-ray diffraction	SCXRD
Singlet (NMR)	s
Sodium hydride	NaH
Sodium hydroxide	NaOH
Sodium nitrite	$NaNO_2$
Staphylococcus aureus	*S.aureus*
Sulphuric acid	H_2SO_4

Tetrabutylammonium	TBA
Triplet (NMR)	t
Ultra-violet	UV
Ultra-violet visible spectroscopy	UV-vis
Water	H_2O

1.0 Introduction

1.1 History of Chemistry

The term supramolecular chemistry originated in 1969 when Jean-Marie Lehn first proposed the term "supermolecule".[2] Lehn defined supramolecular chemistry as "chemistry beyond the molecule", where focus was placed on the association of two or more chemical species that are held together through intermolecular forces.[3,4] The introduction of this field to chemistry led to the award of a Nobel Prize in 1987 to three of its pioneers: John-Marie Lehn, Charles Pederson and Donald Cram.[5]

When compared to other areas of chemistry, as they are known today, supramolecular chemistry is a relatively new discipline. However, its fundamental concepts have long been recognised and date back to the beginning of modern chemistry, when the idea of intermolecular bonds were first introduced by Johannes Diderik van der Waals in 1873.[6] Chemistry, as it is recognised today, was first discovered by German chemist Friedrich Wöhler, when he first synthesised urea from ammonium cyanate in 1828.[7] This discovery was ground breaking, as the process did not obey the laws of vitalism, which stated that organic compounds could not be synthesised in a laboratory from inorganic components because there was a certain essence of life missing.[7] This paved the way for the synthesis of many other organic compounds and how they may be developed without the use of organic reactants and so, vitalism was disproved.[8,9]

As organic chemistry continued to develop over the coming decades, there was still one area of the subject under debate, this was how atoms bond. This became clearer in 1916 when Gilbert Newton Lewis introduced the idea of covalent bonding through the theory of 'valence', where he used dot and cross diagrams (Figure 1) to explain this.[10] Gilbert N. Lewis proposed two different types of covalent bonding, polar and non-polar. Where polar involved the transfer of electrons and non-polar bonds were formed through sharing electrons.[11,12]
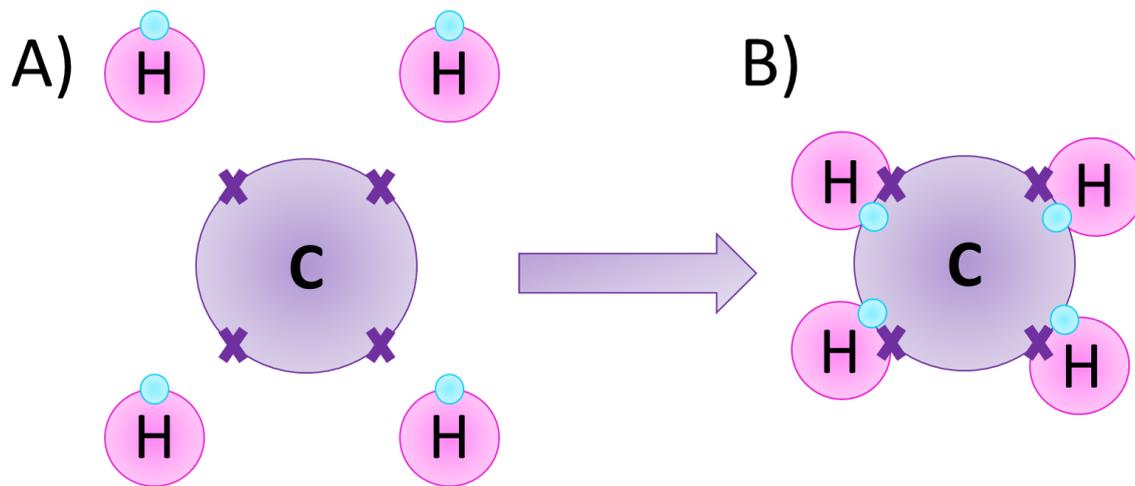
Figure 1 – Example of a dot and cross diagram showing a covalent bond in a methane molecule: A) A carbon atom with four unpaired electrons and four hydrogen atoms with one unpaired electron each, B) The hydrogen atoms are bonded to the carbon atom through the sharing of unpaired electrons.

1.2 Non-Covalent interactions

The existence of non-covalent interactions was first suggested in 1873 by Johannes Diderik van der Waals, forces which are today known as van der Waals interactions.[13–15] This ground breaking work by van der Waals paved the way for new and exciting research, leading Emil Fischer in 1894 to propose a key principle for enzyme activity, known as the 'lock and key' principle.[16] He stated that a substrate of a specific shape, like a key, could fit into the cavity of an enzyme, which he likened to a lock in order for the reaction to proceed[17] (Figure 2). This discovery could be argued as the first description of supramolecular chemistry as it is known today.

| Lock / Host | Key / Guest | Lock-Key / Host-Guest complex |
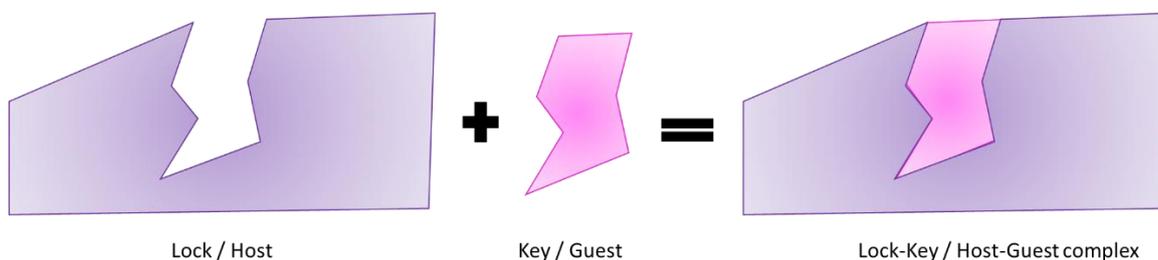
Figure 2 – Illustration depicting the lock and key principle of enzyme-substrate fitting. They must have complimentary shapes to form a complex and are held together through non-covalent interactions.

Later, in 1912, Moore and Winmill hypothesised the existence of the hydrogen bond,[18,19] which would be supported in the future by works published by Latimer and Rodebush.[20] The ideas presented at this time lead to the novel synthesis of several host complexes which selectively bind to guest molecules; included in this series of molecules were those synthesised by: Donald J. Cram, who synthesised the macrocyclic cyclophane, Charles J. Pederson who synthesised the crown ether, and cryptands which were synthesised by Jean-Marie Lehn (Figure 3).[21,22] There have been significant advancements in the field of supramolecular chemistry within the last decade, with the 2016 Nobel Prize being jointly awarded to Jean-Pierre Sauvage, Sir J. Fraser Stoddart and Ben L. Feringa, for their pioneering contributions to the initiation and development of synthetic supramolecular machines.[23,24] Sauvage developed a mechanically-interlocked architecture consisting of two or more interlocked macrocycles called catenanes (Figure 3).[25]
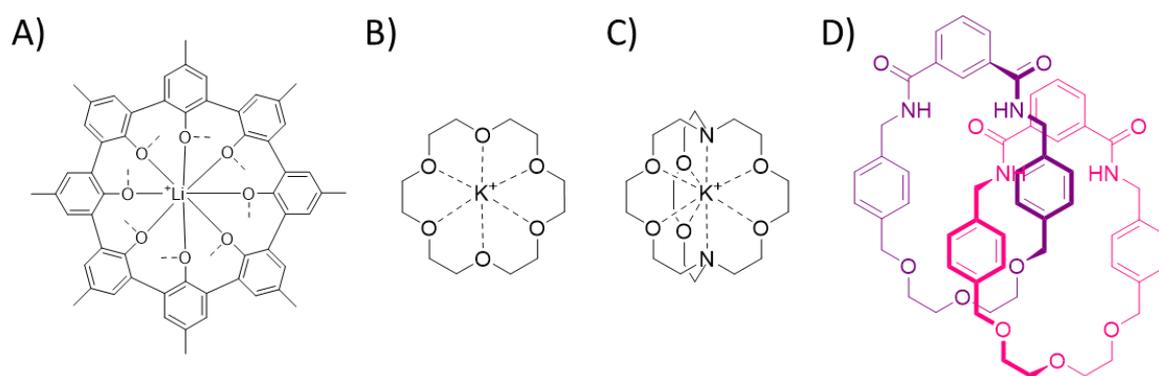
Figure 3 – The series of host-guest complexes synthesised by: A) Cram (spherand), B) Pederson (crown ether), C) Lehn (cryptate) and D) Jean-Pierre (catenane).

Supramolecular complexes can be designed to either self-organise, preorganise or both. Self-organisation is the process by which the molecules of a complex are arranged into more complex structures through the presence of intermolecular, non-covalent interactions.[26] Whilst preorganisation is the process where a molecule has been designed to interact only with specific and complimentary molecules through non-covalent interactions.[27] Preorganisation in molecules is beneficial as it has been shown to increase the binding affinity of molecules in host: guest chemistry by lowering the energy required to bind the guest molecules to the receptor.[28] Although, other factors such a steric interactions play into the binding affinity also, where the steric structure of a

molecule is optimised for specific guest binding, preorganisation of the host molecules have led to higher binding affinities for host: guest complexes. Molecules like this include the carborane cages which are carbon, boron and hydrogen based cages that poses planar preorganized cavities in an uncomplexed state.[29,30] Whereas, traditional macrocycles such as the crown ether do not poses preorganized cavities.

There is a fine balance occurring between electrostatic interactions and solvent interactions in a system that enables the formation of a supramolecular complex, where the predominance of one type of interaction may alter the formation of the complex. There are several types of non-covalent interactions, the most commonly considered are as follows: the dipole-dipole interaction, π-π interaction, ion-ion interactions and lastly the hydrogen bond,[31] which can also be considered as a mixture of covalent and electrostatic interactions.

The dipole-dipole interactions are the weakest type of interaction, with energies of < 5-20 kJ/mol, and are formed through the attraction of one dipole to another (Figure 4A).[32] Due to the nature of these type of interactions, there is a repulsive effect that increases as distance between the molecules decrease. Eventually, a point is reached where the effect of the repulsive forces overshadow the attractive forces, and the distance between the molecules begins to increase.[33] π-π interactions occur between aromatic ring systems through the electropositive and electronegative regions, and have energies of 0-50 kJ/mol.[34] There are three ways the ring systems can stack: face to face (Figure 4B), edge to face (Figure 4C) or offset (Figure 4D).[35]
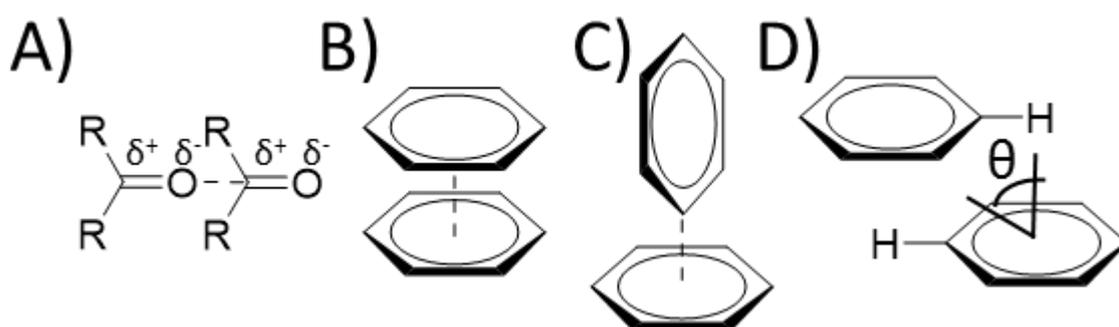
Figure 4 – Illustrations of non-covalent interactions: A) dipole-dipole, B) π-π face to face, C) π-π edge to face, D) π-π offset.

The strongest non-covalent interactions are the ion-ion interaction. These types of interactions have bond energies similar to a covalent bond, with values of 100-350 kJ/mol. A covalent bond will have an energy of < 150 kJ/mol.[36] Within this type of interaction fall the ion-dipole interactions, these types of interactions occur between a charged ion and a dipole from a polar molecule. There are also cation-π and anion-π interactions. Cation-π interactions occur between cationic species and electron rich aromatic ring systems,[37] anion-π interactions occur between anionic species and electron deficient aromatic ring systems[38] (Figure 5).
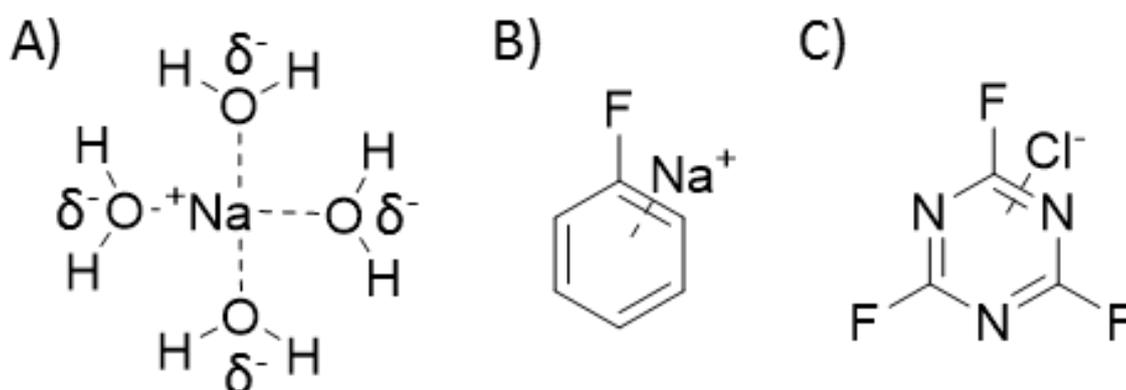
Figure 5 – Illustration of non-covalent interactions: A) ion-dipole, B) cation-π, C) anion-π.

The final non-covalent interaction discussed here is the hydrogen bond, which has been studied in great depth since its discovery.[39–41] With an energy range of 63 – 167 kJ/mol for covalent interactions, 17 – 63 kJ/mol for strong interactions such as electrostatic interactions and <17 kJ/mol for weak electrostatic interactions.[42–45] Hydrogen bond lengths range from 1.5 Å to 3.5 Å.[46,47] Hydrogen bonds are formed between an electropositive hydrogen atom containing group and an electronegative atom.

The hydrogen atom containing group acts as the hydrogen bond donor (HBD) with the other electronegative atom acting as the hydrogen bond acceptor (HBA).[48] When compared to covalent interactions, non-covalent interactions are weak, however, the effects of individual interactions are additive and can be strong enough to stabilise molecular structures and complexes. Hydrogen bonds are able to adopt several different geometrical structures, including: linear, bent, bifurcated

(accepting and donating), trifurcated and three centred bifurcated (Figure 6).[49] Optically formed hydrogen bonds are those that are short range, selective and directional. The selectivity and directionality increases with the strength of the bond formed.[43,48]
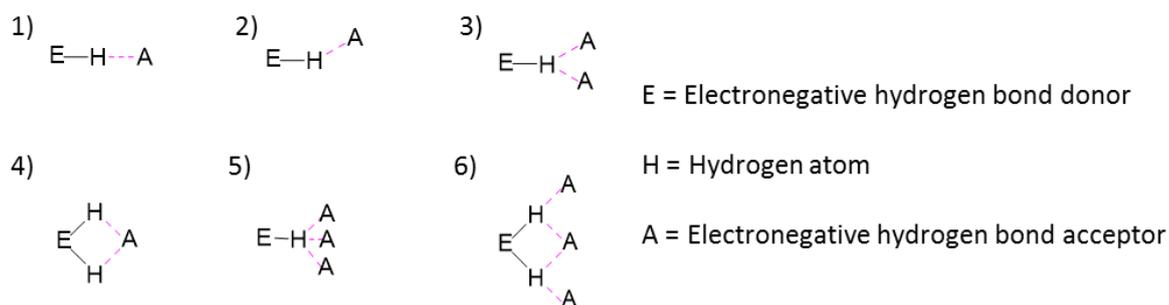
Figure 6 – Examples of geometric structures formed through hydrogen bonding: 1) Linear, 2) Bent, 3) Accepting bifurcated, 4) Donating bifurcated, 5) Trifurcated, 6) Three-centre bifurcated.

Supramolecular complexes are often seen in biological systems and play a vital role in the progression of life. A varied and important example of this is proteins, but more specifically, enzymes. These are often complex protein structures folded through non-covalent interactions that can catalyse chemical reactions within the body,[50] these protein structures also exhibit selectivity to substrates forming tightly bound complexes, such as an antibody bound to its target infection.

An antibody is a specialised structure designed to detect foreign particles within the body and defend against these particles.[51] These final structures are formed through several steps, initially the primary structure is formed and consists of a chain of amino acids, followed by the secondary structure which is the first step of self-assembly through hydrogen bonding, forming α-helices and β-sheets.[52] The tertiary structure then forms, which is where the secondary structure self-assembles further through several non-covalent interactions such as further hydrogen bonding, ionic interactions, sulfonate bridges and hydrophobic interactions.[53] The final step involves the self-assembly of two or more tertiary units to form the quaternary units (Figure 7). These structures are held together using the same non-covalent interactions as present in the tertiary structures.[54]

A) Primary structure   B) Secondary Structure   C) Tertiary structure

α-helix   β-sheet

D) Quaternary protein
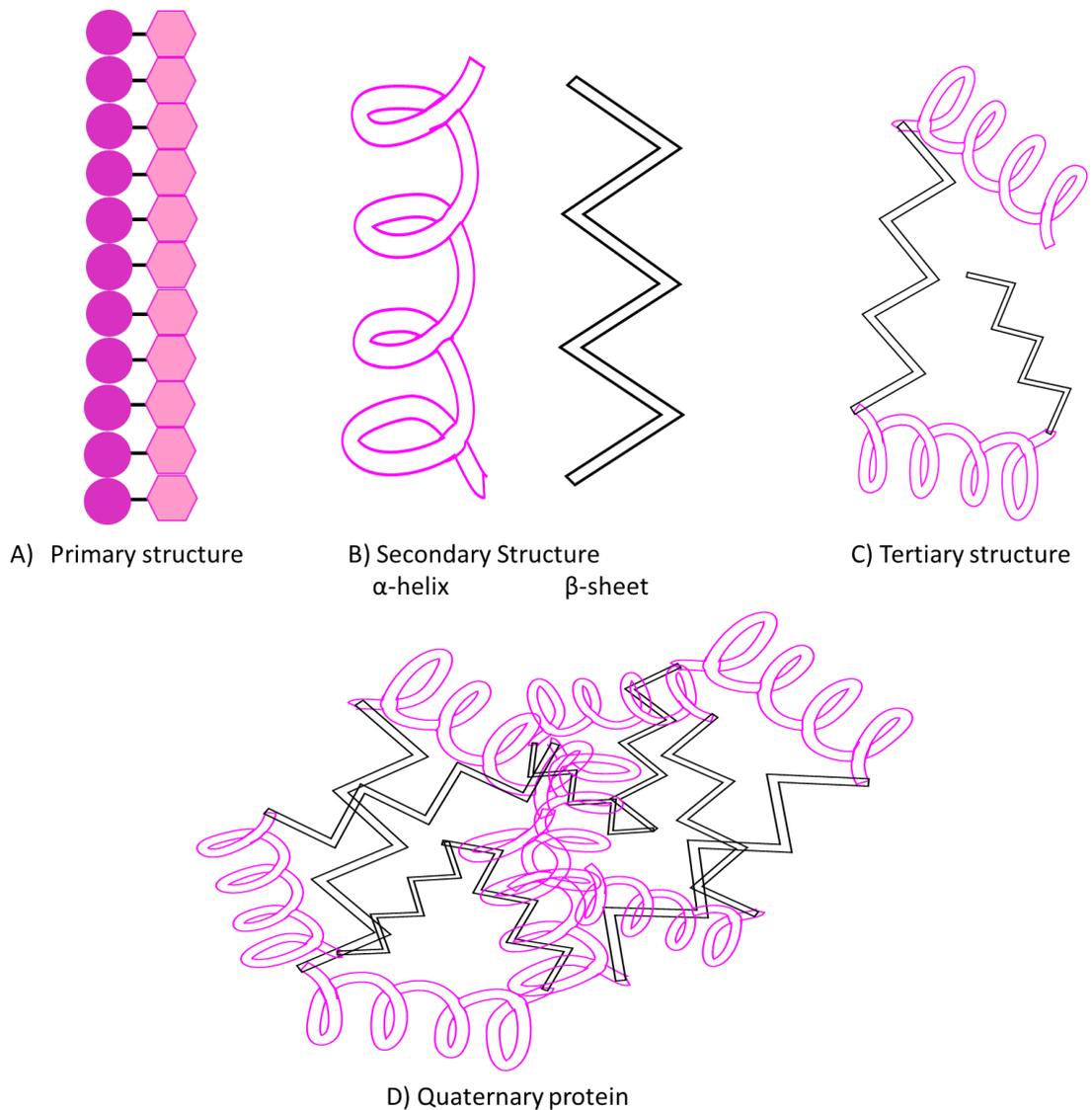
Figure 7 – Illustration of the steps in protein formation: A) Primary protein, the amino-acid chain held together through peptide bonds, B) Secondary protein, eg α-helix and β-sheets held together through hydrogen bonding, C) Tertiary protein formed from the folding of the secondary structure through hydrogen bonds, ionic bonds, hydrophobic interactions and disulphide bridge formation in order to compact the structure, D) Quaternary structure formed from the assembly of two or more tertiary units held together through hydrogen bonds and van der Waals interactions between non-polar side chains.

A complex example of a biological system containing non-covalent interactions is the cell membrane (Figure 8). This naturally occurring structure contains many non-covalent interactions, including those previously discussed.[55] Most notably are the presence of hydrophobic interactions as part of the main body of the cell membrane, the phospholipid bilayer.[56,57] Hydrophobic interactions are non-covalent interactions that occur between water molecules and low water soluble molecules called hydrophobes, such as phospholipids.[58] The phospholipid bilayer is a thin

polar membrane comprised of two layers of phospholipid molecules. These structures exist as components of almost every organism and many viruses too.[59] Their presence is not limited to the cell membrane, but also exist around sub-cellular structures such as liposomes. The bilayers responsibilities include: the protection of the cell, enabling extracellular communication through the transport of substances in and out of the cell and to facilitate the exchange of ions through the cell wall.[60]
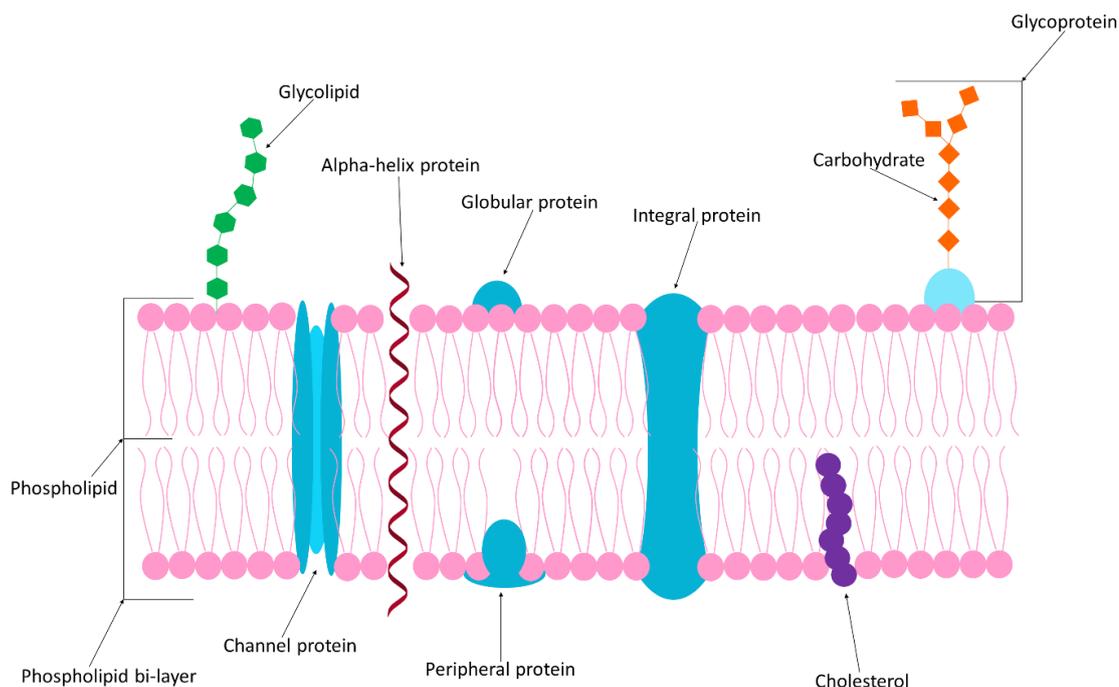
Figure 8 – Illustration of a cell membrane.

The phospholipid bilayer enables the transportations of proteins into the cell. This occurs due to the presence of structures such as membrane proteins.[61] These work by forming complexes with extracellular proteins that when bound, trigger specific reactions either within the cell membrane or within the cell itself.[62] Molecules may also enter the cell through the action of being directly delivered through the membrane and into the cell. In order to achieve effective penetration of the cell membrane long alkyl chains are required in order to achieve this due to their 'oily' like nature when interacting with the phospholipid bilayer. These molecules must also possess the ability to store molecules within their structures, usually bound through non-covalent interactions. An example of molecules that are able to store molecules within their structure, and have the ability

to easily append long alkyl chains are cyclic oligomer derivatives, called calixarenes. These may be the perfect type of compound to act both as a carrier and as delivery device.[63]

1.3 Calixarenes

Calixarene molecules are cyclic compounds composed of repeating units of phenol, and usually range in size from 4-20 repeating units, although other sizes have been synthesised. It has been over 140 years since the first rudimentary calixarene compound was first discovered in 1872 by Adolf von Baeyer.[64] Baeyer discovered simplistic versions of these compounds when he heated aqueous formaldehyde with phenol.

Years later in the early 1900s, Leo Baekeland refined this process and marketed the resinous product as Bakelite[65] (Figure 9)[66]; he referred to these structures as *[1n]metacyclophanes*.[67] Later, Zinke and Ziegler began the synthesis of modern calixarenes in 1941[68] through the synthesis of p-*tert*-butylphenol and formaldehyde to form what today is called *p-tert*-butylcalix[4]arene.[69] Later, the compounds were fully characterised by C. D. Gutsche as calixarenes in the late 1900s.[70]
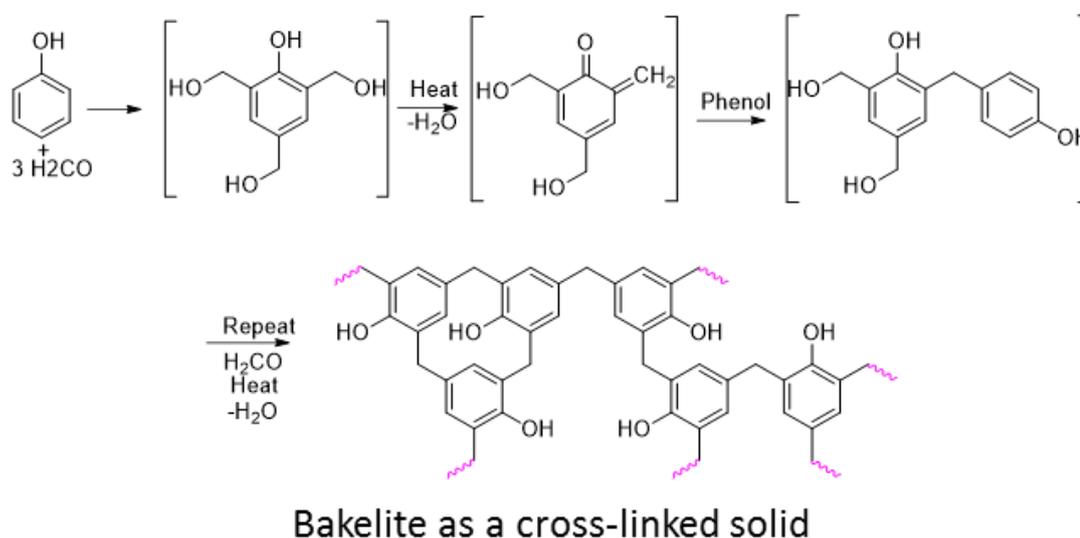

Figure 9 – The synthesis of Bakelite produced as a resinous solid from phenol and formaldehyde.

The word calixarene derives its meaning in two sections. The first being 'calix' from a Greek word meaning chalice, or cup like, and 'arene' which signifies the presence of aromatic rings.[71]

Calixarenes are classified as cyclic oligomers, which are macrocycles comprised of two sections, a narrow, lower endo rim and a wider, upper exo rim (Figure 10).[72,73] They are synthesised through the reactions of phenol and aldehyde in the presence of a strong acid,[72] or a base[74] for larger ring systems. However, the work up from these syntheses are often time consuming and difficult.[75] This may be largely due to the presence of reaction side products and conformers of the desired product. The existence of these species may alter the desired compounds affinity for specific solvents, which increasingly makes purification difficult.
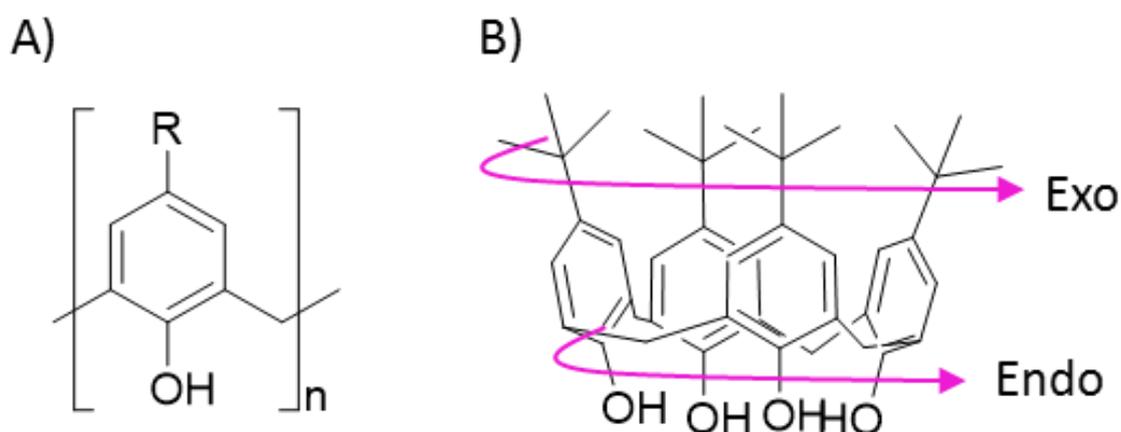
Figure 10 – Illustration of R-calix[4]arene: A) Simplified model, B) Cyclic model displaying exo and endo regions.

The presence of a methylene bridge at the ortho position on the benzene allows for easy maneuverability around this point.[76] This leads to the formation of several kinds of conformers (Figure 11). Functionalization at the upper and lower rim can induce or lock the calixarene into one of these conformations.[77] Calix[n]arenes, where [n] is larger than 4, have reduced conformational energy barriers allowing greater access to alternative conformations during their synthesis.[72] Alternative conformations may lead to induced effects, such as increased efficacy in coordination properties.[72]
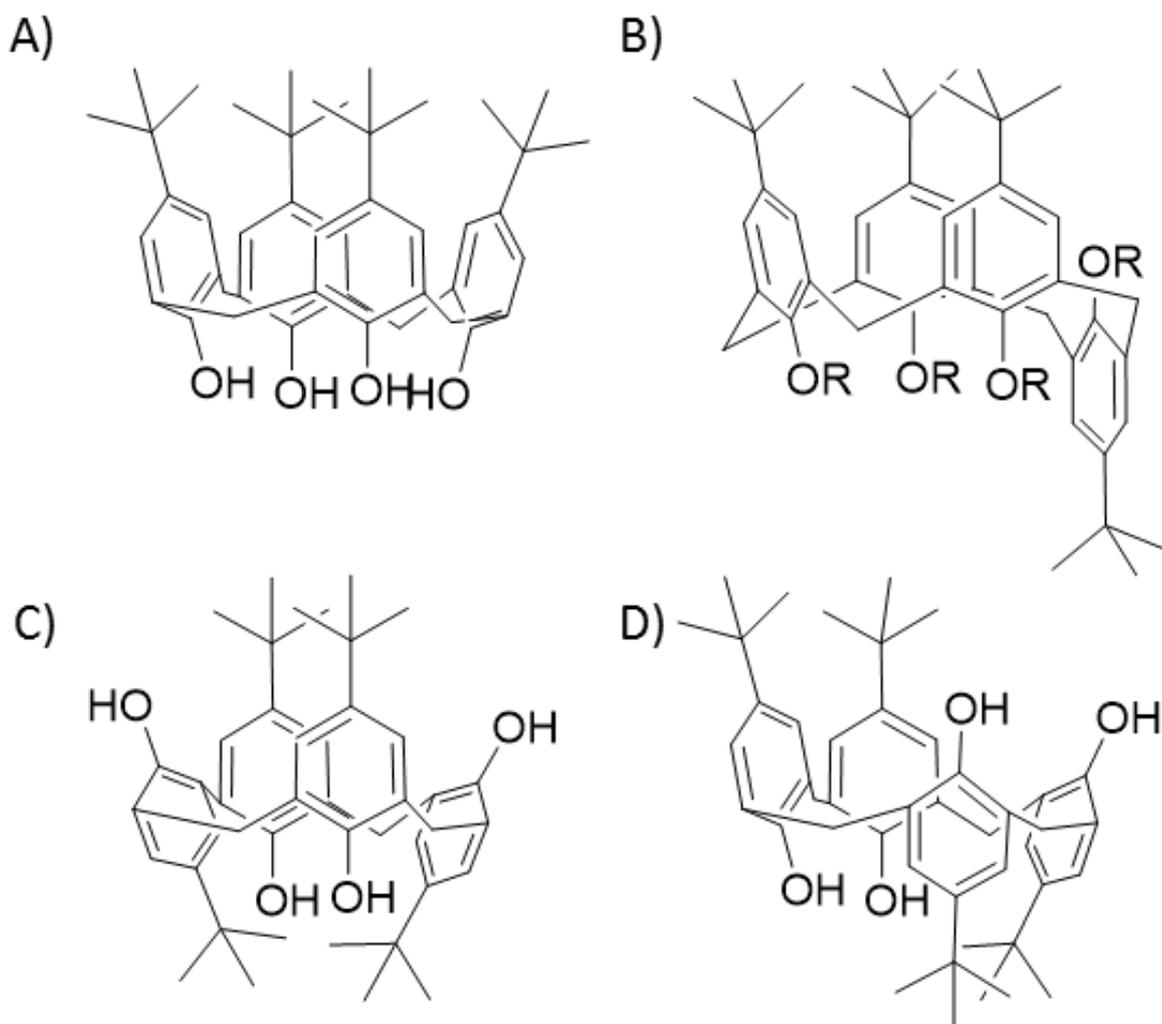
Figure 11: Conformations of p-tert-Butylcalix[4]arene: A) cone conformation, B) partial cone conformation, C) 1,3-alternate conformation, D) 1,2-alternate conformation.

Modification occurs either through, but is not limited to, the derivatisation of the OH group and through the electrophilic substitution of the benzene ring following the removal of the R group in the para position (Figure 12).[78,79] Replacement of the hydroxyl group with specifically selected substituents is a simple route to locking conformation. Alkyl chain-based substituents are popular and often allow for further derivation if it is required. However, modification sites also include the methylene bridges.[78] Modifications in this position may produce yet more conformers, which may occur through standard ring inversion. Conformers produced at these modification sites, with one site substitution are axial and equatorial based, those with two site substitutions produce cis and trans isomers (Figure 12).[76] The group which is appended to the methylene bridge may also

influence which position the functional group sits. For instance, alkyl[80] groups appear to have an increased preference for the equatorial position when compared to aryl groups.[76]
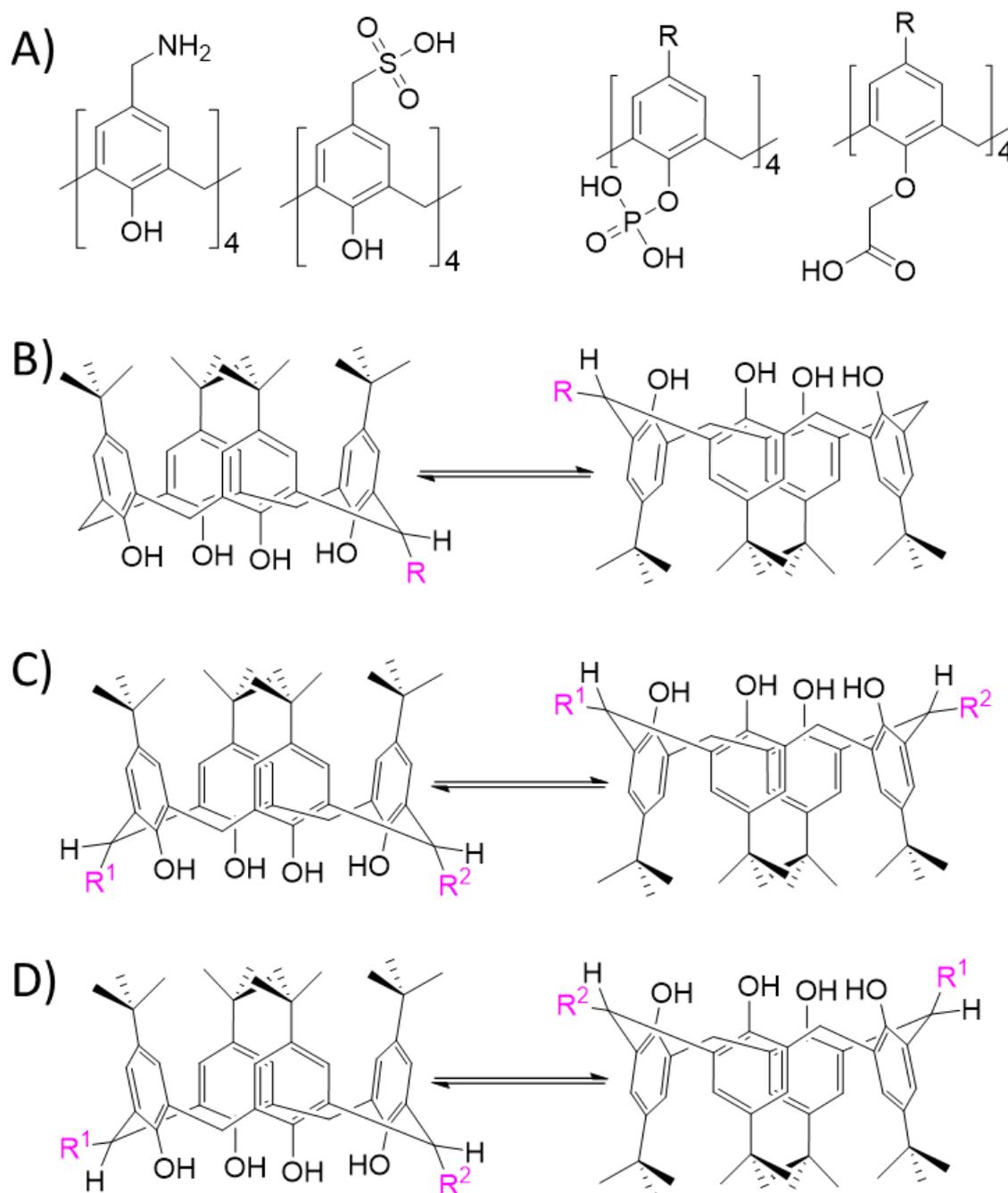
Figure 12 – Examples of different modifications and conformers: A) Examples of modifications in the para and ortho positions, B) Examples of axial and equatorial isomers where one methyl bridge is modified, C) Examples of cis isomers when two methyl bridges are modified, D) Examples of trans isomers when two methyl bridges are modified.

The ability to amend differing functional groups to the positions mentioned, allows the formation of a wide array of calixarene derived compounds (Figure 13).[80,81] The seemingly unlimited alterations which can be made to these compounds have led to a variety of systems with specific

properties and activities. Alterations include the addition of aroyl groups to form 'deep cavity' calixarenes.[77] Deep cavity calixarenes may be designed to have increased hydrogen bonding to a guest in host-guest chemistry.[82] This type of calixarene has also been designed to have properties specific to fluorescence, with enhanced solubility in fluorescent solvents, as well as improved efficacy as fluorescent sensors, along with varied functional groups for molecular recognition.[83]
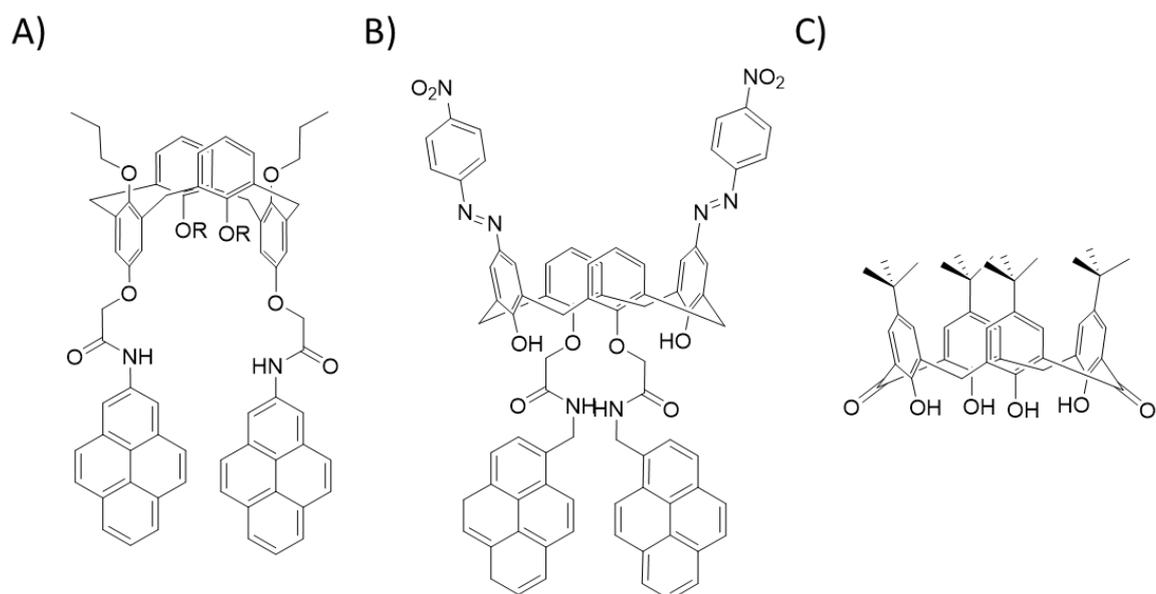
Figure 13 – Examples of different calixarene based compounds: A) 1,3-alternate modified at the ortho and para positions, B) Cone conformation modified at the ortho and para positions, C) Cone conformation modified at the methylene bridge.

Calixarene modification for the application to cell membrane ion transportation has over the years been extremely well documented.[84–89] Calixarenes have been used to enable the process of cross membrane ion transportation to be studied. Derivatives of these structures have shown selectivity to ions and are able to regulate ion transportation whilst forming ion channels in bilayer membranes.[90] When introduced to the membrane, be it a monolayer, bilayer or phospholipid bilayer, derivates of calixarene compounds interact with the cell membrane through non-covalent interactions. These can be through hydrophobic interactions, the formation of hydrogen bonds, ionic interactions and more.[91–93]

Calixarenes designed to mimic ion-channels are often designed as amphiphiles.[94,95] Amphiphiles are molecules that contain both a nonpolar hydrophobic region, often referred to as the 'tail', and a polar hydrophilic region, often referred to as the 'head'.[96] Amphiphilic calixarenes

possess largely hydrophobic 'tails' modified at the lower rim, with hydrophilic 'heads' modified at the upper rim, they may also exhibit self-assembly within the membrane.[97,98] Ion-channel mimicking calixarenes can be activated through several methods, some of which are through ion recognition, through polarization, or through changes in pH.[99–101]

The method through which these compounds are activated depends, of course, upon the structure. There are several functions that synthetic ion channels must have. These compounds must have the ability to transport ions in the range of 10^4 to 10^8 ions per second, it must be able to discriminate between species and must be at least 40 Å in length because this is the average width of a phospholipid membrane.[91] Calixarenes as synthetic ion pores are well suited in this role because of their selectively designed cavities, with aromatic units of 4 being the most effective choice for this role (Figure 14).[91]
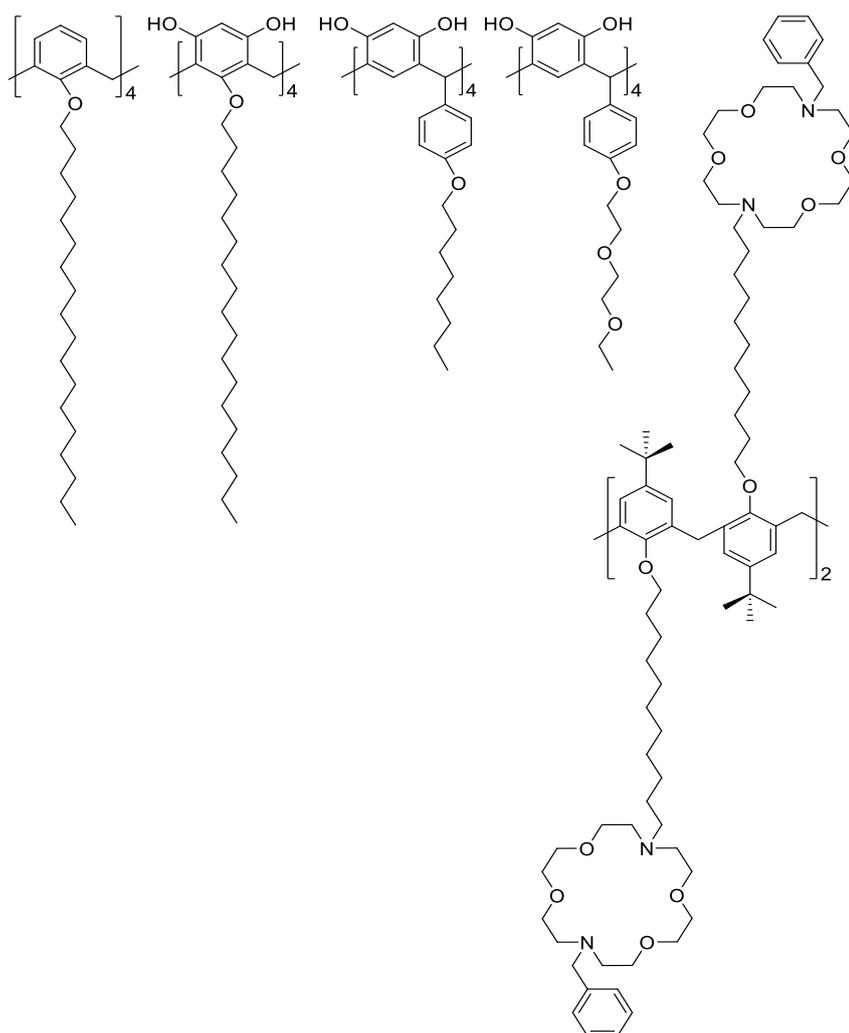

Figure 14 – A range of ion-specific filters inspired by calix[4]arene.

Research into calixarenes moving forward is being centred around applications in biological systems,[102] and environmental systems. Included in this are their application to drug sensing, biotechnology and biosensors[90] and as metallic sensors, which been greatly documented.[74,103–105] When calixarene compounds act as metalloreceptors they are multidentate ligands containing non-covalent binding sites which are often preorganised allowing for secondary interactions with a coordinated substrate.[106] Applications of ligand calixarenes vary, where some have been designed to act as environmental heavy metal detectors,[107] some may act as both detectors and separators of metal ions or species[108] and others have been incorporated into metal-organic frameworks (MOFs) for the detection of nitrogen dioxide, NO_2.[109]

An area of research which cannot be ignored here due to its ever-growing importance in society, is the application of calixarene derivatives to drug delivery. It is something that has provided significant evidence for improved efficiency and efficacy of already in place drug delivery systems, as well as paving the way for new and improved systems.[110] Delivery systems developed include micelles, hydrogels, vesicles and liposomes and supramolecular nanovalves on mesoporous silicas.[111] Calixarene derived drug delivery systems may be triggered to release their pay load through several methods. These include being sensitive to pH[112] (Figure 15) and naturally present receptors.[113] Calixarene based drug carriers interact with the loaded drug through non-covalent interactions. The non-covalent interactions that occur here depend on the designed system, but may include hydrogen bonding, ionic interactions, van der Waals interactions and electrostatic interactions.[114–116]
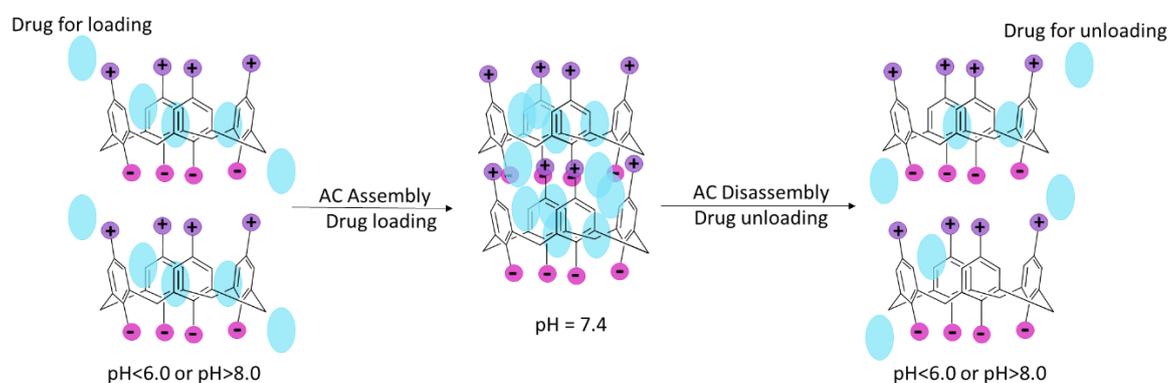

Figure 15 – Illustration of a pH dependant calixarene based drug delivery system, where AC means amphiphilic calixarene.

Amphiphilic calixarenes have been extensively explored in research and are designed with a hydrophilic group and a hydrophobic group, usually in the form of an extensive alkyl chain.[117] Research into calixarene based amphiphiles and supra-amphiphiles has indicated the application of this type of compound to both drug delivery systems and to disease recognition and treatment is an effective system moving forward.[117,118] Not only because of the ease of functionality alterations to the starting compound, but also because these molecules interact through non-covalent interactions.[119]

Amphiphilic calixarenes have been shown to self-assemble into several different forms, including: micelles, vesicles, nano-tubes, rods and fibres.[120] These compounds have also been shown to form different aggregates in differing conditions, changing their form from a micelle structure to a fibrous structure.[121,122] This type of reaction to the environment means that the application of the compound may be altered to cater for different purposes simply by exposing the compounds to different environments.

1.4 Supramolecular Amphiphiles

Amphiphiles are categorized into four groups: anionic, cationic, neutral and zwitterionic.[123] Anionic amphiphiles have an overall negative charge with functional 'head' groups such as sulphates and phosphates (Figure 16A).[124] Cationic amphiphiles carry a positive charge with common 'head' examples such as amines or ammonium ions (Figure 16B).[125] Neutral amphiphiles carry no overall charge, their properties are dependent on the functional groups present and how easily they deprotonate (Figure 16C).[126] Finally, the zwitterionic amphiphiles carry both a positive and a negative charge within the 'head' group (Figure 16D).[127] It is common for the hydrophobic region of an amphiphile to be a long alkyl chain, but this may differ in some cases where there are aromatic ring systems or where trifluoromethyl is present.[128–130] The 'head' region of an amphiphiles will be polar in nature, whilst the 'tail' region will be non-polar by nature.
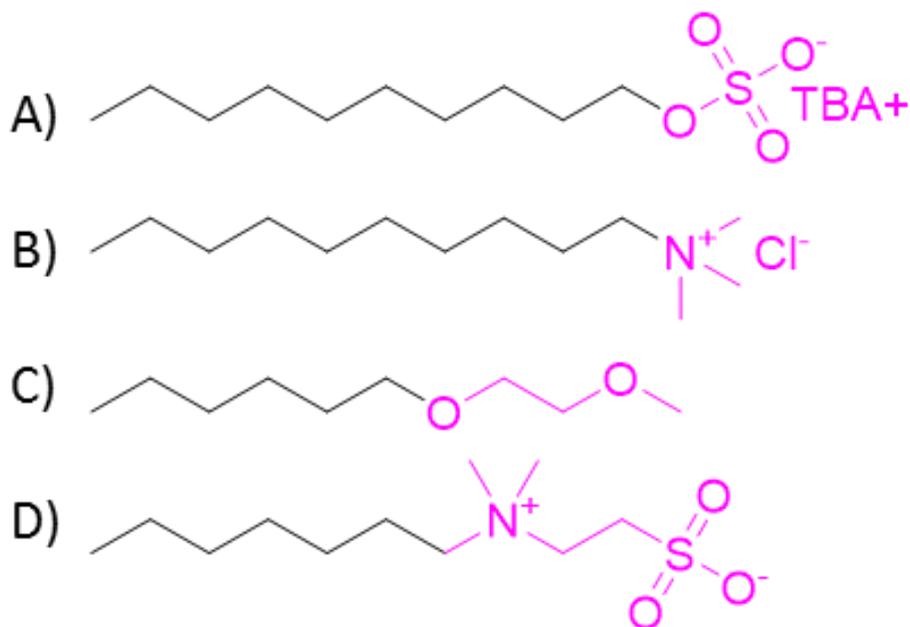
Figure 16 – Examples of different amphiphiles showing the non-polar region in black and the polar region in pink: A) Anionic, B) Cationic, C) Neutral, D) Zwitterionic.

Simplistically, amphiphiles are generally formed through covalently linking a hydrophilic molecule with a hydrophobic molecule.[131] This means there is great availability for the formation of highly diverse amphiphiles. From simpler or smaller molecules such as phospholipids, to larger more complex molecules such as amphiphilic block copolymers.[125,132,133] While amphiphiles that are analogous may be synthesised using the same starting method, the synthesis of other types of amphiphiles varies greatly. For instance, fluorinated 1,2-di-O-alkyll glycerol-PEG is formed with the intended use to reduce the amount of anaesthesia used in operating rooms, whilst also increasing its affects and may be formed under phase transfer catalysis.[134] Whilst a range of amphiphiles can be synthesised for a variety of purposes through the use of click chemistry, as well as copper-catalysed azide-alkyne cycloaddition (CuAAC) reactions (Figure 17).[135] These types of synthesis can be used to form phospholipid based amphiphiles with up to 20 alkyl chains with uses from drug delivery to solubilising bioactive food additives.[135,136]

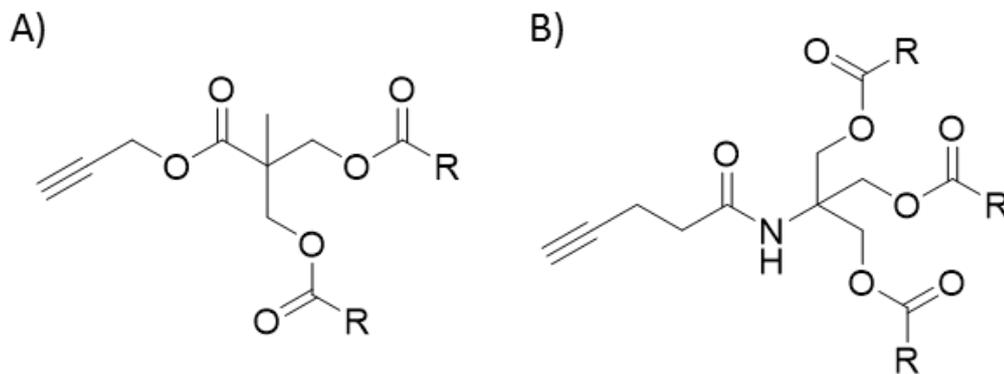Figure 17 – Examples of alkyne attached 'tails' in a phospholipid: A) Double alkyl chain tail where R = $(CH_2)_{12}CH_3$, B) Triple alkyl chain tail where R = $(CH_2)_5CH=CH(CH_2)_7CH_3$.

The general effects that a functional group has on the parent compound is well known and well documented.[137] From electron withdrawing/deactivating groups such as the nitro, ammonium and halogen based groups, to the electron donating/activating groups such as the amide, alkyl and, occasionally, the hydroxyl based groups. Groups such as the hydroxyl group may be both withdrawing and donating depending on the system in which it is in.

However, the effect that functional groups may have on the properties of amphiphiles is something that requires investigation when novel compounds are being synthesised. This because adding electron donating or withdrawing groups affects the electron density of a molecule. This can cause changes to the polarity of the molecules which may result in a change to the ability of a molecule to form non-covalent bonds. Meaning that, changes to the molecules ability to self-associate may occur, or the ability to act as a receptor molecule for different substrates may also change.

Changing the functional group may change the type of the aggregate formed by the amphiphile during self-assembly. For instance, swapping end chain functionalised cyclodextrin for adamantly-functionalized calcein alters the properties of the aggregate formed by changing the diameter of the aggregate as well as the thickness of the aggregate wall.[119] Amphiphiles self-assemble into aggregates when in solution. The structure of the aggregates formed varies depending on the design of the amphiphile as well as the solvent in which it is introduced to, forming structures such as micelles, reverse micelles, vesicles or lipid bilayers.[138,139] Polar solutions will force the formation

of micelles (Figure 18A), whilst non-polar solutions force the formation of reverse micelles (Figure 18B).[140] The presence of hydrophobic groups can also affect the type of aggregate formed, for example, phospholipids with a single hydrocarbon 'tail' can form micelles, whereas those with two or more hydrocarbon 'tails' are too bulky to form micelles and so form structures such as bilayers (Figure 18C) or vesicles (Figure 18D).[141]
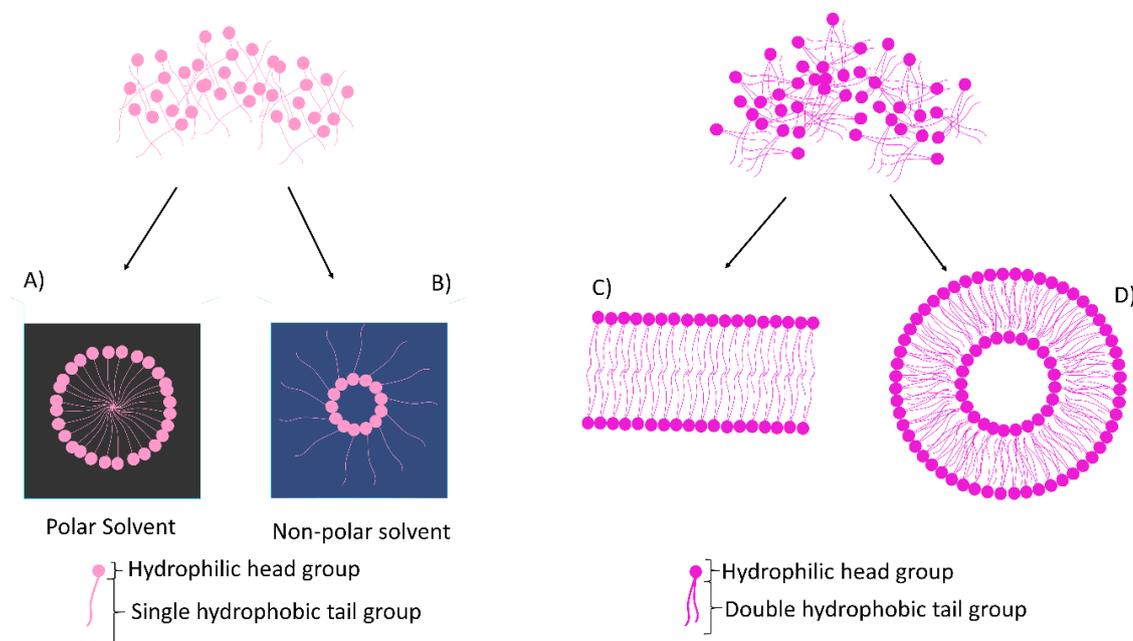

Figure 18 – Examples of amphiphilic aggregates: A) Single hydrophobic chain amphiphile in a polar solvent. B) Single hydrophobic chain amphiphile in a non-polar solvent. C) Double hydrophobic chain amphiphile forming a lipid bilayer. D) Double hydrophobic chain forming a vesicle.

Literature has shown that changing the functional groups on an amphiphile changes some of its properties.[142,143] These properties include the ability to form gels in aqueous solutions, or the ability to act effectively as an antimicrobial agent.[144,145] Most types of antimicrobials work by targeting the DNA of a cell, or enzymes on the membrane of a cell.[146,147] These types of antimicrobials may have higher toxicity to mammalian cells, compared to antimicrobials based on peptides that disrupt the bacterial membrane.[148,149] Peptide amphiphiles are a class of peptide based antimicrobial amphiphiles that were developed in 1995 by Matthew Tirrell and Gregg Fields.[150] This class of amphiphiles work by associating with the bacterial cell membrane, this discovery led to the development of new amphiphilic drugs. Some examples of amphiphilic drugs are: tranquilizers, antihistamines, antidepressants (Figure 19), β-blockers and antibiotics.[151–156]
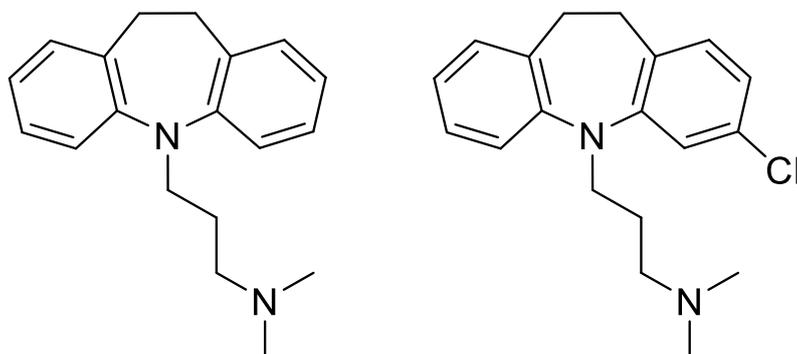
Figure 19 – Examples of two structurally related antidepressant amphiphilic drugs.

Research into amphiphiles has led to the development of supra-amphiphiles, these are molecular machines that interact and are formed through non-covalent interactions.[157] Research published by Wang *et al*. stated that supra-amphiphiles may be formed in two ways, either through the non-covalent combination of a hydrophilic and a hydrophobic component,[158] or to amend a molecule with groups of non-covalent interactions that change the physical properties associated with the molecule.[159] From this, low molecular weight amphiphiles have been shown to self-associate through hydrogen bonding,[160] especially those containing specific functional groups such as the urea functional group.[161]

Faustino *et al*. developed an analogue of anionic urea based salts that were derived from sulphur containing amino acids (Figure 20A, B).[162] The study showed that hydrogen bonding occurred at the urea moiety, did not affect the formation of micelles, but showed no antimicrobial activity. With this in mind, Pittelkow *et al*. synthesised aromatic anionic-urea salts derived from sweeteners (Figure 20C),[163–165] with a focus on the complexation of dendrimers and not the self-association properties. Hiscock *et al*. then went a step further and modified the sulfonate-urea salts with a focus in the self-association properties of these compounds. They discovered some of the amphiphilic salts showed signs of antimicrobial activity (Figure 20D).[166]
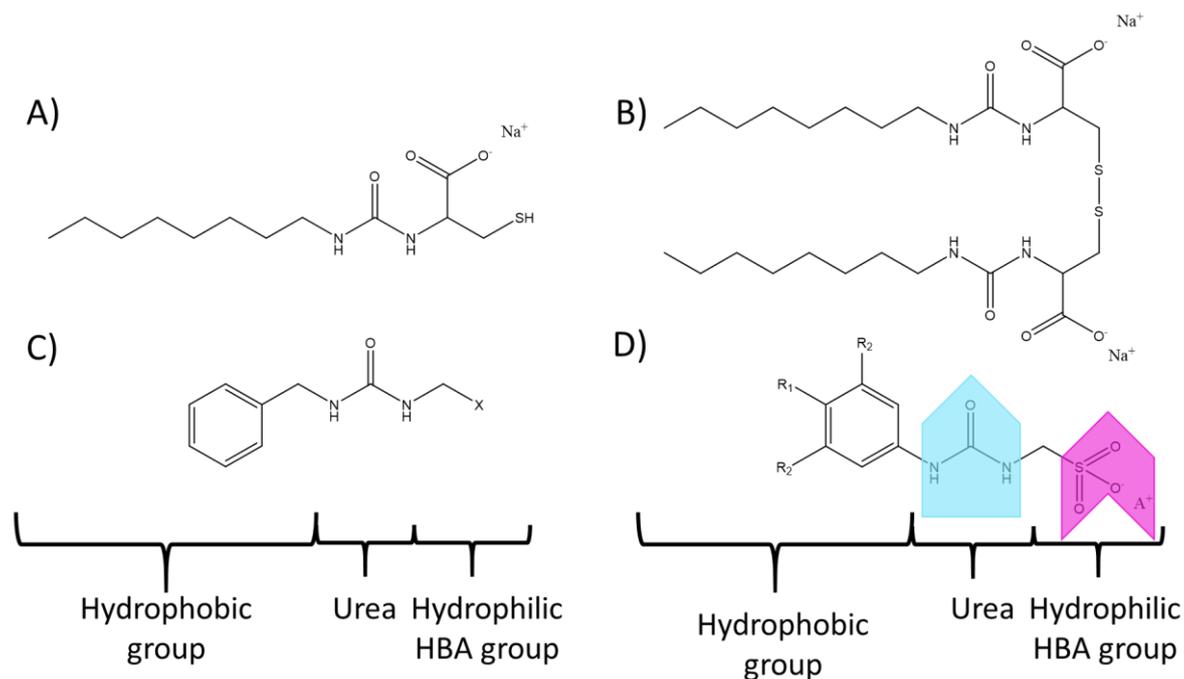
Figure 20 – Depiction of the evolution of the anionic urea amphiphile: A) Anionic monomeric urea amino acid, B) Anionic dimeric urea amino acid, C) Anionic aromatic urea, D) Modified anionic aromatic urea, X = SO_3^- or $C_6H_6CF_3$, A = tetrabutylammonium (TBA^+) counter cation.

The amphiphiles shown above in Figure 20 consist of an anionic hydrophilic HBA group and a urea group. These groups are used to form different binding patterns, but they cannot exist at the same time and so the system becomes 'frustrated'.[166] Hydrogen bonding allows for the amphiphile to self-assemble either through the urea-urea groups or through the urea-anion groups. Binding through each mode creates different structures, where the urea-urea can form either a dimer or a tape like structure, and the urea-anion forms a *syn*-stacked or an *anti*-stacking structure (Figure 21).[167] Concluded from the research by Hiscock *et al.* was that the binding mode was dependant on the molecular structure of the amphiphile, as well as being dependent upon the solvent system used to form the aggregate.

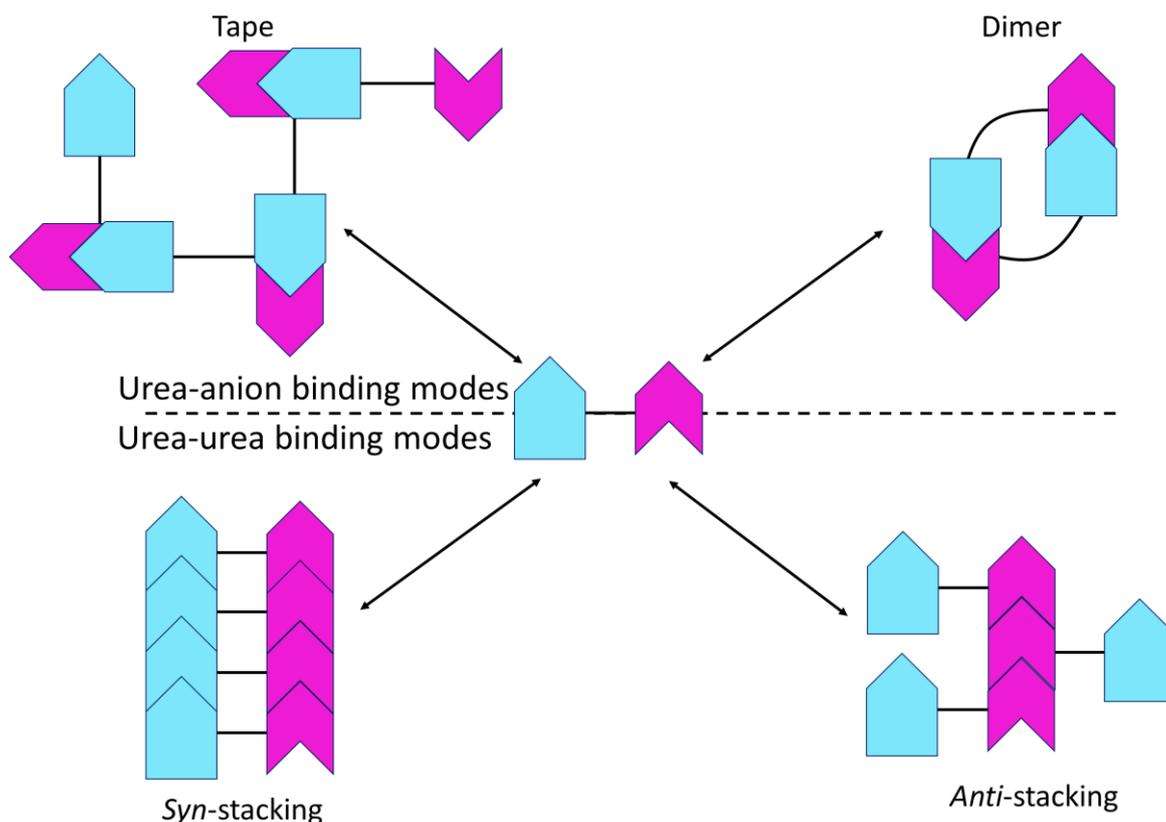Figure 21 – Examples of possible hydrogen bonded self-association modes for this type of anionic urea based amphiphile.

Hiscock *et al*. then proceeded to develop an analogue of novel amphiphiles that kept the same general structure.[167] Functional groups present on the hydrophobic aromatic ring were altered, some electron withdrawing, and some electron donating groups were affixed. These included amide and nitro groups. The urea group was exchanged for a thiourea and the cation used was also exchanged. Studies were conducted on the properties of self-association for these compounds in the solid, liquid and gas phase.[168]

The research explained that compounds containing a urea-anionic group with a weakly coordinated cation forms a urea-anion complex and formed dimeric species in the gas phase and solution state when present in solutions containing high proportions of dimethylsulfoxide (DMSO).[169] When present in a water ethanol solution of mixture 19:1, the compounds formed aggregates that were between 91-460 nm, three of which showed antimicrobial activity towards Methicillin-resistant Staphylococcus aureus (*MRSA*), a gram positive (+ve) cell and towards Escherichia coli (*E.coli*), a gram negative (-ve) cell.[145]

Now that these compounds had shown promise as antimicrobials, the mode of action had to be investigated. Hiscock *et al*. went on to investigate the mode of action in a 95 % water (H$_2$O): 5 % ethanol (EtOH) solution, investigating the aggregates formed in this solvent system. They did this by synthesising a range of intrinsically fluorescent compounds[168] that allowed the mode of action to be studied using transmitted and fluorescence microscopy. The techniques showed that the compounds formed vesicular structures that coat the surface of the *MRSA* cell. The compound then penetrates the cells membrane and internalises before associating with the nucleoid (Figure 22).[170]
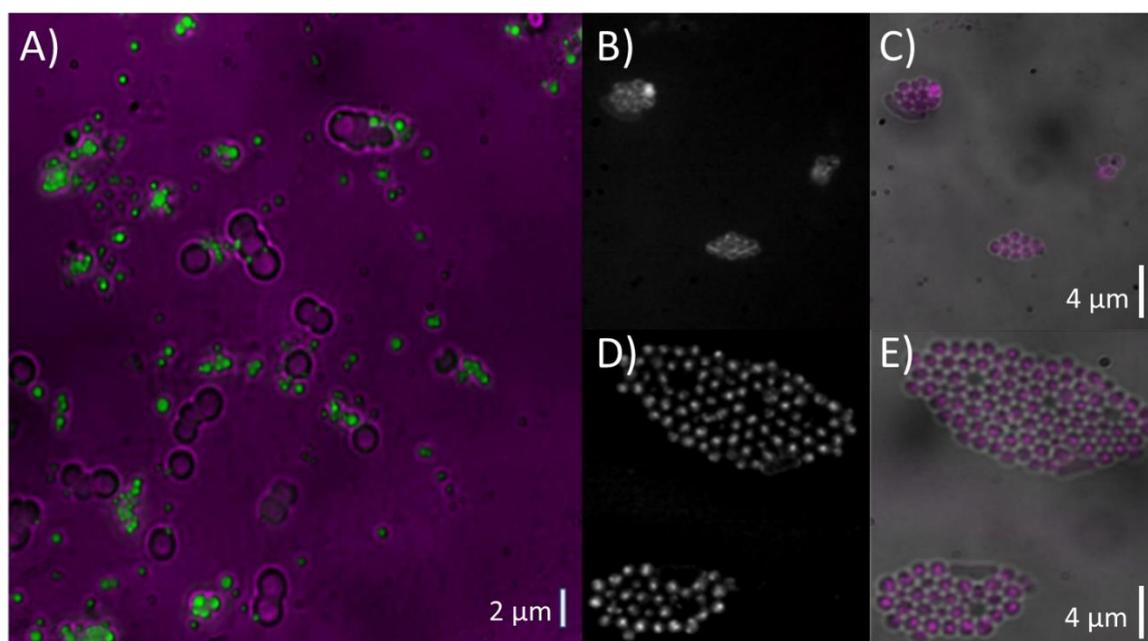

Figure 22 – A) Green vesicular aggregates binding to the bacteria membrane of staphylococcus aureus (*S.aureus)*, B) Fluorescence microscopy image of white aggregates coating the surface of the cell membrane of *S.aureus*, C) Overlaid fluorescence microscopy onto transmitted light microscopy displaying pink aggregates coating the surface of the cell membrane of *S.aureus,* D) Fluorescence microscopy of white aggregates interacting with the nucleoid of the cell *S.aureus*, E) Overlaid fluorescence microscopy onto transmitted light microscopy of pink aggregates interacting with the nucleoid of the cell S.aureus. (Images obtained and produced by Laura Blackholly, Jennifer Hiscock and Dan Mulvihil).

One of the intrinsically fluorescent compounds used within these studies has been published twice by Hiscock *et al*.[168,169] The compound is a tetrabutylammonium (TBA) sulfonate-urea amphiphilic salt (Figure 23) which demonstrated the presence of dimers in the solid state formed through sulfonate-urea hydrogen bonds. Large aggregates of this compound were formed in low amounts of DMSO as shown in quantitative nuclear magnetic resonance (qNMR), with a size >1000

nm and were thought to be smaller aggregates combining to form larger ones. In a 19: 1 H_2O: EtOH solution the compound formed aggregates of size 220 nm.[168]
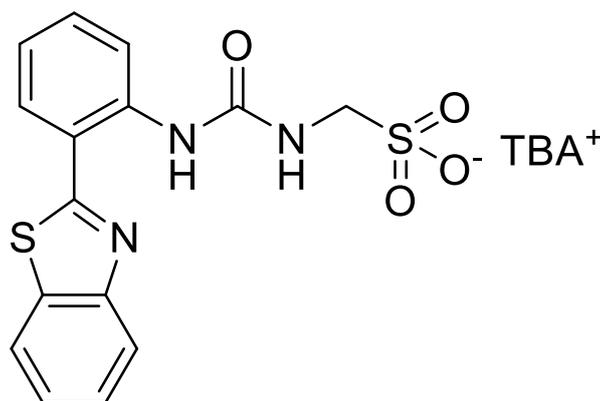

Figure 23 – Structure of novel TBA sulfonate-urea amphiphilic salt from Hiscock *et al*.[168]

The experiments concluded that the properties of amphiphilic surfactants may be predicted based on the capabilities of the HBD urea group to form hydrogen bonds. The formation of these bonds are limited in this compound due to the presence of intramolecular hydrogen bonds formed between the benzothiazole nitrogen and the urea NH.[169]

1.5 Fluorescent Receptors

Fluorescent receptors are receptors that emit a longer wavelength of light than the wavelength of light by which it was excited.[171] The compound shown above, in Figure 17, has the capability to act as a fluorescent receptor. This is because it is intrinsically fluorescent due to the benzothiazole group whilst possessing a urea group, these groups combined enable hydrogen bond formation.[168] Early reports of fluorescent receptor synthesis and design date back to the 1970s,[172] where in 1974, M.J Anderson and M.W Cohen first reported the process of labelling compounds using a fluorescent dye.[173] Whilst the method was revolutionary, it failed to recognise ligand binding sites and instead it detected the receptor proteins.[172] Technologies later developed that focused on the detection of ligand binding sites which thus allowed for processes triggered by ligand-receptor interactions to be monitored.

Compounds that are intrinsically fluorescent are often ones that contain extensively conjugated systems.[174,175] These are systems that usually contain alternating single and double bonds, most commonly seen in ring systems such as benzenes and pyrroles.[176] Compounds containing multiples of these groups may have increased fluorescence, where the light emitted displays an increase in emission intensity.[174] For synthesised compounds to have the ability to act as fluorescent receptors they must possess two fundamental qualities. Firstly, the compounds must be fluorescent and secondly, the compound must have the ability to form non-covalent bonds, usually in the form of hydrogen bonds.[177]

Receptors must be designed to contain complimentary binding sites to the molecules or atoms for which it is designed to bind with.[178] This means designing receptors that contain a sufficient number of available binding sites both in the HBA and HBD regions involved in host-guest chemistry. Receptors may be classed into categories, for instance, by the type of chemical reaction that is induced during the recognition of the analyte. This may include those designed based on a cleavage reaction, a nucleophilic addition reaction, a reduction reaction, a complexation reaction or a deprotonation reaction.[179]

However, the focus here is on the application of supramolecular sensors to the field of molecular recognition or, more specifically, optical sensors. Optical sensors may be categorised as either colorimetric, circular dichroism or fluorescence based.[180] Fluorescent optical sensors are synthetic molecular devices that are designed to bind analytes by non-covalent interactions, producing a change in fluorescence (Figure 24).[181] The change in fluorescence upon the addition of an analyte is indicative of binding, it may also be indicative of the type of analyte bound as different analytes may produce different changes to the fluorescence of the receptor compound. The types of changes which may occur are fluorescence quenching, an increase in fluorescence emission intensity, a shift in the wavelength of the peak maxima of the emission spectrum or it may cause an on/off type 'switch' to the fluorescence.[182–185] These effects are direct results of binding, and do not occur unless a specific analyte is bound.

Figure 24 – Graphical representation of the effects an analyte may have on a fluorescent receptor: A) Receptor in 'off' mode exhibiting no fluorescence along with a selection of analytes, B) Receptor analyte complex in 'on' mode exhibiting fluorescence, C) Receptor analyte complex exhibiting quenching upon binding with a different analyte, shown through a decrease in the number of arrows compared to B, D) Receptor analyte complex exhibiting increased fluorescence intensity upon binding with a different complex, shown through an increase in the number of arrows compared to B, E) Receptor analyte complex representing a shift in peak maxima through a change in the colour of emitted light, compared to B. Hydrogen bonding chemosensors for: F) Urea, G) Creatinine, H) Monosaccharides.

Some common fluorescent compounds are anthracene,[186] fluorescein[187] and quinine.[188] These compounds are good starting points for the development of novel fluorescent receptors. They are already fluorescent, so the first point of alteration should be to add groups that are good HBAs, such as ones containing nitrogen, fluorine and oxygen although, nitrogen and oxygen become HBDs when bonded to a hydrogen atom.[189]

Examples of anthracene based receptors with a variety of analyte detection capabilities and designs have been published (Figure 25).[190–192] From the selective detection of anions, to the

detection of dicarboxylate, anthracene based receptors are just the start. A common moiety included in the structure of fluorescent receptors is the urea group. There are anthracene derivatives,[193] as well as fluorescein derivates[194] which contain this group. The use of a (thio)urea group is effective within a receptor as it acts as an HBD with two positions available for hydrogen bond formation. An article published in 2008 discussed the synthesis and design of an adenine based fluorescent receptor possessing either a thiourea or a urea group.[195] The paper discussed the prevalence of (thio)urea groups to form directed bonds with spherical ions, such as those in the halide group, with tetrahedral phosphates and with planar carboxylate anions.[195] This singular paper alone shows the abilities that one receptor may have to detect multiple different analytes, whilst remaining stabilized and selective.
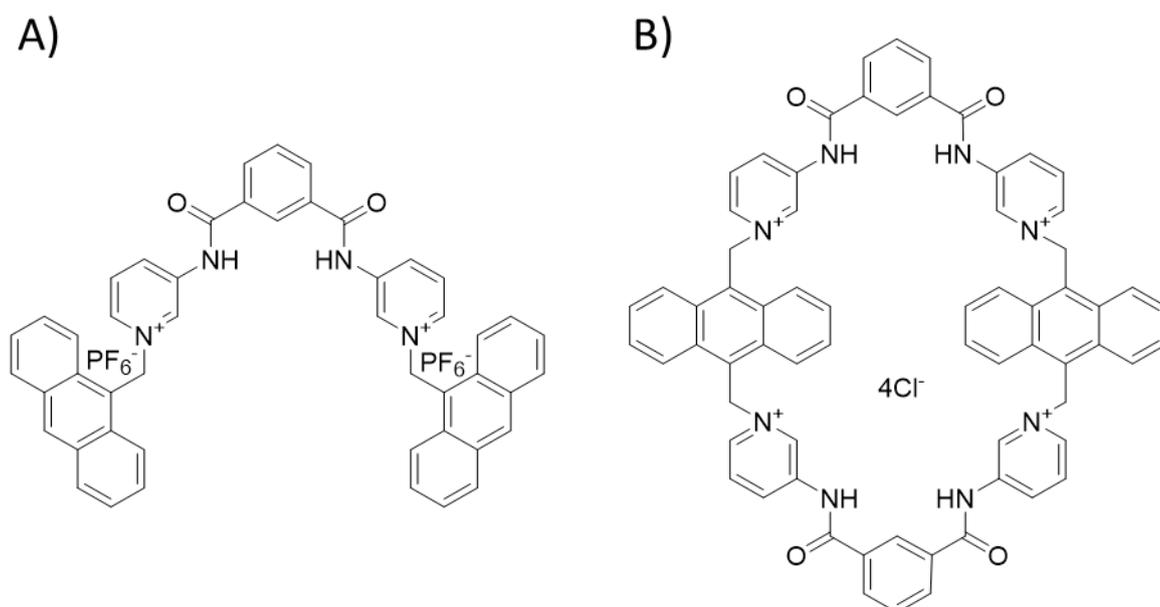

Figure 25 – Anthracene based fluorescent receptors for: A) The selective binding of anions such as $H_2PO_4^-$ and F^-, B) The selective binding of aliphatic carboxylates.

Making receptors that are fluorescent is advantageous because they can be studied using different techniques. Several techniques can be employed including: ultraviolet visible spectroscopy (UV-vis), fluorimetry or through proton nuclear magnetic resonance spectroscopy (^{1}H NMR).[196,197] ^{1}H NMR may be used to detect the change in structural stability or conformation of the fluorescent receptor upon the binding of a guest material. There will often be a change in the NMR spectra seen where a peak representative of the proton present on the urea moiety disappear due

to the formation of hydrogen bonds between them and the guest analyte. Changes exhibited in fluorimetry and UV-vis are described above in Figure 24.

As Hiscock *et al*. demonstrated, the TBA sulfonate-urea amphiphilic salt shown in Figure 23 exhibited the formation of dimers in the solid state, indicating the formation of intermolecular and intramolecular hydrogen bonds.[168] It follows that the benzothiazole-urea section of this compound makes for a good base for the development of novel fluorescent receptors that share this benzothiazole-urea moiety.

1.6 Project Aims

The aims of this project is to synthesise a calix[4]arene based amphiphilic salt that exhibits antimicrobial activity towards *MRSA* and *E.coli*, and/or improve the efficacy of amphiphilic antimicrobial active compounds already published by Hiscock *et al*.[169] Hence, two calix[4]arene inspired compounds will be synthesised and characterised in the gas phase using electrospray ionisation mass spectrometry (ESI-MS) and in the solution state using NMR spectroscopy. Compounds **2**-**9** will be synthesised as precursors to compounds **10** and **11** as the amphiphilic calixarene derivatives.

The characterisation and properties of two novel sulfonate-urea amphiphilic salts will be explored in the solid state, gas phase and solution state using single crystal X-ray diffraction (SCXRD), negative ESI-MS and NMR spectroscopy. Compounds **12** and **13** were synthesised outside of this project and sent for investigation only, previous versions of these amphiphiles have exhibited antimicrobial properties.[145]

Four benzothiazole-urea based fluorescent receptors have been synthesised and characterised in the solid state, gas phase and solution state using single crystal X-ray diffraction, negative ESI-MS, NMR spectroscopy and fluorimetry. Compounds **14-17** were tested against a variety of different anions which were acetate, benzoate, chloride, fluoride, hydroxide, hydrogen-sulphate, phosphate monobasic and sulphate. Compounds **1-17** are shown in Figure 26 below.
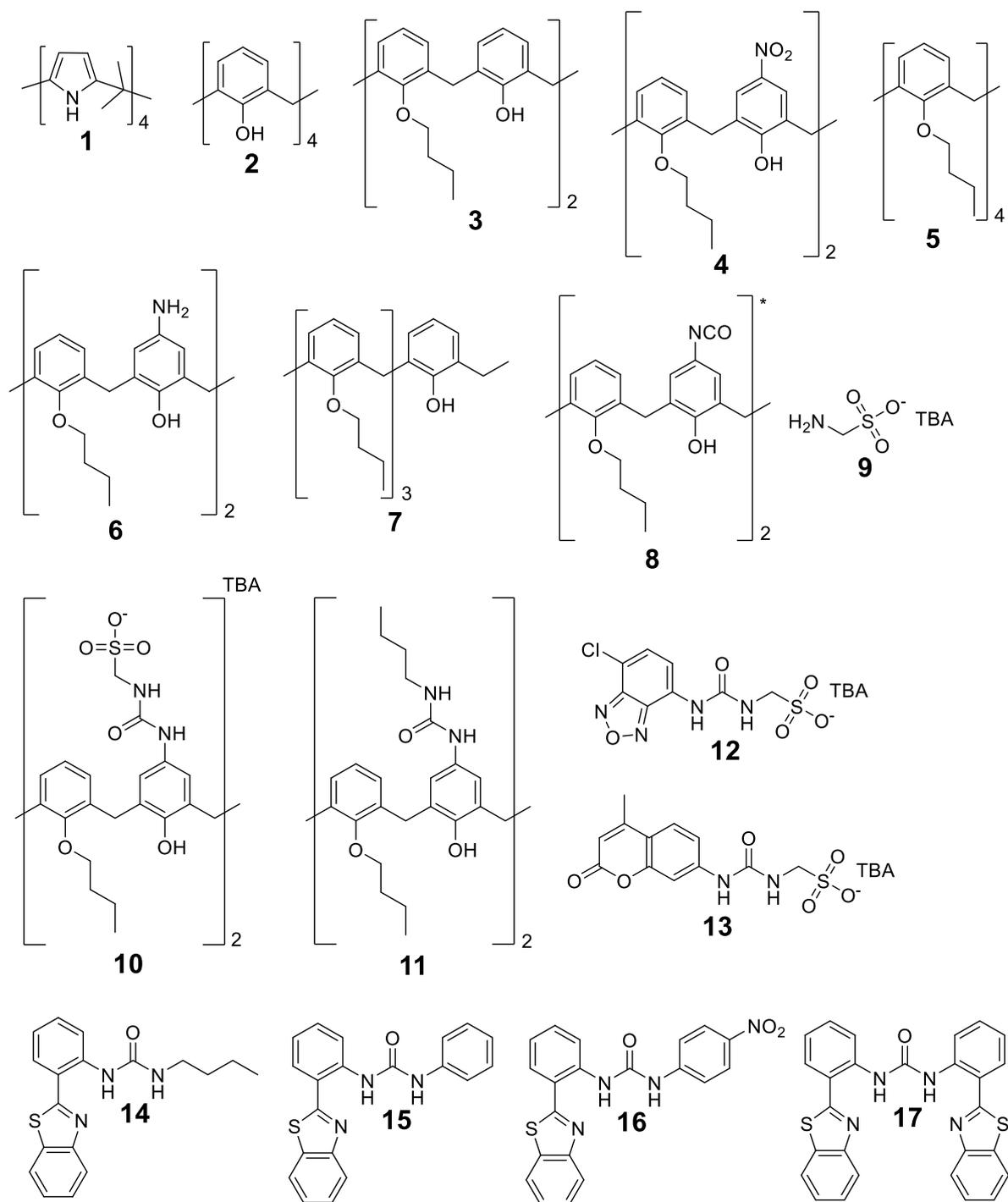
Figure 26 – Structures of compounds **1-17**.

2.0 Supramolecular self-associating amphiphilic calixarenes

A range of calix[4]arene compounds were synthesised to improve the delivery of novel antimicrobial amphiphilic salts as well as to increase the efficacy of their effect. Compound **1** was designed as a receptor molecule for another project. Compounds **2-9** were synthesised as

precursors to compounds **10** and **11**. Compound **10** was designed as an amphiphilic salt, and compound **11** was designed as an aliphatic urea, these were designed as the final structures of the calix[4]arene inspired receptors. Compound **10** and **11** were designed to have different structures so that the efficacy effects could be compared across different structures to better determine which functional group has the greatest effect as either a drug delivery system or as part of a coformulation product with amphiphilic salts.

2.1 Synthesis

Compounds **1-3**, **5** and **9** have been previously published[104,198–200] but are required to synthesise **4**, **6-8**, **10** and **11**, which are novel compounds. Compound **1** was synthesised according to reaction 1 (Scheme 1), by combining pyrrole and acetone, with a yield of 57 %. Compound **2** was synthesised according to reaction 2 (Scheme 1), by reacting p-tert-butylcalix[4]arene and phenol, with a yield of 66 %. Compound **3** was synthesised according to reaction 3 (Scheme 1), by reacting calix[4]arene with butyl iodide in the presence of potassium carbonate (K_2CO_3), producing a yield of 51 %. Compound **4** was synthesised through the direct nitration of compound **3**, reaction 4 (Scheme 1) using 70 % w/w nitric acid (HNO_2) and 95 % w/w sulphuric acid (H_2SO_4) diluted to 80 % w/w with a final yield of 91 %, according to reaction 4. Compound **5** was synthesised according to reaction 5 (Scheme 1) by reacting calix[4]arene with butyl iodide in the presence of sodium hydride (NaH), with a yield of 46 %.
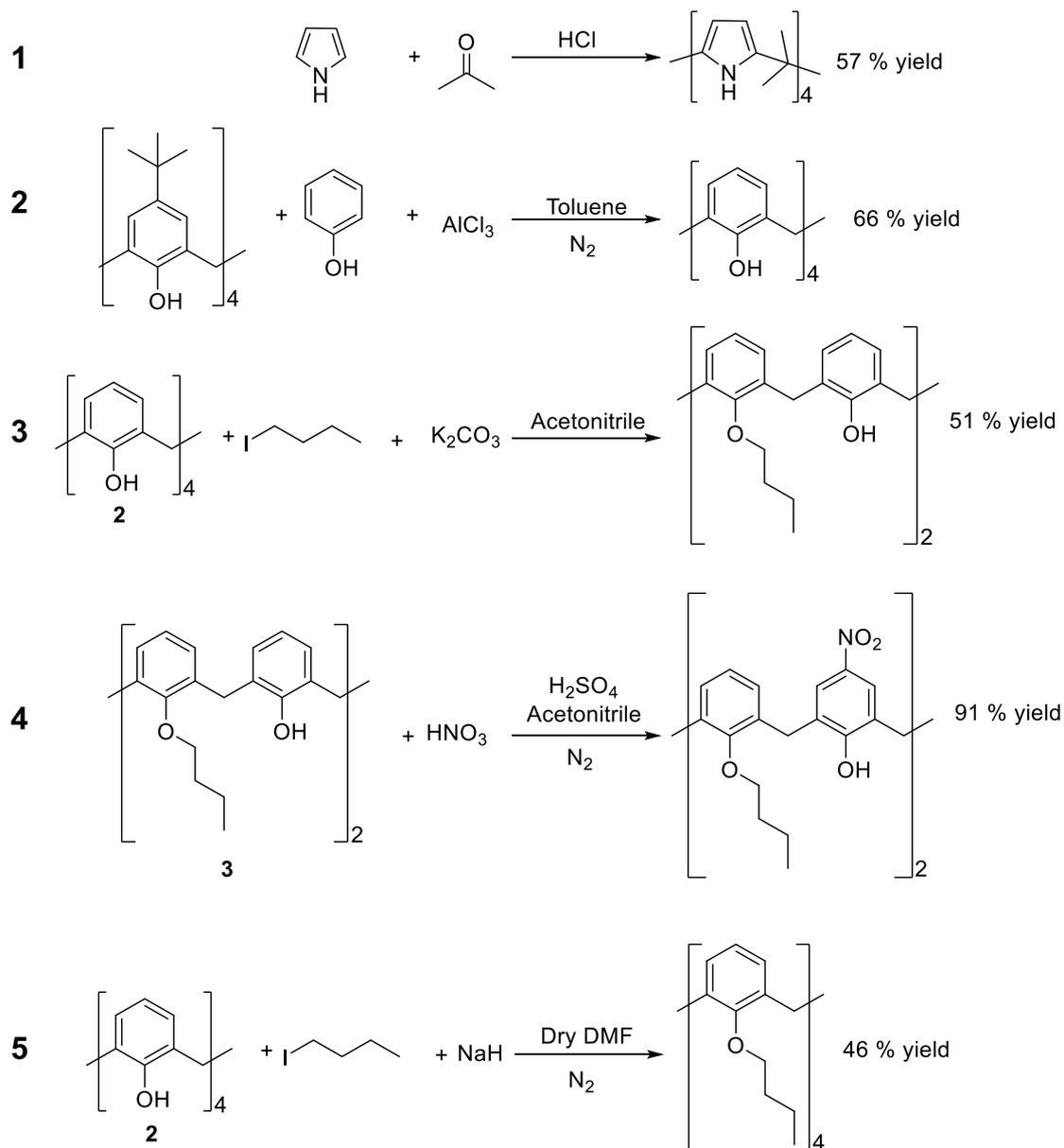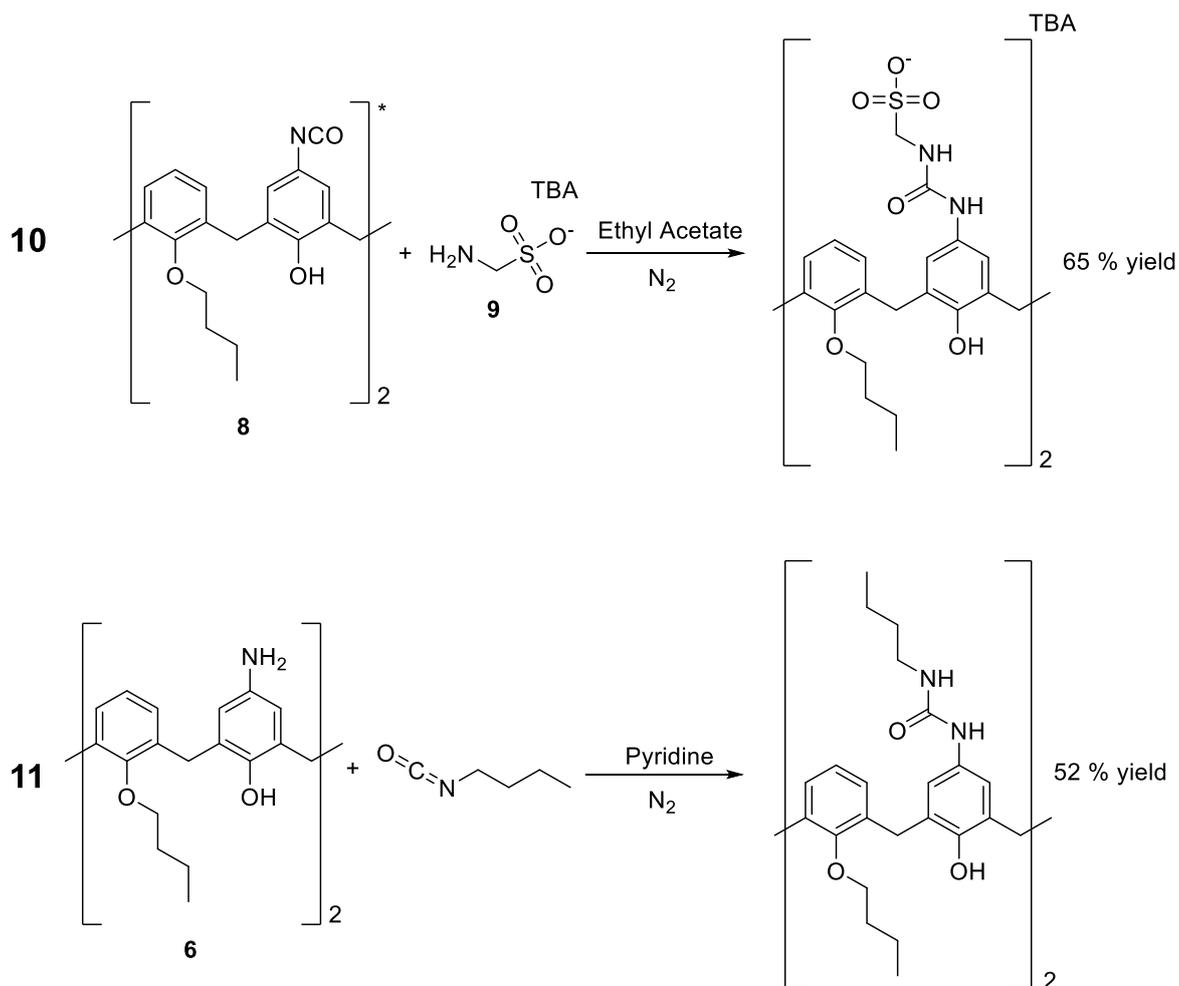
Scheme 1 – Synthesis scheme for compounds **1-5**, conducted at room temperature.

Compound **6** was synthesised through the reduction of compound **4** using a hydrogen gas balloon and palladium on carbon (Pd/C) with a yield of 90 %, according to reaction 6 (Scheme 2). Compound **7** was synthesised according to reaction 7 (Scheme 2), with a yield of 17 %. Compound **8** was synthesised as an intermediate to compound **10** through the reaction of compound **6** with triphosgene with an assumed yield of 100 %, according to reaction 8 (Scheme 2). The yield of compound **8** is assumed to be 100% because it is an unstable intermediate and so cannot be dried and weighed to gain the actual yield. This is the same for compound **9**. Compound **9** was synthesised according to reaction 9 with an assumed yield of 100 % (Scheme 2).
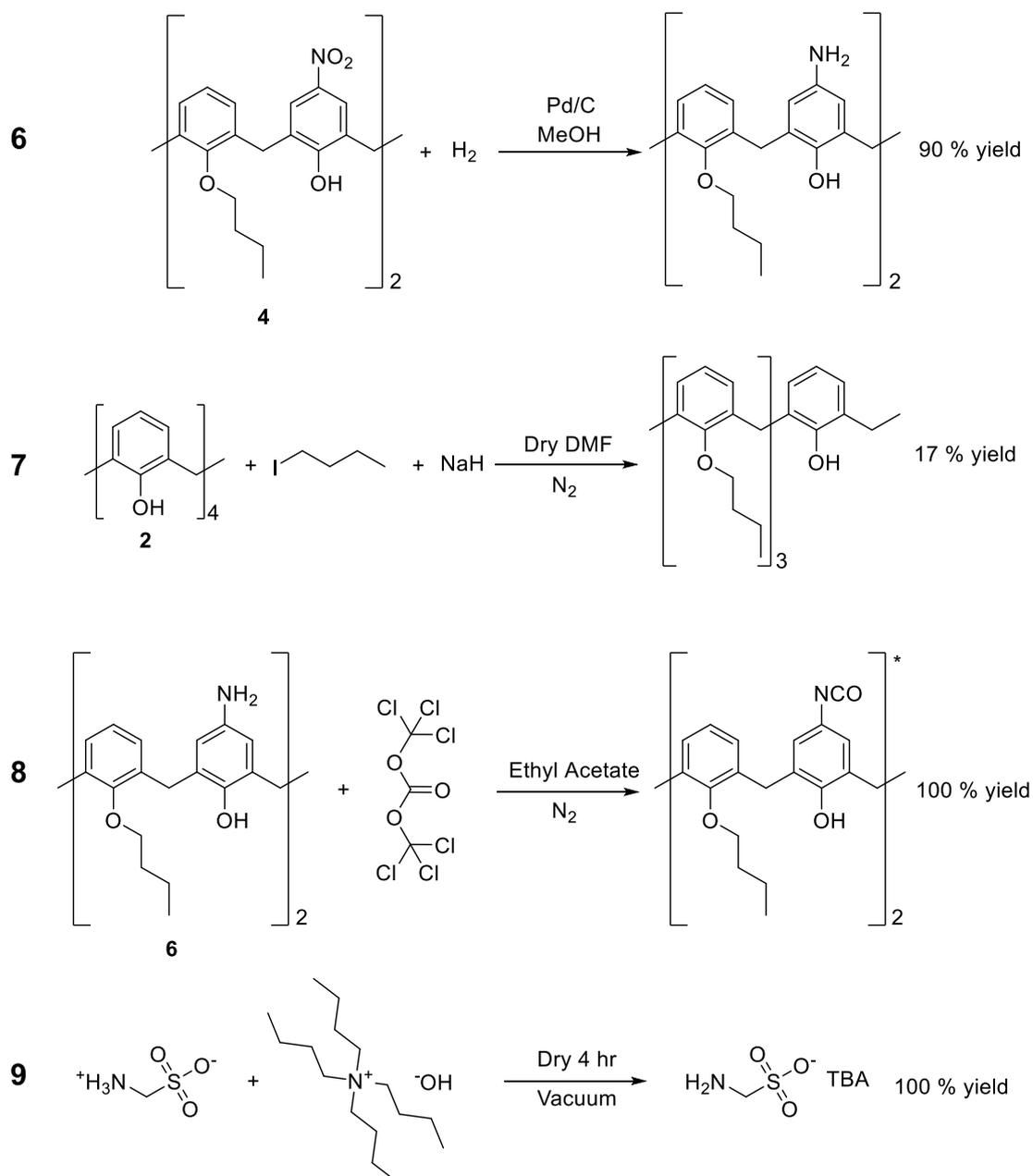
Scheme 2 – Synthesis scheme for compounds **6 – 9**, conducted at room temperature.

Compound **10** was synthesised according to reaction 10 through the reaction of compound **9**, aminomethanesulphonic acid TBA, with compound **10** in ethyl acetate (EtOAc) producing a yield of 65 %. Compound **11** was synthesised according to reaction 11 through the reaction of compound **6** with butyl isocyanate in pure pyridine with a yield of 52 % (Scheme 3).

Scheme 3 – Synthesis scheme for compounds **10** and **11**. TBA = tetrabutylammonium

The synthesis of these compounds varied with difficulty. For instance, compound **1** was relatively easy, as from start to finish the synthesis took one hour to complete. The synthesis of compound **2** on a smaller scale had a simple work up that did not involve too much time or too many steps. Workup on a larger scale became more challenging however, partially due to the evolution of copious amounts of gas.

The synthesis of compound **3** was relatively simple with few reaction steps, though the reaction was a little lengthy, taking two days to complete. The synthesis also worked well on larger scales, where multiple grams of compound **3** were being produced.

One of the most time-consuming issues however occurred when the synthesis of an indirectly nitrated calix[4]arene compound was attempted. Several attempts were made to synthesise a compound such as this (Figure 27A), which ultimately resulted in failure. The synthesis of this

compound was attempted several times, with changes made to the mass of reactants used or which reactants were used. For instance, the use of sodium hydroxide (NaOH) instead of triethylamine as a base catalyst. Finally, the length of time in which the synthesis ran was also altered several times. In each case these experiments did not work; this was proven when only starting materials were isolated after the completion of the reaction.

Some of the experiments attempted were also very lengthy and involved multiple reaction steps. For instance, where compound **3** was reacted with benzoyl chloride (Figure 27B) and NaOH. Compound **3** was first stirred with sodium hydroxide for five hours under nitrogen gas in chloroform (CHCl$_3$). After this it was taken to dryness and placed on the Schlenk line overnight. After which the remaining residue was dissolved into dry dimethylformamide (DMF) and added to this was benzoyl chloride. The solution was then stirred in an ice bath under nitrogen gas for five hours. The solution was then washed with water and dried over magnesium sulphate. The magnesium sulphate was then filtered off and the remaining solution taken to dryness to produce a solid, which after analysis, was shown to be the benzoyl chloride.
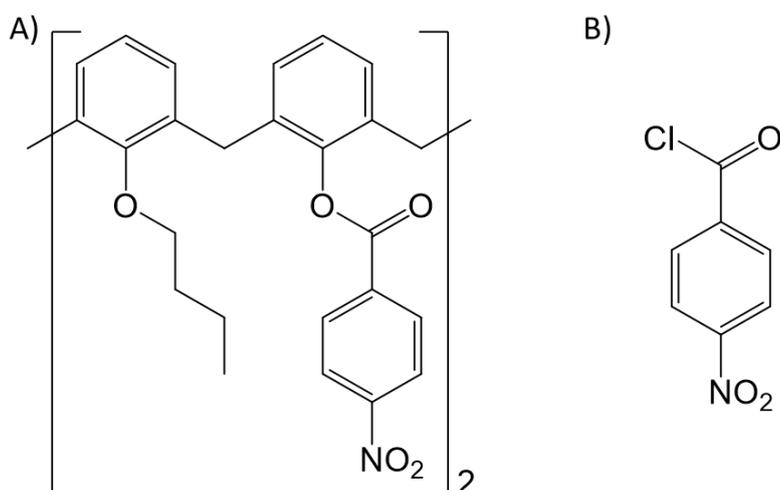

Figure 27 – Compound examples: A) Indirectly nitrated calix[4]arene derived compound, B) Benzoyl chloride.

From here, the decision to abandon attempting to synthesise the indirectly nitrated compounds. A few attempts were made to synthesise compound **4** before it was successful. A complicated reaction involving compound **3**, oxalic acid dihydrate, sodium nitrite (NaNO$_2$) and silicon dioxide (SiO$_2$) was attempted. This took approximately 40 minutes. Though several steps

were involved, such as introducing soda lime, which is a mixture of sodium hydroxide and calcium hydroxide ($Ca(OH)_2$), to neutralise the poisonous gases nitrogen monoxide, (NO) and nitrogen dioxide (NO_2) that were produced during the reaction. The solid SiO_2 was filtered before the reaction mixture was taken to dryness.

This reaction did not work as only starting materials were isolated, and so the use of concentrated nitric acid and sulphuric acid as a catalyst was used to produce compound **4**. This reaction was successful, and the conditions were tweaked slightly in an attempt produce a mono-nitrated version (Figure 28) of compound **4**. The synthesis of this compound was revisited throughout the year, though the reaction remained unsuccessful. Changes were made to the reaction conditions during synthesis, such as: using nitric acid alone, using a single drop of 95 % w/w sulphuric acid, using a more diluted portion of sulphuric acid at 60 % or 70 % w/w instead of the recommended 80 % w/w, and by neutralising the reaction at different times, ranging from 30 seconds to 5 minutes, or where there was an immediate colour change. As the reaction remained unsuccessful, the synthesis was not carried forward.
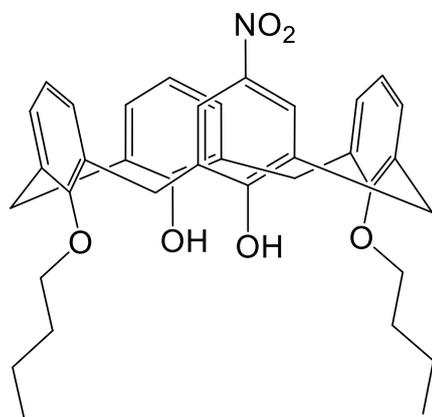
Figure 28 – Mono-nitrated version of compound **4**.

The synthesis for compound **5** was not only lengthy, but also involved a lengthy work up. The reaction itself took in total approximately 26 hours to complete and produced compound **7**, which is the same as compound **5** but with the butyl chains in triple addition as opposed to a quadruple addition of the alkyl chains. To achieve the synthesis of compound **5** the molar amount of sodium hydride was increased to catalyse the reaction to completion within the 26-hour time frame.

Compounds **5** and **7** were synthesised in the aim of producing a compound that would better penetrate the cell membrane by having more butyl chains attached. These compounds were not carried forward due to time constraints. The synthesis of the mono-nitrated version (Figure 29) was unsuccessful and followed the same methodology as that was used to synthesise compound **4**.
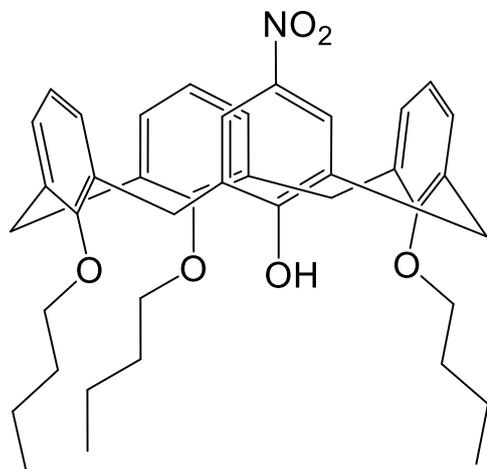

Figure 29 – Example of mono-nitrated version of compound **7**.

The synthesis of compound **6** was relatively simple, though it took between 24 and 72 hours depending on the amount of compound **4** in the reaction. Often compound **4** would not fully dissolve into the methanol (MeOH) but would dissolve as the reaction progressed. Purification of compound **6** from the reaction mixture was difficult, there seemed to always remain a product that could not be removed. Unfortunately, this meant that compound **6** could not be purified enough for characterisation, as shown with ^{1}H NMR, but it was pure enough to progress with experimentally.

Compound **8** was synthesised as an intermediate compound towards the synthesis of compound **10**. This was to enable the formation of a urea functional group within the compound, so that the sulfonate functionality of compound **9** can be amended onto compound **8**. Compound **9** was synthesised whilst the reaction for compound **8** was progressing. Compound **11** was synthesised from compound **6** through the addition of butyl isocyanate. Due to time constraints, compounds **10** and **11** were not purified even though several methods were attempted. Including crystallisation from chloroform, from methanol and from ethyl acetate, precipitation from

chloroform with methanol, or from ethyl acetate with water. Compounds **10** and **11** remained impurified and so, uncharacterised.

The reactions for compounds **8**-**11** were relatively simple and took between 6 and 24 hours to complete. There were several moments which have been discussed here that meant time was a limiting factor. Overall, the progression of the compounds discussed in this chapter was difficult and often involved lengthy method development. However, once specific avenues had been explored the reactions used to synthesise compounds **1**-**11** were relatively easy to follow and complete, though several were time consuming.

2.2 Self-association in the solid state

2.2.1 Single-crystal X-ray diffraction studies

Single crystals are materials in which the crystal lattice of the sample is seen throughout. Max Von Laue suggested the use of single crystals as diffraction gratings in 1912[201] due to the presence of identical repeating units. This is a non-destructive technique that is used to obtain three dimensional structures of materials in the solid state. This technique is also capable of providing other information; for instance it may give information on bond distance, bond angle, conformational structures and intermolecular forces.[202]

Crystal structures of compounds **1** and **2** are previously published[203,204], along with crystals from similar structures to compounds **3** and **5**.[205,206] Single crystal structures of compound **4** were obtained through the slow evaporation of a mixture of $CHCl_3$: MeOH. Crystals of compounds **6, 7, 10** and **11** were not obtained, though many solvent systems were attempted such as a 1:1 ratio of $CHCl_3$: MeOH, a 2:1 ratio of $CHCl_3$: MeOH and a 1:1 ratio of Acetone (Ace): MeOH. The crystal structure of compound **4** was not refined due to time restraints and the coronavirus.

2.2.1.1 Results and discussion

The rudimentary crystal structure of compound **4** obtained directly from a Rigaku Oxford Diffraction Supernova diffractometer demonstrated the position of the nitro group on the phenolic units. Unfortunately, the crystal structure of compound **4** was lost and it was not able to be recovered. The hydroxyl groups present on the calixarene act more favourably to p-substitution than the alkyl groups that are present.[207] This means that nitration of the calixarene occurs on the phenolic units (Figure 30).
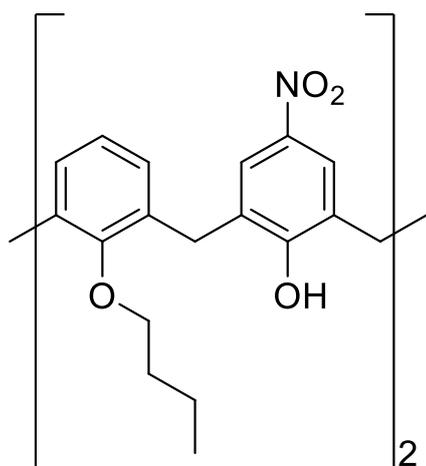
Figure 30 – Structure of compound **4**.

2.3 Self-association in the gas phase

2.3.1 Electrospray ionisation mass spectrometry

This technique provides qualitative information about a sample. It can provide an insight into weak non-covalent bonding which occurs in the gas phase, after ionisation[208] if the molecule is not naturally ionic. This is achieved when the sample compound is injected into an ionisation source.[208] Compound **4** was analysed using negative ESI-MS to determine the presence of low level complexes in the gas phase, which if present, would indicate self-association within, or between the molecules of the compound studied.

2.3.1.1 Results and discussion

Preparation of the samples were standardised in order to make the results comparable across each sample. Approximately 1 mg in of each compound was dissolved into 1 mL of methanol. This solution was further diluted 100-fold before undergoing analysis where 10 μL of each sample was then injected directly into a flow of 10 mM ammonium acetate in 95 % water (flow rate = 0.02 mL/min). Compounds **4** (Figure 30) is neutral, and so must be ionised to produce the monomeric state with a mass to charge ratio (m/z) [M - H$^+$]$^-$ (Table 1).

Table 1 – High Resolution mass spectrometry theoretical and experimentally derived values for compound **4**.

Compound	m/z [M - 2H$^+$]$^-$		m/z [M + M - H$^+$]$^-$	
	Theoretical	Actual	Theoretical	Actual
4	312.1241	Unknown	624.2482	624.3578

The monomeric species [M - 2H$^+$]$^-$ m/z for compound **4** was theoretically observed at 626.2628 – (2 x 1.0073) = 624.2482, 624.2482 / 2 = 312.1241. A loss of two protons is observed here because of the symmetrical bis nature of this compound. Unfortunately, due to lockdown being implemented by the government because of the corona virus the clear section of the mass spectrum containing the peaks situated in the region of 312 is unavailable at this time. If it were, it would depict a clear enhanced version of the spectra displaying this peak, in replacement of this, the whole spectrum is provided with the region in 312 highlighted with a black arrow (Figure 31).
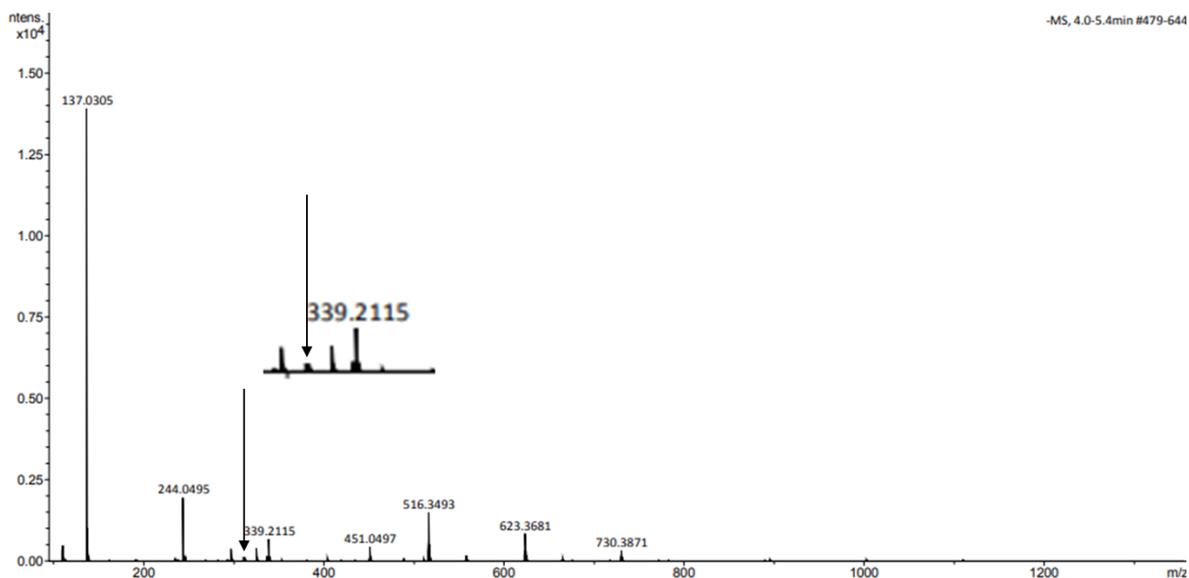
Figure 31 – Full mass spectrum obtained for compound **4**. The arrows indicated the approximate region containing the monomeric peak for compound **4**, with an enlarged section.

The presence of a peak at 624.3578 indicates the presence of a dimer formed in the gas phase. Where the dimer would have an exact mass of 624.2482 x 2 = 1248.4964. So, because this dimer has a charge of -2, we theoretically see a peak at m/z 624.2482, as 1248.4964 / 2 = 624.2482, practically a peak is observed at 624.3578 (Figure 32). It is possible for molecule containing the nitro group to form hydrogen bonds[209] with other species, such as the hydroxide group, which compound **4** contains both these groups. This could be an explanation for the formation of dimers in the gas phase by compound **4**.
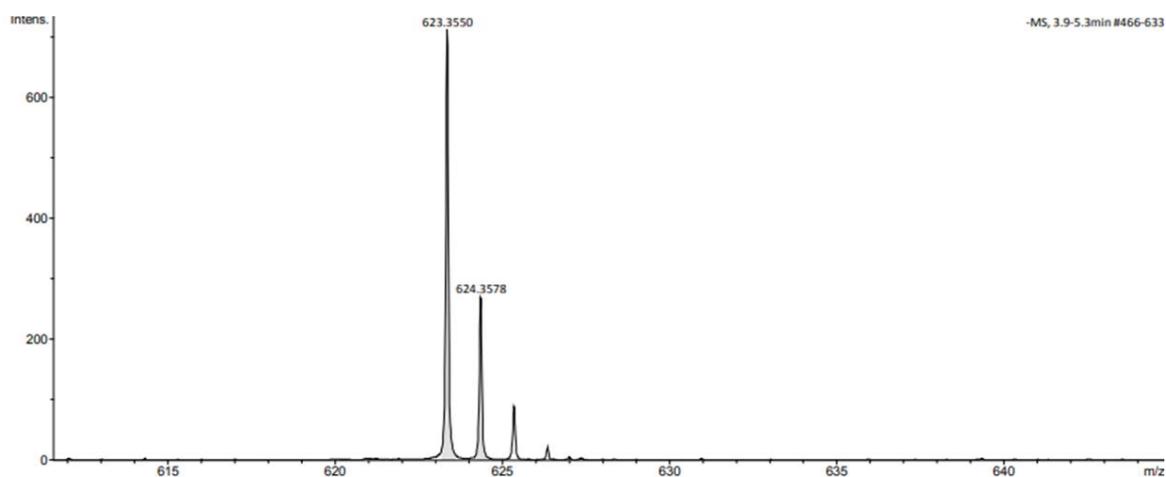
Figure 32 – Electrospray mass spectrometry spectrum of compound **4** showing the monomeric species.

The ESI-MS data for compound **4** reveals there are non-covalent interactions in the gas phase. Compounds **10** and **11** were designed to self-associate. The presence of dimers in their relative ESI-MS would support this theory. The strength of interactions would have to be explored using alternative measures. However, ESI-MS was not obtained for compounds **10** and **11**. Several attempts were made to obtain the data for these compounds, without success.

2.4 Future works

Due to the time restraints and difficulty of synthesis not all studies were completed on this series of compounds. Further studies as well and purification and characterisation are required before any formal assessment of the properties of these molecules can be determined:

- ESI-MS for compounds **10** and **11**.

- Self-association and association properties on compounds **10** and **11**. Quantitative NMR, diffusion-ordered spectroscopy (DOSY), dilution studies, titration studies.

- Dynamic light scattering (DLS) and zeta potential studies.

- Critical micelle concentration (CMC) studies.

- Antimicrobial activity screening.

- Studies on Gram +ve and gram -ve bacteria, such as (*S.aureus*) and (*E.coli*) respectively.

Compounds **10** and **11** were the final compounds for this portion of synthesis and were the end goal. Had more time been available these molecules would have gone on to been tested for their application as antimicrobial active compounds alongside efficacy studies in relation to compounds already published from the Hiscock research group that show antimicrobial activity as well as self-association properties.[145]

3.0 Study of self-associative urea-sulfonate salts

Using knowledge of hydrogen bonded-anion coordination, the urea-anion self-association properties of compounds **12** and **13** have been explored. Several different techniques were employed in the solid, liquid and gaseous states including, the use of single-crystal structures, ^{1}H NMR and mass spectrometry. Compounds **12** and **13** both possess HBA and HBD regions within their structures, as presented by Hiscock *et al* in their publications of self-associating urea-sulfonate salts.[168,198]

3.1 Synthesis

Compounds **12** and **13** (Figure 33) were synthesised by Dr Claudia Caltagirone at the University of Cagliari, Italy.
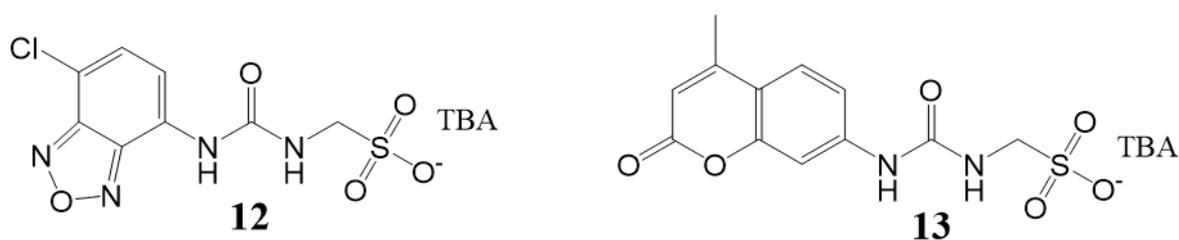
Figure 33 – The structure of compounds **12** and **13**.

3.2 Self-association in the solid state

3.2.1 Single-crystal X-ray diffraction studies

Single crystals were obtained of compound **13** through the precipitation of the compound with water from ethyl acetate. There was difficulty trying to obtain crystallisation through standard methods, so in the hope of obtaining a crystal, the precipitate of compound **13** from ethyl acetate appeared to contain crystals, which it did. No crystals were obtained for compound **12** even though several different systems were attempted, for example, through slow evaporation in methanol,

from methanol with a drop of DMSO, through phase separation using ethyl acetate and water layers and finally though precipitation as a last attempt. All crystallography data was obtained, refined and processed by Dr Jennifer Hiscock.

3.2.1.1 Results and discussion

The crystal structure of compound **13** (Figure 34) shows the full crystal structure of compound **13** along with the TBA counter cation present, also displaying the presence of water within the structure. The structure depicts the formation of intermolecular bonds formed between two molecules of compound **13**. An intermolecular hydrogen bond has also been formed between the urea oxygen of one molecule to the hydrogen on a molecule of water.
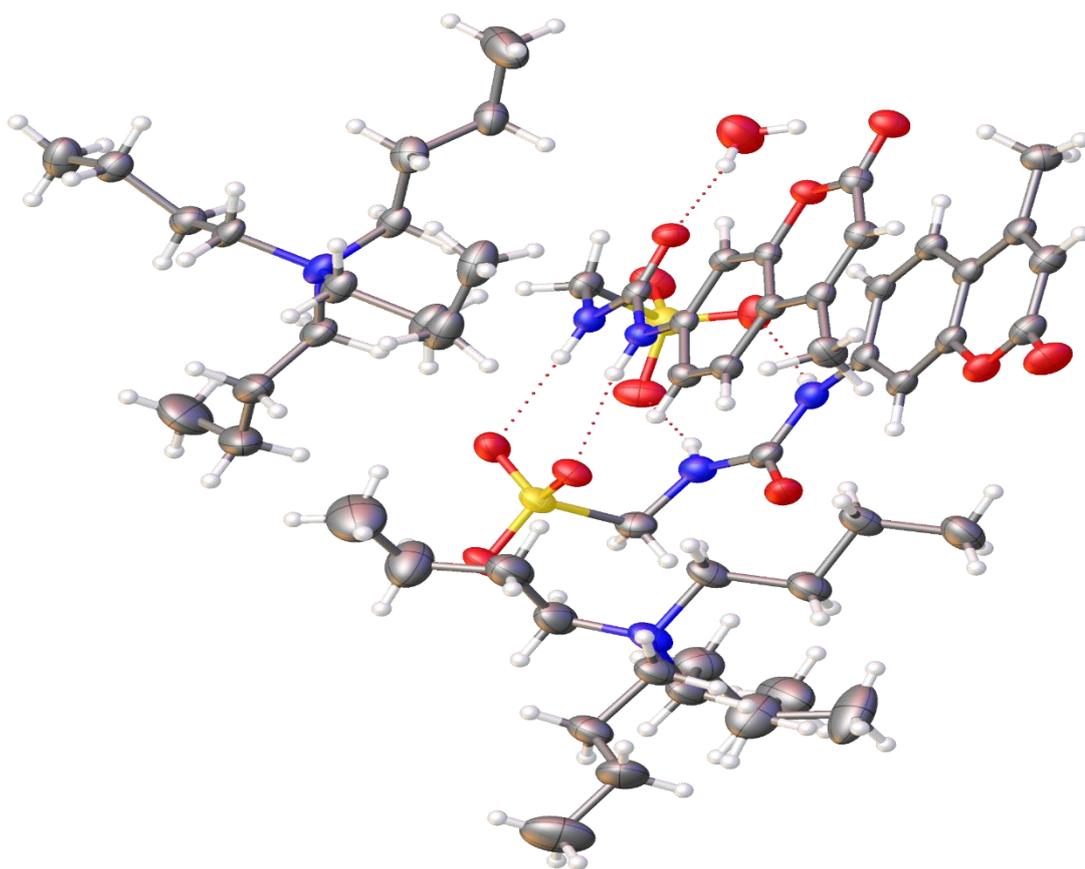
Figure 34 – Single crystal X-ray structure of compound **13**.

The crystal structure of compound **13** (Figure 35) shows the compound self-associates in the solid state through the formation of a hydrogen bonded dimer. The intermolecular hydrogen bonds

are formed between the urea NHs and the sulfonate oxygens. The structure is stabilised by four hydrogen bonds, two originating from each molecule. The urea acts as an HBD group donating the hydrogen bond to the sulfonate oxygens, which act as the HBA group.
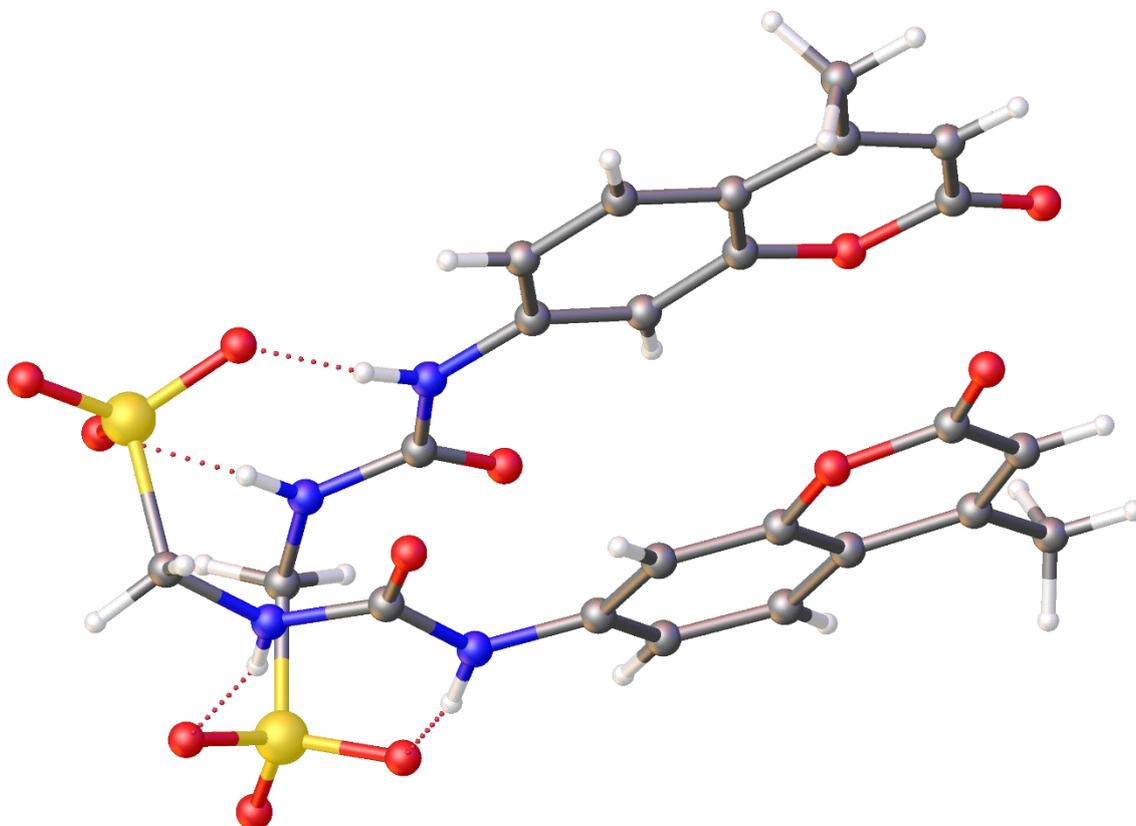
Figure 35 – Single crystal X-ray structure of compound **13** showing self-association in the solid state through the formation of a dimer stabilised through four hydrogen bonds. Water and TBA counter cation omitted for clarity.

The extended crystal packing structure of compound **13** (Figure 36) shows the dimers associate through intermolecular hydrogen bonds formed between the molecules of compound **13** and water. The water molecule acts as an intermediate for the formation of hydrogen bonds between the aromatic carbonyl group of one molecule in a dimer, to the urea oxygen of another molecule of compound **13** situated in a separate dimer. The presence of water within the crystal structure aids in stabilising the formation of the crystal for compound **13**.
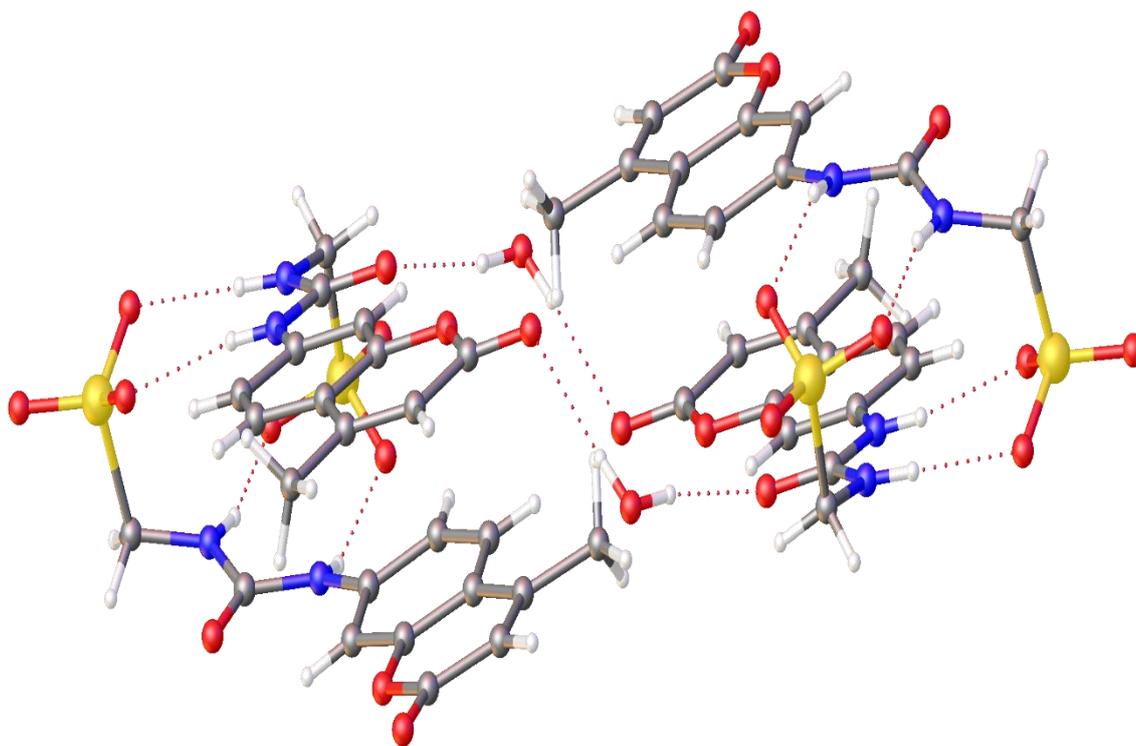
Figure 36 – Single crystal X-ray structure of compound **13** demonstrating its crystal packing arrangement. TBA counter cation omitted for clarity.

The single crystal structure of compound **13** demonstrates that there is self-association occurring in the solid state. The crystal packing shown in Figure 35 demonstrates that the molecules are arranged slightly offset to one another. The aromatic regions of each molecule of compound **13** are stacked above one another, but the molecule twists and bends slightly at the urea group, enabling hydrogen bonding to occur between the two compounds in a structurally stable position. The presence of intermolecular hydrogen bonding in the solid state is a sure sign of self-association, however this method cannot be used alone to define these types of interactions. This is because though these interactions may change in the solution state, or the gas state and so it is important to study the presence of these bonds in these states to define them fully.

3.3 Self-association in the gas phase

Methods that can be employed in both the gas and solution state will indicate the presence of hydrogen bond formation within compounds **12** and **13**. This is particularly helpful here as no crystal

structure was obtained for compound **12**. Although, these methods cannot indicate where these bonds are occurring, like crystallography data can, it can be theorised that as these compounds share similar structures, intermolecular bonding will occur in compound **12** as they did in compound **13** and it can be expected that compound **12** will form dimers.

3.3.1 Electrospray ionisation mass spectrometry

Compounds **12** and **13** were analysed using negative ESI-MS to determine the presence of low-level complexes in the gas phase. Approximately 1 mg in of each compound was dissolved into 1 mL of methanol. This solution was further diluted 100-fold before undergoing analysis where 10 µL of each sample was then injected directly into a flow of 10 mM ammonium acetate in 95 % water (flow rate = 0.02 mL/min).

3.3.1.1 Results and discussion

The data obtained from this experiment shows that the anionic component of compounds **12** and **13** exist as both monomeric and dimeric species in the gas phase. Compounds **12** and **13** are both salts, and therefore exhibit the anionic monomeric state [M]$^-$ and the anionic dimeric state [M + M + H$^+$]$^-$ (Table 2). The anionic components of compounds **12** and **13** are charged species, and so do not require ionisation. Both compounds exhibit a negative charge of one. Meaning that the values obtained from the mass spectra have been divided by one and are representative of the [M]$^-$ and [M + M + H$^+$]$^-$ ions formed.

Table 2 – High Resolution mass spectrometry theoretical and experimentally derived values for compounds **12** and **13**.

Compound	m/z [M]$^-$		m/z [M + M + H$^+$]$^-$	
	Theoretical	Actual	Theoretical	Actual
12	304.9753	304.9765	610.9579	610.9593
13	311.0343	311.0356	623.0759	623.0773

The protonated dimeric species of compounds **12** and **13** were observed. Using compound **12** as an example (Figure 37). The monomeric [M]$^-$ m/z peak is observed at 304.9765 and the protonated dimeric peak [M + M + H$^+$]$^-$ is observed at (2 x 304.9765) + 1.0073 = 610.9593. this calculation indicates that a dimeric species is present in the gas phase and is also apparent for compound **13** (Figure 38).
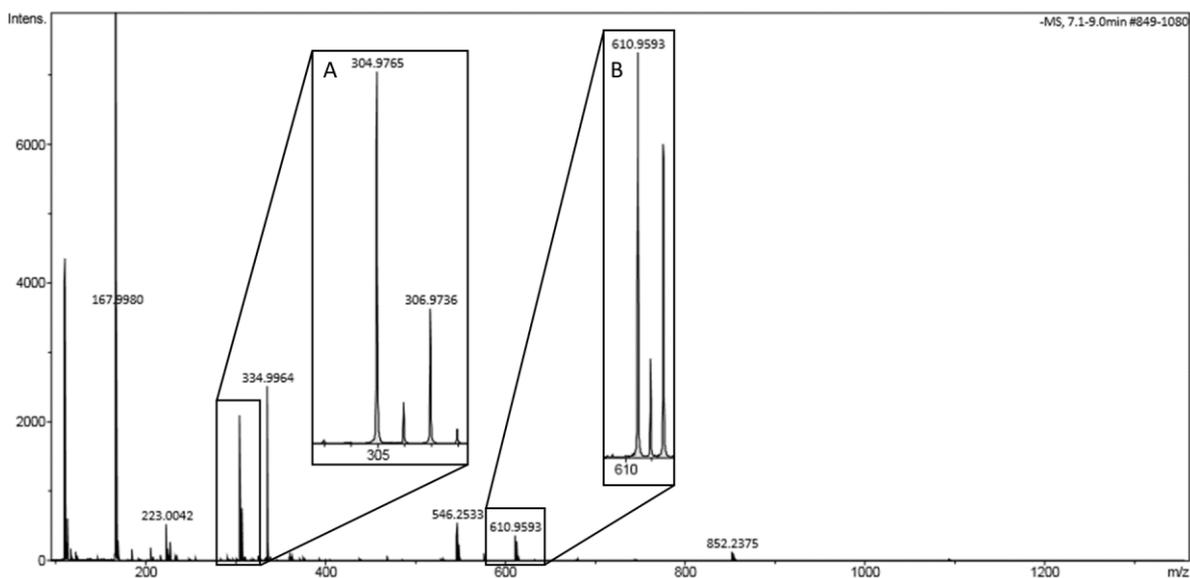
Figure 37 – Electrospray mass spectrometry spectrum of compound **12**, depicting species: A) [M]$^-$, B) [M + M + H$^+$]$^-$.
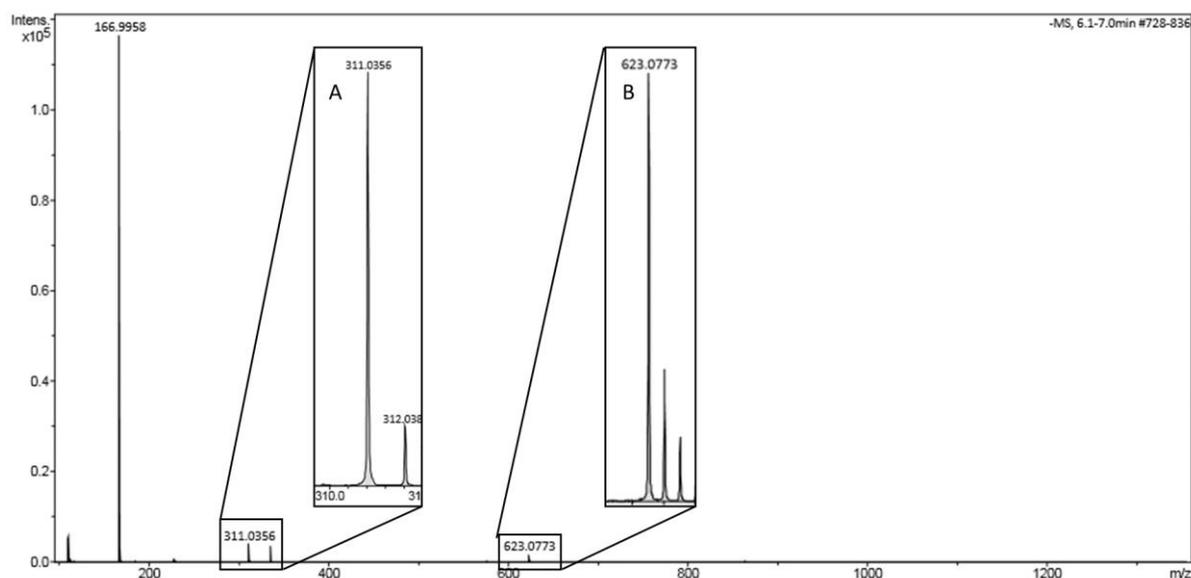
Figure 38 – Electrospray mass spectrometry spectrum of compound **13**, depicting species: A) [M]$^-$, B) [M + M + H$^+$]$^-$.

The presence of dimers in the gas phase indicate the strength of bonds formed between molecules are quite strong, especially proven as the complexed structure of the dimer survives the experimental conditions. The phenomenon of self-association in the gas phase is quite unusual, as the experimental conditions would usually degrade hydrogen bonding in the gas phase. The strength of these interactions is not quantified here in the gas phase and so, will be quantified and studied in the solution state.

3.4 Association in the solution state

Studies in the gas and solid state occur in the absence of solvent. The absence of solvent allows for the interactions between compounds to be observed. However, the existence of solvent-solute interactions has been well documented, therefore it is important to investigate these interactions for novel compounds. Solvent molecules may contain either HBA or HBD groups, which may in turn affect the self-association properties of molecules, such as compounds **12** and **13**.

A common solvent that acts both as an HBA and an HBD is water (Figure 39C). This is due to the polar protic nature of the solvent, in which it interacts through the proton during hydrogen bonding.[210] Whereas, DMSO acts as an HBA only (Figure 39C), this is because it is a polar aprotic solvent. This means that it interacts with solutes through the oxygen atom when acting as a HBA.[211] Previous studies by Hiscock *et al*. have established experimental parameters to determine the association properties of compounds in differing solvent conditions.[167] These techniques have been employed in the studies of compounds **12** and **13** in order to characterise the self-association properties of these compounds in the solution state.
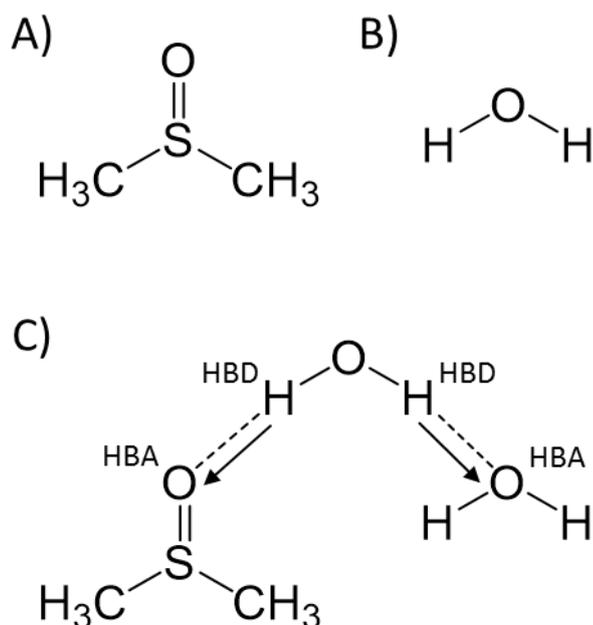
Figure 39 – Structure of solvents showing: A) The structure of DMSO, B) The structure of water, C) The groups involved in acting as HBA and HBD groups for DMSO and water.

3.4.1 ^{1}H NMR quantification studies

Quantitative ^{1}H NMR (qNMR) studies are employed to quantify the interactions occurring within compounds **12** and **13**. ^{1}H NMR possesses an inherent property, that each NMR signal in a spectrum is proportional to the number of nuclei responsible for that peak.[212] Advantage can be taken of this property, where an experiment is devised which employs the technique of using an internal standard that is then compared with a known concentration of the compound. This makes it possible to calculate the proportion of molecules in solution. If the proportion, or percentage of molecules calculated in solution is below 100 % in a given solvent, the 'missing' compound is classified as 'NMR silent' because it exceeds the limitations of this technique and indicates the formation of larger structures, which are too large to be detected.

Solution state NMR possesses several limitations which are: sensitivity, solubility of compounds and the natural abundance of an isotope. One limitation of this experiment that cannot be reduced is the ability for the instrument to detect larger structures in solution. This is often because larger structures that are formed in the solution state may adopt solid like characteristics, meaning they

can no longer be detected by the instrument, thus becoming 'NMR silent'. The larger structures become NMR silent due to their slowing mobility within the solution state, meaning that the NMR is not sensitive enough to detect the spin resonance of slower moving particles.[213] This limitation is taken advantage of in qNMR to indicate the presence larger structure formation in the solution state.

Compounds **12** and **13** were studied under these conditions in a DMSO-d_6. 1 % dichloromethane (DCM) is added to the solvent as an internal standard with a single ^{1}H NMR signal at 5.76 ppm in DMSO-d_6. Deuterated water (D_2O) spiked with 5 % EtOH as the internal standard has also been employed. The EtOH produces a peak at 3.65 ppm in this solvent. These internal standards are used because their peaks appear at a shift that does not overlap with any peak that is representative of compounds **12** or **13**. This means that the internal standard signals can easily be comparatively integrated.

3.4.1.1 Results and discussion

The data obtained from the qNMR studies (Table 3) show that there was a proportion of compound that became NMR silent for compounds **12** and **13** in deuterated DMSO (DMSO-d_6). This was also observed in D_2O: EtOH for compound **12**, but no proportion of compound **13** became NMR silent in this solvent system, possibly due to the solubility of this compound in water.

Table 3 - Overview of the calculated percentage of compound that became NMR silent at a total concentration of 111.12 mM in DMSO-d_6, 1 % DCM. With a total concentration of 5.56 mM in H_2O: EtOH 19:1 solution for compounds **12** and **13**.

Compound	% Loss DMSO-d_6 with 1 % DCM	% Loss D_2O with 5 % EtOH
12	44	19
13	29	0

The results of the experiment indicate that a large portion of the molecules form larger aggregates with solid-like characteristics in DMSO-d_6. This has been seen in previously published data, but often it is reported that no proportion of the molecules become NMR silent in the DMSO solvent conditions.[145] On the other hand, compounds **12** and **13** when observed in the D$_2$O: EtOH solution, only compound **12** showed signs of the compound being NMR silent, indicating the formation of larger structures in this solvent system. Where no molecules became NMR silent in this solvent condition for compound **13**, it indicates that no large aggregates are being formed.

Using compound **13** as an example in DMSO-d_6, the DCM peak is calculated to be 2.95. The CH peak at 7.15 ppm should integrate to be 1, however it integrates for 0.71 (Figure 40). Therefore, it is possible to detect only 71 % of the compound, where 29 % of the compound is 'silenced' by forming larger solid-like aggregates.
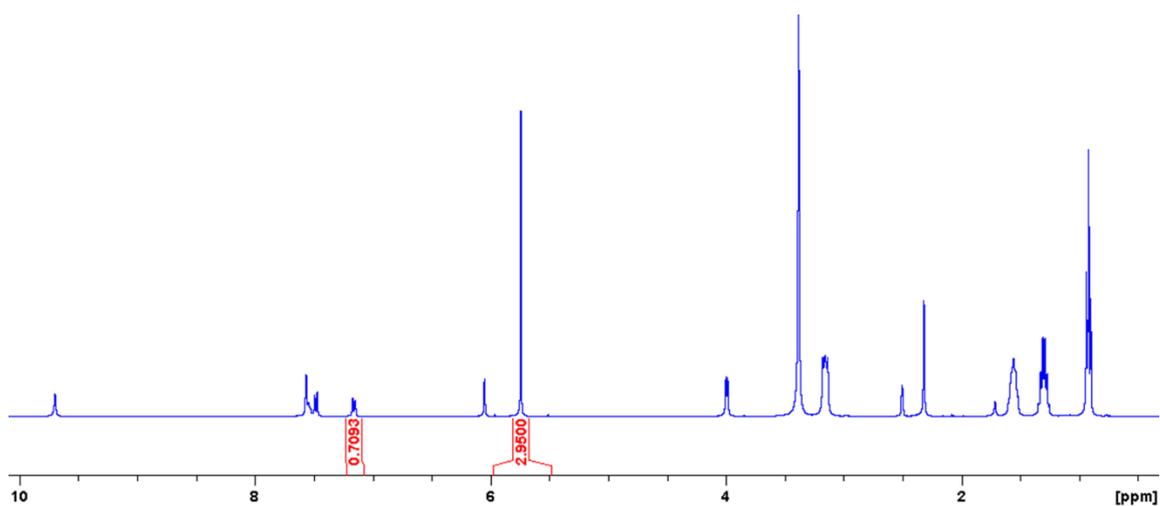
Figure 40 – ^{1}H NMR spectrum (d$_1$ = 60 s) of compound **13** (0.0300 g, 111.12 mM) and DCM (5 μl, 0.08 mM) in DMSO-d_6. 29 % loss of compound observed upon comparative signal integration.

Compound **13** showed that no proportion of molecules formed larger aggregates in the D$_2$O solvent system depicted through comparative integration (Figure 41).
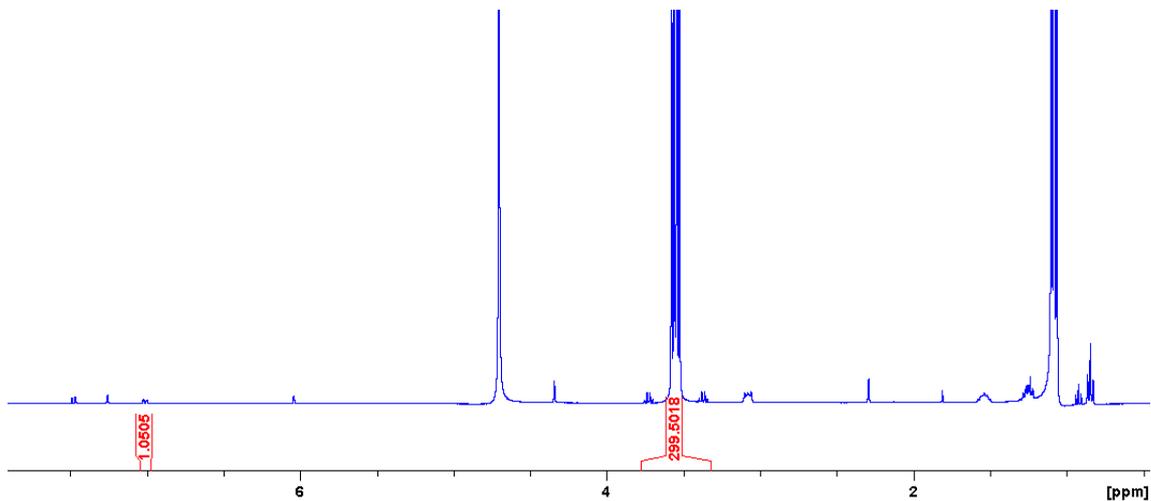
Figure 41 – ^{1}H NMR spectrum (d_1 = 60 s) of compound **13** (0.0015 g, 6.00 mM) and EtOH (5 µl, 0.43 mM) in D$_2$O. No apparent loss of compound observed upon comparative signal integration.

Compound **12** showed a 44 % decrease in the proportion of molecules detected by ^{1}H NMR, shown through comparative integration (Figure 42).
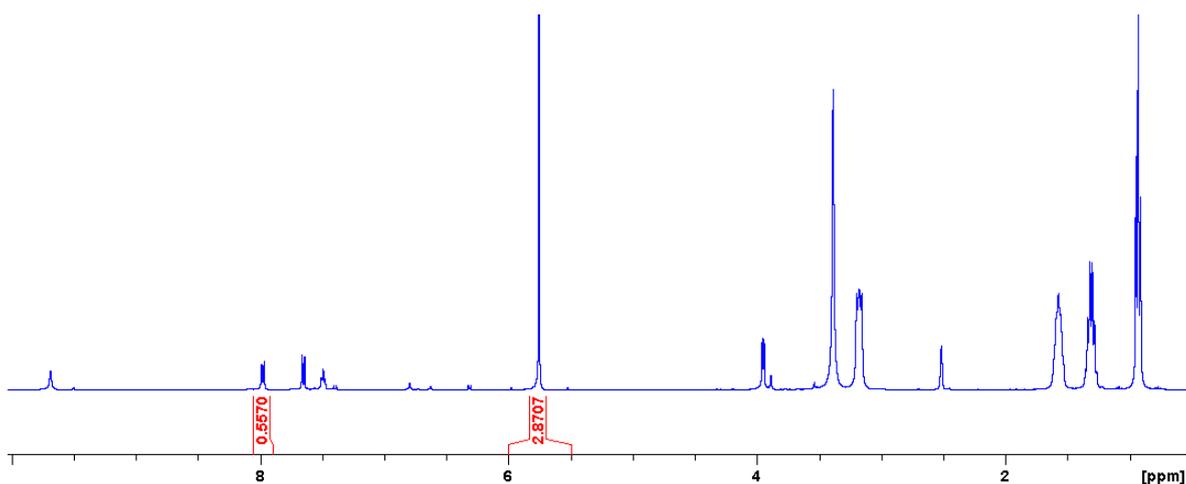
Figure 42 – ^{1}H NMR spectrum (d_1 = 60 s) of compound **12** (0.0300 g, 111.12 mM) and DCM (5 µl, 0.08 mM) in DMSO-d_6. 44 % loss of compound observed upon comparative signal integration.

Compound **12** showed a reduction by 19 % in the number of molecules detected through ^{1}H NMR. This is depicted as a result of comparative integration (Figure 43).
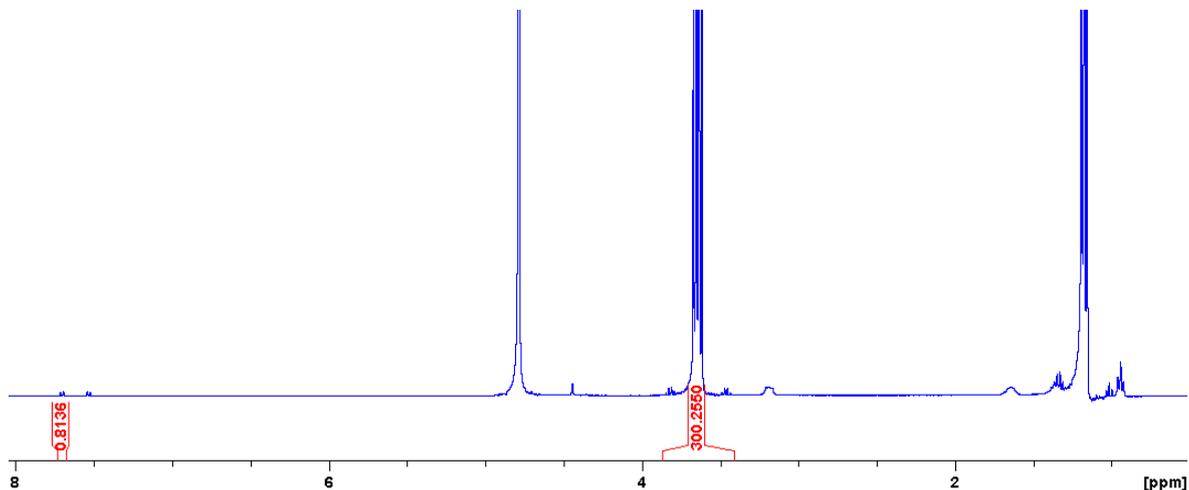
Figure 43 – ^{1}H NMR spectrum (d_1 = 60 s) of compound **12** (0.0015 g, 6.00 mM) and EtOH (5 µl, 0.43 mM) in D_2O. 19 % loss of compound observed upon comparative signal integration.

The data obtained from qNMR shows that in DMSO-d_6 both compounds **12** and **13** form larger aggregates. Whereas, in D_2O only compound **12** is shown to form these larger aggregates. This is evidence of the effect different solvent systems can have on intermolecular hydrogen bonding. Again, it is very unusual that no association is observed in the D_2O solution, but that association is observed in the DMSO-d_6 solvent system for compound **13**. This is new and exciting data! Comparatively, compound **12** has a smaller ring system than compound **13**, due to the presence of a cyclopentadiene ring instead of two benzene rings, this could explain the reduced solubility seen for this compound in both solvent systems that were investigated. The use of comparative integration through the doping of a known amount of solvent has enabled the formation of these larger aggregates in the solution state to be quantified.

3.4.2 ^{1}H NMR DOSY studies

The hydrodynamic radius of a complex in solution can be determined using a ^{1}H NMR DOSY study. This experiment derives the diffusion coefficients for individual resonances in a ^{1}H NMR spectrum. The values can then be substituted into the Stokes-Einstein equation (Equation 1) to enable the solvation sphere diameter to be calculated from the data obtained.

Equation 1 – The Stokes-Einstein equation used to calculate the hydrodynamic diameter d_H from the diffusion coefficient.

$$d_H = \frac{kT}{3\pi\eta D}$$

d_H = Hydrodynamic diameter (m)
k = Boltzmann constant
T = Temperature (K)
η = solvent viscosity (kg/ms)
D = diffusion coefficient (m^2/s)

Practically speaking it is not known if the self-associated structures formed from compounds **12** and **13** form spherical structures. This is a limitation of this experimental technique, as the use of the Stokes-Einstein equation assumes that particles formed in these solvent conditions exist as spherical structures. Because of this assumption, any value for the solvation sphere calculated will be taken as an estimation of size, rather than an exact calculation. For instance, particles which are not spherical are measured across their widest length, giving the false impression of the molecule forming a spherical structure[214] (Figure 44). Experiments for compounds **12** and **13** were carried out in DMSO-d_6.
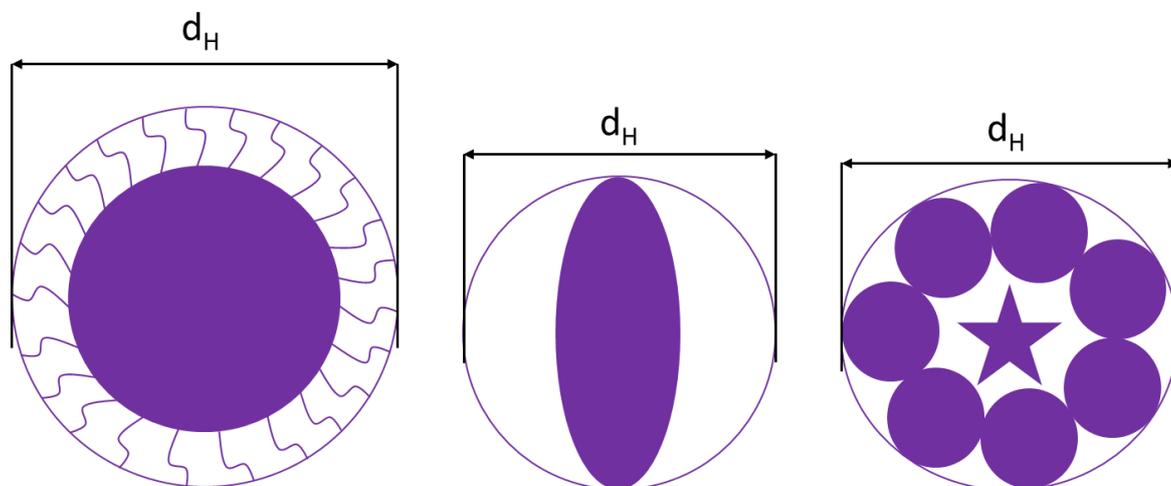
Figure 44 – Examples of non-spherical particles and how the shape may give the impression of a spherical solvation sphere calculated using Equation 1.

3.4.2.1 Results and discussion

The calculated results from the ^{1}H NMR DOSY experiment estimates that compounds **12** and **13** (Table 4) have a hydrodynamic diameter of 1.33 nm and 1.54 nm respectively. This is evidence

supporting the formation of low level self-associated structures such as monomers, dimers or trimers.

Table 4 – Calculated hydrodynamic radius of compounds **12** and **13** (nm) in DMSO-d_6 (111.12 mM).

Compound	Hydrodynamic diameter (nm)	
	Anion	Cation
12	1.33	1.25
13	1.54	1.24

The results obtained from these data show that the anionic and cationic components of compounds **12** and **13** diffuse at different rates. The ^{1}H NMR DOSY spectra and table of diffusion coefficients from the experiment for compound **12** is shown to indicate the difference in diffusion between the anionic and cationic components for compound **12** (Figure 45).
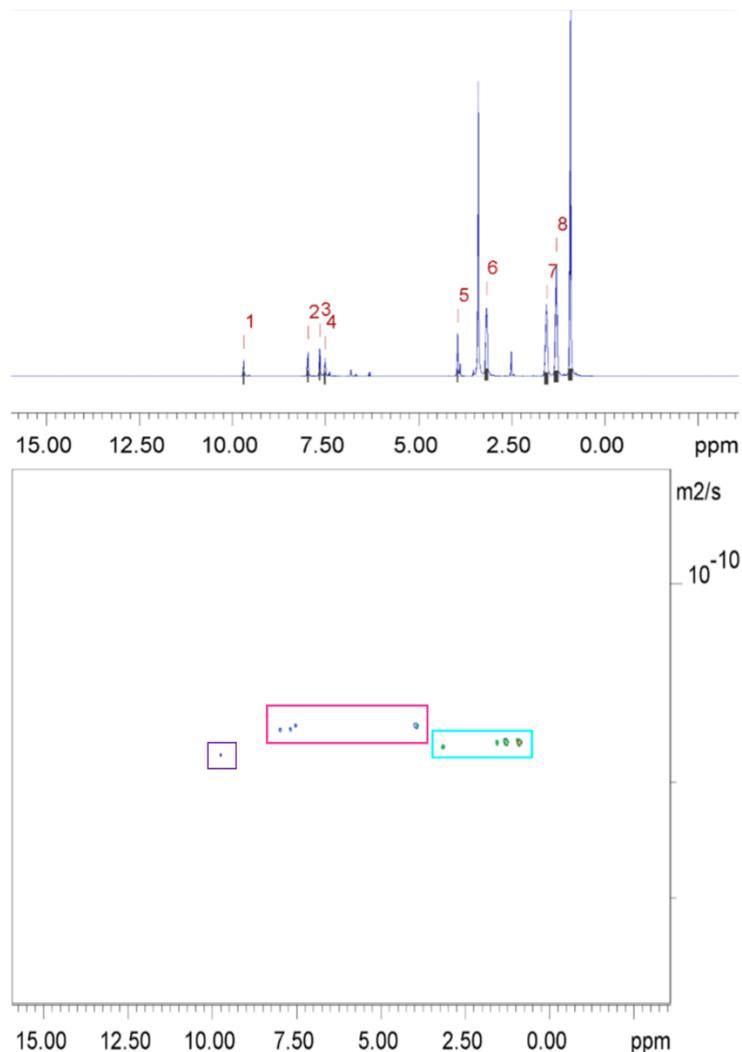
Peak Name	D [m2/s] (x10^-10)	Error [m2/s] (x10^-14 for peaks 1-5) (x10^-15 for peaks 6-9)
1	1.83	4.346
2	1.67	2.579
3	1.66	2.493
4	1.64	3.114
5	1.63	1.432
6	1.78	6.025
7	1.75	5.675
8	1.75	4.505
9	1.75	2.661

Figure 45 – ^{1}H DOSY NMR of compound **12** (111.12 mM) in DMSO-d_6 conducted at 298.15 K. Anionic component is highlighted in purple and pink, TBA counter cation is highlighted in blue. Inclusive of the table which represent the values for the diffusion constant for each peak used to calculate the hydrodynamic diameter (d_H) except for peak 1. This was found to be an outlier, so was not used in the final calculation of the hydrodynamic diameter. Peaks 2-5 correspond to the anion, and peaks 6-9 correspond to the cationic component of compound **12**. For the full set of results from the table see Appendix Figure 94.

Highlighted on the figure above in purple is the peak caused by one of the NH's present in the compound. It has been highlighted in purple because it was found to be an outlier. It is common that NH peaks may often become broad during ^{1}H NMR analysis due to exchange effects. This effect may alter the true value of the diffusion coefficient for that peak. This is the reason it has not been included during the calculation of the hydrodynamic diameter for the anionic component of compound **12**.

The ^{1}H NMR DOSY spectra and table of diffusion coefficients obtained for compound **13** shows the difference in diffusions of the anionic component to the cationic component of compound **13** (Figure 46). All the peaks produced in the ^{1}H NMR spectra of compound **13** are in line, indicating that there are no exchange effects occurring within this compound around the urea NHs.
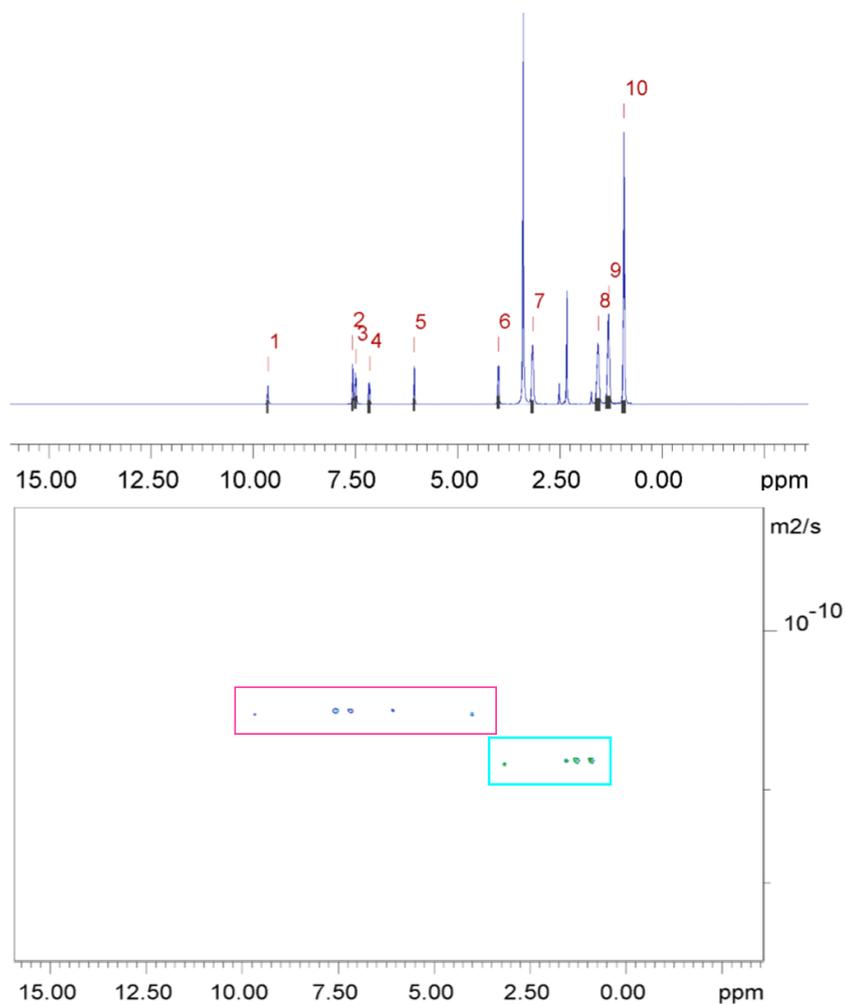
Peak Name	D [m2/s] (x10^-10)	Error [m2/s] (x10^-14 for peaks 1-6) (x10^-15 for peaks 7-10)
1	1.44	2.526
2	1.42	1.607
3	1.42	1.121
4	1.42	1.994
5	1.42	1.911
6	1.43	1.160
7	1.78	6.146
8	1.76	6.139
9	1.76	4.974
10	1.76	2.714

Figure 46 – ^{1}H DOSY NMR of compound **13** (111.12 mM) in DMSO-d_6 conducted at 298.15 K. Anionic component highlighted in pink, TBA counter cation highlighted in blue. Inclusive of the table which represents the values for the diffusion constant for each peak used to calculate the hydrodynamic diameter (d_H). Peaks 1-6 correspond to the anion, where peaks 7-10 correspond to the cationic component of compound **13**. For the full set of results from the table see Appendix Figure 95.

The results obtained here are representative only of self-associative interactions of the molecule within a DMSO-d_6 environment and do not correspond to any other solvent system. It is possible that the size of these molecules could differ in other solvent systems. However, in the solvent system employed here, the counter cation TBA has a similar size, which is to be expected as it is the same compound. It may be possible that the aggregates contain both anionic and cationic species which would result in a charge balance. However, when assessing compounds **12** and **13** it is important to note that the cation is the same for both and so should exhibit very similar data sets.

The results also indicate that compound **13** is slightly larger than compound **12**, with values of 1.54 nm and 1.33 nm respectively. This may be expected though, as compound **13** possesses a larger ring system than compound **12**. Although, the structures of compounds **12** and **13** are similar, the difference in size of the anionic component observed for both compounds may be due to experimental error. It is important to remember here that the values calculated for compounds **12** and **13** from the ^{1}H NMR DOSY experiment are estimations of the size of particulates formed, they are not exact measurements.

3.4.3 ^{1}H NMR self-association studies

The strength of molecular interactions between compounds can be determined using a series of ^{1}H NMR dilution studies. This study was conducted using compounds **12** and **13** in DMSO-d_6 with 0.5 % H_2O. This solvent system was employed as it allowed for the study of the hydrogen bond donating group, urea NHs to be studied. Information from the DOSY data indicated the compounds form only low complex species which is advantageous in the ^{1}H NMR dilution studies. The data obtained from the dilution studies was used to calculate the self-association constants using a software called Bindfit v0.5.[215]

The data from the ^{1}H dilution studies was be fitted to two different self-associative models. The first being dimerization / equal K (EK). This model assumes that all self-association constants are identical for each successive event.[216] The second model is the cooperative equal K (CoEK). This

model is based on the assumption that the first self-association event differs from the energy of any successive self-association event.[216] Both models however, share one assumption, which is the assumption that one-dimensional homogenous aggregations are formed.[217]

3.4.3.1 Results and discussion

The results of the self-association studies for compound **12** indicate that the chemical shift of the urea NH's increase downfield as concentration increases (Figure 47). This movement in chemical shift may indicate the formation of self-associated hydrogen bonded molecules using the urea NH. This is explained by the urea NH's becoming increasingly de-shielded as concentration increases.
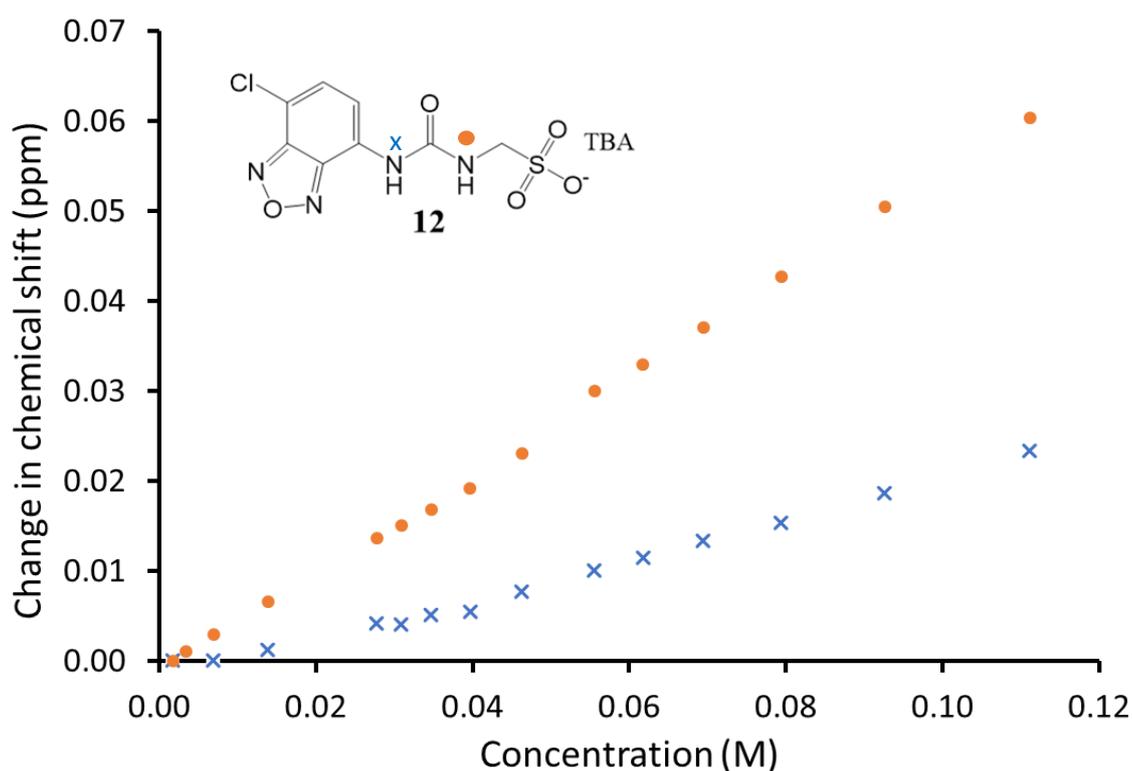
Figure 47 – Graph illustrating the ^{1}H NMR down-field change in chemical shift of NH resonances with increasing concentration of compound **12** in DMSO-d_6: 5 % H_2O (298.15 K).

Compound **13** also shows a downfield change in chemical shift with respect to the urea NH's (Figure 48). This again indicates increased de-shielding with increased concentration as well as the formation of hydrogen bonds at these points.
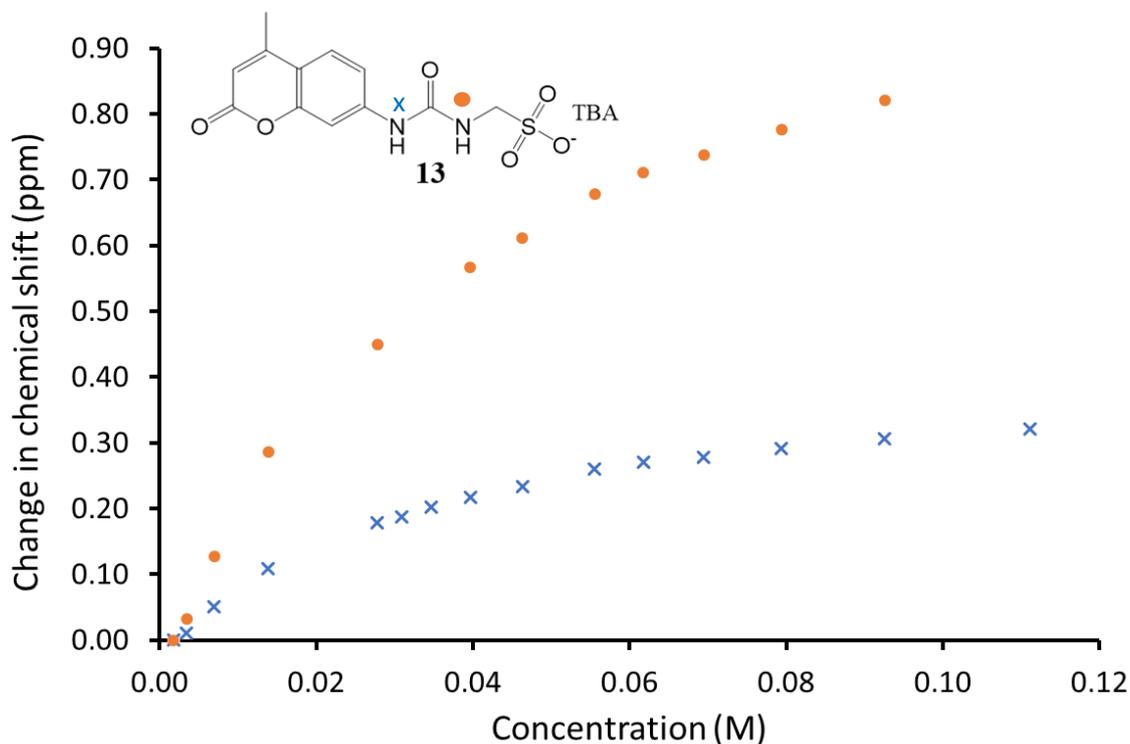
Figure 48 – Graph illustrating the ^{1}H NMR down-field change in chemical shift of NH resonances with increasing concentration of compound **13** in DMSO-d_6: 0.5 % H_2O (298.15 K).

Both compounds were successfully fitted to the dimerization/EK and CoEK models (Table 4). However, it can be determined that compound **12** fits better to the EK model due to having negative values obtained from the fitting of the data to the CoEK model. The values obtained from the CoEK model were -3.36 M^{-1} for the K_e, -1.68 M^{-1} for the K_{dim} and 0.71 for P M^{-1}. These values cannot be the best model fit for compound **12** because it is not possible to obtain negative self-association energies for the formation of complexed structures. Though the values for the EK model are still small, with values of 0.000887 M^{-1} for the K_e, and 4.43 M^{-1} for the K_{dim}, they are a better fit than negative values.

For compound **13**, the values obtained from both models are good. The association values are higher for the CoEK model. However, so are the error values, it is because of this that the EK model for compound **13** becomes the most appropriate fit. As both compounds fit the EK model more suitably, it can be concluded that the better fit to the EK model for compounds **12** and **13** is evidence to support the formation of dimers.

Table 5 – Self-association constants (M^{-1}) calculated for both compound **12** and **13**, in DMSO-d_6 with a 0.5 % H_2O solution at 298 K. The values of constants were obtained from fitting ^1H NMR dilution data, which was refined to EK and CoEK models using Bindfit v0.5[215]. The links created by the Bindfit software are provided within the appendix.

Compound	EK Model (M^{-1})		CoEK Model (M^{-1})		
	K_e	K_{dim}	K_e	K_{dim}	P
12	$8.87e^{-4}$ (± 0.05 %)	4.43 (± $2.6e^{-2}$ %)	-3.36 (± -3.3 %)	-1.68 (± -1.6 %)	0.71 (± 1.5 %)
13	21.89 (± 1.6 %)	10.95 (± 0.8 %)	30.69 (± 1.8 %)	15.35 (± 0.9 %)	0.68 (± 7.2 %)

The values obtained here should be considered with care. The data produced from the ^1H dilution experiment considers the energy of one self-associative event. There are multiple different self-associative events occurring at the same time within this solvent system that cause the formation of larger structures, as seen in the qNMR experiments.

3.5 Low Level *in-silico* modelling

It is common to use computational chemistry to support hypothesis formed during experimentation. The hypothesis of molecular interactions with specific compounds can be modelled using computational chemistry in synthetic chemistry.[218] Electrostatic potential maps (ESPMs) can be calculated that depict areas of electropositivity and electronegativity (E_{max} and E_{min} respectively).[219] They are used to depict surface charge distributions of molecules in three dimensional structures. Where knowledge of charge distributions can be used to determine how molecules interact with each other.

Computational calculations to identify primary hydrogen bond donating and accepting sites were conducted in line with studies reported by Hunter using Spartan 16'.[220,221] Calculations were performed using semi-empirical PM6 methods, after energy minimisation calculations, to identify E_{min} and E_{max} values. PM6 was used over AM1 in line with research conducted by Stewart.[222] Data refined and produced by R. Ellaby.

3.6.1 Results and discussion

The E_{min} of a compound is generally used to represent the HBA group and the E_{max} is used to represent the HBD groups. The ESPM of compound **12** (Figure 49) shows the E_{min} regions of the compound to be situated around the urea oxygen and the sulfonate oxygens. With the most electronegative point calculated at -699.476 kJ/mol. The map depicts the sulfonate oxygens as the principle HBA group of compound **12**. The map also shows the areas of E_{max}, these areas are focused around the urea NHs, with a calculated energy value of -26.5103 kJ/mol, where this area is the principle HBD group. This is indicative evidence of where the intermolecular hydrogen bonds would form within the single crystal x-ray structure, in the absence of a crystal structure for compound **12**.
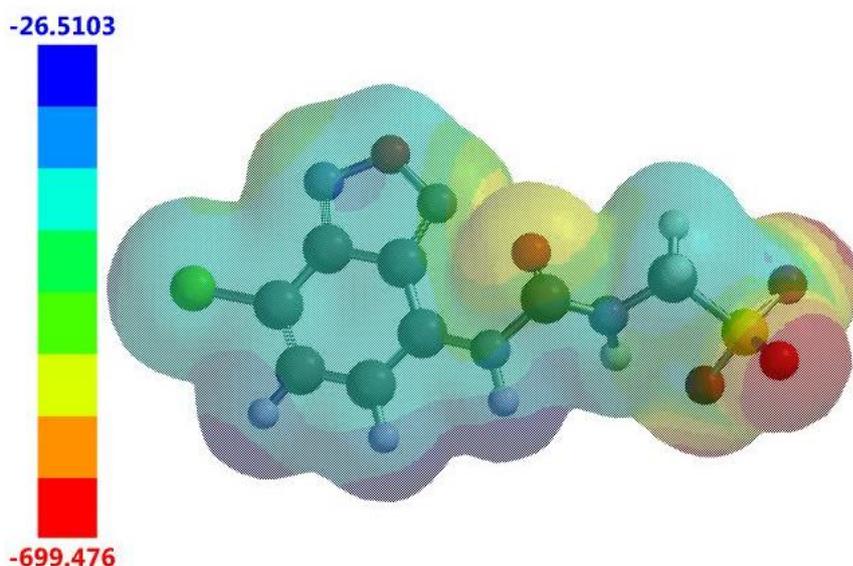
Figure 49 - Electrostatic potential map calculated for compound **12**. E_{max} (deep blue) and E_{min} (bright red) values depicted in the Figure legends are given in kJ/mol.

The ESPM of compound **13** (Figure 50) shows the E_{min} regions of the compound to be situated around the urea oxygen and the sulfonate oxygens. With the most electronegative point calculated at -699.979 kJ/mol, a value similar to that calculated for compound **12**. The map depicts the sulfonate oxygens as the principle HBA group of compound **13**. The map also shows the areas of

E_{max}, these areas are focused around the aromatic methyl group, as well as the urea NHs, with a calculated energy value of -37.5145 kJ/mol. The urea NH situated closest to the sulfonate group possesses an approximate energy value of -195 kJ/mol, whilst the urea NH closest to the aromatic group possesses an energy value of approximately -53 kJ/mol.

Though the colour scheme of the map depicts the aromatic methyl group to possess the most electropositive region, the urea NHs are the principle HBD group, as is supported within the single crystal x-ray structure of compound **13**. There is an energy difference of approximately 16 kJ/mol between the methyl group and the urea NH nearest the aromatic group. This difference is not a lot in the grand scheme of ESPMs and methyl groups are not commonly considered to be HBD groups. The crystal structure of compound **13** confirms the urea NHs to be the principle HBD group.
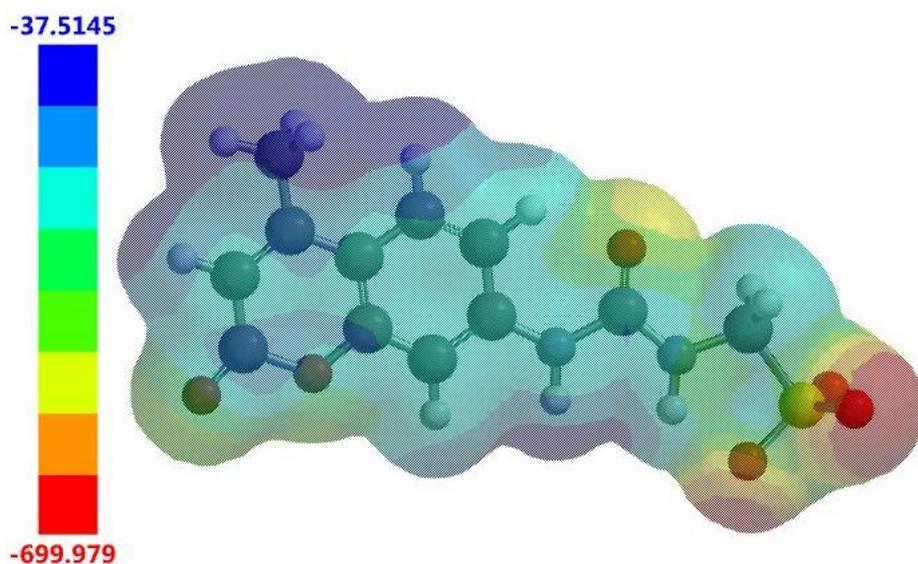
Figure 50 - Electrostatic potential map calculated for compound **13**. E_{max} (deep blue) and E_{min} (bright red) values depicted in the Figure legends are given in kJ/mol.

The ESPMs for compounds **12** and **13** have been used as supportive, or indicative evidence of the positions in which intermolecular hydrogen bond formation occurs. This indicative evidence with regards to compound **12** and is supportive evidence in the case of compound **13** to the formation of these bonds.

3.6 Conclusion

Based on the data collected for the self-association properties of compounds **12** and **13**, it can be determined that there is certainly self-association occurring within both compounds. Both compounds exhibited self-associative characteristics during the qNMR studies. This study showed for three quarters of the experiments that loss of compound occurred in the solvent systems tested. This is an indication of self-association due to the formation of larger, solid-like aggregates. An overall loss of 44 % for compound **12**, 29 % for compound **13** in DMSO-d_6: 0.5 % DCM. A 19 % loss for compound **12** was observed through comparative integration in the D$_2$O: EtOH solvent system.

The DOSY studies also suggest the presence of self-association with both compounds. Though the association between cation and anion is weak due to having different diffusion constants, the presence of monomers, dimers and trimers is indicated through the size of the compounds. Where a size of 1.33 nm and 1.54 nm for compound **12** and **13** respectively indicates the presence of low-level complex formation in the remaining sample which was not 'lost' to forming larger structures.

Finally, self-association constants were determined using ^{1}H NMR dilution studies. However, the self-associations occurring between the compounds is weak, with values of 8.87e^{-4} M^{-1} and 4.43 M^{-1}, 21.89 M^{-1} and 10.95 M^{-1} for compounds **12** and **13** respectively, fitted to the EK model. The EK model had the most appropriate fit due to larger errors and negative values associated with the CoEK model. It should be noted that relatively speaking, the strength of self-association for compound **13** is stronger than that of compound **12**.

3.7 Future works

The self-association and association properties of these novel amphiphiles were studied. They showed the formation of aggregates in the two solvent systems used. Some properties are similar to previously published results for similar compounds from Hiscock *et al*. However, some results were not similar, so further testing is required which was not carried out here due to time restraints and masses of compounds available:

- Antimicrobial screening from compounds **12** and **13**.

- If they pass the antimicrobial screening, they will be taken further where the minimum inhibitory concentration (MIC$_{50}$) will be calculated from Gram +ve (*S.aureus*) and Gram -ve (*E.coli*) bacteria.

- DLS and Zeta potential studies will be carried out for compounds **12** and **13** in DMSO. CMC studies will also be conducted for compounds **12** and **13**.

4.0 Fluorescent anionic receptors

Fluorescent receptors designed based on the structure of the urea-sulfonate salt produced by Hiscock *et al.*[168] have been successfully synthesised. Fluorescent receptors **14**-**17** have been designed as receptors to a range of different anions. The presence of a benzothiazole group within each receptor designed here is what makes compounds **14**-**17** intrinsically fluorescent. The addition of the urea moiety to each compound enables the formation of intermolecular hydrogen bonds, which lead to the detection of anions in solution. The urea functionality may also cause intramolecular bonding.

Compounds that are intrinsically fluorescent are those that exhibit colour very shortly after being excited by a specific wavelength of light, usually in the ultraviolet (UV) or X-ray region.[223] There is a release of energy during de-excitation that appears as colour, or fluorescence.[224] The term 'fluorescence' was coined by Sir George Gabriel Stokes,[225] which led Edmond Becquerel to be the first to make the observation that the light emitted from a fluorescent compound had a longer wavelength than the light absorbed.[226] He was also the pioneer of rudimentary fluorimeters, called a phosphoroscope. An instrument used to measure the intensity and duration of fluorescence of Uranium following excitation by differing wavelengths.[227]

4.1 Synthesis

Compounds **14**-**17** (Figure 51) were synthesised through the reaction of 2-(2-aminophenyl)benzothiazole with the appropriate isocyanate compounds. Compound **14** (Figure 51A) was synthesised through the reaction of 2-(2-aminophenyl)benzothiazole with butyl isocyanate in pyridine at room temperature, obtained a yield of 55 %. Compound **15** (Figure 51B) was synthesised through the reaction of 2-(2-aminophenyl)benzothiazole with phenyl isocyanate in pure pyridine stirred at room temperature to a yield of 78 %. Compound **16** (Figure 51C) was synthesised through the reaction of 2-(2-aminophenyl)benzothiazole with 4-Nitrophenyl isocyanate, with 1 mL of pyridine and 9 mL of chloroform stirred at room temperature to produce a yield of 46 %. Compound **17** (Figure 51D) was synthesised through the reaction of 2-(2-aminophenyl)benzothiazole with half molar equivalents to triphosgene in ethyl acetate at 60 °C under nitrogen to form the isocyanate intermediate. A further equivalence of 2-(2-aminophenyl)benzothiazole was added to the reaction mixture. The final compound was obtained in a yield of 25 %.
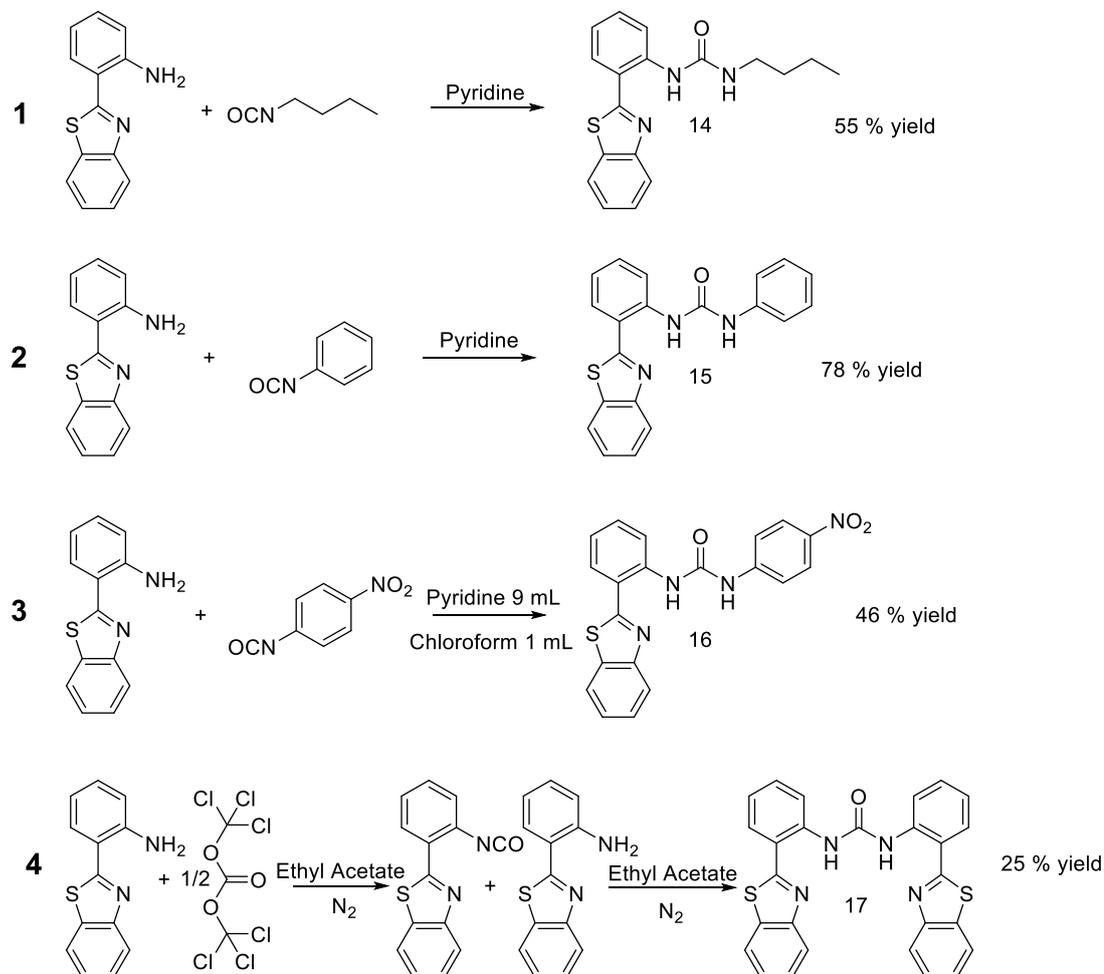
Figure 51 – Synthesis of: 1) Compound **14**, 2) Compound **15**, 3) Compound **16**, 4) Compound **17**.

4.2 Self-association in the solid state

4.2.1 Single crystal X-ray diffraction

Single crystals of compounds **14** and **16** were obtained through slow evaporation of a CHCl$_3$: MeOH, 19:1 solution. The crystal structures allow the identification of intramolecular self-association occurring in the solid state. The collection of crystals suitable for SCXRD was attempted for compounds **15** and **17** were attempted but were unsuccessful even though several solvent systems were attempted. Including: a 1:1 ratio of DMSO: CHCl$_3$, a 19:1 ratio of CHCl$_3$: MeOH, through the slow evaporation of chloroform and finally, using a 2:1 ratio of CHCl$_3$: acetonitrile (ACN). These data were obtained, refined and produced by Dr Jennifer Hiscock.

4.2.1.1 Results and discussion

The single crystal x-ray structure of compound **14** (Figure 52) shows the presence of a single hydrogen bond between the urea NH and the nitrogen present in the benzothiazole ring system. The presence of a bond here may play a role in the energy required for the formation of a host: guest complex. Wherein, more energy may be required for the formation of this complex, as this intramolecular bond must be broken to allow optimised host: guest complex formation.
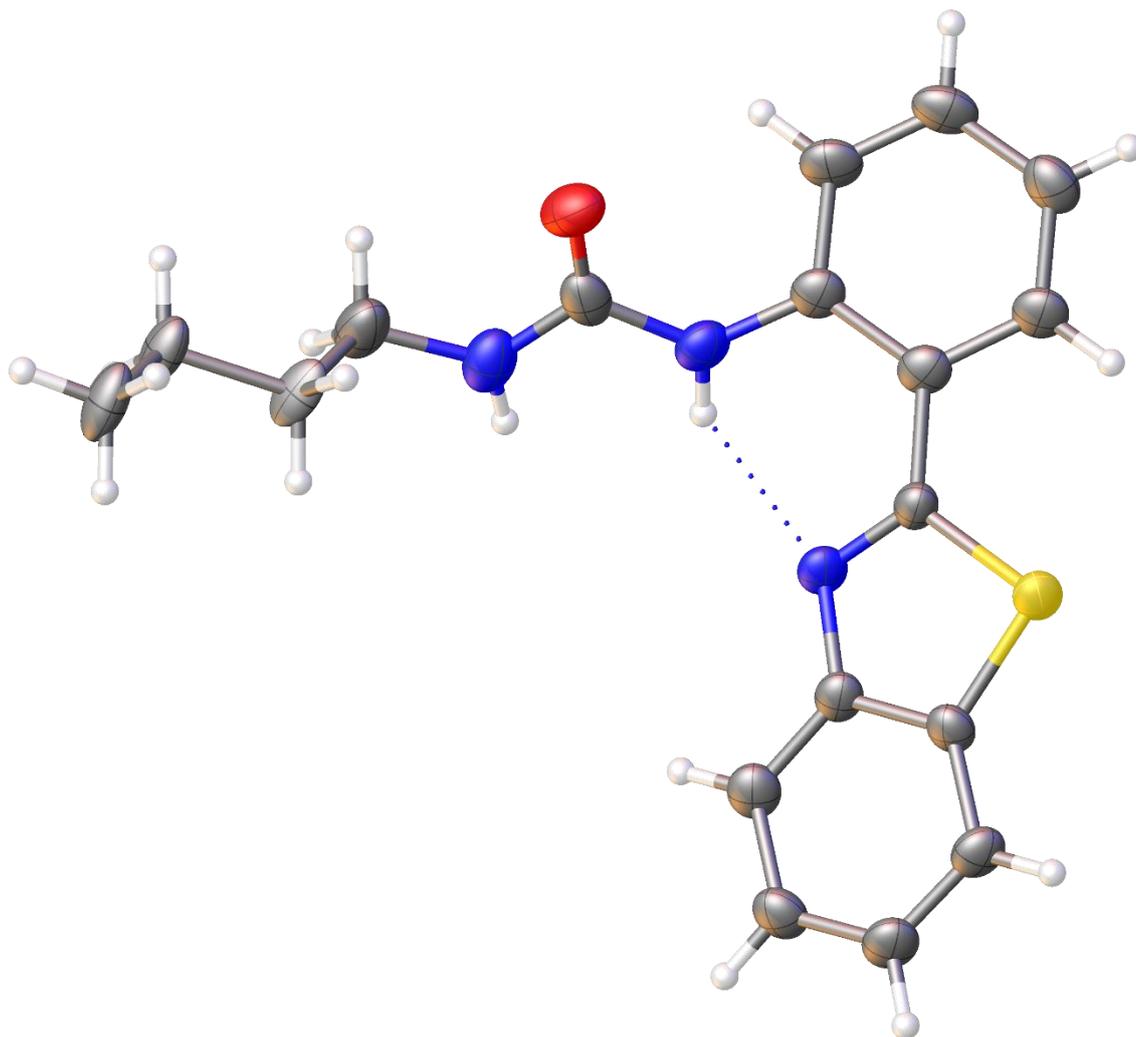
Figure 52 – Single crystal X-ray structure of compound **14**.

Compound **14** also displays intermolecular hydrogen bonding occurring between molecules (Figure 53). These bonds occur between both the urea NH's on one molecule, to the urea oxygen of another molecule. The molecules produce a planar stack, arranging themselves directly on top of one another.
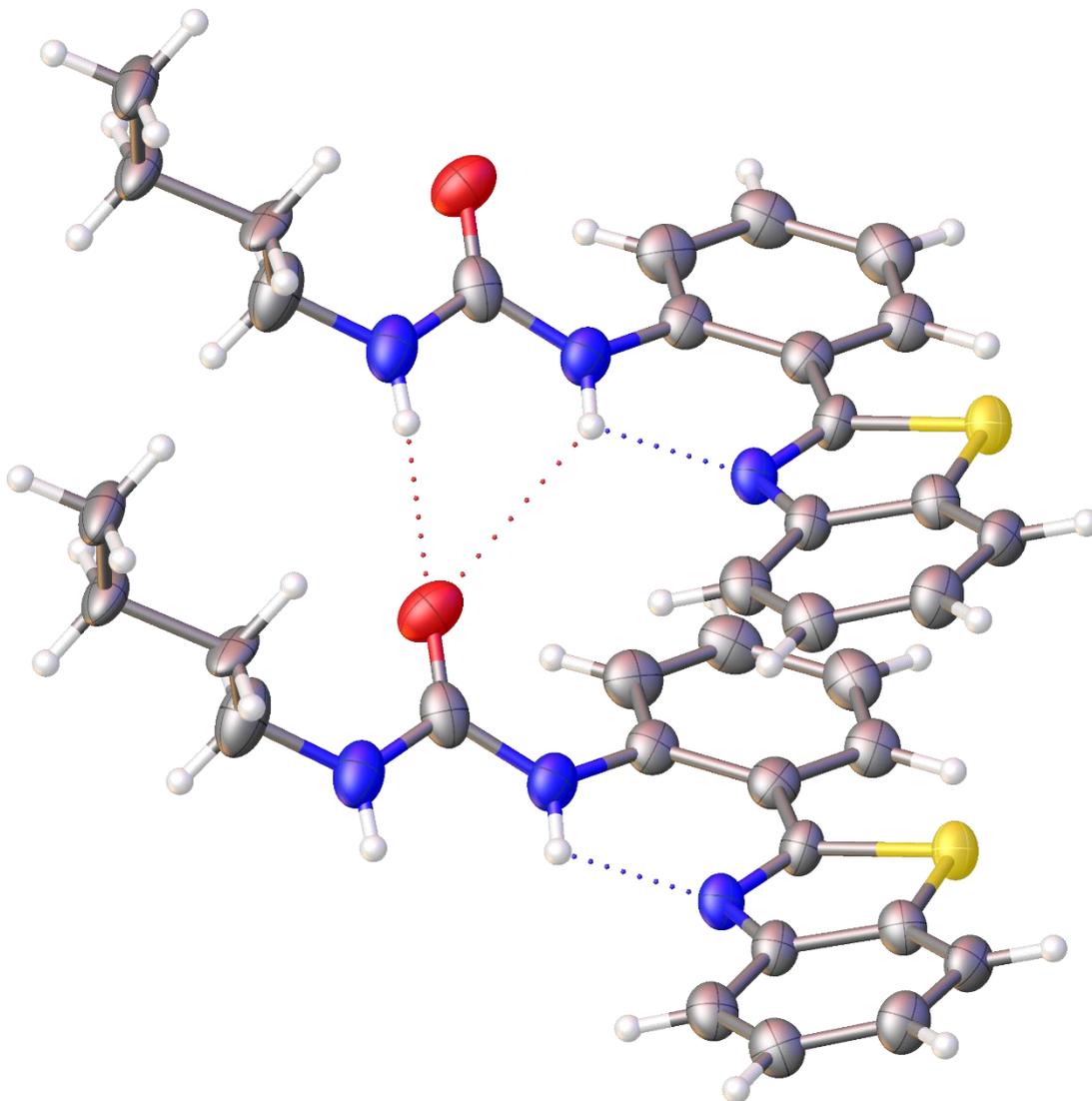
Figure 53 – Single crystal X-ray structure of compound **14**, exhibiting the extended structure.

The single crystal x-ray structure of compound **16** (Figure 54) shows the presence of hydrogen bonding occurring between a urea NH and the nitrogen present in the benzothiazole ring system. This is the same as that which was seen for compound **14**. The crystal structure also shows hydrogen bonding occurring between compound **16** and DMSO. Where both urea NH's are interacting with the oxygen present in the DMSO. The DMSO in this instance is left over from purification processes.
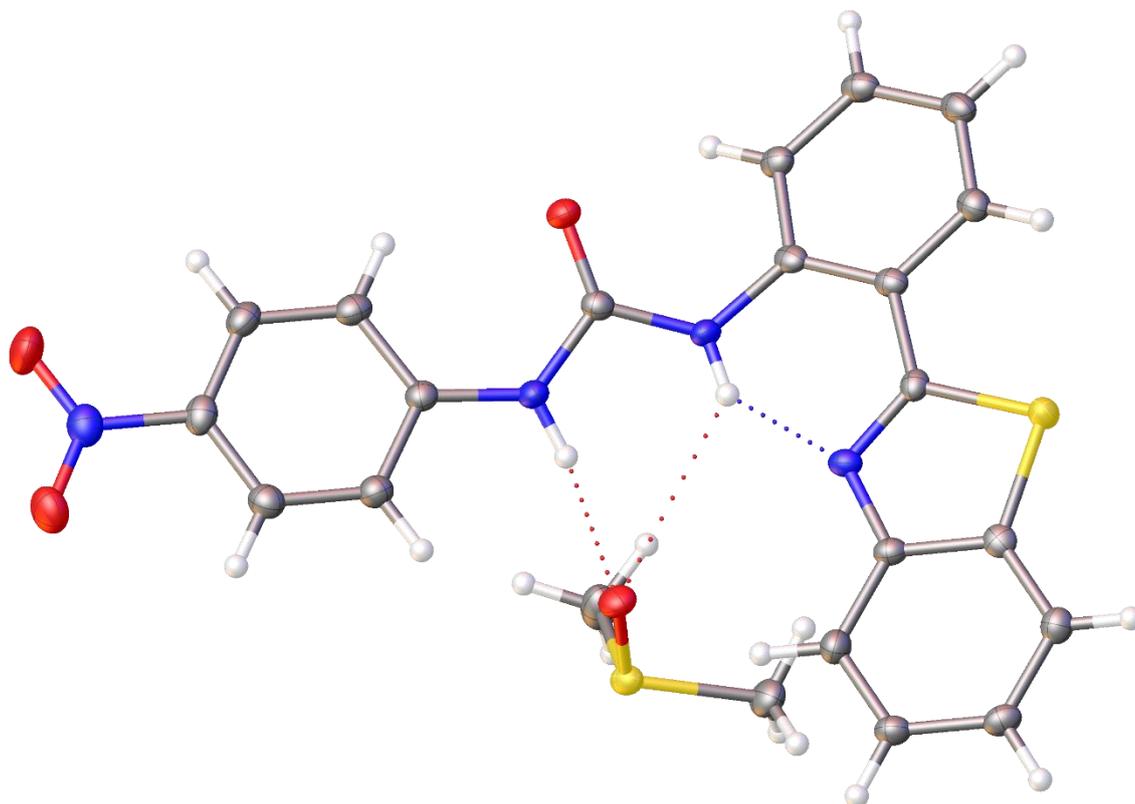
Figure 54 – Single crystal X-ray structure of compound **16**, exhibiting intramolecular bonding with DMSO.

Although crystals were not obtained for every compound in the group **14**-**17**, it can be theorised that compounds **15** and **17** would also possess a singular intramolecular hydrogen bond present between the urea NH and the benzothiazole nitrogen. This is because this basic structure is present in compounds **14**-**17**.

4.3 Self-association in the gas phase

4.3.1 Electrospray ionisation mass spectrometry

High resolution mass spectrometry was performed using a Bruker microTOF-Q mass spectrometer and spectra recorded and processed using Bruker's Compass Data Analysis software. Compounds **14**-**17** were analysed using negative ESI-MS in order to determine the presence of self-associative complexes in the gas phase and also for the purpose of molecular characterisation.

4.3.1.1 Results and discussion

These data obtained from the ESI-MS shows that compounds **14**, **15** and **17** demonstrate only monomers in the gas phase, where **16** also demonstrates dimerization in the gas phase. Approximately 1 mg of each compound was dissolved in 1 mL of methanol. This solution was further diluted 100-fold before undergoing analysis where 10 µL of each sample was then injected directly into a flow of 10 mM ammonium acetate in 95 % water (flow rate = 0.02 mL/min). Samples were prepared by L. White. As compounds **14**-**17** are neutral they require ionisation to show the monomeric state $[M – H^+]^-$ and dimeric state $[M + M - H^+]^-$ (Table 6).

Table 6 – High resolution mass spectrometry theoretical and experimentally derived values for compounds **14**-**17**.

Compound	m/z $[M - H^+]^-$		m/z $[M + M - H^+]^-$	
	Theoretical	Actual	Theoretical	Actual
14	324.1176	324.1162	649.2425	N/A
15	344.0863	344.0853	689.1799	N/A
16	389.0714	389.0688	779.1501	779.1438
17	477.0849	477.0810	955.1771	N/A

Compounds **14**-**17** were ionised to produce an ion with a charge of negative one. This means the position of the peaks are representative of the monomeric states for each compound as it is calculated as a mass/charge (m/z) ratio. The monomeric $[M - H^+]^-$ m/z peak for compound **16** is theoretically observed at 390.0787 – 1.0073 = 389.0714, and experimentally observed at 389.0688 (Figure 55). The dimeric species $[M + M - H^+]^-$ m/z of compound **16** is observed experimentally at 779.1438. Theoretically it is observed at m/z (389.0707 x 2) - 1.0073 = 779.1501, this indicates the presence of a dimeric species in the gas phase for compound **16** (Figure 56).
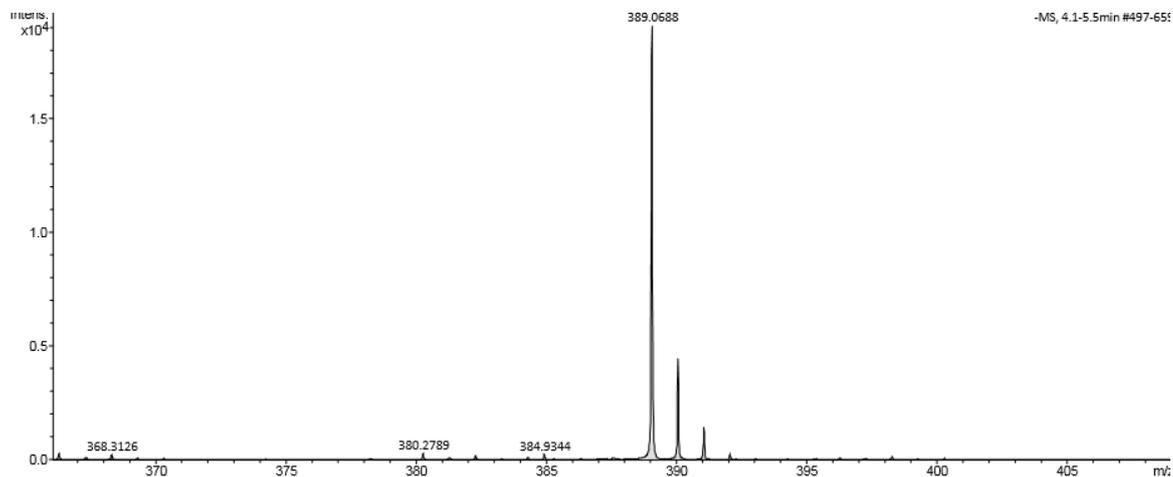
Figure 55 – Negative electrospray mass spectrometry spectrum of compound **16** showing the monomeric species.
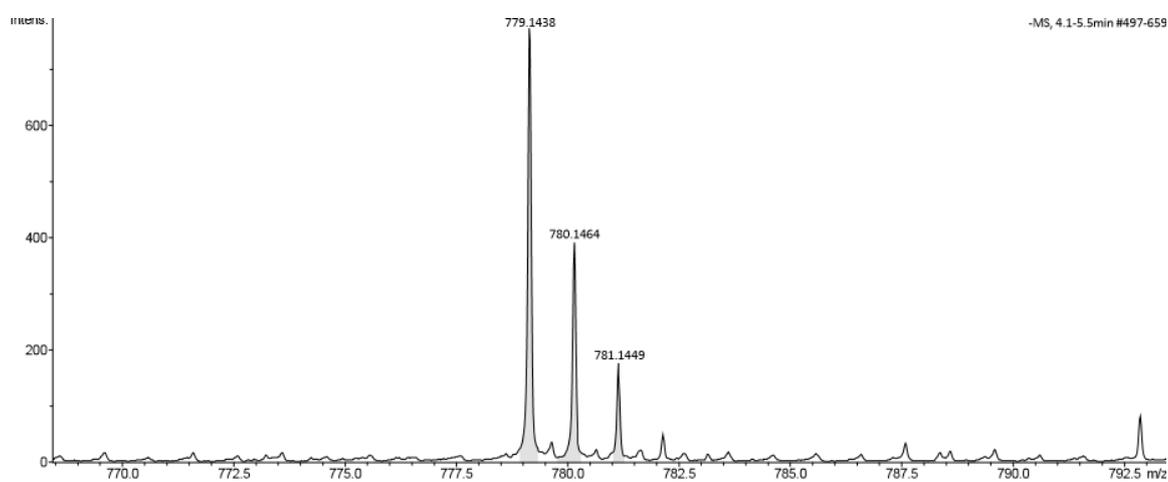
Figure 56 – Negative electrospray mass spectrometry spectrum of compound **16** showing the dimeric species.

Although there are interactions occurring in the gas a phase, a limitation of this experiment is the inability to measure the strength of the interactions under these conditions, this is something that must be done in the solution state. Compound **14** exhibited the monomeric state [M]⁻ at m/z 324.116 (Figure 57), which exists theoretically as 324.1176.
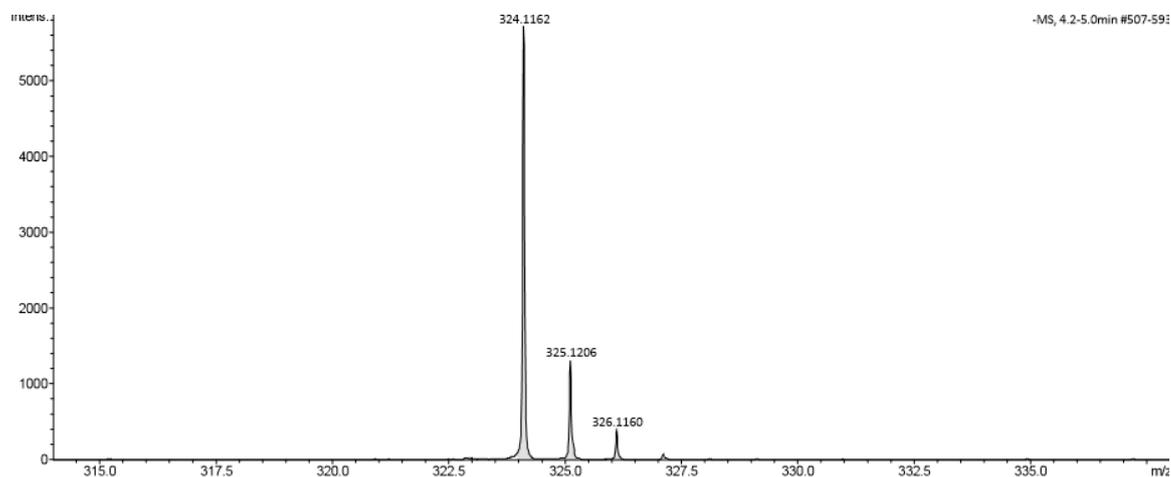
Figure 57 – Negative electrospray mass spectrometry spectrum of compound **14** showing the monomeric species.

Compound **15** exhibits the monomeric state [M]⁻ theoretically at m/z 334.0863 and experimentally at m/z 334.0853 (Figure 58).
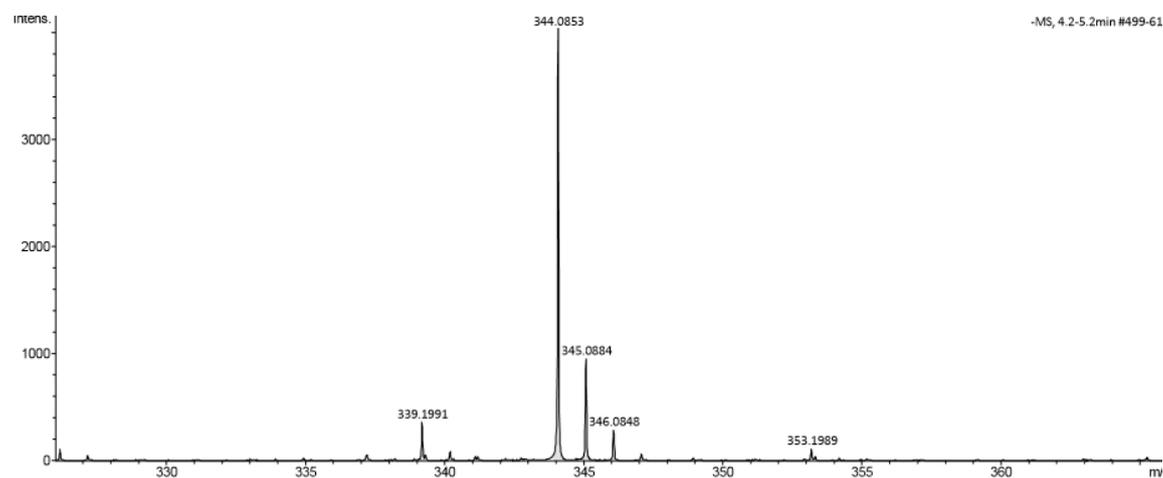
Figure 58 – Negative electrospray mass spectrometry spectrum of compound **15** showing the monomeric species.

Compound **17** exhibits the monomeric state [M]⁻ theoretically at m/z 477.0849 and experimentally at m/z 447.0810 (Figure 59).
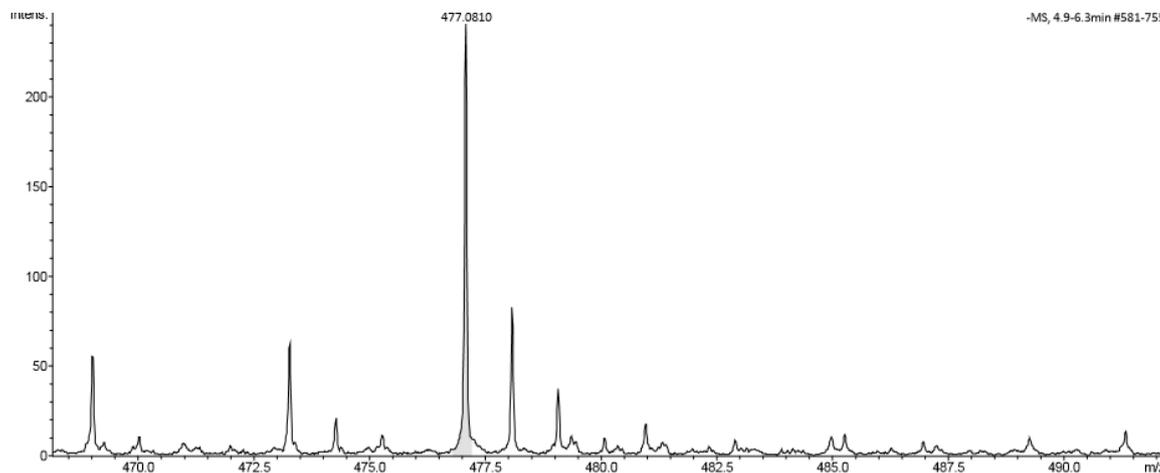
Figure 59 – Negative electrospray mass spectrometry spectrum of compound **17** showing the monomeric species.

The results from the high resolution negative ESI-MS indicate the possible presence of intermolecular bonding in the case of compound **16**. The presence of dimers here is an indicator that compound **16** has self-associative properties in the gas phase. The presence of these properties has therefore been be explored in the solution state. For compounds **14**, **15** and **17** however, only monomers were found to be present. This indicates there are no self-associative properties linked to these compounds in the gas phase.

4.4 Associations in the solution state

No self-association was detected in the solution state for any of the compounds **14**-**17**, as there were no signs of peak broadening within the ^{1}H NMR spectra obtained for compounds **14**-**17** which is an indication that no self-association is occurring. All fluorescent related experiments conducted herein were done so in chloroform due to solubility issues. Acetonitrile was the first solvent chosen for these experiments, but compound **16** had solubility issues in this solvent. In order to keep the conditions as closely the same as possible the solvent chloroform was selected instead.

4.4.1 Fluorescent titration studies

A series of fluorescent titrations were conducted where compounds **14**-**17** acted as the host molecules and several TBA salts acted as guest molecules. Fluorescence was chosen as the method

for conducting the titrations for a few reasons, namely due to the sensitivity of the instrument but also because there were solubility issues for compounds **14**-**17** at the concentrations required for use with NMR. The anions used were acetate, benzoate, chloride, fluoride, hydroxide, hydrogen-sulphate, phosphate monobasic and sulphate. These anions were selected for testing as they offered a variety of geometries which would enable the understanding of the selectivity of compounds **14**-**17** to anions of specific geometries.

The interactions that occurred during these titration studies were plotted into Microsoft excel and fitted using Bindfit v0.5[215] where the strength of interactions between host-guest molecules was determined. The data was fitted using the Nelder-Mead fitting method[228] as is common for this type of data interpretation.[229,230] It is common to see a change in the fluorescent intensity of an emission spectra during a fluorescent titration.[231] There is either a shift in maximum intensity, i.e. that the wavelength where the maximum intensity occurs changes, or there is a change in fluorescent output. This type of interaction can reduce fluorescent intensity, in a result called fluorescent quenching, as well as causing a fluorescence increase or a shift in the wavelength of fluorescence emission.

The terms binding isotherm is shown by the curve on a graph, the binding event is the formation of the host: guest complex and the association constant is the equilibrium constant for the formation of the host: guest complex. The data was fitted to three binding isotherms, 1:1, 1:2 and 2:1, which assume the same parameter; that there is no dilution of the host compound during the titration. A change of 2.5 % in volume was allowed before dilution was considered to have a significant effect on the concentration of the sample. Stock solutions of the compounds **14**-**17** were made in the scale of 100 mL, of which a 2,000 μL aliquot was taken for each titration experiment. 50 μL of guest sample was titrated in over 25 additions to the curvette. The curvette was the shaken and inverted before being inserted into the instrument for testing. All fluorescent titrations were conducted using a Cary Eclipse Fluorescence Spectrophotometer.

4.4.1.1 Results and discussion

Results from the fluorescent titration data were fitted into Bindfit. Some of the results produced binding isotherms that could not be taken forward because they produced binding events that either had negative association constants, or had errors that were too high, with values above 11 %. The data presented in Table 7 demonstrates the results of fitting the experimental data to the 1:1 binding isotherm with association constants (M⁻¹) for all host: guest interactions. This is shown here because where a model could be fitted within the acceptable parameters, all data fitted to the 1:1 isotherm. All secondary association constants for the 1:2 and 2:1 isotherm have been calculated individually from the first association constant.[217,232] All titration data and Bindfit fit links can be found in the appendix (Figures 38-61), (Tables 3-33).

Table 7 – Association constants (M⁻¹) calculated for each host (compounds **14**-**17**) titrated against each anionic guest with a TBA Counter cation; acetate, benzoate, chloride, fluoride, hydroxide, hydrogen-sulphate, phosphate monobasic and sulphate for a 1:1 association constant. Conducted in CHCl₃ at 293 K. a = data could not be differentiated between a host: guest 1:1 and a 1:2 binding isotherm b = no full data set obtained due to experimental limitations. Data provided to the nearest whole number and error values provided to 1 decimal place.

Anion Guest (TBA)	Compound **14**	Compound **15**	Compound **16**	Compound **17**
	K (M⁻¹) Error (± %)	K (M⁻¹) Error (± %)	K (M⁻¹) Error (± %)	K (M⁻¹) Error (± %)
Acetate	0 ± 2.5 %	895 ± 39.4 %	8263 ± 13.6 %	243860 ± 19.2 %
Benzoate	0 ± 0.5 %	352 ± 9.3 %	1166 ± 2.4 %	0 ± 3.9 %
Chloride	94878 ± 17.6 %	95863 ± 15.4 %	73 ± 4.1 %	15241 ± 10.7 %
Fluoride	2426 ± 4.7 %	9855 ± 6.6 %	11597 ± 21.3 %	0 ± 2.3 %
Hydroxide	1544	2053		77551

	± 7.7 %	± 5.8 %	b	± 16.0 %
Hydrogen-Sulphate	15042[a]	5596	136	0
	± 10.5 %	± 4.9 %	± 4.9 %	± 1.2 %
Phosphate monobasic	3087	428	753	8816
	± 5.5 %	± 3.9 %	± 4.6 %	± 9.0 %
Sulphate	0	1874	0	15556
	± 0.0 %	± 20.4 %	± 1.7 %	± 9.8 %

Bindfit data produced from fitting the experimental results to binding isotherms fall into three ranked orders of association. Weak, or no real interactions, are those that have values below 100 M^{-1}. Medium strength interactions are those that have association constants with values between 100 M^{-1} and 1000 M^{-1}. While strong association constants are those that have values in excess of 1000 M^{-1}.

The titration results of compound **14** with the TBA acetate show a decrease in fluorescence of compound **14** upon increased concentration of the guest (Figure 60). Data obtained from Bindfit indicate these compounds have an association constant of 0 M^{-1}, indicating that no measurable interaction was occurring between compound **14** and the acetate anion.
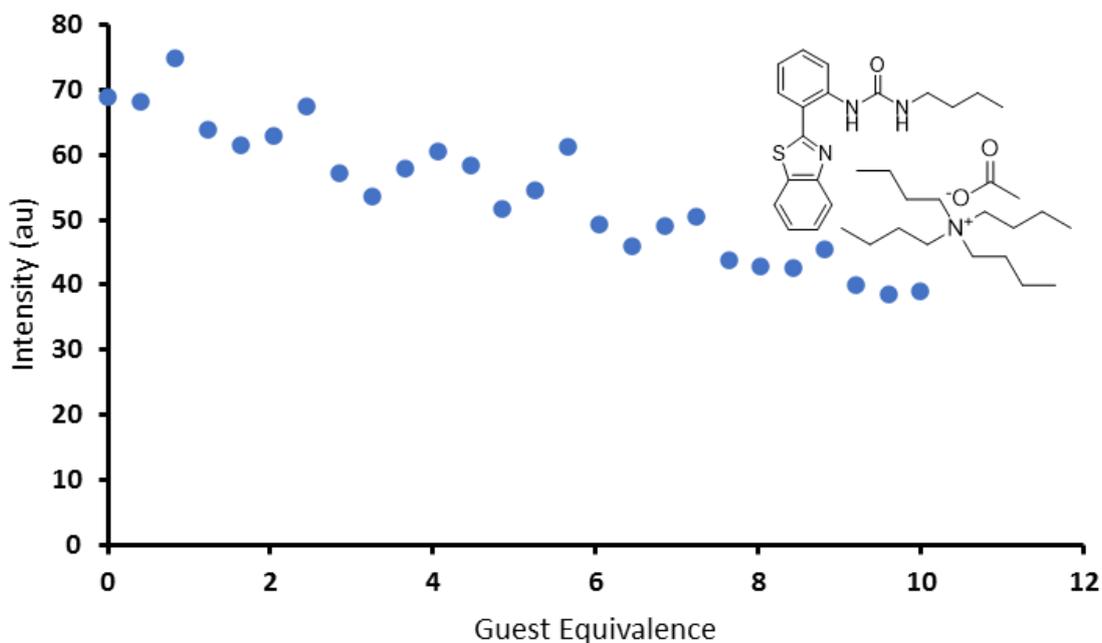
Figure 60 – A graph showing a decrease in emission intensity of compound **14** (host) upon increasing equivalence of TBA acetate (guest), CHCl$_3$ (298 K).

Table 8 displays the data obtained from fitting the experimental results of compound **14** with the anion acetate on a host: guest 1:1, 1:2 and 2:1 M^{-1} ratio using Bindfit.

Table 8 – Association constants (M^{-1}) calculated for compound **14** (host) titrated against TBA acetate (guest) in CHCl$_3$. The links for the Bindfit data is provided within the appendix.

Host: Guest	1:1	1:2		2:1	
	K	K_{11}	K_{12}	K_{11}	K_{21}
Association constant (M^{-1})	0.015 (± 2.461 %)	-0.22 (± -32.119 %)	165182.65 (± 378.861 %)	-3.09 (± -7.464 %)	380529.91 (± 5.739 %)

The titration results of compound **16** with the TBA benzoate show association between the two compounds (Figure 61). Data obtained from Bindfit indicate these compounds have a strong interaction with an association constant of 1166 M^{-1}, though the association constant is towards the lower end of the strong binding scale. Bindfit also indicated the compounds interact on a 1:1

ratio, due to the numbers calculated for the 1:2 and 2:1 host: guest ratios being either too large or being negative.
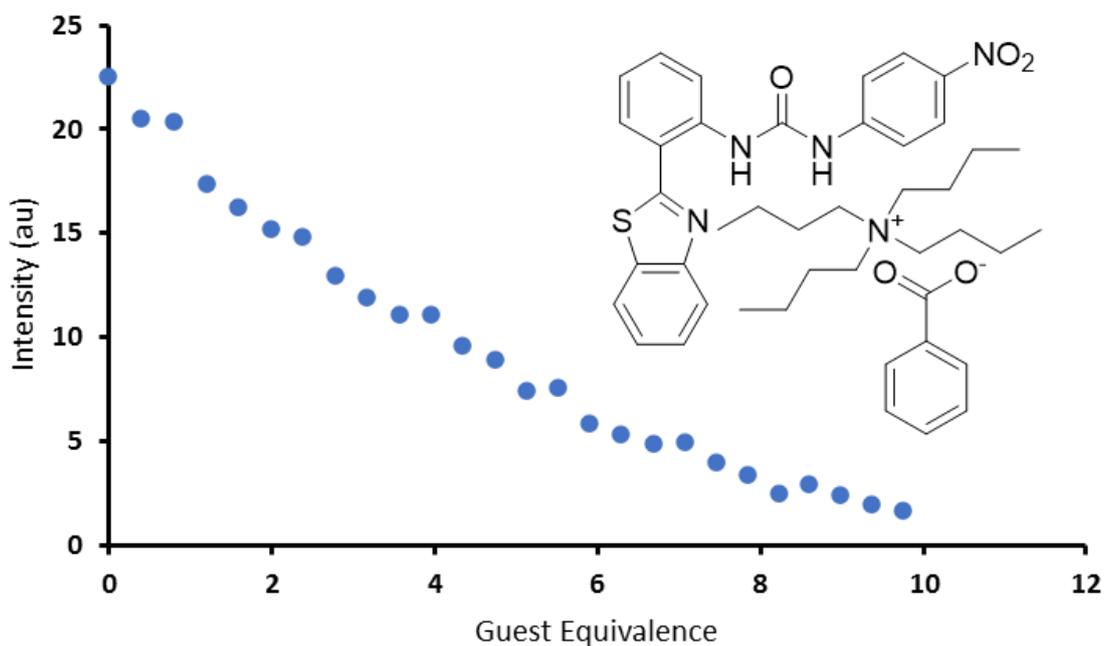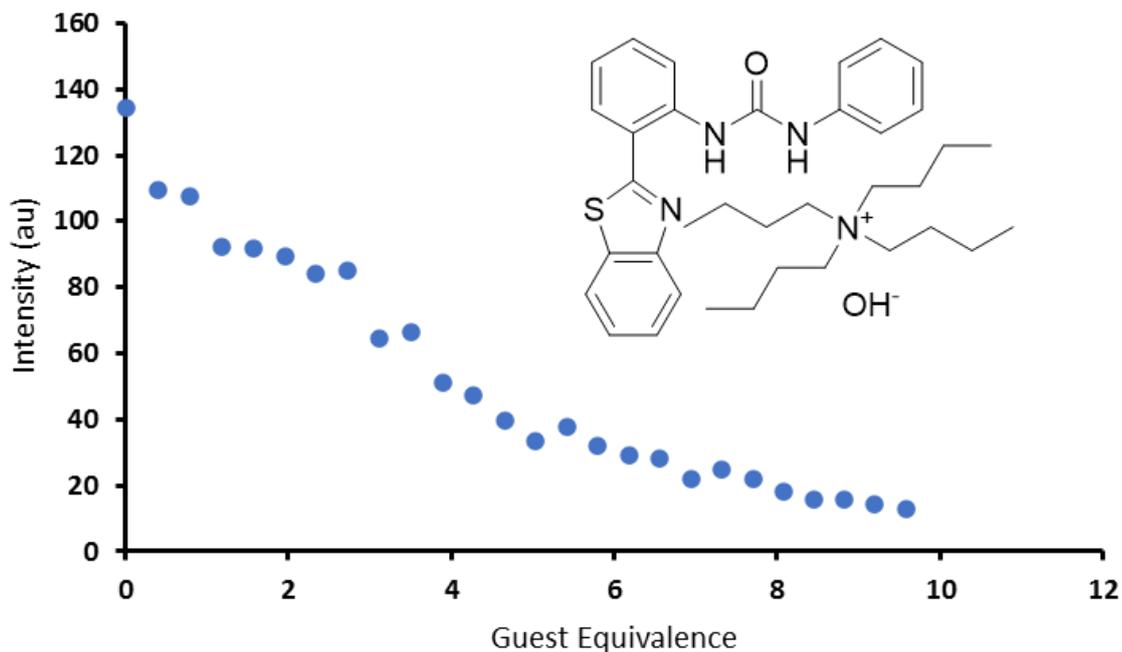

Figure 61 – A graph showing a decrease in emission intensity of compound **16** (host) upon increasing equivalence of TBA benzoate (guest). CHCl$_3$ (298 K).

Table 9 displays the data produced from fitting the experimental data of compound **16** with the benzoate anion on a host: guest 1:1, 1:2 and 2:1 M^{-1} ratio, using Bindfit.

Table 9 – Association constants (M^{-1}) calculated for compound **16** (host) titrated against TBA benzoate (guest) in CHCl$_3$. The links for the Bindfit data is provided within the appendix.

Host: Guest	1:1	1:2		2:1	
	K	K$_{11}$	K$_{12}$	K$_{11}$	K$_{21}$
Association constant (M^{-1})	1166.91 (± 2.369 %)	319.91 (± 3.241 %)	-1600.02 (± -5.623 %)	0.19 (± 9.040 %)	4878632.27 (± 1.644 %)

The titration results of compound **17** with the TBA chloride show association occurring between the two compounds (Figure 62). Data obtained from Bindfit indicate these compounds have a strong interaction with an association constant of 15241 M^{-1}. Bindfit indicated the

compounds interact on a 1:1 ratio, due to the numbers calculated for the 1:2 and 2:1 host: guest ratios being either too large or being negative.
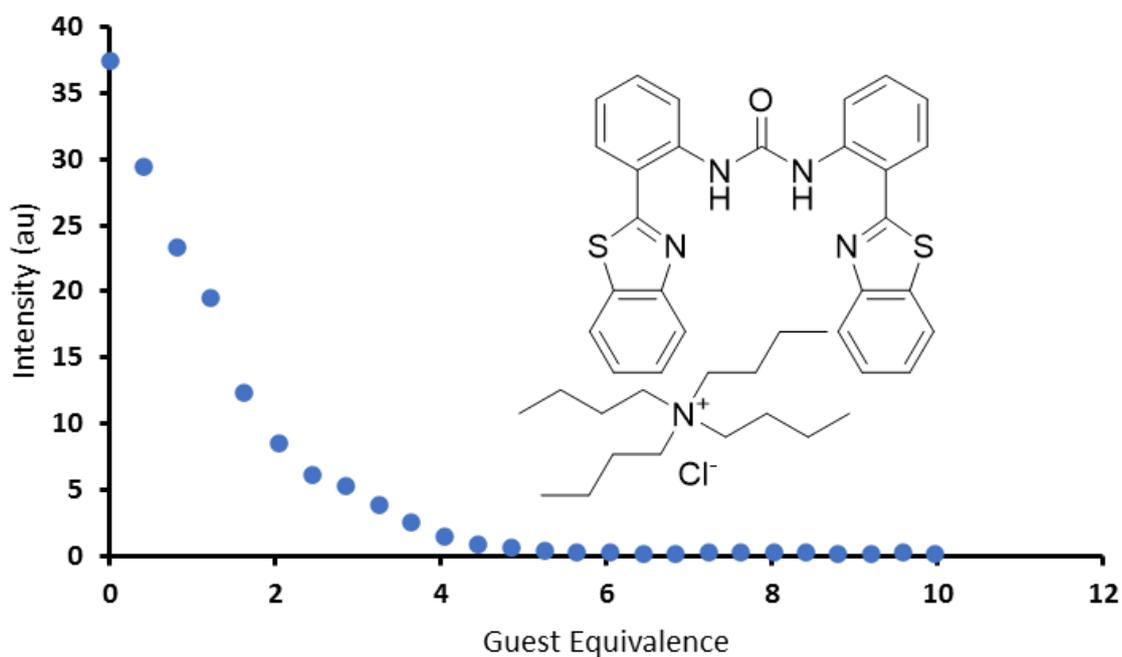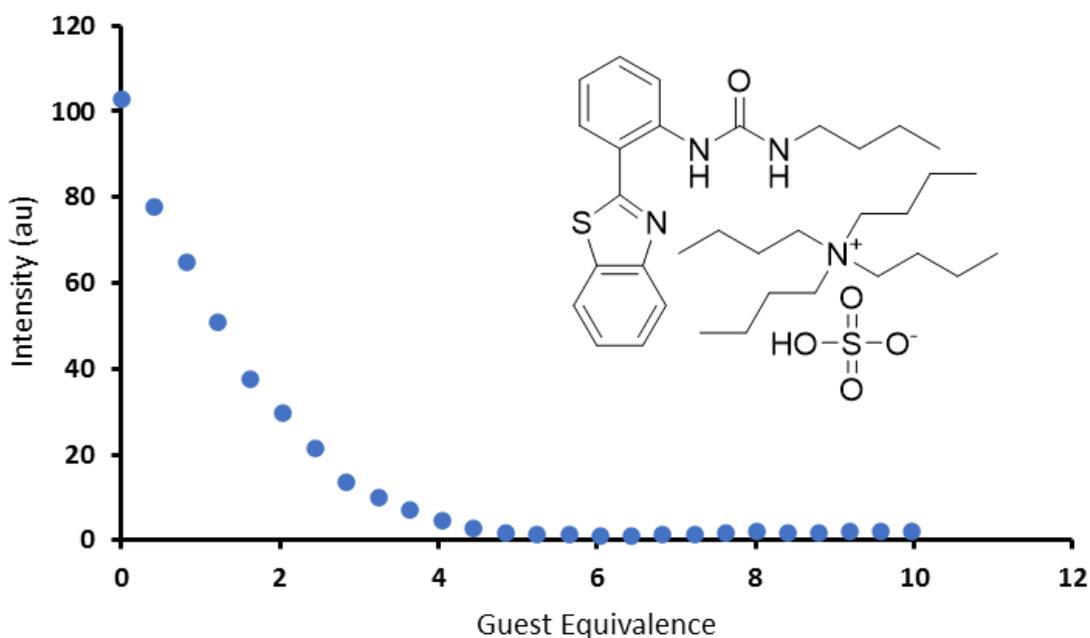

Figure 62 – A graph showing a decrease in emission intensity of compound **17** (host) upon increasing equivalence of TBA chloride (guest). CHCl₃ (298 K).

Table 10 displays the fit data obtained from the experimental results of compound **17** with the chloride anion in a host: guest 1:1, 1:2 and 2:1 M⁻¹ ratio.

Table 10 – Association constants (M^{-1}) calculated for compound **17** (host) titrated against TBA chloride (guest) in CHCl₃. The links for the Bindfit data is provided within the appendix.

Host: Guest	1:1	1:2		2:1	
	K	K_{11}	K_{12}	K_{11}	K_{21}
Association constant (M^{-1})	15241.79 (± 10.667 %)	9292.99 (± 18.511 %)	29606.66 (± 57.646 %)	4725.77 (± 5.399 %)	-3943.36 (± -1.692 %)

The titration results of compound **15** with the TBA fluoride show a correlation between the two compounds (Figure 63). Data obtained from Bindfit indicates these compounds have a strong interaction compared to the results obtained for other interactions, such as compound **14** with TBA

acetate. Compound **15** with fluoride has an association constant of 9855 M^{-1}. Bindfit also indicated the compounds interact on a 1:1 ratio, due to the numbers calculated for the 1:2 and 2:1 host: guest ratios being either too large or being negative.
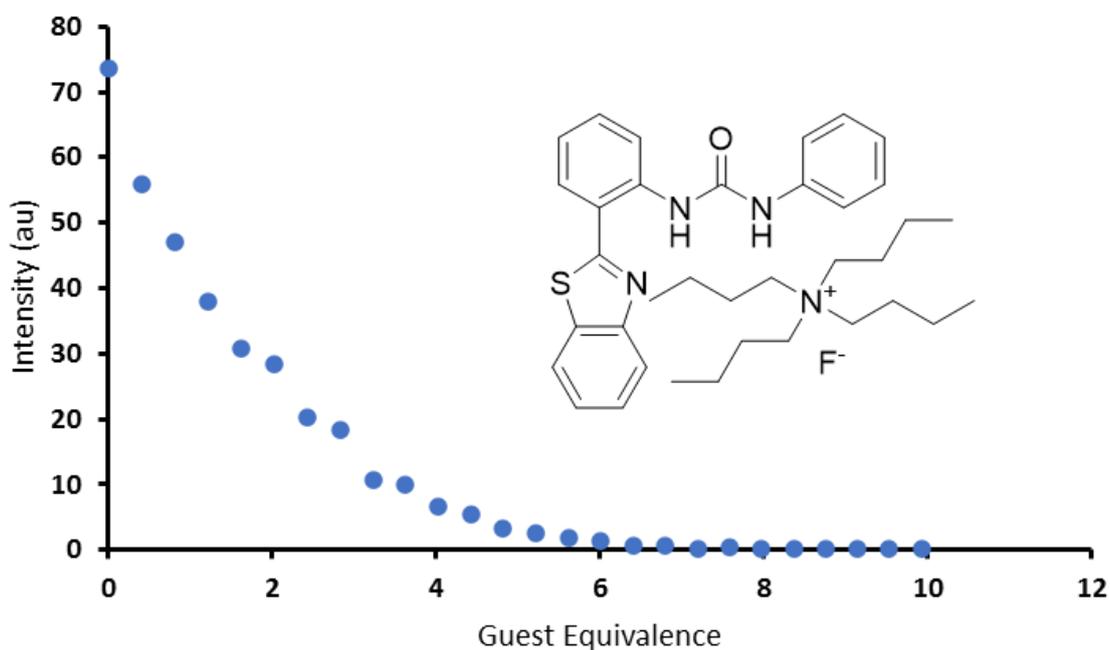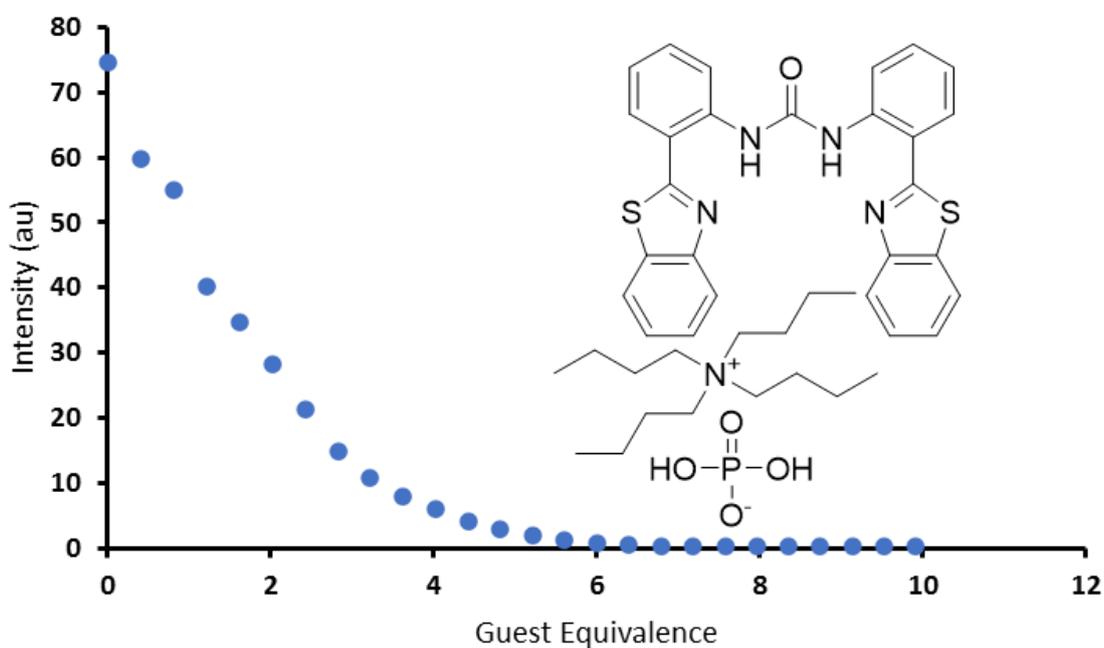

Figure 63 – A graph showing a decrease in emission intensity of compound **15** (host) upon increasing equivalence of TBA fluoride (guest). $CHCl_3$ (298 K).

Table 11 shows the data obtained from fitting the experimental results of compounds **15** and fluoride into Bindfit with a host: guest ratio of 1:1, 1:2 and 2:1 M^{-1}.

Table 11 – Association constants (M^{-1}) calculated for compound **15** (host) titrated against TBA fluoride (guest) in $CHCl_3$. The links for the Bindfit data is provided within the appendix.

Host: Guest	1:1	1:2		2:1	
	K	K_{11}	K_{12}	K_{11}	K_{21}
Association constant (M^{-1})	9855.59 (± 6.593 %)	5193.55 (± 4.252 %)	-137.62 (± -7.028 %)	3.45 (± 3.869 %)	2379388.45 (± 0.738%)

The titration results of compound **15** with the TBA hydroxide show interactions occurring between the two compounds (Figure 64). Although, urea containing receptors such as those

described in this body of work may undergo deprotonation in the presence of strongly acidic anions, such as hydroxide which has a pKa value of 14.[233] This is because the urea functionality has a pKa value of 0.1[234] and chloroform a pKa value of 15.7.[235] In addition to this, the presence of electron withdrawing groups such as the phenol group attached to compound **15**, may lead to polarisation of the NH bonds within the urea, causing an increase in hydrogen bond donation properties. This leads to the urea group becoming more acidic as it loses the hydrogen atom more readily. Meaning that the urea is comparatively more acidic than the hydroxide anion, which becomes more basic than the urea group as it takes on the hydrogen atom more readily.[236] These characteristics combined means that it is not unlikely there may be deprotonation of the receptor before the formation of a host: guest complex.

Data obtained from Bindfit indicate these compounds have a strong interaction with an association constant of 2053 M^{-1} when compared to 1:1 association constants obtained from fitting experimental data to Bindfit for other compound combinations. Bindfit also indicated the compounds interact on a 1:1 ratio, due to the numbers calculated for the 1:2 and 2:1 host: guest ratios being either too large or being negative. A full titration with 25 additions was not possible to obtain for compound **16** with this anion even after several attempts.

This is because of the release of second order emission.[237] second order emission is the process by which an emission of light is produced at twice the excitation wavelength. Usually, it is possible to produce an emission spectra where the second order emission does not have an impact on the spectra produced. However, in this example the second order emission was too close to the emission value and so the spectra could not be produced without interference from the second order peak. During this experiment, the intensity for the second order emission rose to above 1000 au by addition number 7. The maximum intensity that can be read by the detector is 1000 au, because the experiment had reached this value it was decided not to carry on with the experiment as samples producing this kind of value over repeated runs can cause damage to the detector.

Figure 64 – A graph showing a decrease in emission intensity of compound **15** (host) upon increasing equivalence of TBA hydroxide (guest). CHCl$_3$ (298 K).

Table 12 displays the data obtained for the Bindfit fit of the experimental data obtained from compound **15** with TBA hydroxide with host: guest ratios 1:1, 1:2 and 2:1 M^{-1}.

Table 12 – Association constants (M^{-1}) calculated for compound **15** (host) titrated against TBA hydroxide (guest) in CHCl$_3$. The links for the Bindfit data is provided within the appendix.

Host: Guest	1:1	1:2		2:1	
	K	K_{11}	K_{12}	K_{11}	K_{21}
Association constant (M^{-1})	2053.74 (± 5.8439 %)	875.30 (± 7.5713 %)	-852.18 (± -13.5117 %)	0.0274 (± 15.0113 %)	60896310.08 (± 2.7483 %)

The titration results of compound **14** with the TBA hydrogen-sulphate shows interactions occurring between the two compounds (Figure 65). Data obtained from Bindfit indicate these compounds have one of the strongest interactions observed for a 1:1 binding isotherm for any combination of compounds tested. However, the results obtained for a 1:1 and a 1:2 (Table 13) were too similar and cannot be distinguished without further testing. The results indicate a strong

interaction for both binding isotherms, with an association constant of 15042 M^{-1} for a 1:1 ratio, and association constants of 3266 M^{-1} and 15262 M^{-1} for the 1:2 binding isotherm. The numbers calculated for the 2:1 host: guest ratio indicate that this isotherm does not fit due to the numbers being too large or negative.

Figure 65 – A graph showing a decrease in emission intensity of compound **14** (host) upon increasing equivalence of TBA hydrogen-sulphate (guest). $CHCl_3$ (298 K).

Table 13 shows the data produced from fitting the experimental results of combining compound **14** and hydrogen-sulphate in a host: guest 1:1, 1:2 and 2:1 M^{-1} ratio.

Table 13 – Association constants (M^{-1}) calculated for compound **14** (host) titrated against TBA hydrogen-sulphate (guest) in $CHCl_3$. The links for the Bindfit data is provided within the appendix.

Host: Guest	1:1	1:2		2:1	
	K	K_{11}	K_{12}	K_{11}	K_{21}
Association constant (M^{-1})	15042.74 (± 10.526 %)	3266.93 (± 3.253 %)	15262.76 (± 8.485 %)	3273.53 (± 3.139 %)	-2782.41 (± -0.888 %)

The titration results of compound **17** with the TBA phosphate monobasic show that the two compounds are interacting with each other (Figure 66). Data obtained from Bindfit indicate these compounds have a strong interaction with an association constant of 8816 M^{-1}. The association constant produced here from Bindfit is stronger than that seen for other compound combinations within this series on a 1:1 host: guest ratio. Bindfit indicated the compounds interact on a 1:1 ratio, due to the numbers calculated for the 1:2 and 2:1 host: guest ratios being either too large or being negative.

Figure 66 – A graph showing a decrease in emission intensity of compound **17** (host) upon increasing equivalence of TBA phosphate monobasic (guest). CHCl$_3$ (298 K).

Table 14 displays the data obtained from fitting the experimental results of compound **17** with phosphate monobasic on a host: guest ratio of 1:1, 1:2 and 2:1 M^{-1}.

Table 14 – Association constants (M^{-1}) calculated for compound **17** (host) titrated against TBA phosphate monobasic (guest) in CHCl$_3$. The links for the Bindfit data is provided within the appendix.

Host: Guest	1:1	1:2		2:1	
	K	K$_{11}$	K$_{12}$	K$_{11}$	K$_{21}$
Association constant (M^{-1})	8816.24 (± 9.003 %)	973.44 (± 4.182 %)	43149.22 (± 16.130 %)	3026.37 (± 4.199 %)	-3793.05 (± -1.217 %)

The titration results of compound **17** with the TBA sulphate show association occurring between the two compounds (Figure 67). Data obtained from Bindfit indicate these compounds have a strong interaction with an association constant of 15556 M^{-1}, even when compared to other strong interaction between compounds, such as between compound **17** and phosphate monobasic. Bindfit also indicated the compounds interact on a 1:1 ratio, due to the numbers calculated for the 1:2 and 2:1 host: guest ratios being either too large or being negative.
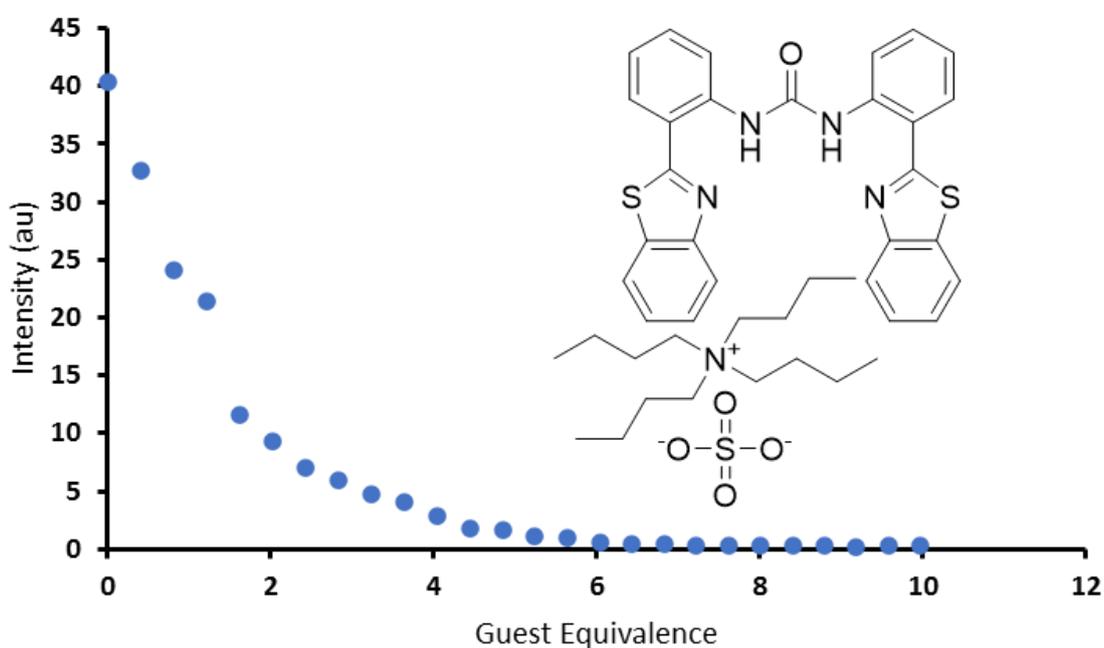
Figure 67 – A graph showing a decrease in emission intensity of compound **17** (host) upon increasing equivalence of TBA sulphate (guest). CHCl$_3$ (298 K).

Table 15 shows the data obtained from Bindfit for the interaction of compound **17** with sulphate in a host: guest ratio of 1:1, 1:2 and 2:1 M^{-1}.

Table 15 – Association constants (M^{-1}) calculated for compound **17** (host) titrated against TBA sulphate (guest) in $CHCl_3$. The links for the Bindfit data is provided within the appendix.

Host: Guest	1:1	1:2		2:1	
	K	K_{11}	K_{12}	K_{11}	K_{21}
Association constant (M^{-1})	15556.98 (± 9.783 %)	192788.2 (± 101.172 %)	21076.04 (± 18.802 %)	9116.08 (± 6.174 %)	-4950.07 (± -0.0003 %)

The examples given above are those that represent the strongest association constants calculated from Bindfit for each anionic guest, on a host: guest 1:1 binding isotherm.

Overall, compound **14** (Figure 68) showed the strongest interactions with TBA acetate and TBA hydrogen sulphate (Table 16). Although, for acetate the association constant is almost 0, meaning that no interactions are occurring, this was still the highest association constant produced for acetate. This means that acetate does not bind strongly to any of the host compounds **14**-**17**. Whereas, the hydrogen sulphate anion showed a high association constant, meaning that it bound strongly to compound **14** and compound **15.** However, the anion had a moderate association constant with compound **16** and a weak association constant with compound.
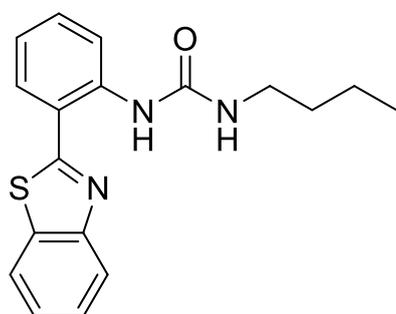
Figure 68 – Structure of compound **14**.

Table 16 – Association constants (M^{-1}) calculated for each host (compounds **14**-**17**) titrated against anionic guest with a TBA Counter cation; acetate and hydrogen-sulphate for a 1:1 association constant. Conducted in CHCl$_3$ at 293 K. Data provided to two decimal places and error values provided to 1 decimal place.

Anion Guest (TBA)	Compound **14**	Compound **15**	Compound **16**	Compound **17**
	K (M^{-1}) Error (± %)	K (M^{-1}) Error (± %)	K (M^{-1}) Error (± %)	K (M^{-1}) Error (± %)
Acetate	0.02 ± 2.5 %	895.18 ± 39.4 %	8263.55 ± 13.6 %	243860.54 ± 19.2 %
Hydrogen-Sulphate	15042.74 ± 10.5 %	5596.21 ± 4.9 %	136.03 ± 4.9 %	0.01 ± 1.2 %

Compound **15** (Figure 69) showed the highest interactions with TBA fluoride and TBA hydroxide (Table 17). TBA fluoride also showed a high association with compound **14.** The anion produced an unreliable association constant value with compound **16** as the associated error value is too large. TBA fluoride produced a weak association constant value with compound **17**, demonstrating no binding is occurring. TBA hydroxide produced a high association constant with compound **14** also. A full data set was not obtained for hydroxide with compound **16** as previously discussed. With compound **17**, hydroxide produced an unreliable result due to a high error value.
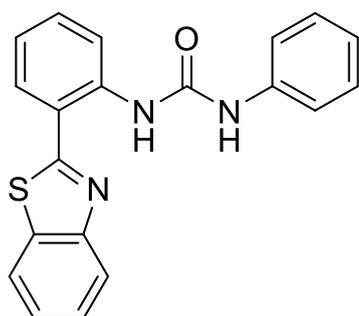
Figure 69 – Structure of compound **15**.

Table 17 – Association constants (M^{-1}) calculated for each host (compounds **14**-**17**) titrated against anionic guest with a TBA Counter cation; fluoride and hydroxide for a 1:1 association constant. Conducted in CHCl$_3$ at 293 K. b = no full data set obtained due to experimental limitations. Data provided to the two decimal places and error values provided to 1 decimal place.

Anion Guest (TBA)	Compound **14**	Compound **15**	Compound **16**	Compound **17**
	K (M^{-1}) Error (± %)	K (M^{-1}) Error (± %)	K (M^{-1}) Error (± %)	K (M^{-1}) Error (± %)
Fluoride	2426.88 ± 4.7 %	9855.59 ± 6.6 %	11597.53 ± 21.3 %	0.01 ± 2.3 %
Hydroxide	1544.66 ± 7.7 %	2053.74 ± 5.8 %	b	77551.09 ± 16.0 %

Compound **16** (Figure 70) showed the strongest interaction with TBA benzoate (Table 18). TBA benzoate produced results with compounds **14** and **17** that indicate no association between the host: guest compounds. When titrated with compound **15** a moderate strength association constant was produced.
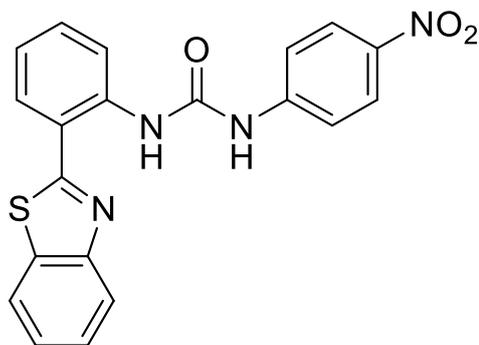
Figure 70 – Structure of compound **16**.

Table 18 – Association constants (M^{-1}) calculated for each host (compounds **14**-**17**) titrated against anionic guest with a TBA Counter cation benzoate for a 1:1 association constant. Conducted in CHCl$_3$ at 293 K. Data provided to two decimal places and error values provided to 1 decimal place.

Anion Guest (TBA)	Compound **14**	Compound **15**	Compound **16**	Compound **17**
	K (M^{-1}) Error (± %)	K (M^{-1}) Error (± %)	K (M^{-1}) Error (± %)	K (M^{-1}) Error (± %)
Benzoate	0.01 ± 0.5 %	352.09 ± 9.3 %	1166.91 ± 2.4 %	0.02 ± 3.9 %

Finally, compound **17** (Figure 71) showed the strongest interactions with TBA chloride, TBA phosphate monobasic and TBA sulphate (Table 19). An unreliable result was produced for TBA chloride with compounds **14** and **15** due to the error value being above 11 %. When titrated against compound **16**, TBA chloride produced a weak association constant. TBA phosphate monobasic produced a strong association constant with compound **14**. Compounds **15** and **16** produced moderate association constants with TBA chloride. TBA sulphate showed no interaction with compounds **14** and **16**, and an unreliable value was produced when TBA sulphate was titrated against compound **15** due to a high error value.
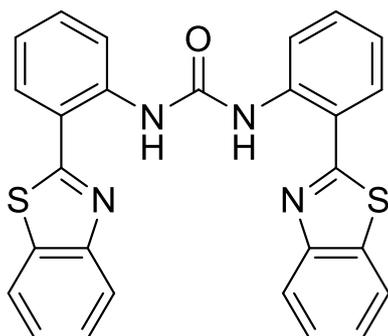
Figure 71 – Structure of compound **17**.

Table 19 – Association constants (M^{-1}) calculated for each host (compounds **14**-**17**) titrated against anionic guest with a TBA Counter cation; chloride, phosphate monobasic and sulphate for a 1:1 association constant. Conducted in CHCl$_3$ at 293 K. Data provided to two decimal places and error values provided to 1 decimal place.

Anion Guest (TBA)	Compound **14**	Compound **15**	Compound **16**	Compound **17**
	K (M^{-1}) Error (± %)	K (M^{-1}) Error (± %)	K (M^{-1}) Error (± %)	K (M^{-1}) Error (± %)
Chloride	94878.33 ± 17.6 %	95863.48 ± 15.4 %	73.20 ± 4.1 %	15241.79 ± 10.7 %
Phosphate monobasic	3087.76 ± 5.5 %	428.45 ± 3.9 %	753.60 ± 4.6 %	8816.24 ± 9.0 %
Sulphate	0.00 ± 0.0 %	1874.16 ± 20.4 %	0.01 ± 1.7 %	15556.98 ± 9.8 %

The data obtained for these experiments shows that all compounds showed strong interactions on a 1:1 ratio, apart from compound **14** with TBA chloride and hydrogen-sulphate, compound **15** with TBA acetate, chloride and sulphate, compound **16** with TBA acetate and fluoride and finally, compound **17** with TBA acetate. Though Bindfit did fit the data to an isotherm, the error values associated with the data means that it was not reliable, and therefore no reliable fit was obtained for these sets of data.

All titrated host compounds showed some degree of fluorescent quenching when exposed to the guest molecule, apart from compound **15** with TBA acetate and sulphate. The fluorescent quenching seen here is negligible, graphs of which can be found in the appendix (Figures 62-93). Quenching is a phenomenon that relies on the direct interactions of the fluorescing compound with the quencher,[238] usually the guest molecule, which proves the fluorescent quenching occurring during the titrations is a direct results or host: guest interactions.

Upon the addition of the guest anions fluoride and hydroxide to compound **16** a colour change from clear to pale yellow and to deep yellow (Figure 72) was observed. This is most likely due to

the presence of the nitro functionality; it facilitates the removal of a hydrogen atom from the host molecule.[239] A ^{1}H NMR spectrum depicting this change was attempted, but unfortunately the phenomenon was reversed upon exposure to cold temperatures. A test sample of this solution was prepared at room temperature which showed the colour change observed in Figure 72 below. However, upon placing the sample into the fridge for storage the colour change reversed to the image Figure 72A.
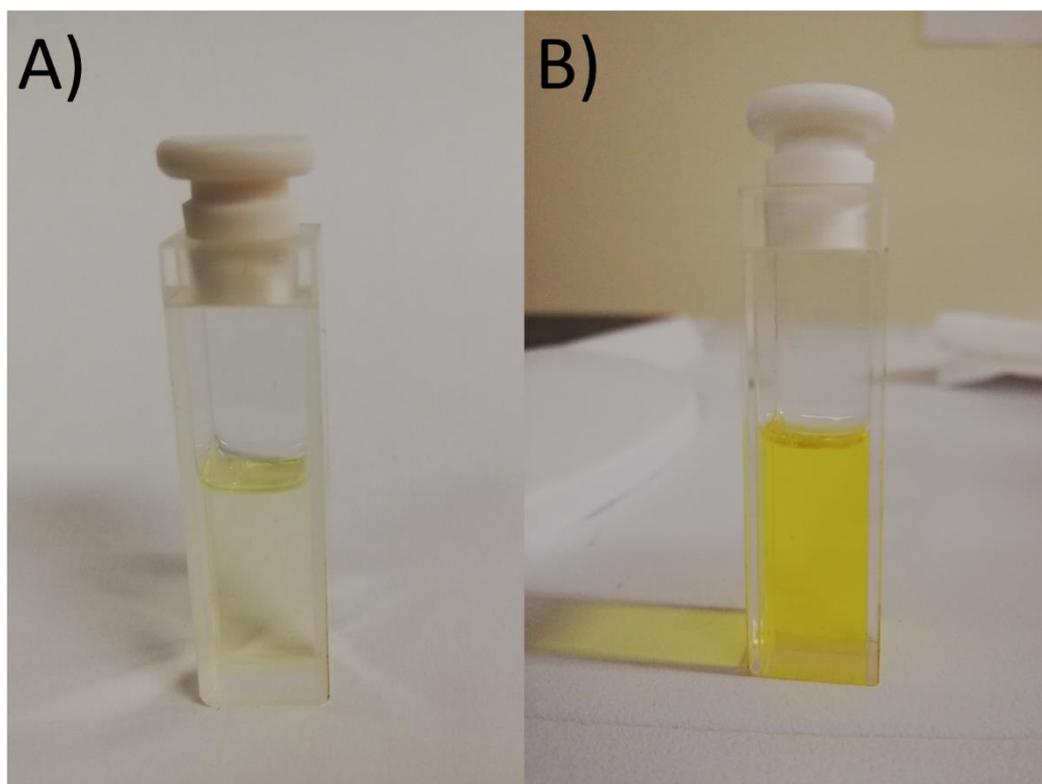
Figure 72 – Image: A) host: guest solution of compound **16** with TBA fluoride, forcing deprotonation, B) host: guest solution of compound **16** with TBA hydroxide, forcing deprotonation.

The data obtained from the fluorescent titrations of compounds **14**-**17** with the respective anions show a trend, this trend can be related to the Hofmeister series. The Hofmeister trend is the order in which anions and cations may be placed with regards to their reliable ability to cause an effect on the physical properties of proteins.[240] However, more recent research has highlighted the series application in a variety of different chemical processes and settings.[241] The order of anions in the series relates several properties; the ability to form hydration spheres but more notably

included in this is the order in which the anions are placed depending on their selectivity to bind with a host molecule.[242] Figure 73 below gives the order of anions in the Hofmeister series.
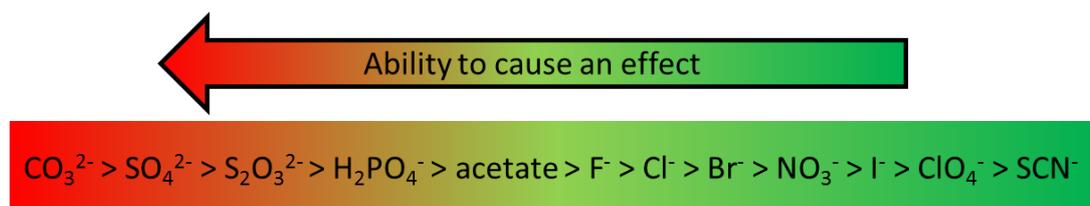
Figure 73 - The Hofmeister series represented with a range of anions.

Although the order of anions[243,244] shown above may vary slightly depending on what the environmental application is,[245] the overall trend doesn't change. Variations from this trend are rare, especially those that exhibit and inverse in selectivity.[242] HBD receptors normally display selectivity in the order shown in Figure 74, however the HBD fluorescent receptors **14**-**17** exhibit an inverse of the trend. The data obtained from the fluorescent titrations exhibit this reverse order selectivity for binding to a host molecule. Some anions showed a reversed order selectivity to specific compounds from compounds **14**-**17**. The anions which would be expected to exhibit higher association constants have been shown here to exhibit lower association constants. Those that would be expected to exhibit lower association constants have been shown to exhibit higher association constants than expected if the Hofmeister series is followed.
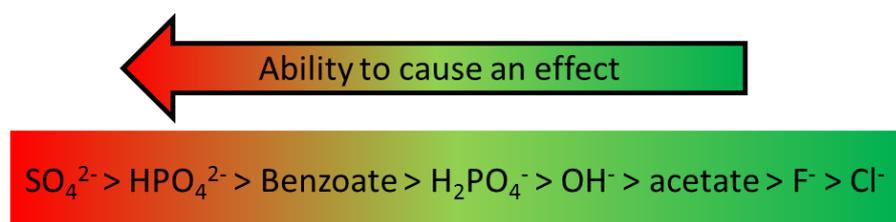
Figure 74 – Hofmeister series for the anions used within these experiments.

Using the examples of a host: guest 1:1 binding isotherm for TBA sulphate and TBA chloride as examples, it would be expected that the sulphate anion would have a higher association constant with compounds **14**-**17** than the chloride anion exhibited with compounds **14**-**17**, if the trend in the Hofmeister series is followed. However overall, we see the opposite trend (Figure 75) For

compound **14** the sulphate anion has an association constant of 0 M^{-1}, whilst the chloride anion has an association constant of 94878 M^{-1}.
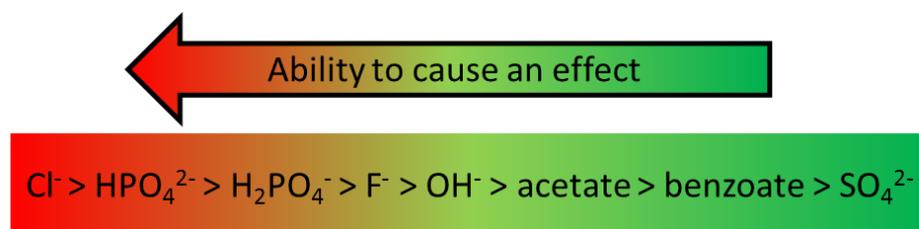
Figure 75 – The trend shown for each anion for compound **14**.

The trend seen for compound **15** (Figure 76) with the sulphate anion has an association constant of 1874 M^{-1}, whilst the chloride anion has an association constant of 95863 M^{-1} which magnifies the selectivity demonstrated with this anion.
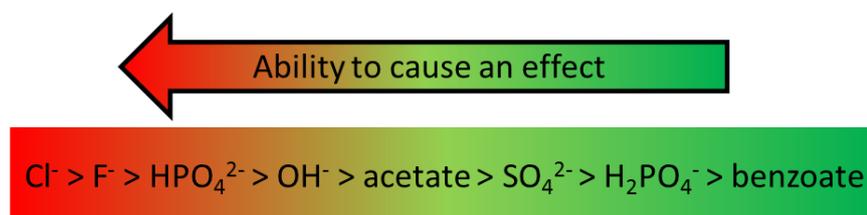
Figure 76 – The trend shown for each anion for compound **15**.

For compound **16**, the trend in the Hofmeister series (Figure 77) shows both association constants are weak, but the chloride ion still maintains the higher association constant. The sulphate anion has an association constant of 0 M^{-1} and the chloride anion has an association constant of 73 M^{-1}.
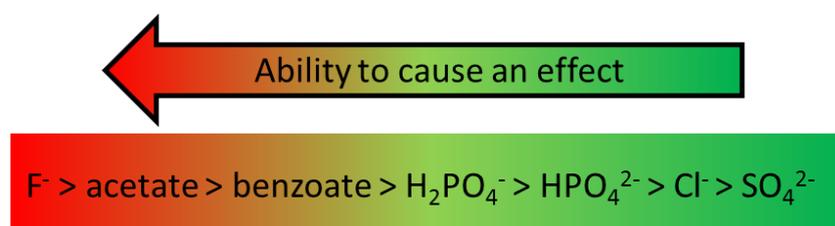
Figure 77 – The trend shown for each anion for compound **16**.

Finally, for compound **17** the trend seen in the series (Figure 78) shows association constants for both ions are low, with the sulphate ion producing the slightly stronger association constant. Though this follows the Hofmeister series, it should be expected that due to their positions in the

series, the sulphate anion would have a significantly stronger association constant. The association constant of the sulphate anion with compound **17** is 15557 M^{-1} and the association constant for the chloride anion is 15242 M^{-1}, demonstrating that the chloride anion is able to bind equally as well as the sulphate anion to compound **17**.

Ability to cause an effect

$OH^- >$ acetate $> SO_4^{2-} > Cl^- > H_2PO_4^- >$ benzoate $> F^- > HPO_4^{2-}$
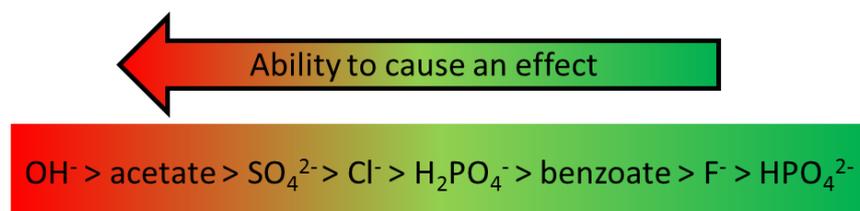
Figure 78 – The trend shown for each anion for compound **16**.

At this time, it cannot be definitively stated why this reverse trend is present within the body of work presented. One may theorise that the structure of the host compounds **14**-**17** will play a significant role in the binding events occurring with the anionic guests. Which lead to the formation of intramolecular bonds. In addition to this, the presence of a conjugated ring system on the benzothiazole region of each compound may certainly provide additional support to the theory of why the structure of the compounds may contribute to a reverse in the trend, as depicted here. However, further study is required here in order to fully ascertain the reason for the reverse in binding affinities which is something that will be conducted in the future.

This would include the use of single crystal x-ray on crystals produced of the host: guest complexes produced in the work discussed here. This would demonstrate the binding of the guest to the host compound, which may indicate why some anions show higher binding than others to the same compound. The use of ^1H NMR may also be valuable for determining the change in urea NH resonance if the solubility issues experienced within can be over-come.

4.4.2 Fluorescent dilution studies

A series of fluorescent dilutions were performed on compounds **14**-**17** in order to determine whether the concentration at which the samples for the titrations were conducted was free of a

phenomenon known as the inner filter effect (IFE). This phenomenon arises during fluorescent measurements when the concentration of a sample is high enough to prevent all the emitted light from reaching the detector.[246] Some of the emitted light is usually re-absorbed by the solution for secondary excitation at these concentrations, reducing the signal intensity produced from fluorescent molecules during experimentation.[247] It should be noted that IFE is not the same as quenching.[246]

The concentration at which this occurs is different for each compound,[248] but this event usually occurs when samples have an absorbance larger than 0.1 au[249] in which supportive evidence can also be obtained from Uv-Vis experiments. However, most modern fluorimeters correct for this effect by having the detector at a 90 ° angle to the sample from which the light will emit.[250] The fluorimeter used in these experiments has this set up,[251] however this does not correct inner filter effects for samples that have a high absorbance.[250]

Stock solutions of compounds **14**-**17** were made with a maximum concentration that was 30 times more concentrated than the stock solutions made for the titrations. This concentration was used for several reasons. Firstly, if IFE were occurring in the samples used for the titrations, it would also occur in more concentrated samples, with increasing effect as the concentration increases until no / little light is detected. If this effect was to occur, during the dilution experiment a decrease in fluorescent intensity would be seen[252] upon increasing concentration of compounds **14**-**17**.

Secondly, this concentration was used as it was the strongest concentration attainable for compounds **14**-**17** before the limit of solubility was reached. A 10 mL stock solution was produced of each compound in chloroform at a concentration of 0.003 M. From these stock solutions a 2000 µL aliquot was taken and used as the start point for the experiment. From this point on, a 200 µL aliquot was removed from the curvette, and then replaced with 200 µL of the chloroform solvent. This procedure was carried out until there was little change being observed in the intensity output. Of compounds **14**-**17** the only compound which exhibited signs of inner filter effect was compound **17**. This effect occurred only at the highest concentrations, in the range of approximately 0.0017 – 0.0030 M.

4.4.2.1 Results and discussion

The results of the dilution studies conducted on compounds **14**-**17** indicated that no inner filter effect is occurring during the titrations at the specified concentration. The fluorescent intensity is seen to increase with increasing concentration of each host sample, which is what would be expected in a sample where no IFE is occurring.

Compound **14** showed no signs of inner filter effect throughout the dilution study at the concentrations tested (Figure 79). This can be seen because the curve continues in an exponential trend throughout. The data point highlighted by the pink circle is highlighted because it appears as an anomalous result. It is not an indication of IFE as there are three data points at higher concentrations that fit the trend with the initial nine data points.
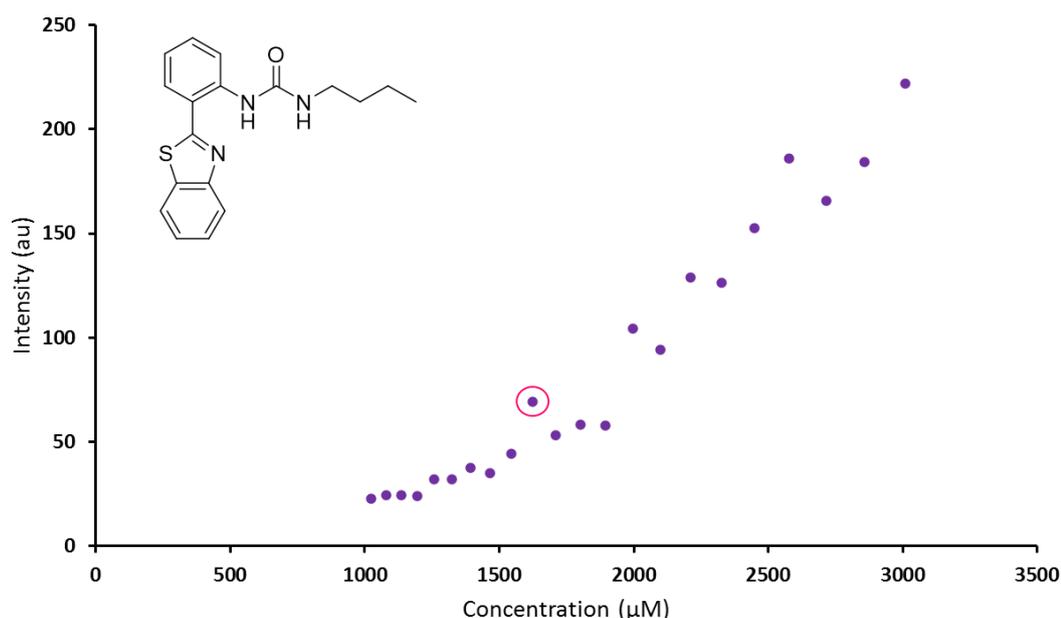
Figure 79 – Graph illustrating the increase in intensity as concentration of compound **14** increases. CHCl$_3$ (298 K).

The results for compound **15** indicate that there is no inner filter effect occurring at the lowest concentration as the trend proceeds linearly (Figure 80). However, because the trend changes slightly at the higher concentrations, highlighted in pink, this may be evidence of IFE. This does not affect the results obtained for the fluorescent titrations, as the concentration used in those experiments falls within the linear region of the dilution study for compound **15**.
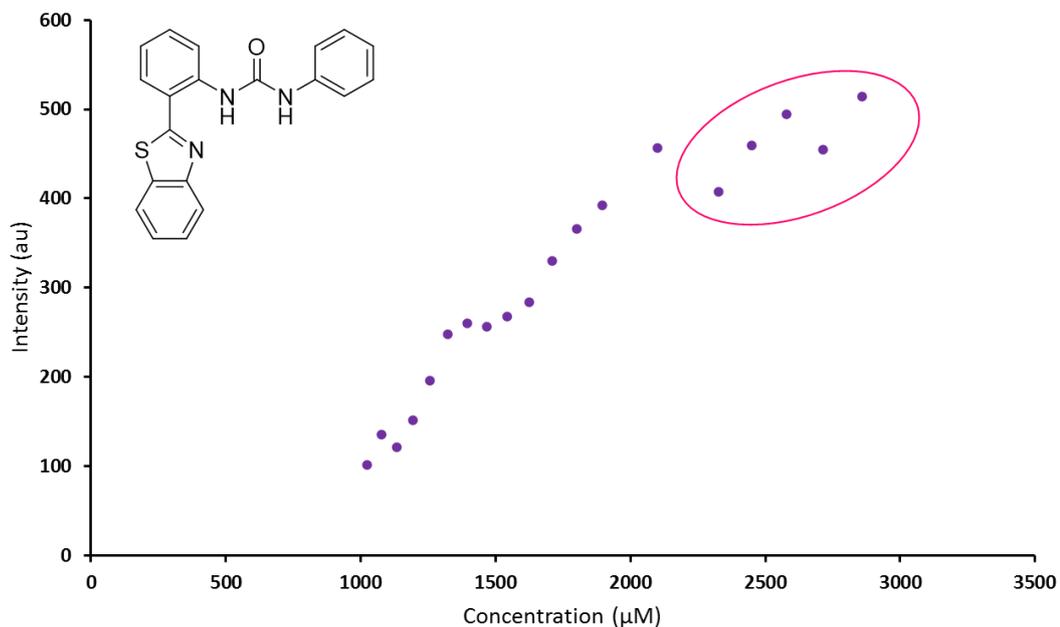
Figure 80 – Graph illustrating the increase in intensity as concentration of compound **15** increases. CHCl₃ (298 K).

The data obtained for compound **16** shows that no IFE is occurring during the titrations as there is no presence of this event at the lower concentrations (Figure 81). Although there is a slight change in trend at the lower concentrations, highlighted in pink, this is not an overall change that would affect the results, alluding to the presence of IFE.
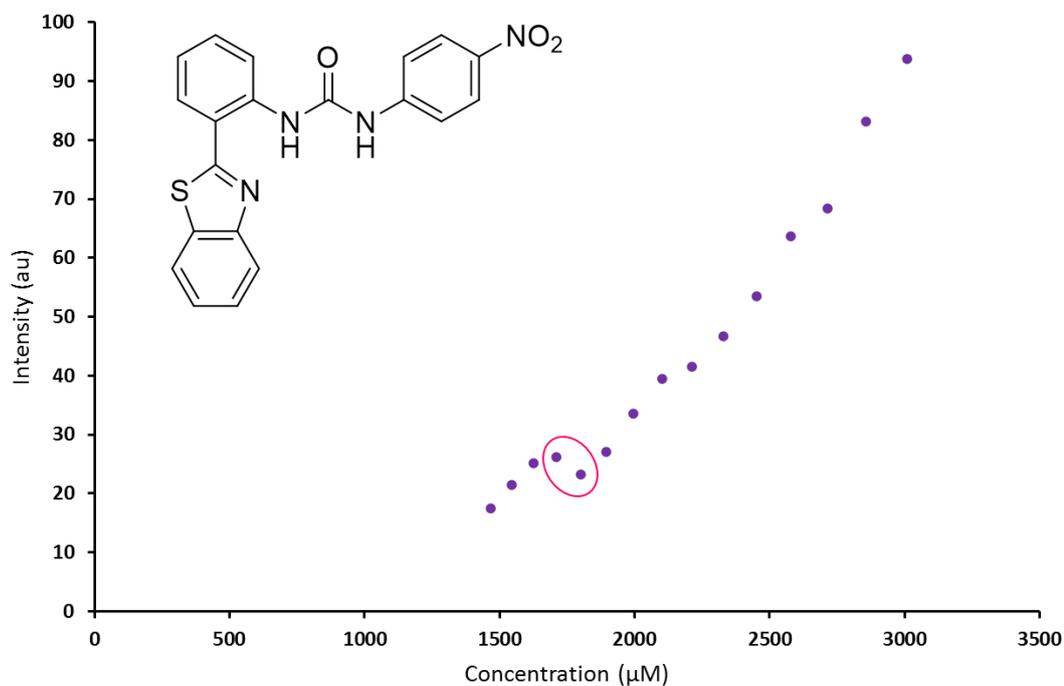
Figure 81 – Graph illustrating the increase in intensity as concentration of compound **16** increases. CHCl₃ (298 K).

The data obtained for compound **17** indicates that at the higher concentrations, it is likely there is IFE occurring, highlighted in pink (Figure 82). This can be seen where the emitted intensity begins to decrease with increasing concentration of compound **17**. The decrease in intensity begins at a concentration of 1800 µM, with an emission intensity value of 678 au and is highlighted in blue. The data value before this was at a concentration of 1710 µM with an emission intensity of 878 au. This demonstrates a sharp and noticeable drop in the emission intensity of compound 17, alluding to the presence of IFE at the ten highest concentrations. However as there is no evidence of IFE occurring at the lower concentrations, there is no IFE present at the concentration used for the titrations.
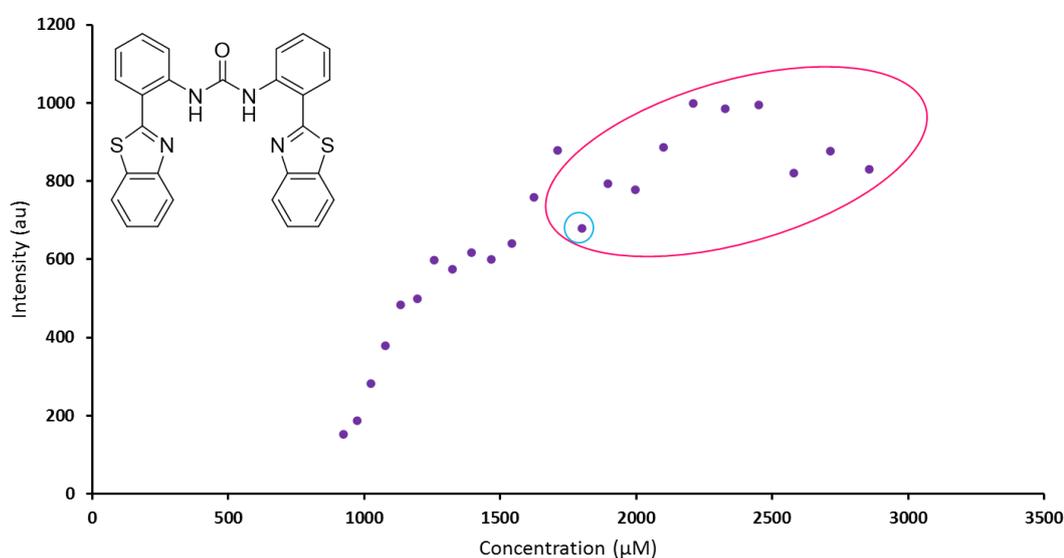
Figure 82 – Graph illustrating the increase in intensity as concentration of compound **17** increases. CHCl$_3$ (298 K).

The data produced from the dilution studies show no IFE occurring at the lowest concentrations. This means that no special measures need to be taken to correct for this in the data produced from the titration experiments.

4.5 Low level *in-silico* modelling

Computational chemistry is used within to model ESPMs for compounds **14**-**17** using Spartan'16[253] with energy minimised semi-empirical PM6[254] modelling methods to derive

comparative E_{min} and E_{max} values. Comparative E_{min} and E_{max} values are displayed using a colour spectrum where red denotes the E_{min} and blue denotes the E_{max}. All computation chemistry herein was produced by Dr J. Hiscock.

4.5.1 Results and discussion

The ESPM for compound **14** (Figure 83) show the most negative point on the surface (E_{min}) of the molecule is located around the urea oxygen and the aromatic nitrogen. The aromatic nitrogen is most likely therefore to be an HBA. The most positive points (E_{max}) on the map are situated around the butyl chain, as well as the outer most parts of the aromatic rings. However, the most positive area can be found on one of the urea NHs and is the principle HBD group. The map also confirms the intramolecular hydrogen bond from the crystal structure (Figure 52) where a hydrogen bond is present between the aromatic nitrogen and the urea NH, where there is an area of high negativity and an area of high positivity spatially close to one another the formation of hydrogen bonds can be expected.
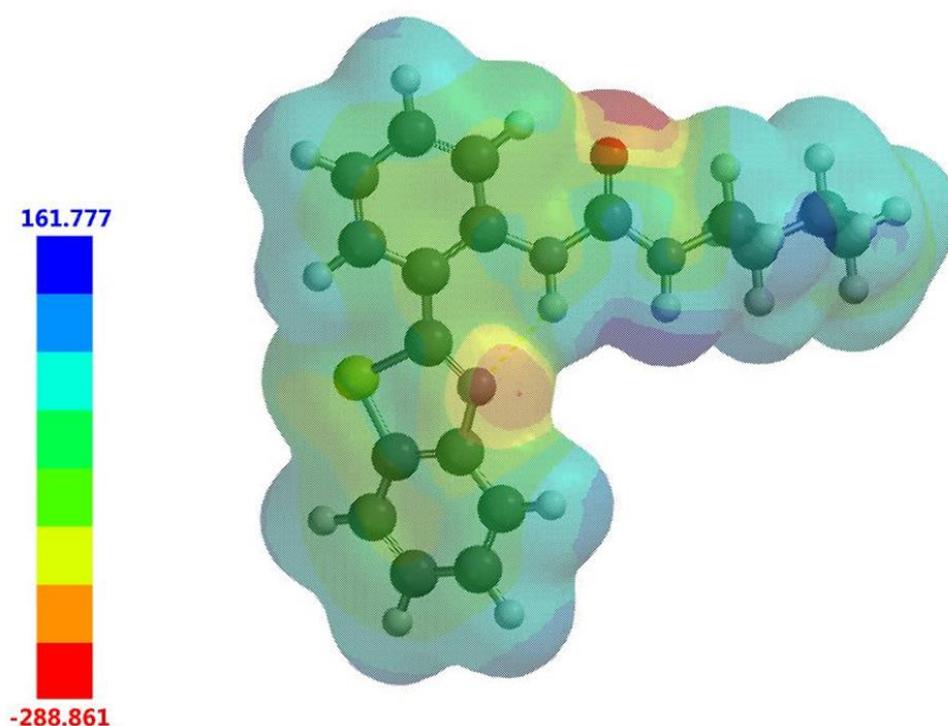
Figure 83 - Electrostatic potential map calculated for compound **14**. E_{max} (deep blue) and E_{min} (bright red) values depicted in the Figure legends are given in kJ/mol.

The ESPM for compound **15** (Figure 84) shows the most negative point on the surface (E_{min}) of the molecule is around the urea oxygen and the aromatic nitrogen. The groups are therefore identified as the principle HBA groups. The most positive points (E_{max}) on the map are situated around the outer edges of the aromatic functionalities, with the highest area of positivity situated around one of the urea NHs which is identified as the principle HBD group.
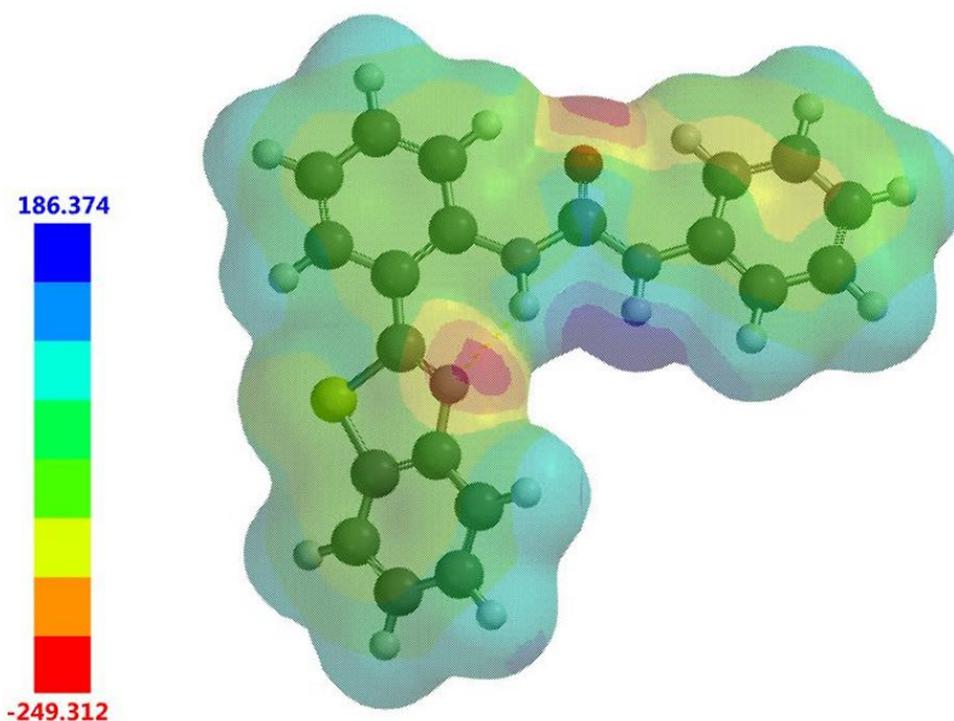
Figure 84 – Electrostatic potential map calculated for compound **15**. E_{max} (deep blue) and E_{min} (bright red) values depicted in the Figure legends are given in kJ/mol.

The ESPM for compound **16** (Figure 85) show the most negative point on the surface (E_{min}) of the molecule is predominantly the aromatic nitrogen, the urea oxygen and even more significantly around the nitro functionality. These areas are therefore identified as the primary HBA groups. The most positive point (E_{max}) on the map is situated around one of the urea NHs and will most likely be an HBD groups. The crystal structure of compound **16** (Figure 54) shows the presence of a hydrogen bond between the highly electropositive urea NH and the highly electronegative aromatic nitrogen. Along with hydrogen bonds from the urea NHs to the oxygen on a DMSO molecule. Oxygen is a well-known HBA, indicating further that the urea NH is an HBD.
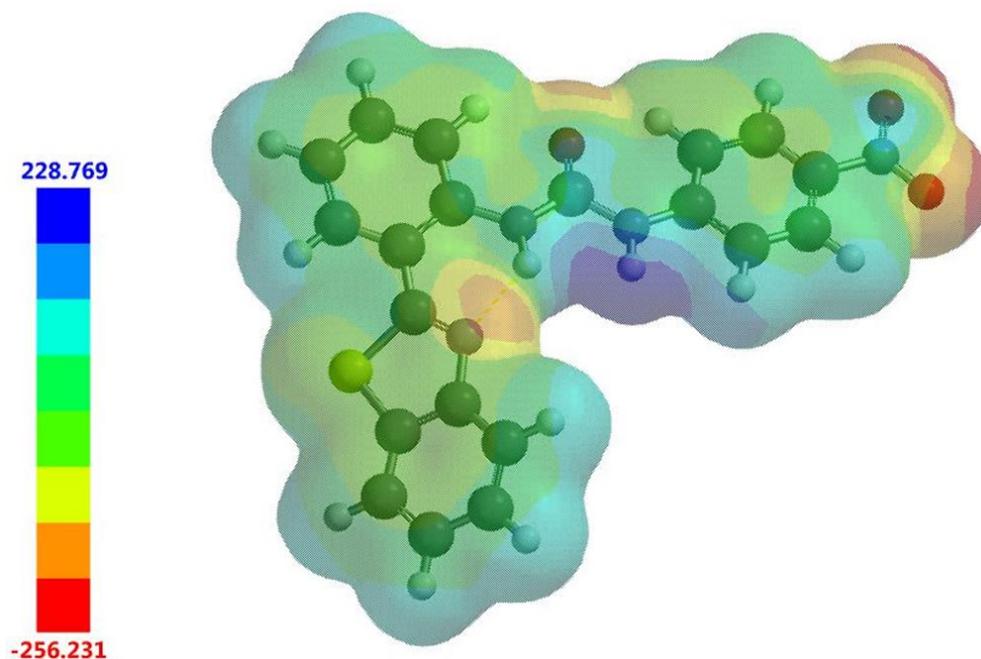
Figure 85 – Electrostatic potential map calculated for compound **16**. E_{max} (deep blue) and E_{min} (bright red) values depicted in the Figure legends are given in kJ/mol.

The ESPM for compound **17** (Figure 86) shows the most negative point on the surface (E_{min}) of the molecule is predominantly the aromatic nitrogen. Another area of electronegativity however is also the urea oxygen; therefore, these groups are identified as the primary HBA groups. The most positive point (E_{max}) on the map is situated around the urea NHs. These areas are presented as the principle HBD groups. Though there is high electropositivity around the outer edges of the aromatic functionalities also. Figure 85 above shows there is a slight bend in the positioning of the lower benzothiazole region, which may be due to repulsion from the sulphur and nitrogen components of the compound. This may also indicate that the binding event may be affected by steric factors.
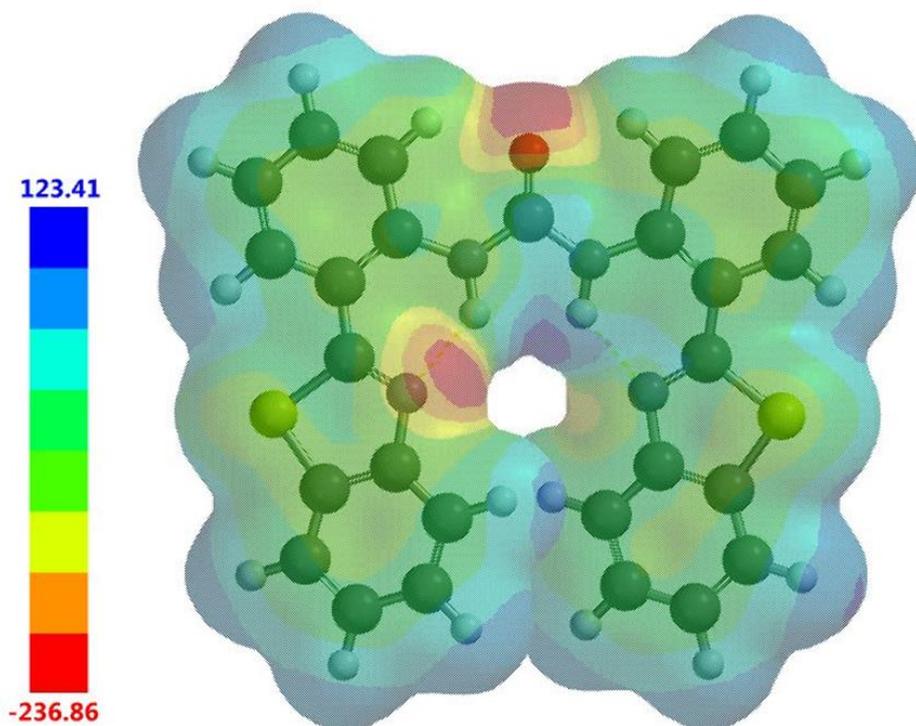
Figure 86 – Electrostatic potential map calculated for compound **17**. E_{max} (deep blue) and E_{min} (bright red) values depicted in the Figure legends are given in kJ/mol.

The data calculated for compounds **14**-**17** shows that the highest area of E_{min} is situated around the aromatic nitrogen on compounds **14**-**17**, whilst highest area of E_{max} is located around the urea NHs on compounds **14**-**17**. It has been theorised that the use of low-level computational chemistry can be used to help predict where hydrogen bonding will occur within a chemical system.

For the relative E_{min} values, ordered from least electronegative to most electronegative compounds **14**-**17** are ordered as: compound **17**, 236 kJ/mol, compound **15**, 249 kJ/mol, compound **16**, 256 kJ/mol and compound **14** with 288 kJ/mol. When ordered from least electronegative to most electronegative using the relative E_{max} values, compounds **14**-**17** are ordered as such: compound **17**, 123 kJ/mol, compound **14**, 161 kJ/mol, compound **15**, 186 kJ/mol and compound **16** with 228 kJ/mol.

When discussing the formation of host: guest complexes the formation of intermolecular hydrogen bonds is focused around the primary HBD groups present on the host compound. These groups are represented by the E_{max} values calculated, or the areas coloured dark blue. When compounds **14**-**17** are ordered based on their relative selectivity to anionic guests, the compounds

are ordered as: compound **16** with a high association constant to one anion, benzoate. Then, compounds **15** and **17** show selectivity to three anionic guests each: compound **15** with chloride, fluoride and hydroxide and compound **17** with hydroxide, phosphate monobasic and sulphate. This may also be a result of increased steric contributions from the structure of compounds **15** and **17**.

Finally compound **14** shows selectivity to four anionic guests which are: fluoride, hydroxide, hydrogen sulphate and phosphate monobasic. In other words, the compounds can be ordered as: compound **16**, compounds **15** and **17** jointly and finally compound **14**. This follows the same order observed when the compounds are ordered according to their relative E_{mas} values. Therefore, the data calculated for the electrostatic potential maps for compounds **14-17**, supports the data obtained from the fitting of the experimental results to a host: guest 1:1 binding isotherm calculated by Bindfit.

This data produced from the electrostatic potential maps show evidence of the presence of areas of high electronegativity at the binding sites. This originates from the aromatic nitrogen. Where anions are negative, they may be repelled by this area of high electronegativity and so have reduced association constants. It would then in turn make sense that those anions which are less negative would feel the force of repulsion less, and therefore have higher association constants. Whilst this data is supportive of this trend, it is not conclusive. Further experimentation is required to definitively say what is causing this reversed Hofmeister series effect.

4.6 Conclusion

In conclusion, four novel fluorescent receptors have been synthesised, characterised and host: guest properties were investigated. Compounds **14**-**17** all act as good anionic receptors and detectors in chloroform. Compound **17** showed strong interactions with the highest number of anions, followed by compound **14** and then compound **15** and finally compound **16** with the strongest interaction occurring with one guest species. All receptors fitted with their guest on a 1:1 binding isotherm, apart from compound **14** with hydrogen-sulphate where the difference could not

be determined without the need for further study. The results showed a reverse trend to the Hofmeister series with anions such as chloride displaying stronger binding events than an anion such as sulphate.

The results from the dilution studies show that no inner filter effect was occurring for any receptor at the titration concentration used during the titrations, as these concentrations were markedly above those used in the titrations. Apart from compound **17**, where there is evidence of this phenomenon occurring at the higher concentrations tested. Electrostatic potential maps for compounds **14**-**17** have been employed and show the areas of highest electronegativity to be around the aromatic nitrogen, with the areas of highest electropositivity to be located around the urea NHs.

4.7 Future Works

Further study of why an inverse in the Hofmeister trend is observed, through the use of methods such as single crystal x-ray of the host: guest complexes, the use of ^{1}H NMR and qNMR.

5.0 Experimental techniques

5.1 General Remarks

All reactions associated with compounds **1**-**11** and compound **17** were conducted under slight positive pressure of N_2 gas using oven dried glassware. NMR spectra were obtained using a Bruker AV2 400 MHz or Bruker AVNEO 400 MHz spectrometer with the chemical shifts reported in parts per million (ppm), with the calibration set to the centre of the solvent peak set. The data was produced using Bruker's NMR software TopSpin 3.6.2. All solvents and starting materials used were purchased from commercially available sources where appropriate. High-resolution mass spectra were collected using a Bruker microOTOF-Q mass spectrometer. Melting points were obtained in open capillaries using a Stuart SMP10 melting point apparatus. Infrared (IR) spectra were recorded

using a Shimadzu IR-Affinity 1 where the data was analysed in wavenumbers (cm^{-1}) using IRsolution software. Fluorescent emission spectra were obtained using a Cary Eclipse Fluorescence Spectrophotometer from Agilent Technologies. A 1 cm^3 quartz curvette was used for these measurements.

5.2 Single-crystal X-ray studies

A suitable crystal of each relevant compound was selected and mounted onto a Rigaku Oxford Diffraction Supernova diffractometer. Data was collected using Cu Kα radiation at 293 K. Structures were solved with either ShelXT[255] or ShelXS structure solution programs via Direct Methods and refined with ShelXL[256] by the Least Squares minimisation. Olex2[257] was used as an interface to all the ShelX programs. (CCDC 1866274-1866275). Data refined by Dr J. Hiscock.

5.3 High-resolution mass spectra studies

Approximately 1 mg of each compound was dissolved in 1 mL of methanol. This solution was further diluted 100-fold before undergoing analysis where 10 μL of each sample was then injected directly into a flow of 10 mM ammonium acetate in 95 % water (flow rate = 0.02 mL/min). Mass spectra were acquired in the negative ion mode and the data was processed in Bruker's Compass Data Analysis software by both R. Ellaby and L. White.

5.4 Self-association and association constant calculations

All association constants were calculated and obtained using the widely available Bindfit NMR program (http://app.supramolecular.org/bindfit/). All data used to obtain association constants can be accessed online through the use of the appropriate link provided in the appendix for each complexation event. DCM doping studies were conducted with 5 μL of H_2O to enable the amount of water present in the DMSO-d_6 to be monitored.

5.5 Fluorescence Spectrometry

All data produced for fluorescent spectrometry was obtained using the Scan software provided by Cary Eclipse. The data was then opened and manipulated in Microsoft Excel to produce representative graphs. All association constants were calculated using the online Bindfit UV-Vis

program (http://app.supramolecular.org/bindfit/). All data used to obtain association constants can be accessed online using the appropriate link provided in the appendix for each titration complex.

6.0 Synthesis

Compound 1: (Figure 87) This compound was synthesised in line with previously published methods. Proton NMR were found to match the previously published data.[200] The reactants were added into a round bottom flask, stirred for 30 minutes producing a pale-yellow precipitate, which was filtered and washed with methanol producing a white precipitate. ^{1}H NMR (400 MHz, 298 K, CDCl$_3$): 7.00 (s, 4NH), 5.90 (d, J = 2.72 Hz, 8H), 1.51 (s, 24H).
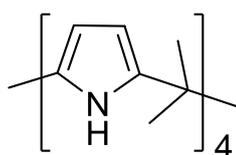
Figure 87 – Structure of compound **1**.

Compound 2: (Figure 88) This compound was synthesised in line with previously published methods. Proton NMR were found to match the previously published data.[199] The solution containing compound **2** was washed with dilute hydrochloric acid, where the toluene layer was then dried with magnesium sulphate to remove any water remaining from the acid wash in the separating funnel. To the toluene was added methanol and a white precipitate formed, which was separated through filtration. If the product was not pure it was dissolved into chloroform and precipitated out with methanol before being filtered off. ^{1}H NMR (400 MHz, 298 K, CDCl$_3$): 10.22 (s, 4OH), 7.08 (d, J = 7.59 Hz, 8H), 6.75 (t, J = 15.17 Hz, 4H), 3.92 (br d, J = 284.90 Hz, 8H).
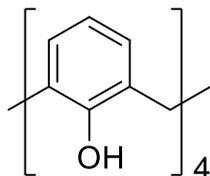
Figure 88 – Structure of compound **2**.

Compound 3: (Figure 89) This compound was synthesised in line with previously published methods. Proton NMR were found to match the previously published data.[104] Compound **2** was dissolved into acetonitrile and K_2CO_3 was added. The mixture was heated to reflux for 24 hours. Extracted into dichloromethane and wash with water, it was then dried over $MgSO_4$ and precipitated out into a swirling flask of MeOH producing a white solid. ^{1}H NMR (400 MHz, 298 K, CDCl$_3$): 8.26 (s, 2OH), 7.05 (d, J = 7.42 Hz, 4H), 6.92 (d, J = 7.80 Hz, 4H), 6.74 (t, J = 15.38 Hz, 2H), 6.64 (t, J = 14.84 Hz, 2H), 4.32 (d, J = 13.19 Hz, 4H), 4.00 (t, J = 13.19 Hz, 4H), 3.37 (d, J = 13.19 Hz, 4H), 2.04 (m, J = 28.03 Hz, 4H), 1.79 (m, J = 37.09 Hz, 4H), 1.09 (t, J = 14.01 Hz, 6H).
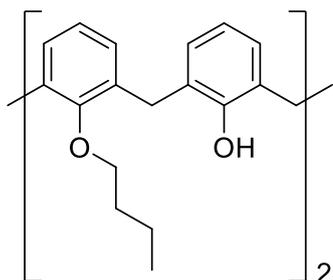
Figure 89 – Structure of compound **3**.

Compound 4: (Figure 90) A mixture of 80 % w/w HNO_2 and 70 % w/w H_2SO_4 was added to a stirring solution of compound **3** (0.200 g, 0.37 mM) in acetonitrile at room temperature. The product was extracted with chloroform (30 mL) and then water washed (20 mL x3) then the organic phase was taken to dryness. Yield 91 % (0.211 g, 0.34 mM). Melting point: >200 °C; ^{1}H NMR (400 MHz, 298 K, CDCl$_3$): 9.40 (s, 2H), 8.04 (s, 4H),*- 6.98 (d, J = 8.36 Hz, 4H), 6.84 (t, J = 13.93 Hz, 2H), 4.29 (d, J = 13.09 Hz, 4H), 4.04 (t, J = 13.09 Hz, 4H), 3.50 (d, J = 13.09 Hz, 4H), 2.05 (m, J = 28.37 Hz, 4H), 1.77 (m, J = 37.09 Hz, 4H), 1.11 (t, J = 13.09 Hz, 6H). ESI-MS: 624.3578 [M+M-H$^+$]$^-$.
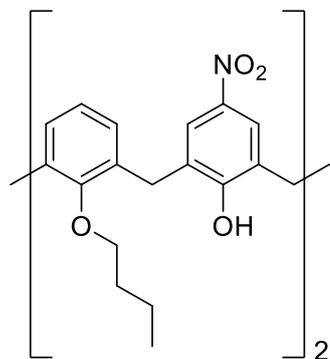
Figure 90 – Structure of compound **4**.

Compound 5: (Figure 91) This compound was synthesised in line with previously published methods. Proton NMR were found to match the previously published data.[104] The sodium hydride was washed with hexane to remove the mineral oil and placed into a round bottom flask under N_2, to this compound **2** was added. Through the septum dry DMF was added and the mixture stirred for ten minutes, then butyl-iodide was added through the septum drop-wise and the solution stirred for 26 hours at room temperature. Once complete, the reaction mixture was then poured into a 2 M solution of hydrochloric acid, producing a pale-yellow viscous substance. The viscous substance was then dissolved into ethyl acetate, the organic layer was then washed with water five times, followed by saturated sodium hydrogen carbonate and then finished with a brine wash. The solution was then dried over magnesium sulphate and then vacuumed down to produce a whiteish powder. ^{1}H NMR (400 MHz, 298 K, CDCl₃): 6.57 (m, J = 32.22 Hz, 12H), 4.45 (d, J = 12.24 Hz, 4H), 3.89 (t, J = 14.69 Hz, 8H), 3.14 (d, J = 14.69 Hz, 4H), 1.89 (m, J = 29.38 Hz, 8H), 1.45 (m, J = 39.17 Hz, 8H), 0.99 (t, J = 14.69 Hz, 12H).
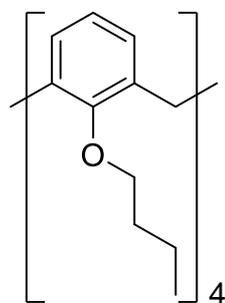
Figure 91 – Structure of compound **5**.

Compound 6: (Figure 92) Hydrogen gas was added through a hydrogen balloon to a stirring solution of compound **4** (0.250 g, 0.95 mM) and Pd/C (0.050 g, 0.47 mM) in methanol (25 mL) and stirred for 48 hours until the balloon had deflated fully. The solution was filtered to remove the Pd/C, and then taken to dryness. Yield: 90 % (0.483 g, 0.85 mM); ^{1}H NMR (400 MHz, 298 K, CDCl$_3$): 8.56 (s, 2H), 7.97 (s, 2H), 6.77 (m, J = 178.52 Hz, 8H), 4.22 (t, J = 23.14 Hz, 4H), 3.95 (m, J = 23.14 Hz, 4H), 3.38 (m, J = 66.12 Hz, 4H), 1.97 (d, J = 3.31 Hz, 4H), 1.72 (d, J = 6.61 Hz, 4H), 1.03 (m, J = 16.53 Hz, 6H).
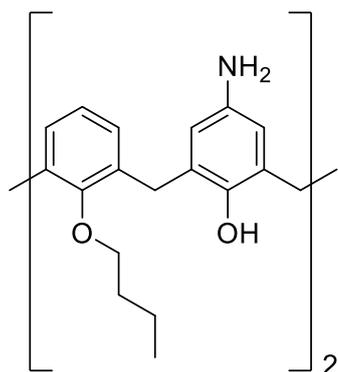
Figure 92 – Structure of compound **6**.

Compound 7: (Figure 93) 1-Iodobutane (0.2 mL, 1.76 mM) was added to a stirring mixture of compound **2** (0.100 g, 0.23 mM) and sodium hydride (0.200 g, 8.33 mM) in dry DMF (20 mL). The solution was then filtered to remove the sodium hydride before acid washing (20 mL x5), then water washing (20 mL x3). The compound was then extracted using chloroform and taken to dryness. Yield: 17 % (0.023 g, 0.04 mM); ^{1}H NMR (400 MHz, 298 K, CDCl$_3$): 10.20 (s, 1H), 7.05 (d, J = 7.15 Hz, 2H), 6.72 (t, J = 15.29 Hz, 1H), 6.57 (m, J = 32.05 Hz, 9H), 4.44 (d, J = 13.84 Hz, 3H), 3.91 (br d, J = 288.17 Hz, 2H), 3.88 (t, J = 15.82 Hz, 6H), 3.14 (d, J = 13.84 Hz, 3H), 1.89 (m, J = 29.66 Hz, 7H), 1.44 (m, J = 37.57 Hz, 7H), 0.99 (t, J = 15.82, 11H).
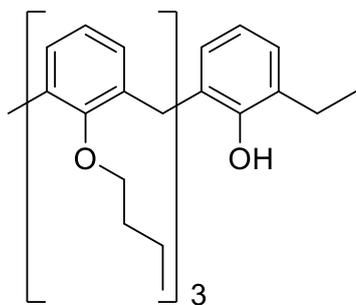
Figure 93 – Structure of compound **7**.

Compound 8: (Figure 94) Triphosgene (0.264 g, 0.89 mM) was added to a stirring solution of compound **6** (0.416 g, 0.73 mM) in ethyl acetate (30 mL) and heated to 60 °C. Attached was a bubbler filled with a saturated solution of sodium carbonate to neutralise any phosgene gas produced. This product was synthesised as an intermediate to compound **10** with an assumed yield of 100 %.
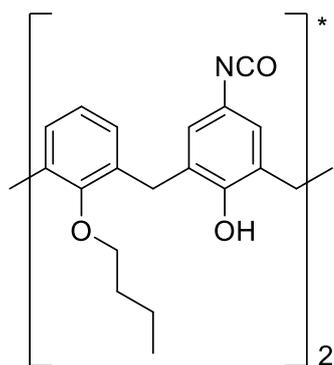
Figure 94 – Structure of compound **8**.

Compound 9: (Figure 95) This compound was synthesised in line with previously published methods. Proton NMR were found to match the previously published data.[198] To a round bottom flask aminomethane sulfonic acid was added dissolved into methanol to which tetrabutylammonium hydroxide (TBA OH) was added and the solution dried on the rota-vap for a minimum of four hours to remove all the methanol. This was then dissolved into ethyl acetate and added to the reaction mixture of compound **8** through a septum. Assumed yield of 100 %, taken straight through to react.
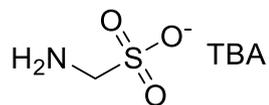
Compound 10: (Figure 96) Compound **9** (0.256 g, 0.73 mM) was dissolved into ethyl acetate (10 mL) and added to a stirring solution of compound **8** (0.451 g, 0.73 mM) in ethyl acetate (30 mL). The solution was then filtered to remove any precipitate and taken to dryness. Crude yield: 65 % (0.397 g, 0.47 mM).
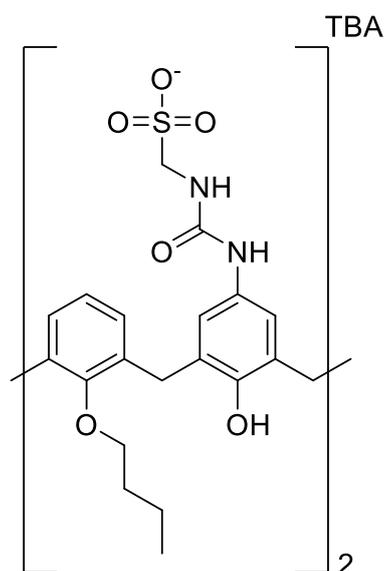
Compound 11: (Figure 97) Butyl isocyanate (0.223 g, 2.24 mM) was added to a stirring solution of compound **6** (0.395 g, 0.69 mM) in pure pyridine. The solid was filtered from the solvent and washed with methanol (20 mL). Crude yield of 52 % (0.274 g, 0.35 mM).
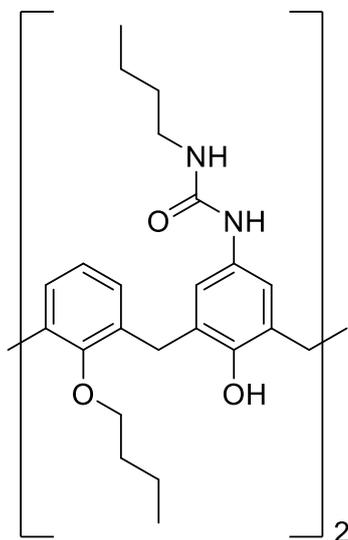
Figure 97 – Structure of compound **11**.

Compound 12: (Figure 98) Melting point: 130 °C; ^{1}H NMR: (400 MHz, 298 K, DMSO-d_6): δ: 9.66 (s, NH), 7.97 (d, J = 8.28 Hz, 1H), 7.65 (d, J = 7.9 Hz, 1H), 7.45 (t, J = 11.88 Hz, NH), 3.91 (d, J = 5.76, 2H), 3.16 (t, J = 16.68, 8H), 1.56 (m, J = 31.23, 8H), 1.30 (m, J = 36.91 Hz, 8H), 0.92 (t, J = 14.65 Hz, 12H). ^{13}C{^{1}H} NMR: (100 MHz, 298 K, DMSO-d_6): δ: 154.2 (C), 148.3 (C), 145.6 (C), 133.8 (CH), 127.8 (C), 113.2 (CH), 109.6 (C), 57.7 (CH$_2$), 56.0 (CH$_2$), 23.2 (CH$_2$), 19.3 (CH$_2$), 13.6 (CH$_3$); IR (film): v = 2962 (NH stretch), 1699 (C=O stretch), 1215 (S=O stretch). ESI-MS: 304.9765 [M]$^-$, 610.9593 [M+M+H$^+$]$^-$.
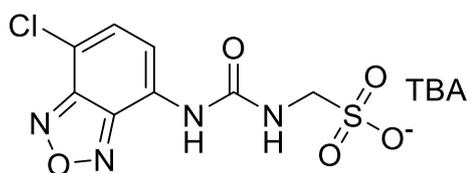
Figure 98 – Structure of compound **12**.

Compound 13: (Figure 99) Melting point: 176 °C; ^{1}H NMR: (400 MHz, 298 K, DMSO-d_6): δ: 9.62 (s, NH), 7.55 (d, J = 2.06 Hz, 1H), 7.47 (d, J = 8.40 Hz, 2H), 7.15 (d, J = 6.75 Hz, 1H), 6.04 (s, 1H), 3.99 (d, J = 6.05 Hz, 2H), 3.15 (t, J = 16.77 Hz, 8H), 2.31 (s, 3H), 1.55 (m, J = 31.10 Hz, 8H), 1.29 (m, J = 36.56, 8H), 0.91 (t, J = 14.80, 12H). ^{13}C{^{1}H} NMR: (100 MHz, 298 K, DMSO): δ: 160.6 (C), 154.4 (C), 153.9 (C), 153.6 (C), 144.4 (C), 125.4 (CH), 114.4 (CH), 113.1 (C), 110.9 (CH), 103.8 (CH), 57.7 (CH$_2$), 56.1 (CH$_2$), 23.2 (CH$_2$), 19.3 (CH$_2$), 18.1 (CH$_3$), 13.6 (CH$_3$); IR (film): v = 2960 (NH stretch), 1703 (C=O stretch), 1215 (S=O stretch). ESI-MS: 311.0356 [M]$^-$, 623.0773 [M+M+H$^+$]$^-$.
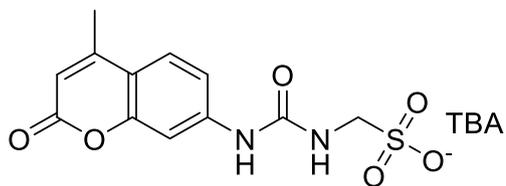
Figure 99 – Structure of compound **13**.

Compound 14: (Figure 100) Butyl isocyanate (0.202 g, 2.04 mM) was added to a solution of 2-(2-aminophenyl)benzothiazole (0.407 g, 1.80 mM) in pure pyridine (10 mL). The solid was then filtered off and washed with water (50 mL) then methanol (20 mL). Yield 55 % (0.321 g, 0.98 mM); Melting point: 158 °C; ^{1}H NMR (400 MHz, 298 K, DMSO-d_6): 11.01 (s, 1H), 8.47 (d, J = 9.91 Hz, 1H), 8.23 (d, J = 7.93 Hz, 1H), 8.13 (d, J = 7.93 Hz, 1H), 7.84 (d, J = 8.69 Hz, 1H), 7.59 (t, J = 16.30 Hz, 1H), 7.46 (m, J = 33.69 Hz, 2H), 7.33 (s, 1H), 7.07 (t, J = 16.30 Hz, 1H), 3.15 (m, J = 19.27 Hz, 2H), 1.48 (m, J = 28.27 Hz, 2H), 1.34 (m, J = 36.62 Hz, 2H), 0.89 (t, J = 14.78 Hz, 3H). ^{13}C{^{1}H} NMR: (100 MHz, 298 K, DMSO-d_6): δ: 168.0 (C), 154.9 (C), 152.5 (C), 139.5 (C), 132.9 (C), 131.6 (CH), 129.9 (CH), 126.5 (CH), 125.8 (CH), 122.9 (CH), 121.9 (CH), 121.2 (CH), 119.9 (CH), 117.7 (C), 31.8 (CH$_2$), 19.6 (CH$_2$), 13.7 (CH$_3$); IR (film): ν = 3302 (NH stretch), 1654 (C=O stretch). ESI-MS: 324.1162 [M-H$^+$]$^-$.
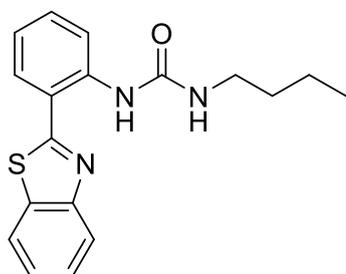
Figure 100 – Structure of compound **14**.

Compound 15: (Figure 101) Phenyl isocyanate (0.328 g, 2.75 mM) was added to a solution of 2-(2-aminophenyl)benzothiazole (0.493 g, 2.17 mM) in pure pyridine (10 mL). The solid was then filtered off and washed with water (50 mL) then methanol (20 mL). Yield 78 % (0.484 g, 1.40 mM); Melting point: >200 °C; ^{1}H NMR (400 MHz, 298 K, DMSO-d_6): 11.17 (s, 1H), 9.73 (s, 1H), 8.38 (d, J = 8.56 Hz, 1H), 8.21 (d, J = 8.56 Hz, 1H), 8.15 (d, J = 17.14 Hz, 1H), 7.90 (d, J = 8.56 Hz, 1H), 7.54 (m, J = 55.66 Hz, 5H), 7.31 (t, J = 15.70 Hz, 2H), 7.17 (t, J = 14.27 Hz, 1H), 7.01 (t, J = 14.27 Hz, 1H). ^{13}C{^{1}H} NMR: (100 MHz, 298 K, DMSO-d_6): δ: 167.7 (C), 152.6 (C), 152.6 (C), 139.6 (C), 138.4 (C), 133.1 (C),

131.6 (CH), 130.0 (CH), 128.7 (CH), 126.6 (CH), 125.9 (CH), 123.1 (CH), 122.3 (CH), 122.2 (CH), 122.0 (CH), 120.9 (CH), 119.2 (CH), 118.9 (C); IR (film): ν = 3286 (NH stretch), 1660 (C=O stretch). ESI-MS: 433.0853 [M-H$^+$]$^-$.
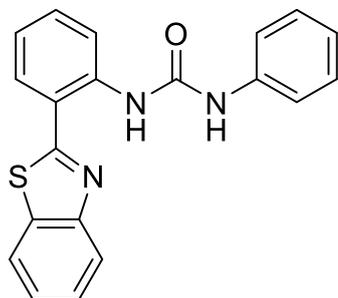
Figure 101 – Structure of compound **15**.

Compound 16: (Figure 102) 4-Nitrophenyl isocyanate (0.290 g, 1.76 mM) was added to a solution of 2-(2-aminophenyl)benzothiazole (0.409 g, 1.80 mM) in chloroform (9 mL) and pyridine (1 mL). The solid was then filtered off and washed with water (10 mL) then methanol (20 mL). Yield 46 % (0.322 g, 0.82 mM); Melting point: >200 °C; ^{1}H NMR (400 MHz, 298 K, DMSO-d_6): 11.36 (s, 1H), 10.51 (s, 1H), 8.36 (d, J = 9.38 Hz, 1H), 8.22 (m, J = 33.44 Hz, 4H), 7.96 (d, J = 9.38 Hz, 1H), 7.81 (m, J = 15.45 Hz, 2H), 7.56 (m, J = 56.70 Hz, 3H), 7.24 (t, J = 16.56 Hz, 1H). ^{13}C{^{1}H} NMR: (100 MHz, 298 K, DMSO-d_6): δ: 167.5 (C), 152.5 (C), 152.1 (C), 146.4 (C), 141.2 (C), 137.6 (C), 133.1 (C), 131.6 (CH), 130.1 (CH), 126.7 (CH), 126.0 (CH), 125.0 (CH), 123.1 (CH), 122.9 (CH), 122.1 (CH), 121.2 (CH), 119.4 (C), 118.0 (CH); IR (film): ν = 3360 (NH stretch), 1685 (C=O stretch). ESI-MS: 389.0688 [M-H$^+$]$^-$, 779.1438 [M+M-H$^+$]$^-$.
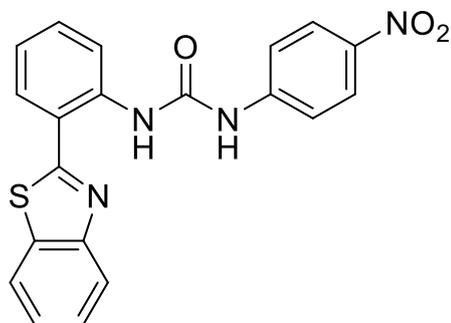
Figure 102 – Structure of compound **16**.

Compound 17: (Figure 103) Triphosgene (0.127 g, 0.42 mM) was added to a stirring solution of 2-(2-aminophenyl)benzothiazole (0.402 g, 1.77 mM) in ethyl acetate (25 mL) and heated to 60 °C for 4 hours, with a quenching solution of saturated sodium bicarbonate attached as a bubbler. With an assumed yield of 100 %, 2-(2-aminophenyl)benzothiazole (0.411 g, 1.81 mM) was added to the solution containing the isocyanate intermediate and stirred over night at 60 °C. The precipitate was then filtered off and washed with methanol (25 mL). Yield 25 % (0.215 g, 0.45 mM); Melting point: >200 °C; ^{1}H NMR (400 MHz, 298 K, DMSO-d_6): 11.42 (s, 2H), 8.29 (d, J = 8.99 Hz, 2H), 8.13 (d, J = 5.99 Hz, 2H), 8.05 (d, J = 7.49 Hz, 2H), 7.86 (d, J = 8.99 Hz, 2H), 7.57 (t, J = 14.98 Hz, 2H), 7.45 (m, J = 38.95 Hz, 4H), 7.29 (t, J = 16.48 Hz, 2H). ^{13}C{^{1}H} NMR: (100 MHz, 298 K, DMSO-d_6): δ: No ^{13}C{^{1}H} NMR data obtained due to solubility issues. IR (film): ν = 1718 (C=O stretch). ESI-MS: 477.0810 [M-H$^+$]$^-$.
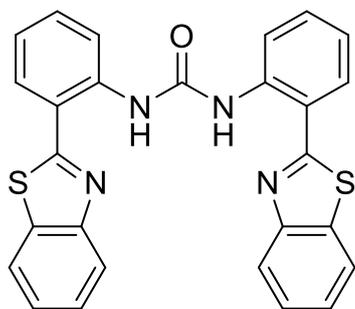
Figure 103 – Structure of compound **17**.

7.0 References

1. Gale, P. A., Howe, E. N. W. & Wu, X. Anion Receptor Chemistry. *Chem* **1**, 351–422 (2016).

2. Ariga, K. Supermolecules. in *Biomaterials Nanoarchitectonics* 25–40 (Elsevier Inc., 2016). doi:10.1016/B978-0-323-37127-8.00003-0

3. Reinhoudt, D. N. Supramolecular Chemistry and Heterocycles. in *Reference Module in Chemistry, Molecular Sciences and Chemical Engineering* (Elsevier, 2013). doi:10.1016/b978-0-12-409547-2.05396-8

4. Kinne-Saffran, E. & Kinne, R. K. Vitalism and synthesis of urea. From Friedrich Wohler to Hans A. Krebs. *Am. J. Nephrol.* **19**, 290–294 (1999).

5. INOUYE, M. Functional Dyes for Molecular Recognition: Chromogenic and Fluorescent Receptors. in *Colorants for Non-Textile Applications* 238–274 (Elsevier Science, 2000). doi:10.1016/b978-044482888-0/50037-4

6. Johannes Diderik van der Waals - Biographical - NobelPrize.org. Available at: https://www.nobelprize.org/prizes/physics/1910/waals/biographical/. (Accessed: 21st April 2020)

7. Kinne-Saffran, E. & Kinne, R. K. Vitalism and synthesis of urea. From Friedrich Wohler to Hans A. Krebs. *Am. J. Nephrol.* **19**, 290–294 (1999).

8. Travis, A. S. Perkin's Mauve: Ancestor of the Organic Chemical Industry. *Technol. Cult.* **31**, 51 (1990).

9. De Klerk, G. J. M. Mechanism and vitalism. A history of the controversy. *Acta Biotheor.* **28**, 1–10 (1979).

10. Lewis, G. N. The atom and the molecule. *J. Am. Chem. Soc.* **38**, 762–785 (1916).

11. Lewis, G. N. Introductory address: Valence and the electron. *Transactions of the Faraday Society* **19**, 452–458 (1923).

12. Gillespie, R. J. & Robinson, E. A. Gilbert N. Lewis and the chemical bond: The electron pair and the octet rule from 1916 to the present day. *J. Comput. Chem.* **28**, 87–97 (2007).

13. Tang, K. T. & Toennies, J. P. Johannes Diderik van der Waals: A pioneer in the molecular sciences and nobel prize winner in 1910. *Angewandte Chemie - International Edition* **49**, 9574–9579 (2010).

14. Dalgarno, A. & Davison, W. D. The Calculation of Van Der Waals Interactions. *Adv. At. Mol. Opt. Phys.* **2**, 1–32 (1966).

15. Andersson, Y. *et al.* Van der Waals Interactions in Density Functional Theory BT - Electronic Density Functional Theory: Recent Progress and New Directions. in *Electronic Density Functional Theory* (eds. Dobson, J. F., Vignale, G. & Das, M. P.) 243–260 (Springer US, 1998). doi:10.1007/978-1-4899-0316-7_17

16. Lichtenthaler, F. W. 100 Years "Schlüssel-Schloss-Prinzip": What Made Emil Fischer Use this Analogy? *Angewandte Chemie International Edition in English* **33**, 2364–2374 (1995).

17. Behr, J. P. *The Lock-and-Key Principle, The State of the Art--100 Years On*. *The Lock-and-Key Principle, The State of the Art--100 Years On* **1**, (2007).

18. Hendricks, S. B., Wulf, O. R., Hilbert, G. E. & Liddel, U. Hydrogen Bond Formation between Hydroxyl Groups and Nitrogen Atoms in Some Organic Compounds. *J. Am. Chem. Soc.* **58**, 1991–1996 (1936).

19. Chenon, B. & Sandorfy, C. Hydrogen bonding in the amine hydrohalides: I. General aspects. *Can. J. Chem.* **36**, 1181–1206 (1958).

20. Smith, D. A. A Brief History of the Hydrogen Bond. in 1–5 (1994). doi:10.1021/bk-1994-0569.ch001

21. Pedersen, C. J. The Discovery of Crown Ethers (Noble Lecture). *Angewandte Chemie International Edition in English* **27**, 1021–1027 (1988).

22. Sherman, J. C. Donald J. Cram. *Chem. Soc. Rev.* **36**, 148–150 (2007).

23. Leigh, D. A. Genesis of the Nanomachines: The 2016 Nobel Prize in Chemistry. *Angew. Chemie - Int. Ed.* **55**, 14506–14508 (2016).

24. Richards, V. 2016 Nobel Prize in Chemistry: Molecular machines. *Nature Chemistry* **8**, 1090 (2016).

25. Marrs, C. N. & Evans, N. H. The rapid synthesis and dynamic behaviour of an isophthalamide [2]catenane. *Org. Biomol. Chem.* **13**, 11021–11025 (2015).

26. Northrop, B. H., Zheng, Y. R., Ki-Whan, C. H. I. & Stang, P. J. Self-organization in coordination-driven self-assembly. *Acc. Chem. Res.* **42**, 1554–1563 (2009).

27. Wittenberg, J. B. & Isaacs, L. Complementarity and Preorganization. in *Supramolecular Chemistry* (John Wiley & Sons, Ltd, 2012). doi:10.1002/9780470661345.smc004

28. McGrath, J. M. & Pluth, M. D. Understanding the effects of preorganization, rigidity, and steric interactions in synthetic barbiturate receptors. *J. Org. Chem.* **79**, 711–719 (2014).

29. Adams, R. D., Kiprotich, J., Peryshkov, D. V. & Wong, Y. O. Opening of Carborane Cages by Metal Cluster Complexes: The Reaction of a Thiolate-Substituted Carborane with Triosmium Carbonyl Cluster Complexes. *Inorg. Chem.* **55**, 8207–8213 (2016).

30. Murugan, R. & Sutharchanadevi, M. Rings containing Other Elements. in *Comprehensive Heterocyclic Chemistry II: A Review of the Literature 1982-1995* **9**, 1033–1037 (Elsevier Ltd, 1996).

31. Lin, X. & Grinstaff, M. W. Ionic supramolecular assemblies. *Israel Journal of Chemistry* **53**, 498–510 (2013).

32. Parkin, I. P. Supramolecular chemistry. J.W. Steed and J.L. Atwood. John Wiley & Sons Ltd, Chichester, 2000. 745 pages. 29.95 (paperback). ISBN 0-471-98791-3. *Appl. Organomet. Chem.* **15**, 236–236 (2001).

33.   Ninham, B. W. & Parsegian, V. A. van der Waals Forces: Special Characteristics in Lipid-Water Systems and a General Method of Calculation Based on the Lifshitz Theory. *Biophys. J.* **10**, 646–663 (1970).

34.   Waters, M. L. Aromatic interactions in model systems. *Current Opinion in Chemical Biology* **6**, 736–741 (2002).

35.   Zhuang, W. R. *et al.* Applications of π-π stacking interactions in the design of drug-delivery systems. *Journal of Controlled Release* **294**, 311–326 (2019).

36.   Davarcioglu, B. The General Characteristic of Weak Intermolecular Interactions in Liquids and Crstals. *Int. J. Mod. Eng. Res. www.ijmer.com* **1**, 443–454

37.   Dougherty, D. A. The cation-π interaction. *Acc. Chem. Res.* **46**, 885–893 (2013).

38.   Schottel, B. L., Chifotides, H. T. & Dunbar, K. R. Anion-π interactions. *Chemical Society Reviews* **37**, 68–83 (2008).

39.   Conn, M. M. & Rebek, J. Self-assembling capsules. *Chem. Rev.* **97**, 1647–1668 (1997).

40.   Stončius, S. *et al.* Design and synthesis of a C2-symmetric self-complementary hydrogen-bonding cleft molecule based on the bicyclo,[3.3.1]nonane and 4-oxo-5-azaindole framework. Formation of channels and inclusion complexes in the solid state. *J. Org. Chem.* **69**, 5196–5203 (2004).

41.   Ono, G., Izuoka, A., Sugawara, T. & Sugawara, Y. Structure and physical properties of a hydrogen-bonded self-assembled material composed of a carbamoylmethyl substituted TTF derivative. *J. Mater. Chem.* **8**, 1703–1709 (1998).

42.   Dannenberg, J. J., Haskamp, L. & Masunov, A. Are Hydrogen Bonds Covalent or Electrostatic? A Molecular Orbital Comparison of Molecules in Electric Fields and H-Bonding Environments. *J. Phys. Chem. A* **103**, 7083–7086 (1999).

43.   MacLeod, J. M. & Rosei, F. Directed Assembly of Nanostructures. in *Comprehensive Nanoscience and Technology* **1–5**, 13–68 (Elsevier Inc., 2011).

44.   Deng, W., You, Y. & Zhang, A. Supramolecular network-based self-healing polymer materials. in *Recent Advances in Smart Self-healing Polymers and Composites* 181–210 (Elsevier Ltd, 2015). doi:10.1016/B978-1-78242-280-8.00007-8

45.   Gupta, V. P. Topological Analysis of Electron Density—Quantum Theory of Atoms in Molecules. in *Principles and Applications of Quantum Chemistry* 359–384 (Elsevier, 2016). doi:10.1016/b978-0-12-803478-1.00011-x

46.   Yamada, K. *Recent Applications of Solid-State 17O NMR*. *Annual Reports on NMR Spectroscopy* **70**, (Academic Press, 2010).

47.   Shoji, M. *et al.* Large-Scale QM/MM Calculations of Hydrogen Bonding Networks for Proton Transfer and Water Inlet Channels for Water Oxidation-Theoretical System Models of the Oxygen-Evolving Complex of Photosystem II. in *Advances in Quantum Chemistry* **70**, 325–413 (Academic Press Inc., 2015).

48.   Schaeffer, L. The Role of Functional Groups in Drug-Receptor Interactions. in *The Practice of Medicinal Chemistry: Fourth Edition* 359–378 (Elsevier Inc., 2008). doi:10.1016/B978-0-12-417205-0.00014-6

49.   Taylor, R. & Kennard, O. Hydrogen-Bond Geometry in Organic Crystals†. *Acc. Chem. Res.* **17**, 320–326 (1984).

50.   Feyereisen, R. INSECT P450 ENZYMES. *Annu. Rev. Entomol.* **44**, 507–533 (1999).

51.   Hahn, B. H. Antibodies to DNA. *New England Journal of Medicine* **338**, 1359–1368 (1998).

52.   Leippe, M. *et al.* Primary and secondary structure of the pore-forming peptide of pathogenic Entamoeba histolytica. *EMBO J.* **11**, 3501–3506 (1992).

53.   Fromme, R., Katiliene, Z., Fromme, P. & Ghirlanda, G. Conformational gating of dimannose binding to the antiviral protein cyanovirin revealed from the crystal structure at 1.35 Å resolution. *Protein Sci.* **17**, 939–944 (2008).

54.   Halls, S. C. & Lewis, N. G. Secondary and quaternary structures of the (+)-pinoresinol-forming dirigent protein. *Biochemistry* **41**, 9455–9461 (2002).

55.   Noncovalent Bonds - Molecular Cell Biology - NCBI Bookshelf. Available at: https://www.ncbi.nlm.nih.gov/books/NBK21726/. (Accessed: 8th March 2020)

56.   Cerbón, J. NMR Evidence for the hydrophobic interaction of local anaesthetics. Possible relation to their potency. *BBA - Biomembr.* **290**, 51–57 (1972).

57.   Lis, L. J., McAlister, M., Fuller, N., Rand, R. P. & Parsegian, V. A. Interactions between neutral phospholipid bilayer membranes. *Biophys. J.* **37**, 657–665 (1982).

58.   Meyer, E. E., Rosenberg, K. J. & Israelachvili, J. Recent progress in understanding hydrophobic interactions. *Proceedings of the National Academy of Sciences of the United States of America* **103**, 15739–15746 (2006).

59.   Schober, M. E. Docosahexaenoic Acid and Omega 3 Fatty Acids. in *New Therapeutics for Traumatic Brain Injury: Prevention of Secondary Brain Damage and Enhancement of Repair and Regeneration* 287–306 (Elsevier Inc., 2017). doi:10.1016/B978-0-12-802686-1.00018-3

60.   Jonas, J. High Pressure Studies Using NMR Spectroscopy. in *Encyclopedia of Spectroscopy and Spectrometry* 760–771 (Elsevier, 1999). doi:10.1006/rwsp.2000.0117

61.   Cell Membranes - The Cell - NCBI Bookshelf.pdf.

62.   Silver, P. A. How proteins enter the nucleus. *Cell* **64**, 489–497 (1991).

63.   Costa, P. J., Marques, I. & Félix, V. Interaction of a calix[4]arene derivative with a DOPC bilayer: Biomolecular simulations towards chloride transport. *Biochim. Biophys. Acta - Biomembr.* **1838**, 890–901 (2014).

64. Jose, P. & Menon, S. Lower-rim substituted calixarenes and their applications. *Bioinorganic Chemistry and Applications* **2007**, 65815 (2007).

65. Bakelite, B. & Nagel, M. C. Profiles in chemistry. *Journal of Chemical Education* **57**, 811–812 (1980).

66. Structure – Bakelite. Available at: https://bakelitegroup62.wordpress.com/2016/09/25/structure/. (Accessed: 21st April 2020)

67. Gutsche, C. D., Rogers, J. S., Stewart, D. & See, K. A. Calixarenes: Paradoxes and paradigms in molecular baskets. *Pure Appl. Chem.* **62**, 485–491 (1990).

68. Gutsche, C. D., Iqbal, M. & Stewart, D. Calixarenes. 18. Synthesis Procedures for p -tert - Butylcalix[4]arene. *J. Org. Chem.* **51**, 742–745 (1986).

69. Kappe, T. The early history of calixarene chemistry. *J. Incl. Phenom. Mol. Recognit. Chem.* **19**, 3–15 (1994).

70. Gutsche, C. D. Calixarenes. *Acc. Chem. Res.* **16**, 161–170 (1983).

71. Sardjono, R. E. & Rachmawati, R. Green Synthesis of Oligomer Calixarenes. in *Green Chemical Processing and Synthesis* (InTech, 2017). doi:10.5772/67804

72. Roundhill, D. M. Calixarenes. in *Comprehensive Coordination Chemistry II* 485–491 (Elsevier, 2003). doi:10.1016/B0-08-043748-6/01054-9

73. Asfari, Z. (Zouhair). *Calixarenes 2001*. *Calixarenes 2001* (Kluwer Academic Publishers, 2006). doi:10.1007/0-306-47522-7

74. Guérineau, V. *et al.* The synthesis and characterization of giant Calixarenes. *Nat. Commun.* **10**, 113 (2019).

75. Makha, M., Raston, C. L., Skelton, B. W. & White, A. H. A more benign approach to the synthesis of calixarenes. *Green Chem.* **6**, 158 (2004).

76.   Biali, S. E. *et al.* Alkanediyl bridged calix[4]arenes: Synthesis, conformational analysis, and rotational barriers. *J. Am. Chem. Soc.* **118**, 12938–12949 (1996).

77.   Gutsche, C. D. & Pagoria, P. F. Calixarenes. 16. Functionalized Calixarenes: The Direct Substitution Route. *J. Org. Chem.* **50**, 5795–5802 (1985).

78.   Simaan, S. & Biali, S. E. Synthesis of p-tert-butylcalix[4]arene derivatives with trans-alkyl substituents on opposite methylene bridges. *J. Org. Chem.* **68**, 3634–3639 (2003).

79.   Español, E. S. & Villamil, M. M. Calixarenes: Generalities and their role in improving the solubility, biocompatibility, stability, bioavailability, detection, and transport of biomolecules. *Biomolecules* **9**, 90 (2019).

80.   Slavík, P., Eigner, V. & Lhoták, P. A general method for obtaining calix[4]arene derivatives in the 1,2-alternate conformation. *Tetrahedron* **72**, 6348–6355 (2016).

81.   Kumar, R., Jung, Y. & Kim, J. S. Fluorescent calixarene hosts. in *Calixarenes and Beyond* 743–760 (Springer, 2016). doi:10.1007/978-3-319-31867-7_28

82.   Deska, M., Dondela, B. & Sliwa, W. Calixarenes containing modified meso bridges. *Arkivoc* **2015**, 29–47 (2014).

83.   Osipov, M., Chu, Q., Geib, S. J., Curran, D. P. & Weber, S. G. Synthesis of deep-cavity fluorous calix[4]arenes as molecular recognition scaffolds. *Beilstein J. Org. Chem.* **4**, 36 (2008).

84.   Mutihac, L. Calix[n]arenes as synthetic membrane transporters: A minireview. *Anal. Lett.* **43**, 1355–1366 (2010).

85.   Mutihac, L. Functionalized Calix[n]arenes as Membrane Transporters for Biological Compounds.A Minireview. *Curr. Drug Discov. Technol.* **5**, 98–104 (2008).

86.   Jin, T. Photocontrol of Na+ transport across a phospholipid bilayer containing a bisanthroylcalix[4]arene carrier. *Chem. Commun.* 1379–1380 (2000). doi:10.1039/b002034f

87. Perret, F. *et al.* Anionic fullerenes, calixarenes, coronenes, and pyrenes as activators of oligo/polyarginines in model membranes and live cells. *J. Am. Chem. Soc.* **127**, 1114–1115 (2005).

88. CORNFORTH, J. W., HART, P. D., NICHOLLS, G. A., REES, R. J. & STOCK, J. A. Antituberculous effects of certain surface-active polyoxyethylene ethers. *Br. J. Pharmacol. Chemother.* **10**, 73–88 (1955).

89. Perret, F., Bonnard, V., Danylyuk, O., Suwinska, K. & Coleman, A. W. Conformational extremes in the supramolecular assemblies of para-sulfonato-calix[8]arene. *New J. Chem.* **30**, 987–990 (2006).

90. Nimse, S. B. & Kim, T. Biological applications of functionalized calixarenes. *Chem. Soc. Rev.* **42**, 366–386 (2013).

91. Iqbal, K. S. J. & Cragg, P. J. Transmembrane ion transport by calixarenes and their derivatives. *Dalt. Trans.* 26–32 (2007). doi:10.1039/b613867p

92. Schühle, D. T., Peters, J. A. & Schatz, J. Metal binding calixarenes with potential biomimetic and biomedical applications. *Coordination Chemistry Reviews* **255**, 2727–2745 (2011).

93. Fayzullin, D. A. *et al.* Influence of Nature of Functional Groups on Interaction of Tetrasubstituted at Lower Rim p-tert-Butyl Thiacalix[4]arenes in 1,3-Alternate Configuration with Model Lipid Membranes. *Appl. Magn. Reson.* **40**, 231–243 (2011).

94. Xu, Z. *et al.* Heteromultivalent peptide recognition by co-assembly of cyclodextrin and calixarene amphiphiles enables inhibition of amyloid fibrillation. *Nat. Chem.* **11**, 86–93 (2019).

95. Lee, M., Lee, S. J. & Jiang, L. H. Stimuli-responsive supramolecular nanocapsules from amphiphilic calixarene assembly. *J. Am. Chem. Soc.* **126**, 12724–12725 (2004).

96.   Subramani, K. & Ahmed, W. Self-assembly of proteins and peptides and their applications in bionanotechnology and dentistry. in *Emerging Nanotechnologies in Dentistry: Second Edition* 231–249 (Elsevier, 2018). doi:10.1016/B978-0-12-812291-4.00012-1

97.   Strobel, M. *et al.* Self-assembly of amphiphilic calix [4]arenes in aqueous solution. *Adv. Funct. Mater.* **16**, 252–259 (2006).

98.   Seganish, J. L. *et al.* Regulating supramolecular function in membranes: Calixarenes that enable or inhibit transmembrane Cl- transport. *Angew. Chemie - Int. Ed.* **45**, 3334–3338 (2006).

99.   Tieke, B., Toutianoush, A. & Jin, W. Selective transport of ions and molecules across layer-by-layer assembled membranes of polyelectrolytes, p-sulfonato-calix[n]arenes and Prussian Blue-type complex salts. *Advances in Colloid and Interface Science* **116**, 121–131 (2005).

100.   Akieh, M. N., Ralph, S. F., Bobacka, J. & Ivaska, A. Transport of metal ions across an electrically switchable cation exchange membrane based on polypyrrole doped with a sulfonated calix[6]arene. *J. Memb. Sci.* **354**, 162–170 (2010).

101.   Sesta, B. & D'Aprano, A. Ionic transport across lipid bilayers activated by cryptands and alkyl-cryptands. in *Colloids and Surfaces A: Physicochemical and Engineering Aspects* **140**, 119–126 (Elsevier Sci B.V., 1998).

102.   SHINKAI, S. ChemInform Abstract: Functionalization of Crown Ethers and Calixarenes: New Applications as Ligands, Carriers, and Host Molecules. *ChemInform* **24**, no-no (2010).

103.   Demirkol, D. O., Yildiz, H. B., Sayin, S. & Yilmaz, M. Enzyme immobilization in biosensor constructions: Self-assembled monolayers of calixarenes containing thiols. *RSC Adv.* **4**, 19900–19907 (2014).

104.   Consoli, G. M. L., Granata, G. & Geraci, C. *Calixarene-based micelles. Design and Development of New Nanocarriers* (Elsevier Inc., 2018). doi:10.1016/b978-0-12-813627-0.00003-x

105.	Agrawal, Y. K., Pancholi, J. P. & Vyas, J. M. AGRAWAL at al: Design and synthesis of calixarene. *J. Sci. Ind. Reserch* **68**, 745–768 (2009).

106.	Loeb, S. J. & Cameron, B. R. Calixarene metalloreceptors: Demonstration of size and shape selectivity inside a calixarene cavity. *ACS Symp. Ser.* **757**, 283–295 (2000).

107.	Eddaif, L., Shaban, A. & Telegdi, J. Sensitive detection of heavy metals ions based on the calixarene derivatives-modified piezoelectric resonators: a review. *Int. J. Environ. Anal. Chem.* **99**, 824–853 (2019).

108.	Arora, V., Chawla, M. & Singh, S. P. Special Issue Reviews and Accounts ARKIVOC 2007 (ii) 172-200 Calixarenes as sensor materials for recognition and separation of metal ions ‡ ‡. *Arkivoc* **2007**, 172–200 (2007).

109.	Schulz, M. *et al.* A Calixarene-Based Metal–Organic Framework for Highly Selective NO2 Detection. *Angew. Chemie - Int. Ed.* **57**, 12961–12965 (2018).

110.	Da Silva, E., Lazar, A. N. & Coleman, A. W. Biopharmaceutical applications of calixarenes. *Journal of Drug Delivery Science and Technology* **14**, 3–20 (2004).

111.	Zhou, Y., Li, H. & Yang, Y. W. Controlled drug delivery systems based on calixarenes. *Chinese Chem. Lett.* **26**, 825–828 (2015).

112.	Xue, Y., Guan, Y., Zheng, A. & Xiao, H. Amphoteric calix[8]arene-based complex for pH-triggered drug delivery. *Colloids Surfaces B Biointerfaces* **101**, 55–60 (2013).

113.	Mo, J., Eggers, P. K., Yuan, Z. X., Raston, C. L. & Lim, L. Y. Paclitaxel-loaded phosphonated calixarene nanovesicles as a modular drug delivery platform. *Sci. Rep.* **6**, 1–12 (2016).

114.	Li, P., Chen, Y. & Liu, Y. Calixarene/pillararene-based supramolecular selective binding and molecular assembly. *Chinese Chem. Lett.* **30**, 1190–1197 (2019).

115.	Rebek Jr., J. Host–guest chemistry of calixarene capsules. *Chem. Commun.* 637–643 (2000). doi:10.1039/a910339m

116. Kim, H. J., Lee, M. H., Mutihac, L., Vicens, J. & Kim, J. S. Host-guest sensing by calixarenes on the surfaces. *Chemical Society Reviews* **41**, 1173–1190 (2012).

117. Wang, J., Ding, X. & Guo, X. Assembly behaviors of calixarene-based amphiphile and supra-amphiphile and the applications in drug delivery and protein recognition. *Advances in Colloid and Interface Science* **269**, 187–202 (2019).

118. Shahgaldian, P., Sciotti, M. A. & Pieles, U. Amino-substituted amphiphilic calixarenes: Self-assembly and interactions with DNA. *Langmuir* **24**, 8522–8526 (2008).

119. Yu, G., Jie, K. & Huang, F. Supramolecular Amphiphiles Based on Host-Guest Molecular Recognition Motifs. *Chemical Reviews* **115**, 7240–7303 (2015).

120. Basilio, N., Francisco, V. & Garcia-Rio, L. Aggregation of p-sulfonatocalixarene-based amphiphiles and supra-amphiphiles. *International Journal of Molecular Sciences* **14**, 3140–3157 (2013).

121. Guan, B., Jiang, M., Yang, X., Liang, Q. & Chen, Y. Self-assembly of amphiphilic calix[6]crowns: From vesicles to nanotubes. *Soft Matter* **4**, 1393–1395 (2008).

122. Helttunen, K. & Shahgaldian, P. Self-assembly of amphiphilic calixarenes and resorcinarenes in water. *New Journal of Chemistry* **34**, 2704–2714 (2010).

123. Zhang, J. Amphiphilic Molecules. in *Encyclopedia of Membranes* 1–4 (Springer Berlin Heidelberg, 2014). doi:10.1007/978-3-642-40872-4_1789-1

124. Taylor, R. M. *et al.* Anionic amphiphile and phospholipid-induced conformational changes in human neutrophil flavocytochrome b observed by fluorescence resonance energy transfer. *Biochim. Biophys. Acta - Biomembr.* **1663**, 201–213 (2004).

125. Findlay, B., Zhanel, G. G. & Schweizer, F. Cationic amphiphiles, a new generation of antimicrobials inspired by the natural antimicrobial peptide scaffold. *Antimicrobial Agents and Chemotherapy* **54**, 4049–4058 (2010).

126.   Barthelemy, P. *et al.* Supramolecular assemblies of DNA with neutral nucleoside amphiphiles. *Chem. Commun.* 1261–1263 (2005). doi:10.1039/b412670j

127.   Wu, A., Gao, Y. & Zheng, L. Zwitterionic amphiphiles: Their aggregation behavior and applications. *Green Chemistry* **21**, 4290–4312 (2019).

128.   Tian, J. *et al.* Electrospun nanofibers for food and food packaging technology. in *Electrospinning: Nanofabrication and Applications* 455–516 (Elsevier, 2018). doi:10.1016/B978-0-323-51270-1.00015-7

129.   Nishikawa, T., Narita, H., Ogi, S., Sato, Y. & Yamaguchi, S. Hydrophobicity and CH/π-interaction-driven self-assembly of amphiphilic aromatic hydrocarbons into nanosheets. *Chem. Commun.* **55**, 14950–14953 (2019).

130.   Thawarkar, S. *et al.* Trifluoromethyl-Directed Supramolecular Self-Assembly of Fullerenes: Synthesis, Characterization and Photovoltaic Applications. *ChemistrySelect* **5**, 1115–1121 (2020).

131.   Hada, D., Rathore, K., Chauhan, N. P. S., Sharma, K. & Mozafari, M. Functional protein to polymer surfaces: an attachment. in *Advanced Functional Polymers for Biomedical Applications* 191–210 (Elsevier, 2019). doi:10.1016/b978-0-12-816349-8.00010-2

132.   Adams, M. L., Lavasanifar, A. & Kwon, G. S. Amphiphilic block copolymers for drug delivery. *Journal of Pharmaceutical Sciences* **92**, 1343–1355 (2003).

133.   Alberts, B. *et al.* The Lipid Bilayer - Molecular Biology of the Cell - NCBI Bookshelf. *Alberts B, Johnson A, Lewis J, et al. Molecular Biology 4th edition. New York: Garland Science;* (2002). Available at: https://www.ncbi.nlm.nih.gov/books/NBK26871/. (Accessed: 12th April 2020)

134.   Parlato, M. C., Jee, J. P., Teshite, M. & Mecozzi, S. Synthesis, characterization, and applications of hemifluorinated dibranched amphiphiles. *J. Org. Chem.* **76**, 6584–6591 (2011).

135. Feast, G. C. *et al.* The search for new amphiphiles: Synthesis of a modular, high-throughput library. *Beilstein J. Org. Chem.* **10**, 1578–1588 (2014).

136. Hutt, O. E., Mulet, X. & Paul Savage, G. Click-chemistry as a mix-and-match kit for amphiphile synthesis. *ACS Comb. Sci.* **14**, 565–569 (2012).

137. Hehre, W. J., Radom, L. & Pople, J. A. Molecular Orbital Theory of the Electronic Structure of Organic Compounds. XII. Conformations, Stabilities, and Charge Distributions in Monosubstituted Benzenes. *J. Am. Chem. Soc.* **94**, 1496–1504 (1972).

138. Sorrenti, A., Illa, O. & Ortuño, R. M. Amphiphiles in aqueous solution: Well beyond a soap bubble. *Chemical Society Reviews* **42**, 8200–8219 (2013).

139. Knight, H. Life science. *Engineer* **293**, 18–19 (2005).

140. Alexandridis, P. & Andersson, K. Reverse micelle formation and water solubilization by polyoxyalkylene block copolymers in organic solvent. *J. Phys. Chem. B* **101**, 8103–8111 (1997).

141. Hashidzume, A. & Harada, A. Micelles and Vesicles. in *Encyclopedia of Polymeric Nanomaterials* 1238–1241 (Springer Berlin Heidelberg, 2015). doi:10.1007/978-3-642-29648-2_56

142. Polarz, S., Kunkel, M., Donner, A. & Schlötter, M. Added-Value Surfactants. *Chemistry - A European Journal* **24**, 18842–18856 (2018).

143. Jiao, T. *et al.* Self-assembly and headgroup effect in nanostructured organogels via cationic amphiphile-graphene oxide composites. *PLoS One* **9**, e101620 (2014).

144. Sliwa, W. & Girek, T. Calixarene complexes with metal ions. *J. Incl. Phenom. Macrocycl. Chem.* **66**, 15–41 (2010).

145. Tyuleva, S. N. *et al.* A symbiotic supramolecular approach to the design of novel amphiphiles with antibacterial properties against MSRA. *Chem. Commun.* **55**, 95–98 (2019).

146. Bolhuis, A. & Aldrich-Wright, J. R. DNA as a target for antimicrobials. *Bioorg. Chem.* **55**, 51–59 (2014).

147. Bush, K. Antimicrobial agents targeting bacterial cell walls and cell membranes. *OIE Rev. Sci. Tech.* **31**, 43–56 (2012).

148. Lalatsa, A., Leite, D. M., Figueiredo, M. F. & O'Connor, M. Nanotechnology in brain tumor targeting. in *Nanotechnology-Based Targeted Drug Delivery Systems for Brain Tumors* 111–145 (Elsevier, 2018). doi:10.1016/B978-0-12-812218-1.00005-1

149. Tomich, J. M., Wessel, E., Choi, J. & Avila, L. A. Nonviral Gene Therapy: Peptiplexes. in *Nucleic Acid Nanotheranostics* 247–276 (Elsevier, 2019). doi:10.1016/b978-0-12-814470-1.00008-3

150. Seroski, D. T. & Hudalla, G. A. Self-Assembled Peptide and Protein Nanofibers for Biomedical Applications. in *Biomedical Applications of Functionalized Nanomaterials: Concepts, Development and Clinical Translation* 569–598 (Elsevier, 2018). doi:10.1016/B978-0-323-50878-0.00019-7

151. ATTWOOD, D. & TOLLEY, J. A. Self-association of analgesics in aqueous solution: association models for codeine, oxycodone, ethylmorphine and pethidine. *Journal of Pharmacy and Pharmacology* **32**, 761–765 (1980).

152. Causon, D. *et al.* Ultrasonic relaxations associated with aggregation in drugs. *J. Chem. Soc. Faraday Trans. 2 Mol. Chem. Phys.* **77**, 143–151 (1981).

153. ATHERTON, A. D. & BARRY, B. W. Photon correlation spectroscopy of surface active cationic drugs. *J. Pharm. Pharmacol.* **37**, 854–862 (1985).

154. Sarmiento, F., López-Fontán, J. L., Prieto, G., Attwood, D. & Mosquera, V. Mixed micelles of structurally related antidepressant drugs. *Colloid Polym. Sci.* **275**, 1144–1147 (1997).

155. Attwood, D., Mosquera, V., Garcia, M., Suarez, M. J. & Sarmiento, F. A comparison of the micellar properties of structurally related antidepressant drugs. *J. Colloid Interface Sci.* **175**, 201–206 (1995).

156.   ATTWOOD, D. & AGARWAL, S. P. The surface activity and self-association of some β-adrenoceptor blocking agents in aqueous solution. *J. Pharm. Pharmacol.* **31**, 392–395 (1979).

157.   Kang, Y. & Zhang, X. CHAPTER 1. Evolution of Supra-Amphiphiles from Amphiphiles. in 1–22 (Royal Society of Chemistry, 2017). doi:10.1039/9781788010566-00001

158.   Zhang, X. & Wang, C. Supramolecular amphiphiles. *Chemical Society Reviews* **40**, 94–101 (2011).

159.   Wang, C., Wang, Z. & Zhang, X. Amphiphilic building blocks for self-assembly: From amphiphiles to supra-amphiphiles. *Acc. Chem. Res.* **45**, 608–618 (2012).

160.   Sikder, A. & Ghosh, S. Hydrogen-bonding regulated assembly of molecular and macromolecular amphiphiles. *Materials Chemistry Frontiers* **3**, 2602–2616 (2019).

161.   Mohmeyer, N. & Schmidt, H. W. A new class of low-molecular-weight amphiphilic gelators. *Chem. - A Eur. J.* **11**, 863–872 (2005).

162.   Faustino, C. M. C., Calado, A. R. T. & Garcia-Rio, L. Dimeric and monomeric surfactants derived from sulfur-containing amino acids. *J. Colloid Interface Sci.* **351**, 472–477 (2010).

163.   Pittelkow, M., Nielsen, C. B., Kadziola, A. & Christensen, J. B. Molecular recognition: Minimizing the acid-base interaction of a tunable host-guest system changes the selectivity of binding. *J. Incl. Phenom. Macrocycl. Chem.* **63**, 257–266 (2009).

164.   Pittelkow, M., Christensen, J. B. & Meijer, E. W. Guest-host chemistry with dendrimers: Stable polymer assemblies by rational design. *J. Polym. Sci. Part A Polym. Chem.* **42**, 3792–3799 (2004).

165.   Pittelkow, M. *et al.* Molecular recognition: Comparative study of a tunable host-guest system by using a fluorescent model system and collision-induced dissociation mass spectrometry on dendrimers. *Chem. - A Eur. J.* **11**, 5126–5135 (2005).

166. Hiscock, J. R., Bustone, G. P., Wilson, B., Belsey, K. E. & Blackholly, L. R. In situ modification of nanostructure configuration through the manipulation of hydrogen bonded amphiphile self-association. *Soft Matter* **12**, 4221–4228 (2016).

167. Blackholly, L. R., Shepherd, H. J. & Hiscock, J. R. 'Frustrated' hydrogen bond mediated amphiphile self-assembly-a solid state study. *CrystEngComm* **18**, 7021–7028 (2016).

168. White, L. J. *et al.* Towards quantifying the role of hydrogen bonding within amphiphile self-association and resultant aggregate formation. *Chem. Sci.* **8**, 7620–7630 (2017).

169. White, L. J. *et al.* Towards the Prediction of Global Solution State Properties for Hydrogen Bonded, Self-Associating Amphiphiles. *Chem. - A Eur. J.* **24**, 7761–7773 (2018).

170. Blackholly, L. R. Design, Characterisation and Synthesis of Novel Amphiphilic Supramolecular Antimicrobials.

171. Valeur, B. Molecular Fluorescence. in *digital Encyclopedia of Applied Physics* 477–531 (Wiley-VCH Verlag GmbH & Co. KGaA, 2009). doi:10.1002/3527600434.eap684

172. Leopoldo, M., Lacivita, E., Berardi, F. & Perrone, R. Developments in fluorescent probes for receptor research. *Drug Discovery Today* **14**, 706–712 (2009).

173. Anderson, M. J. & Cohen, M. W. Fluorescent staining of acetylcholine receptors in vertebrate skeletal muscle. *J. Physiol.* **237**, 385–400 (1974).

174. Yamaguchi, Y., Matsubara, Y., Ochi, T., Wakamiya, T. & Yoshida, Z. I. How the π conjugation length affects the fluorescence emission efficiency. *J. Am. Chem. Soc.* **130**, 13867–13869 (2008).

175. Zhang, H. *et al.* Why Do Simple Molecules with 'isolated' Phenyl Rings Emit Visible Light? *J. Am. Chem. Soc.* **139**, 16264–16272 (2017).

176. Baranczak, A. *et al.* Fluorogenic small molecules requiring reaction with a specific protein to create a fluorescent conjugate for biological imaging-what we know and what we need to learn. *Biopolymers* **101**, 484–495 (2014).

177. Li, A. F., Wang, J. H., Wang, F. & Jiang, Y. B. Anion complexation and sensing using modified urea and thiourea-based receptors. *Chemical Society Reviews* **39**, 3729–3745 (2010).

178. Dey, S., Sain, D. & Goswami, S. Naphthyridine based fluorescent receptors for the recognition of uric acid. *RSC Adv.* **4**, 428–433 (2014).

179. MA, K., WA, S., BA, B. & M, G. Fluorescent Synthetic Receptors for Signaling Hydrogen Sulphide in Living Systems. *Biochem. Anal. Biochem.* **08**, 1–4 (2019).

180. You, L., Zha, D. & Anslyn, E. V. Recent Advances in Supramolecular Analytical Chemistry Using Optical Sensing. *Chemical Reviews* **115**, 7840–7892 (2015).

181. Bell, T. W. & Hext, N. M. Supramolecular optical chemosensors for organic analytes. *Chemical Society Reviews* **33**, 589–598 (2004).

182. Quenching of Fluorescence. in *Principles of Fluorescence Spectroscopy* 277–330 (Springer US, 2006). doi:10.1007/978-0-387-46312-4_8

183. Tanaka, F., Mase, N. & Barbas, C. F. Determination of cysteine concentration by fluorescence increase: Reaction of cysteine with a fluorogenic aldehyde. *Chem. Commun.* **4**, 1762–1763 (2004).

184. FIKRY, M., OMAR, M. M. & ISMAIL, L. Z. Effect of host medium on the fluorescence emission intensity of Rhodamine B in liquid and solid phase. in 210–219 (World Scientific Pub Co Pte Lt, 2011). doi:10.1142/9789814317511_0025

185. Zhang, M., Yin, B. C., Tan, W. & Ye, B. C. A versatile graphene-based fluorescence 'on/off' switch for multiplex detection of various targets. *Biosens. Bioelectron.* **26**, 3260–3265 (2011).

186. Abou-Hatab, S., Spata, V. A. & Matsika, S. Substituent Effects on the Absorption and Fluorescence Properties of Anthracene. *J. Phys. Chem. A* **121**, 1213–1222 (2017).

187. Sjöback, R., Nygren, J. & Kubista, M. Absorption and fluorescence properties of fluorescein. *Spectrochim. Acta Part A Mol. Spectrosc.* **51**, L7–L21 (1995).

188. Chen, R. F. Some characteristics of the fluorescence of quinine. *Anal. Biochem.* **19**, 374–387 (1967).

189. Taylor, R. The hydrogen bond between N-H or O-H and organic fluorine: Favourable yes, competitive no. *Acta Crystallogr. Sect. B Struct. Sci. Cryst. Eng. Mater.* **73**, 474–488 (2017).

190. Ghosh, K., Sarkar, A. R. & Masanta, G. An anthracene based bispyridinium amide receptor for selective sensing of anions. *Tetrahedron Lett.* **48**, 8725–8729 (2007).

191. Ghosh, K. & Sarkar, A. R. Anthracene-based macrocyclic fluorescent chemosensor for selective sensing of dicarboxylate. *Tetrahedron Lett.* **50**, 85–88 (2009).

192. Huang, W., Lin, H., Cai, Z. & Lin, H. A novel anthracene-based receptor: Highly sensitive fluorescent and colorimetric receptor for fluoride. *Talanta* **81**, 967–971 (2010).

193. Kim, S. K. *et al.* Anthracene derivatives bearing two urea groups as fluorescent receptors for anions. *Tetrahedron* **61**, 4545–4550 (2005).

194. Moragues, M. E., Santos-Figueroa, L. E., Ábalos, T., Sancenón, F. & Martínez-Máñez, R. Synthesis of a new tripodal chemosensor based on 2,4,6-triethyl-1,3,5- trimethylbencene scaffolding bearing thiourea and fluorescein for the chromo-fluorogenic detection of anions. *Tetrahedron Lett.* **53**, 5110–5113 (2012).

195. Ghosh, K. & Sen, T. Adenine-based urea receptors in fluorescent recognition of iodide. *Tetrahedron Lett.* **49**, 7204–7208 (2008).

196.   Ramachandram, B. & Samanta, A. How important is the quenching influence of the transition metal ions in the design of fluorescent PET sensors? *Chem. Phys. Lett.* **290**, 9–16 (1998).

197.   Xu, K. X., Qing, G. Y., He, Y. B., Qin, H. J. & Hu, L. Chiral fluorescent receptors based on amino acid unit: Synthesis and their enantioselective recognition. *Supramol. Chem.* **19**, 403–409 (2007).

198.   White, L. J. *et al.* Towards the Prediction of Global Solution State Properties for Hydrogen Bonded, Self-Associating Amphiphiles. *Chem. - A Eur. J.* **24**, 7761–7773 (2018).

199.   Stremple, P., Baenziger, N. C., Coucouvanis, D., About, M. & Article, T. complexes . Synthesis and structural characterization. *Communications* **2**, 10–13 (2002).

200.   Chauhan, S. M. S., Garg, B. & Bisht, T. Syntheses of calix[4]pyrroles by amberlyst-15 catalyzed cyclocondensations of pyrrole with selected ketones. *Molecules* **12**, 2458–2466 (2007).

201.   Eckert, M. Max von Laue and the discovery of X-ray diffraction in 1912. *Annalen der Physik* **524**, (2012).

202.   Batsanov, A. S. X-Ray Diffraction, Small Molecule Applications. in *Encyclopedia of Spectroscopy and Spectrometry* 656–666 (Elsevier, 2016). doi:10.1016/B978-0-12-409547-2.11370-8

203.   Davis, F. & Higson, S. Heterocalixarenes and Calixnaphthalenes. in *Macrocycles* 126–189 (John Wiley & Sons, Ltd, 2011). doi:10.1002/9780470980200.ch5

204.   Atwood, J. L., Barbour, L. J. & Jerga, A. Storage of methane and freon by interstitial van der Waals confinement. *Science (80-.).* **296**, 2367–2369 (2002).

205.   Vita, F. *et al.* Synthesis and recognition properties of calix[4]arene semitubes as ditopic hosts for: N -alkylpyridinium ion pairs. *CrystEngComm* **18**, 5017–5027 (2016).

206.   Iwamoto, K., Araki, K. & Shinkai, S. Conformations and Structures of Tetra- 0 -alkyl-p -tert -

butylcalix[Ilarenes. *J. Am. Chem. Soc.* **29**, 4955–4962 (1991).

207. Kundrat, O. & Lhoták, P. Meta substitution of calixarenes. in *Calixarenes and Beyond* 43–73 (Springer, 2016). doi:10.1007/978-3-319-31867-7_3

208. Ho, C. S. *et al.* Electrospray ionisation mass spectrometry: principles and clinical applications. *Clin. Biochem. Rev.* **24**, 3–12 (2003).

209. Baitinger, W. F., Schleyer, P. von R., Murty, T. S. S. R. & Robinson, L. Nitro groups as proton acceptors in hydrogen bonding. *Tetrahedron* **20**, 1635–1647 (1964).

210. Raghavendra, B. & Arunan, E. Hydrogen bonding with a hydrogen bond: The methane-water complex and the penta-coordinate carbon. *Chem. Phys. Lett.* **467**, 37–40 (2008).

211. Protti, S., Mezzetti, A., Cornard, J. P., Lapouge, C. & Fagnoni, M. Hydrogen bonding properties of DMSO in ground-state formation and optical spectra of 3-hydroxyflavone anion. *Chem. Phys. Lett.* **467**, 88–93 (2008).

212. Evilia, R. F. Quantitative NMR spectroscopy. *Analytical Letters* **34**, 2227–2236 (2001).

213. Wallace, M., Iggo, J. A. & Adams, D. J. Using solution state NMR spectroscopy to probe NMR invisible gelators. *Soft Matter* **11**, 7739–7747 (2015).

214. Achuthan, S., Chung, B. J., Ghosh, P., Rangachari, V. & Vaidya, A. A modified Stokes-Einstein equation for Aβ aggregation. *BMC Bioinformatics* **12**, S13 (2011).

215. MeijerK. S. and V. E. P Thordarson. BindFit v0.5 | Supramolecular. Available at: http://app.supramolecular.org/bindfit/. (Accessed: 3rd December 2019)

216. Martin, R. B. Comparisons of indefinite self-association models. *Chemical Reviews* **96**, 3043–3064 (1996).

217. Von Krbek, L. K. S., Schalley, C. A. & Thordarson, P. Assessing cooperativity in supramolecular systems. *Chemical Society Reviews* **46**, 2622–2637 (2017).

218. Gupta, V. P. Characterization of Chemical Reactions. in *Principles and Applications of Quantum Chemistry* 385–433 (Elsevier, 2016). doi:10.1016/b978-0-12-803478-1.00012-1

219. Tanchoco, F. 'Electropositivity' and 'electronegativity'. *Journal of Chemical Education* **15**, 291 (1938).

220. Hunter, C. A. Quantifying intermolecular interactions: Guidelines for the molecular recognition toolbox. *Angewandte Chemie - International Edition* **43**, 5310–5324 (2004).

221. Wavefunction, Inc. Irvine, C. Spartan'16.

222. Stewart, J. J. P. Optimization of parameters for semiempirical methods V: Modification of NDDO approximations and application to 70 elements. *J. Mol. Model.* **13**, 1173–1213 (2007).

223. Hibbs, A. R. & Hibbs, A. R. What is Fluorescence? in *Confocal Microscopy for Biologists* 187–200 (Springer US, 2004). doi:10.1007/978-0-306-48565-7_8

224. Wouterlood, F. G. & Boekel, A. J. Fluorescence Microscopy in the Neurosciences. in *Encyclopedia of Neuroscience* 253–260 (Elsevier Ltd, 2009). doi:10.1016/B978-008045046-9.00666-5

225. Valeur, B. & Berberan-Santos, M. N. A brief history of fluorescence and phosphorescence before the emergence of quantum theory. *Journal of Chemical Education* **88**, 731–738 (2011).

226. Valeur, B. Introduction: On the Origin of the Terms Fluorescence, Phosphorescence, and Luminescence. in 3–6 (2001). doi:10.1007/978-3-642-56853-4_1

227. Sekiya, M. & Yamasaki, M. Antoine Henri Becquerel (1852–1908): a scientist who endeavored to discover natural radioactivity. *Radiological Physics and Technology* **8**, (2015).

228. Nelder, J. A. & Mead, R. A Simplex Method for Function Minimization. *Comput. J.* **7**, 308–313 (1965).

229. Deiana, M. *et al.* A Light-up Logic Platform for Selective Recognition of Parallel G-Quadruplex Structures via Disaggregation-Induced Emission. *Angew. Chem. Int. Ed. Engl.* ange.201912027 (2019). doi:10.1002/anie.201912027

230. Hisamatsu, Y., Umezawa, N., Yagi, H., Kato, K. & Higuchi, T. Design and synthesis of a 4-aminoquinoline-based molecular tweezer that recognizes protoporphyrin IX and iron(III) protoporphyrin IX and its application as a supramolecular photosensitizer. *Chem. Sci.* **9**, 7455–7467 (2018).

231. Papageorgiou, G. & Govindjee. Changes in Intensity and Spectral Distribution of Fluorescence: Effect of Light Treatment on Normal and DCMU-Poisoned Anacystis nidulans. *Biophys. J.* **7**, 375–389 (1967).

232. Thordarson, P. Binding Constants and Their Measurement. in *Supramolecular Chemistry* (John Wiley & Sons, Ltd, 2012). doi:10.1002/9780470661345.smc018

233. Silverstein, T. P. & Heller, S. T. PKa Values in the Undergraduate Curriculum: What Is the Real pKa of Water? *J. Chem. Educ.* **94**, 690–695 (2017).

234. Information, N. C. for B. Urea. Available at: https://pubchem.ncbi.nlm.nih.gov/compound/Urea.

235. Koyama, M., Kawakami, T., Okazoe, T. & Nozaki, K. Cyanide-Free One-Pot Synthesis of Methacrylic Esters from Acetone. *Chem. – A Eur. J.* **25**, 10913–10917 (2019).

236. Boiocchi, M. *et al.* Anion-induced urea deprotonation. *Chem. - A Eur. J.* **11**, 3097–3104 (2005).

237. Li Yaoqun, Qian Fang, L. Z. Reduction of second-order scattering interference by variable-angle synchronous luminescence spectroscopy.

238. Lakowicz, J. R. *Principles of fluorescence spectroscopy*. *Principles of Fluorescence Spectroscopy* (2006). doi:10.1007/978-0-387-46312-4

239. Mąkosza, M. Nucleophilic substitution in nitroarenes: a general corrected mechanism. *ChemTexts* **5**, 1–12 (2019).

240. Zhang, Y. & Cremer, P. S. Interactions between macromolecules and ions: the Hofmeister series. *Current Opinion in Chemical Biology* **10**, 658–663 (2006).

241. Okur, H. I. *et al.* Beyond the Hofmeister Series: Ion-Specific Effects on Proteins and Their Biological Functions. *Journal of Physical Chemistry B* **121**, 1997–2014 (2017).

242. Dabrowa, K., Ulatowski, F., Lichosyt, D. & Jurczak, J. Catching the chloride: Searching for non-Hofmeister selectivity behavior in systematically varied polyamide macrocyclic receptors. *Org. Biomol. Chem.* **15**, 5927–5943 (2017).

243. Parsons, D. F., Boström, M., Nostro, P. Lo & Ninham, B. W. Hofmeister effects: Interplay of hydration, nonelectrostatic potentials, and ion size. *Physical Chemistry Chemical Physics* **13**, 12352–12367 (2011).

244. Pegram, L. M. & Record, M. T. Quantifying accumulation or exclusion of H+, HO-, and Hofmeister salt ions near interfaces. *Chem. Phys. Lett.* **467**, 1–8 (2008).

245. Nucci, N. V. & Vanderkooi, J. M. Effects of salts of the Hofmeister series on the hydrogen bond network of water. *J. Mol. Liq.* **143**, 160–170 (2008).

246. Puchalski, M. M., Morra, M. J. & von Wandruszka, R. Assessment of inner filter effect corrections in fluorimetry. *Fresenius. J. Anal. Chem.* **340**, 341–344 (1991).

247. Kubista, M., Sjöback, R., Eriksson, S. & Albinsson, B. Experimental correction for the inner-filter effect in fluorescence spectra. *Analyst* **119**, 417–419 (1994).

248. Kothawala, D. N., Murphy, K. R., Stedmon, C. A., Weyhenmeyer, G. A. & Tranvik, L. J. Inner filter correction of dissolved organic matter fluorescence. *Limnol. Oceanogr. Methods* **11**, 616–630 (2013).

249. Omary, M. A. & Patterson, H. H. Luminescence, Theory. in *Encyclopedia of Spectroscopy and Spectrometry* 636–653 (Elsevier Inc., 2017). doi:10.1016/B978-0-12-803224-4.00193-X

250. Gu, Q. & Kenny, J. E. Improvement of inner filter effect correction based on determination of effective geometric parameters using a conventional fluorimeter. *Anal. Chem.* **81**, 420–426 (2009).

251. Quinn, M. Determination of acetylsalicylic acid in aspirin using Total Fluorescence Spectroscopy. *J. Chem. Educ.* 1–2 (1994).

252. Fonin, A. V., Sulatskaya, A. I., Kuznetsova, I. M. & Turoverov, K. K. Fluorescence of dyes in solutions with high absorbance. Inner filter effect correction. *PLoS One* **9**, e103878 (2014).

253. Zakharian, T. Y. & Coon, S. R. Evaluation of Spartan semi-empirical molecular modeling software for calculations of molecules on surfaces: CO adsorption on Ni(111). *Comput. Chem.* **25**, 135–144 (2001).

254. Sen, P., Yildiz, S. Z., Atalay, V. E., Kanmazalp, S. D. & Dege, N. Synthesis, molecular structure and spectroscopic and computational studies on 4-(2-(2-(2-formylphenoxy)ethoxy)ethoxy)phthalonitrile as a functionalized phthalonitrile. *Maced. J. Chem. Chem. Eng.* **38**, 63–74 (2019).

255. Sheldrick, G. M. SHELXT - Integrated space-group and crystal-structure determination. *Acta Crystallogr. Sect. A Found. Crystallogr.* **71**, 3–8 (2015).

256. Yoshioka, S., Inokuma, Y., Hoshino, M., Sato, T. & Fujita, M. Absolute structure determination of compounds with axial and planar chirality using the crystalline sponge method. *Chem. Sci.* **6**, 3765–3768 (2015).

257. Dolomanov, O. V., Bourhis, L. J., Gildea, R. J., Howard, J. A. K. & Puschmann, H. OLEX2: A complete structure solution, refinement and analysis program. *J. Appl. Crystallogr.* **42**, 339–341 (2009).

8.0 Appendix

8.1 Characterisation NMR
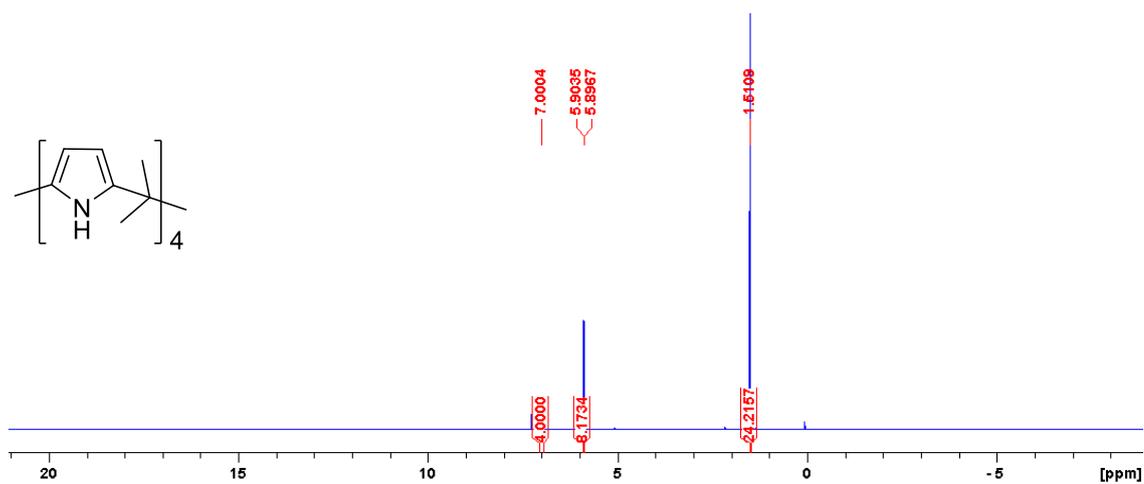
Figure 1 – ^{1}H NMR of Compound **1** in CDCl$_3$.
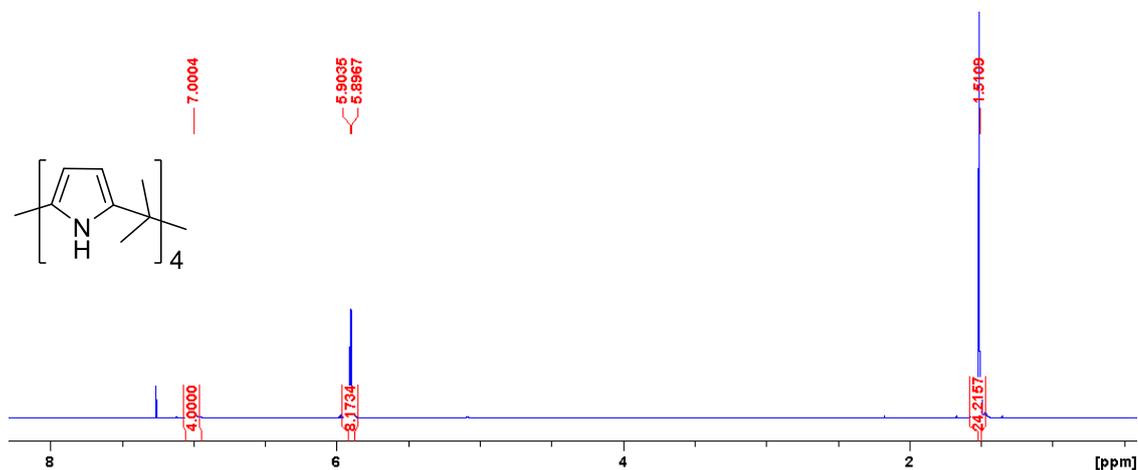
Figure 2 – Enlarged ^{1}H NMR of Compound **1** in CDCl$_3$.
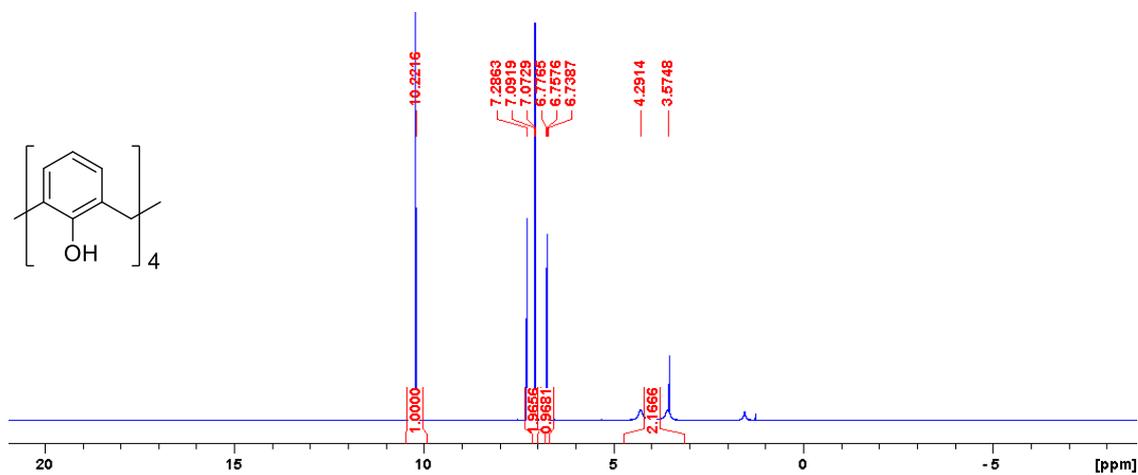
Figure 3 – ^{1}H NMR of Compound **2** in CDCl$_3$.
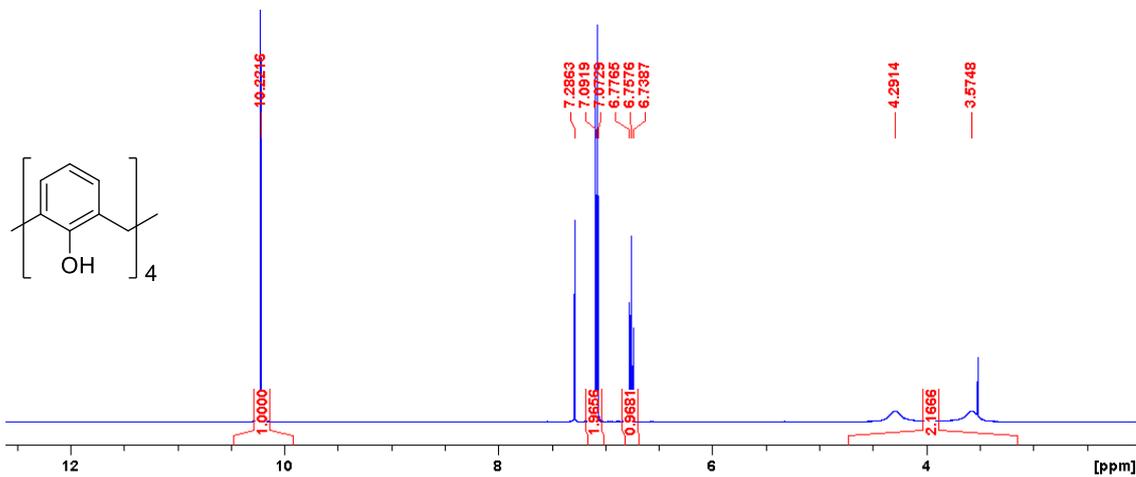
Figure 4 – Enlarged ^{1}H NMR of Compound **2** in CDCl$_3$.
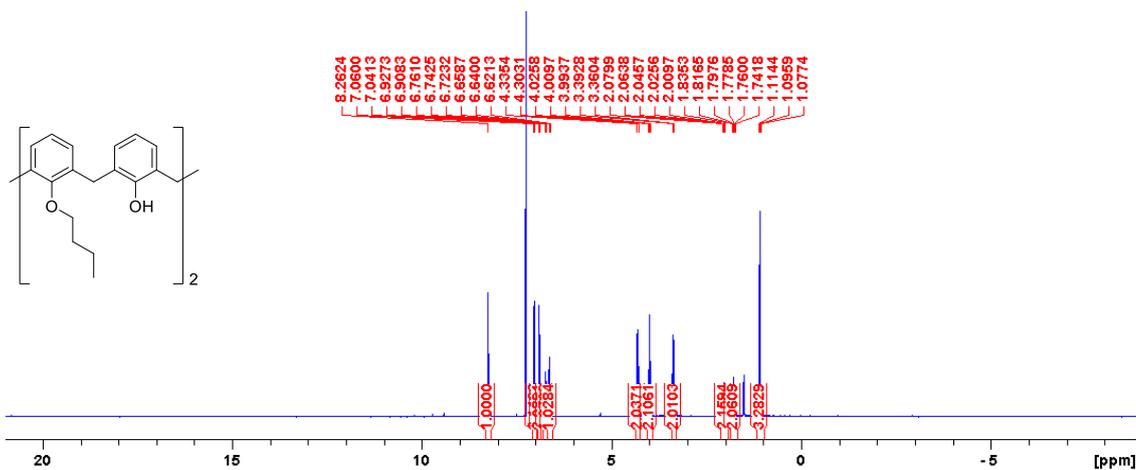
Figure 5 – ^{1}H NMR of Compound **3** in CDCl$_3$.
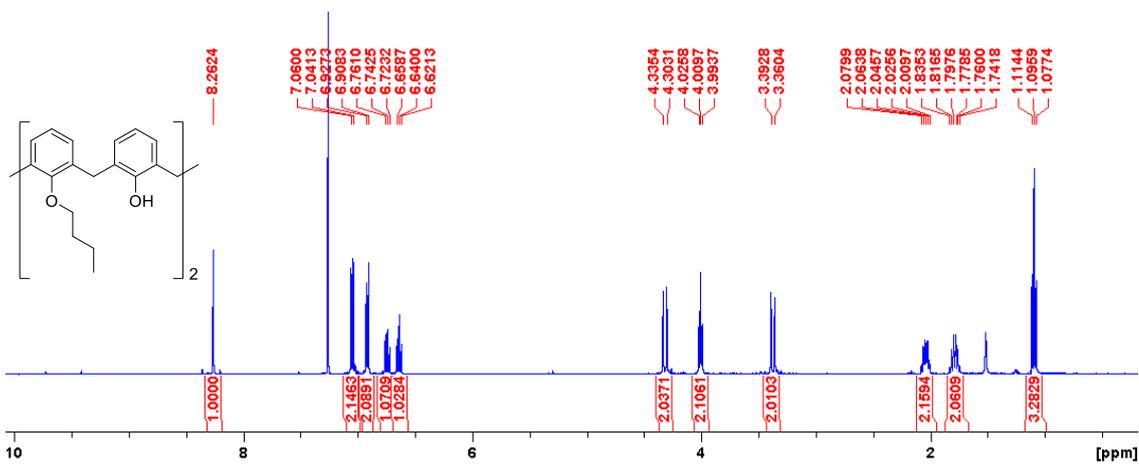
Figure 6 – Enlarged ^{1}H NMR of Compound **3** in CDCl$_3$.
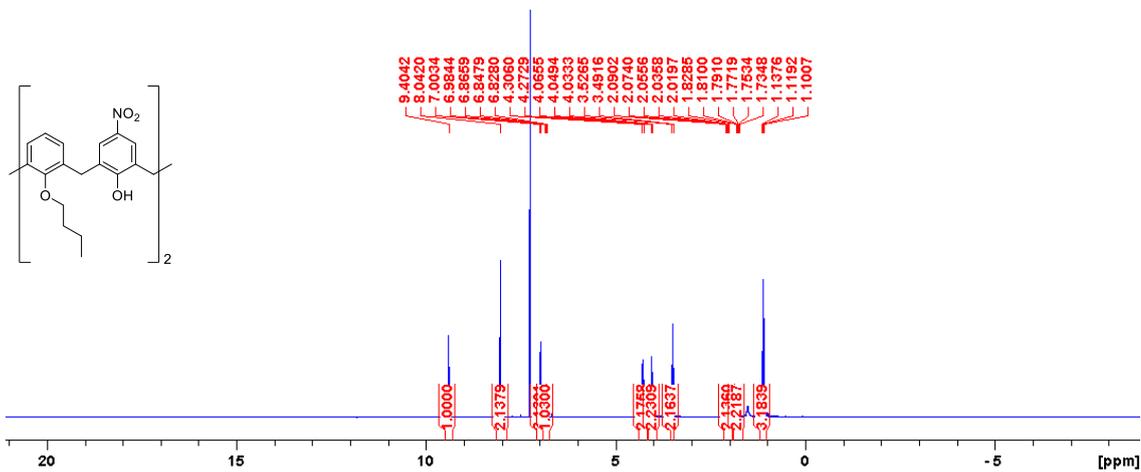
Figure 7 – ^{1}H NMR of Compound **4** in CDCl$_3$.
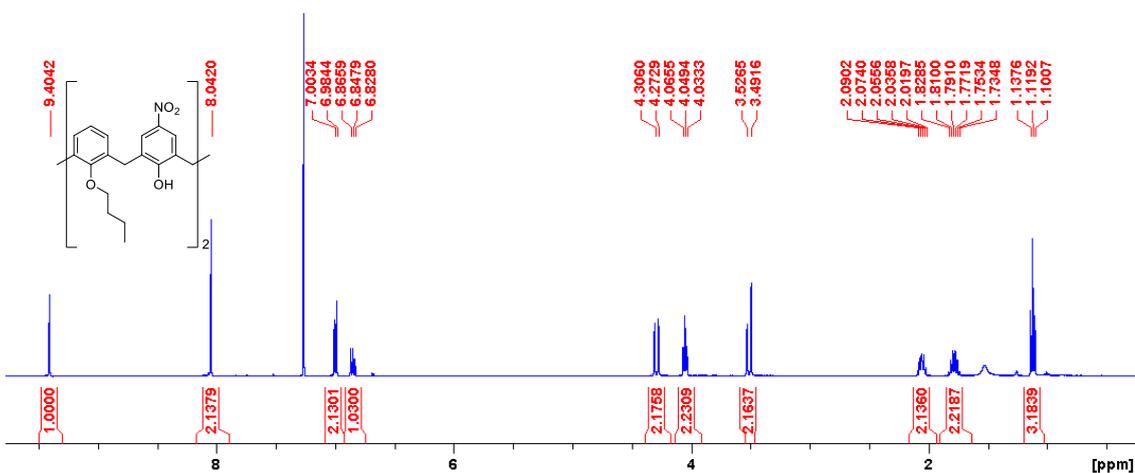
Figure 8 – Enlarged ^{1}H NMR of Compound **4** in CDCl$_3$.
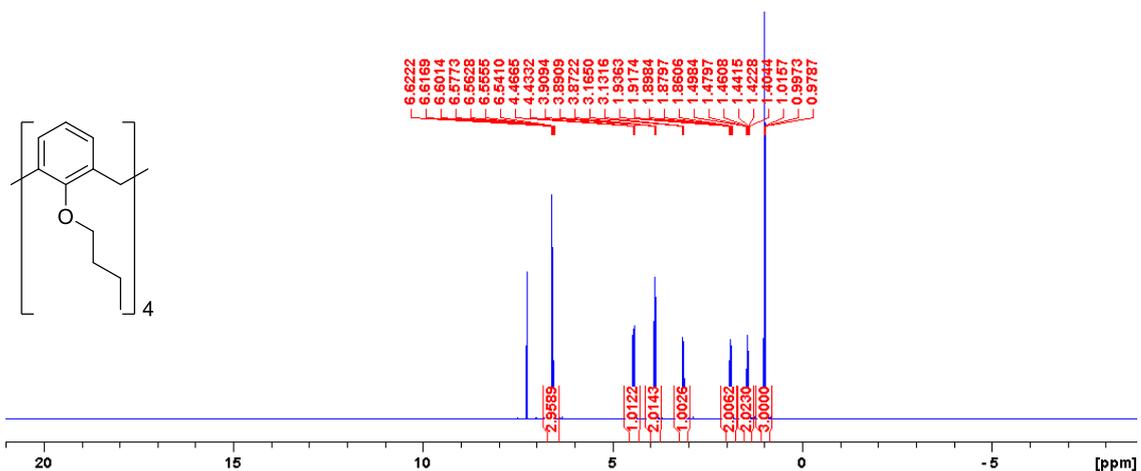
Figure 9 – ^{1}H NMR of Compound **5** in CDCl$_3$.
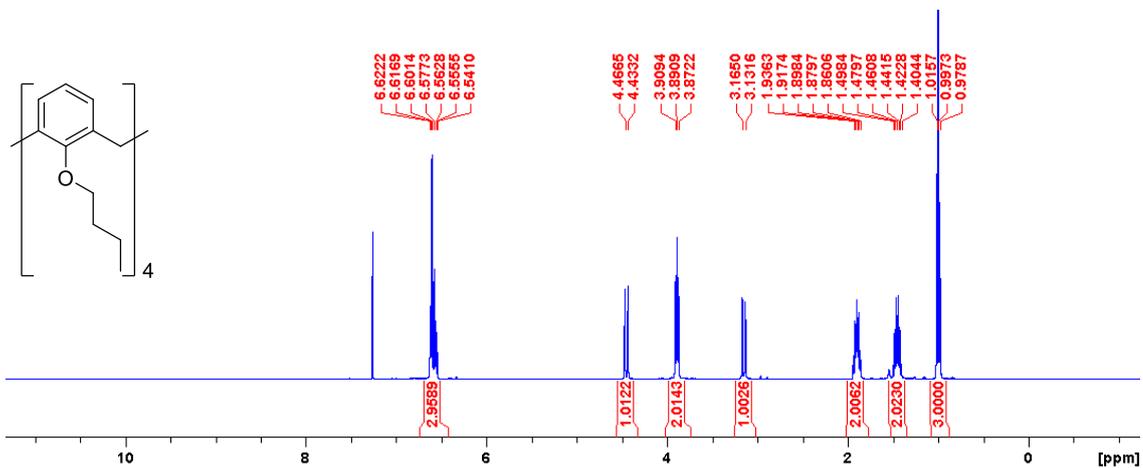
Figure 10 – Enlarged ^{1}H NMR of Compound **5** in CDCl$_3$.
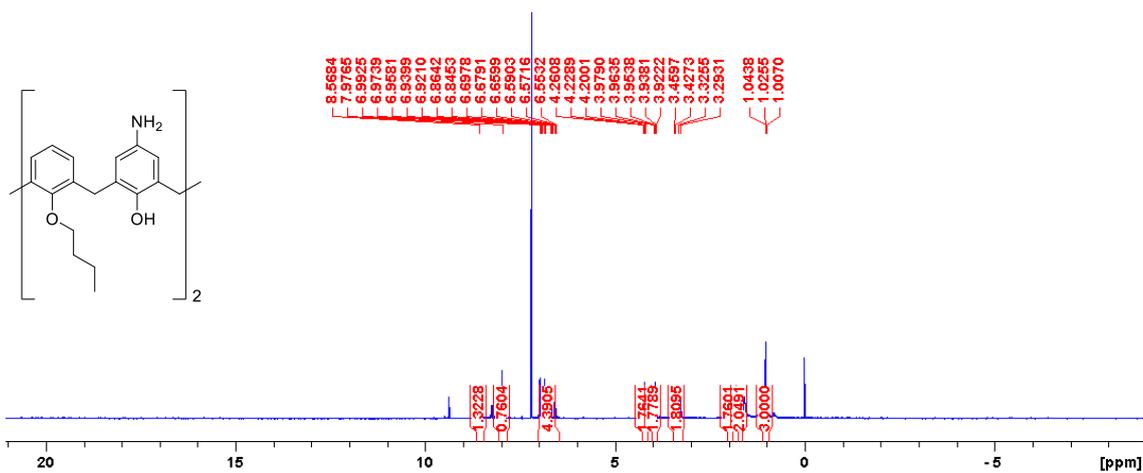
Figure 11 – ^{1}H NMR of Compound **6** in CDCl$_3$.
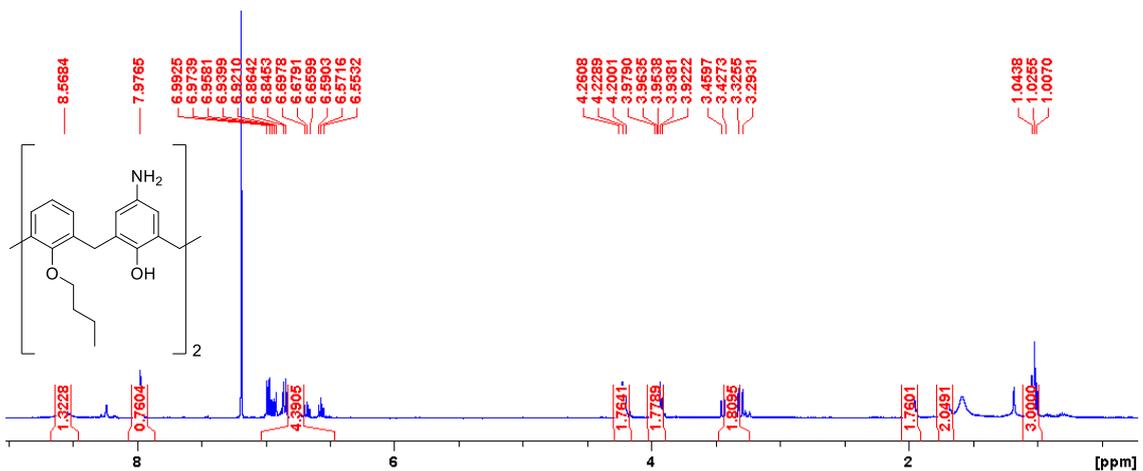
Figure 12 – Enlarged ^{1}H NMR of Compound **6** in CDCl$_3$.
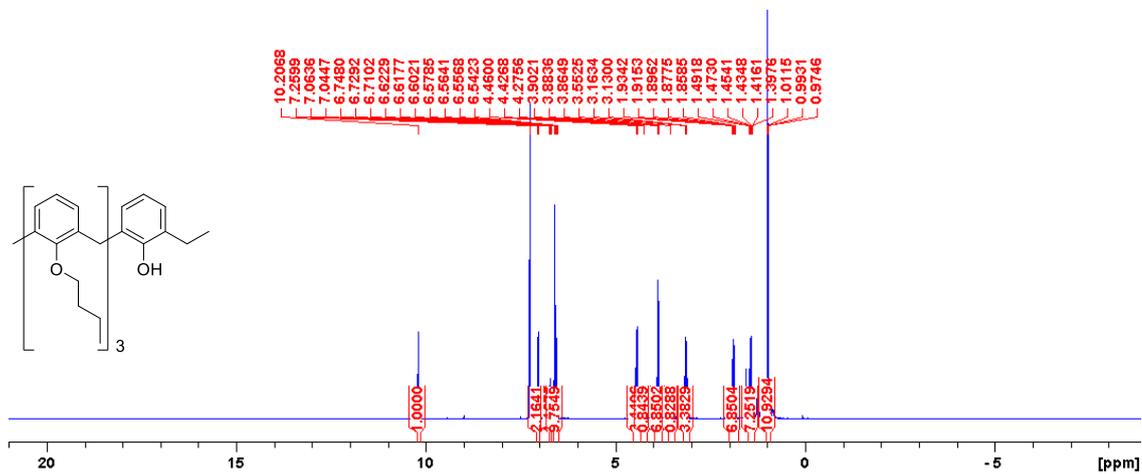
Figure 13 – ^{1}H NMR of Compound **7** in CDCl$_3$.
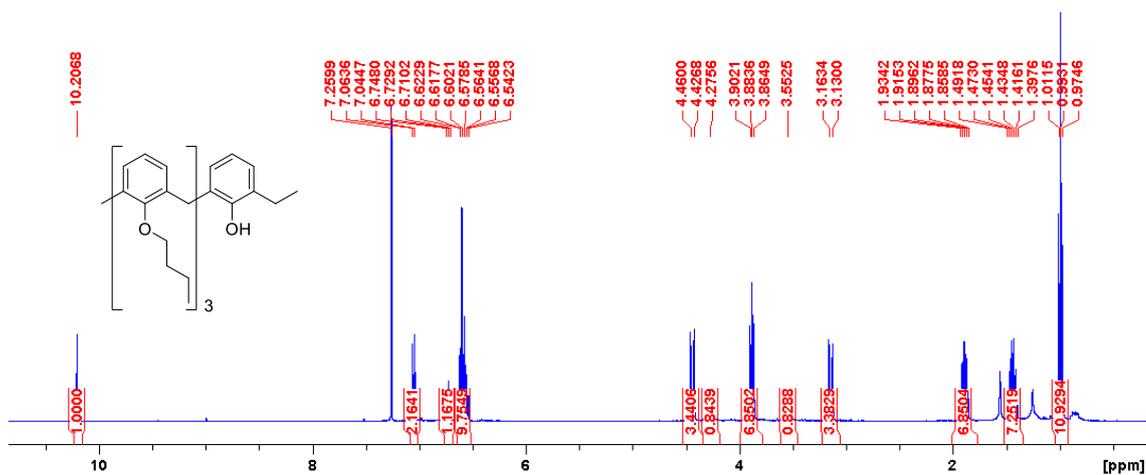
Figure 14 – Enlarged ^{1}H NMR of Compound **7** in CDCl$_3$.
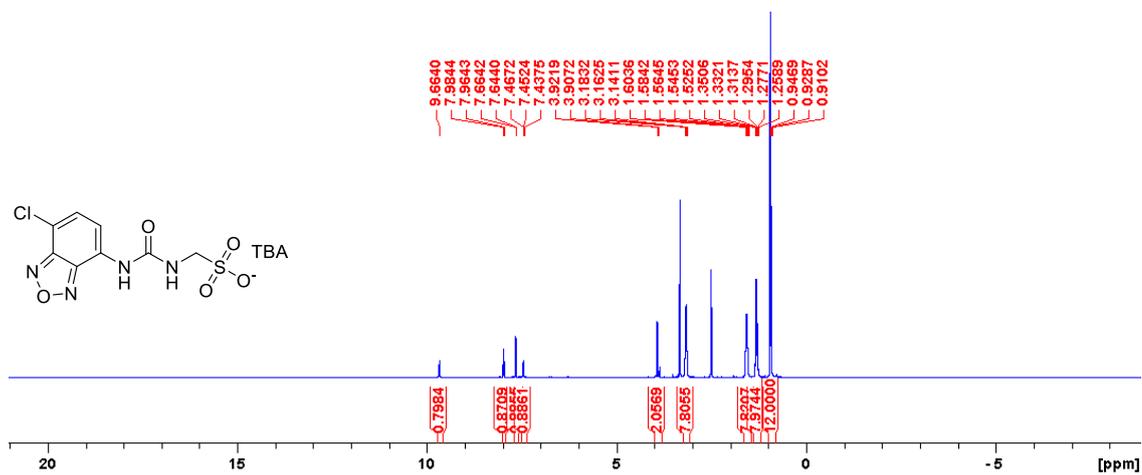
Figure 15 – ^{1}H NMR of Compound **12** in DMSO-d_6.
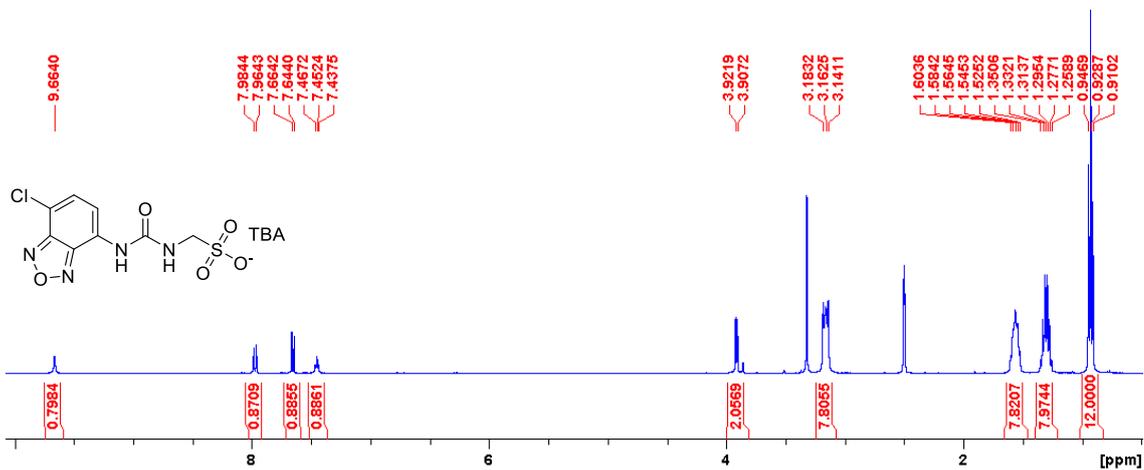
Figure 16 – Enlarged ¹H NMR of Compound **12** in DMSO-*d₆*.
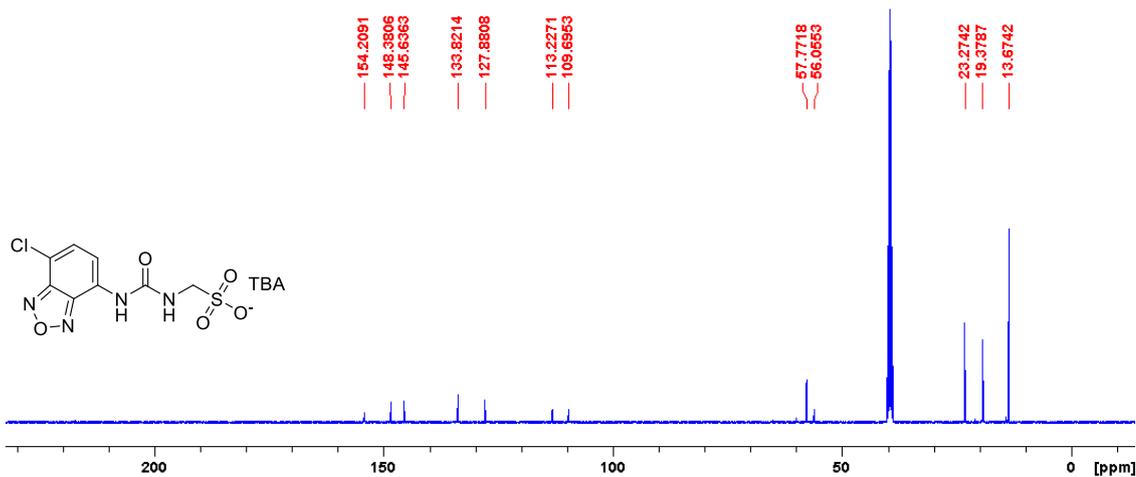
Figure 17 – ¹³C NMR of Compound **12** in DMSO-*d₆*.
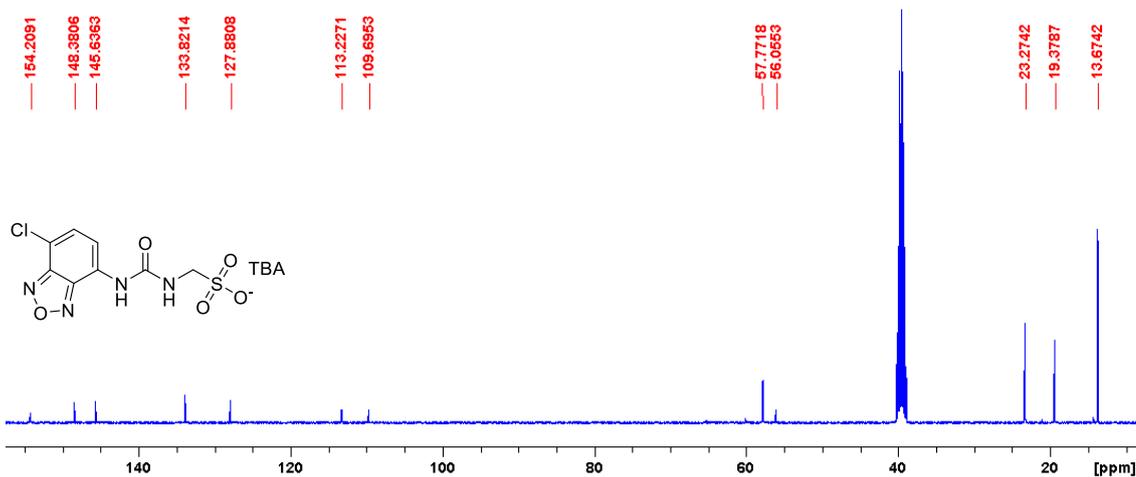
Figure 18 – Enlarged ¹³C NMR of Compound **12** in DMSO-*d₆*.
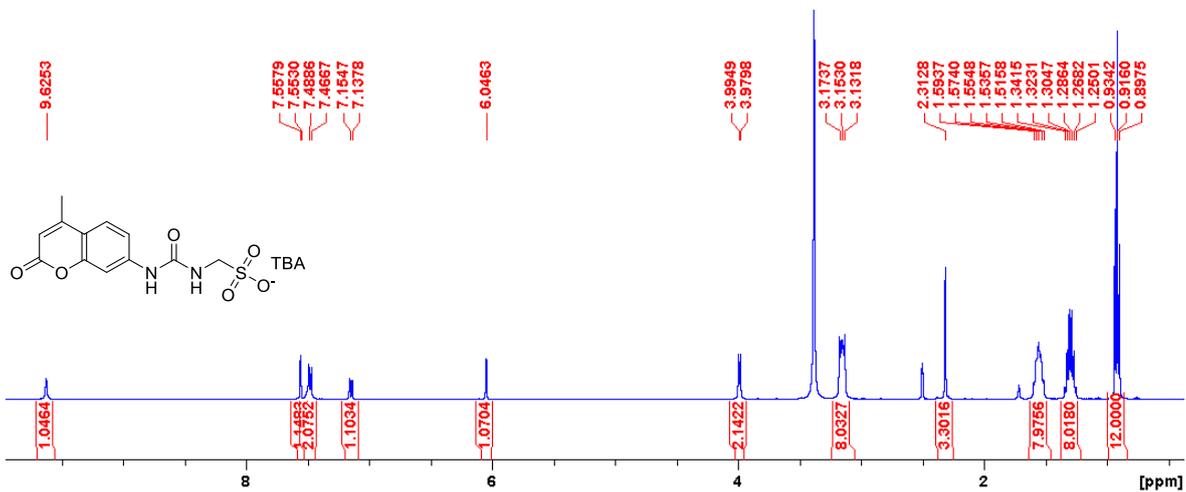
Figure 19 – ^{1}H NMR of Compound **13** in DMSO-*d$_6$*.
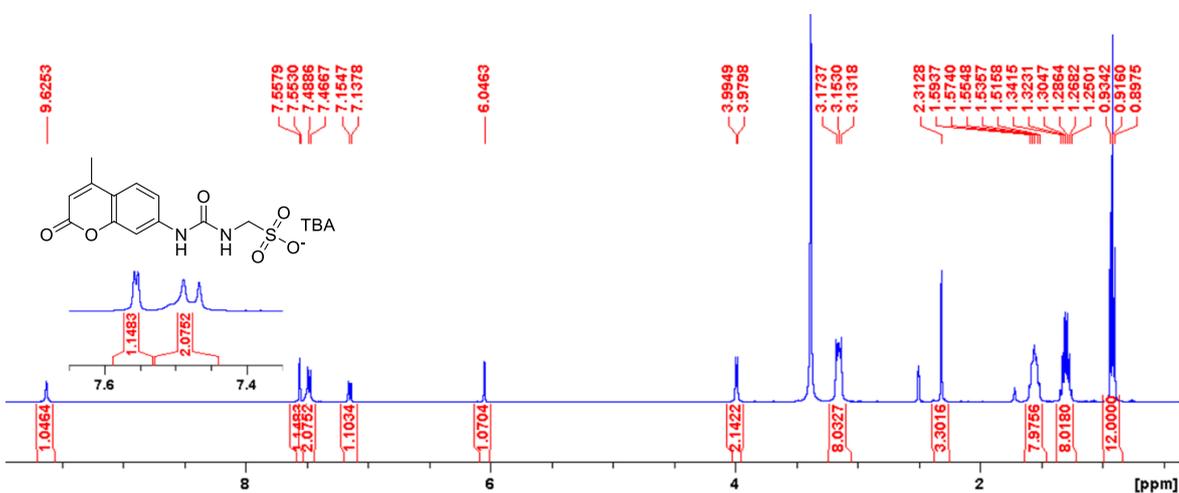
Figure 20 – Enlarged ^{1}H NMR of Compound **13** in DMSO-*d$_6$*.
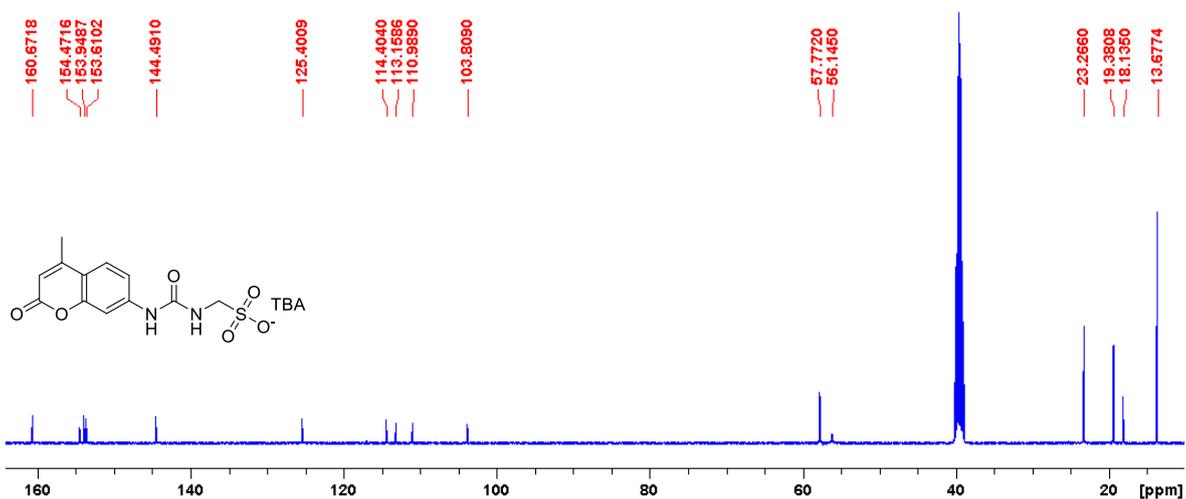
Figure 21 – ^{13}C NMR of Compound **13** in DMSO-*d$_6$*.
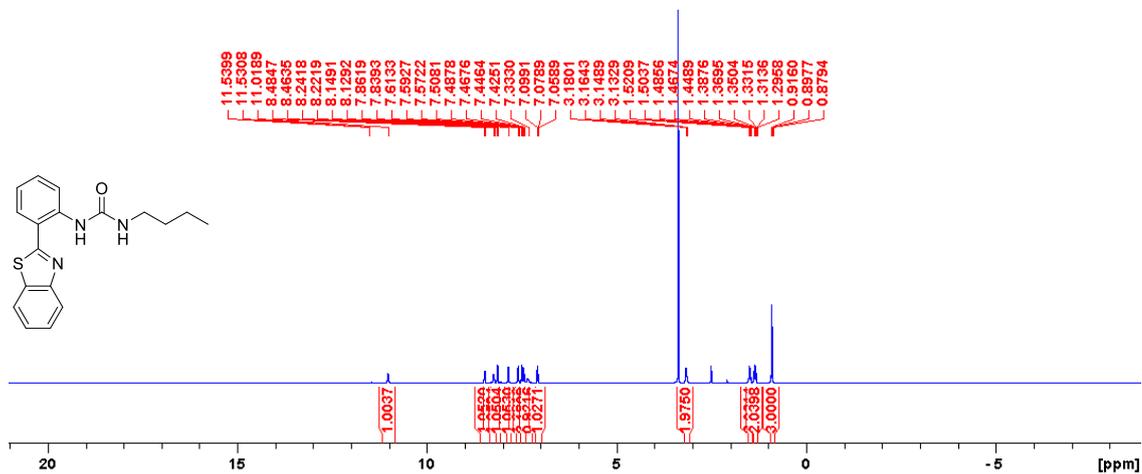
Figure 22 – ^{1}H NMR of Compound **14** in DMSO-d_6.
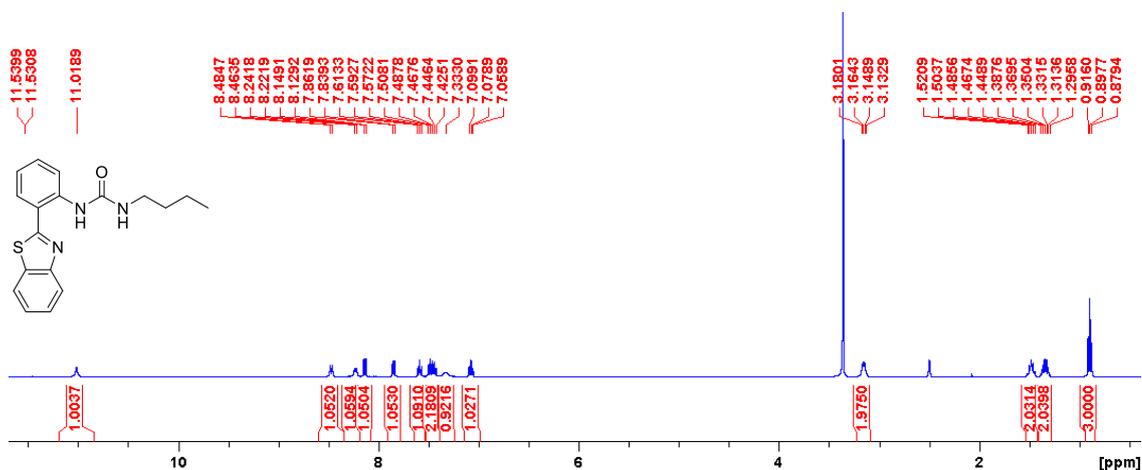
Figure 23 – Enlarged ^{1}H NMR of Compound **14** in DMSO-d_6.
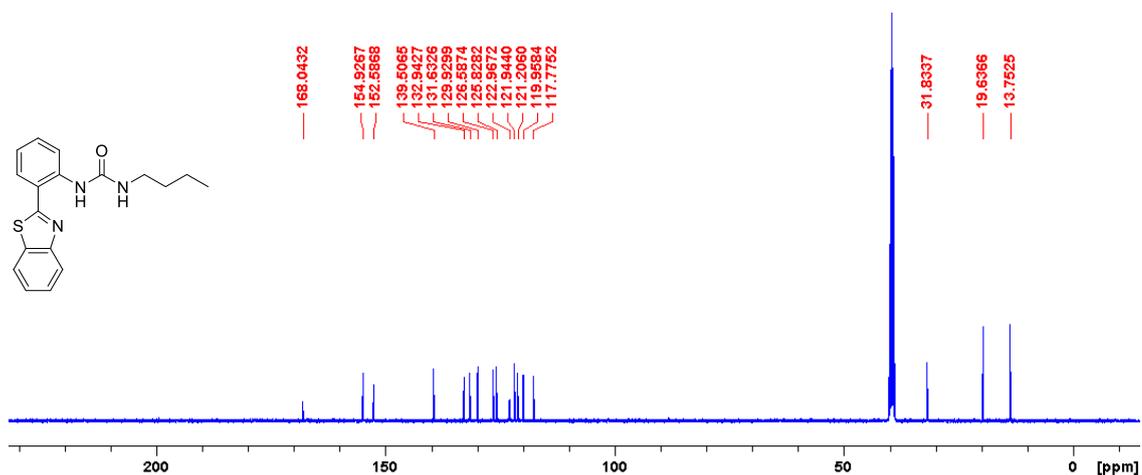
Figure 24 – ^{13}C NMR of Compound **14** in DMSO-d_6.
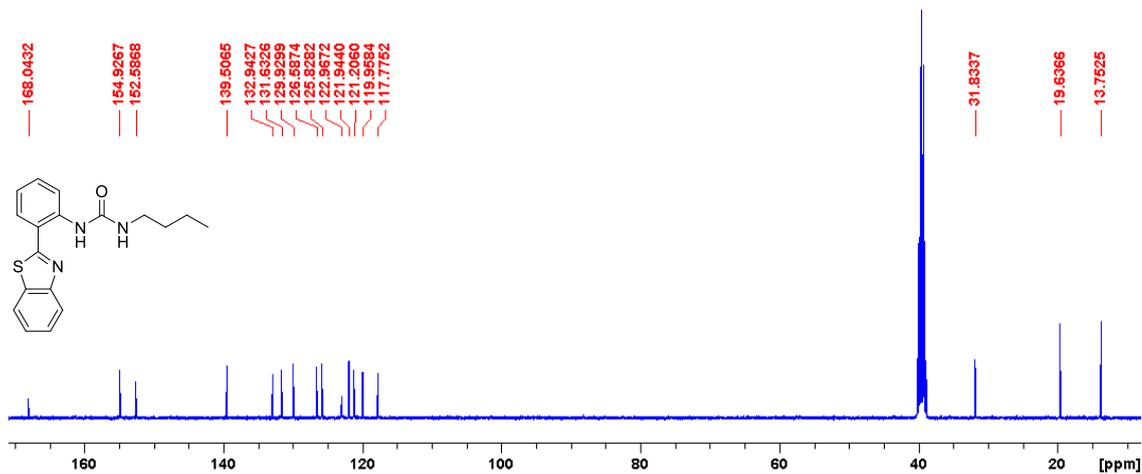
Figure 25 – Enlarged ^{13}C NMR of Compound **14** in DMSO-d_6.
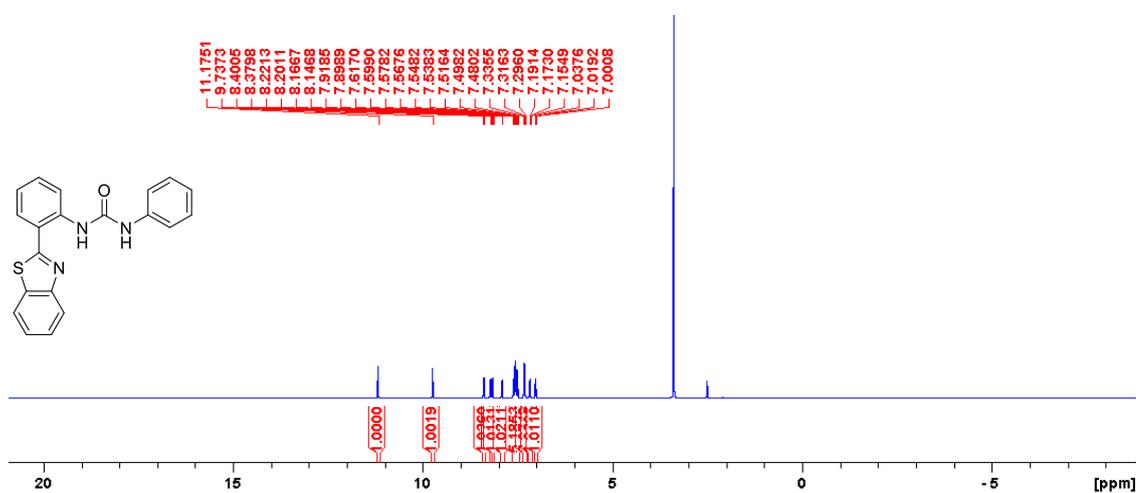
Figure 26 – ^{1}H NMR of Compound **15** in DMSO-d_6.
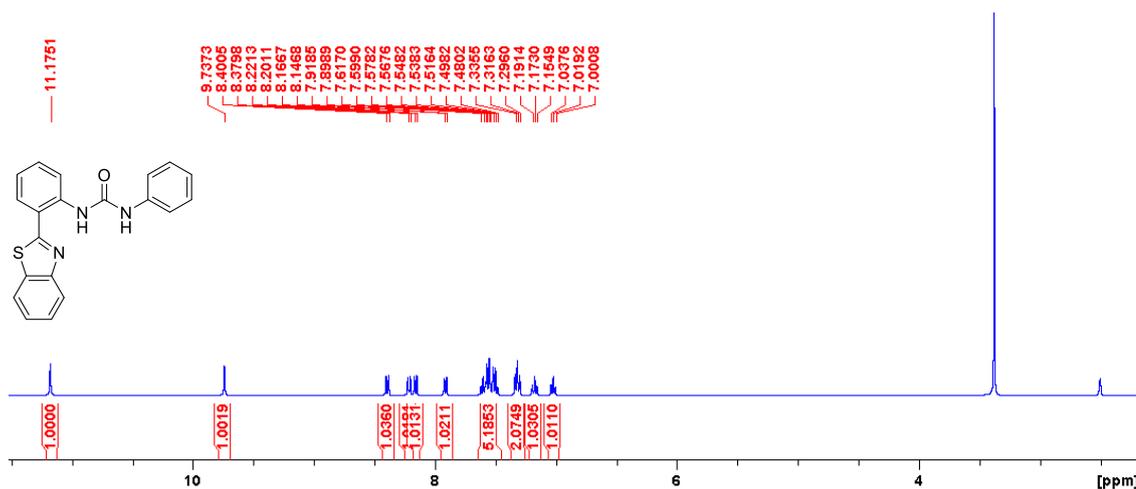
Figure 27 – Enlarged ^{1}H NMR of Compound **15** in DMSO-d_6.
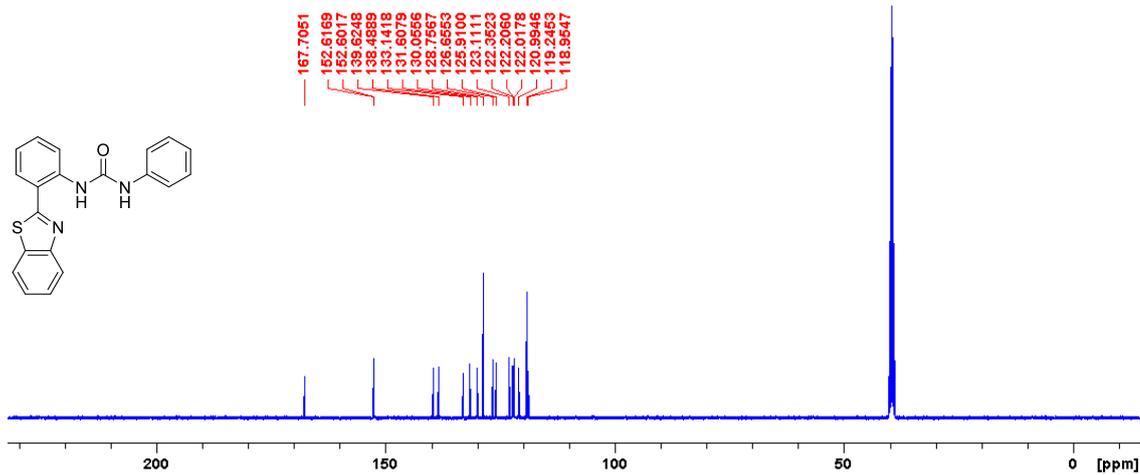
Figure 28 – ^{13}C NMR of Compound **15** in DMSO-d_6.
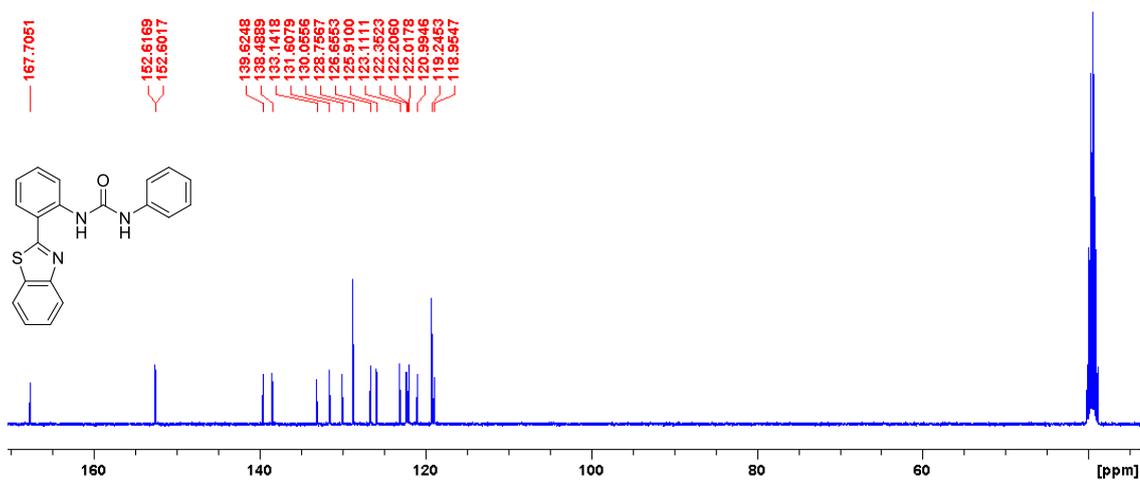
Figure 29 – Enlarged ^{13}C NMR of Compound **15** in DMSO-d_6.
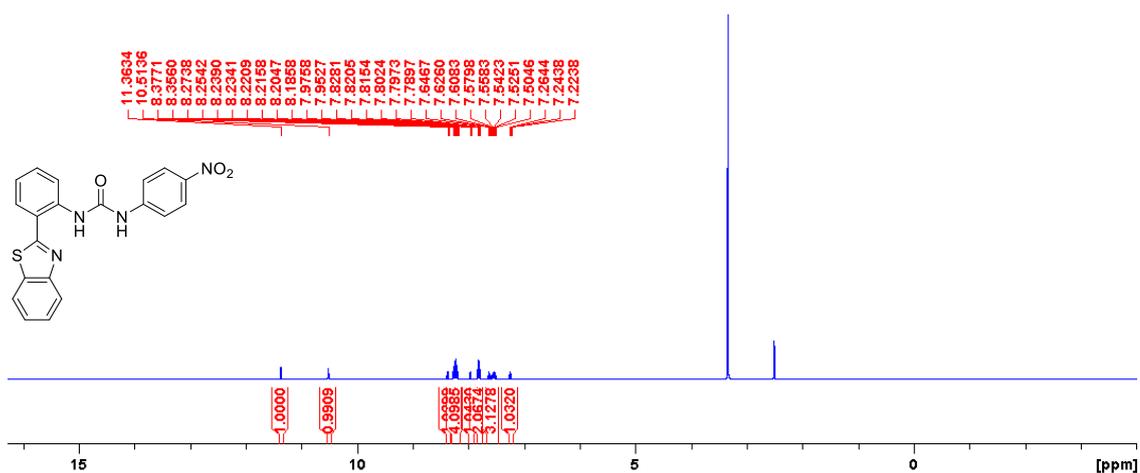
Figure 30 – ^{1}H NMR of Compound **16** in DMSO-d_6.
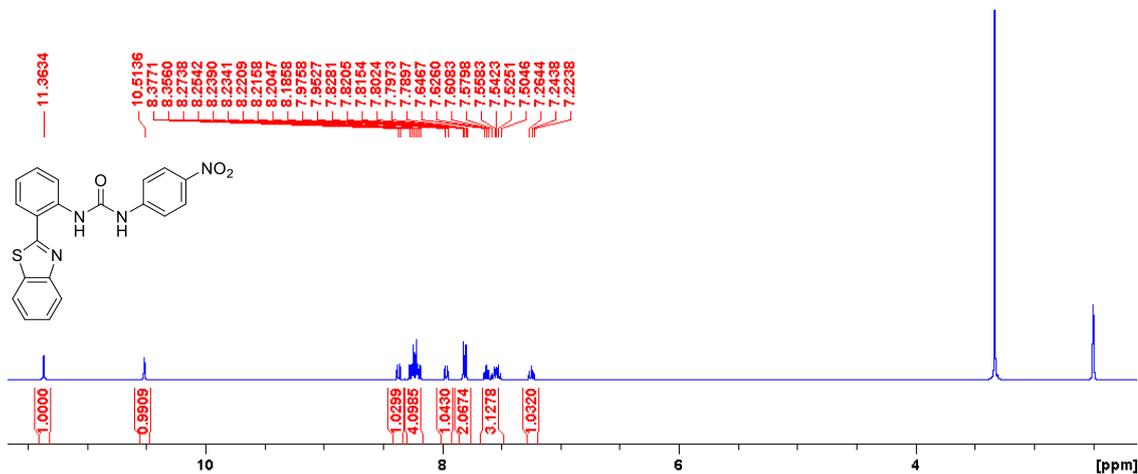
Figure 31 – Enlarged ^{1}H NMR of Compound **16** in DMSO-d_6.
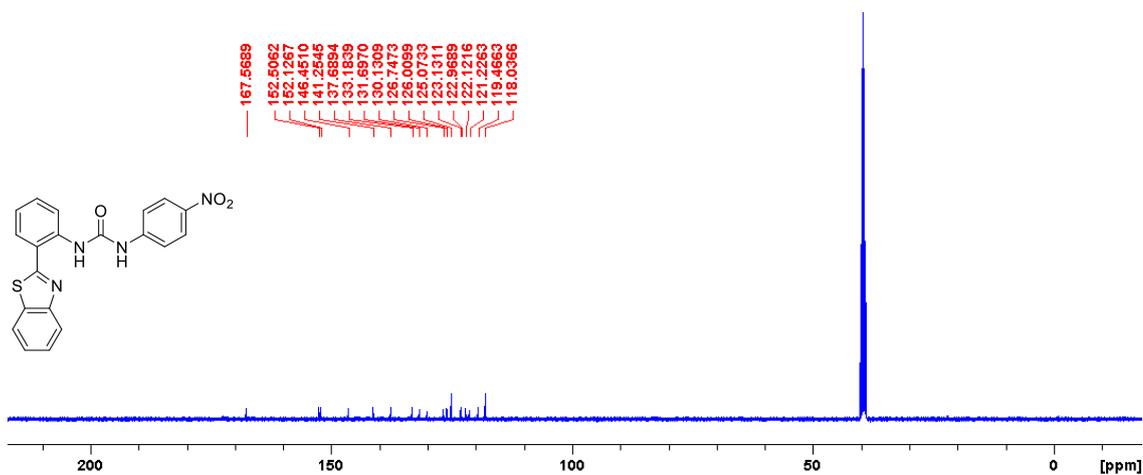
Figure 32 – ^{13}C NMR of Compound **16** in DMSO-d_6.
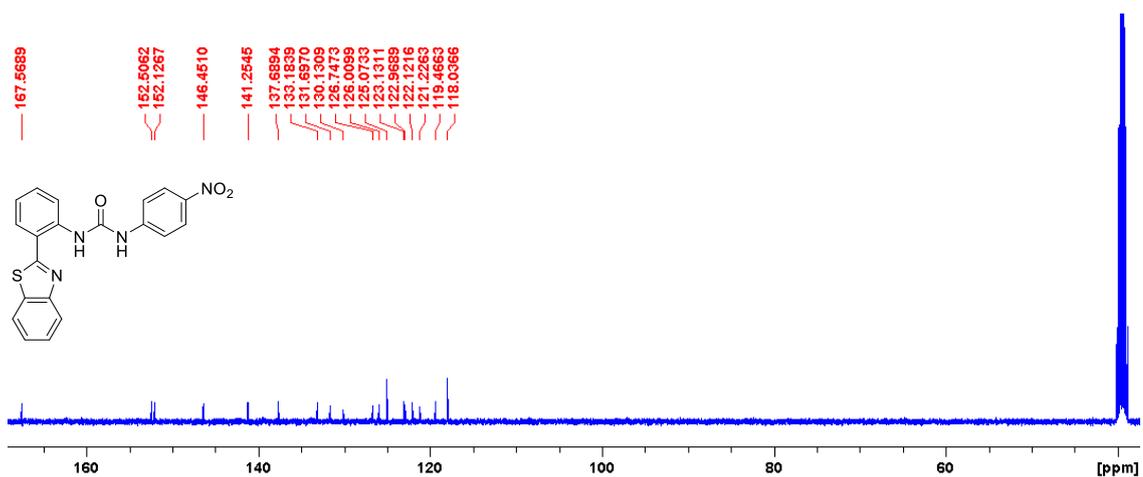
Figure 33 – Enlarged ^{13}C NMR of Compound **16** in DMSO-d_6.
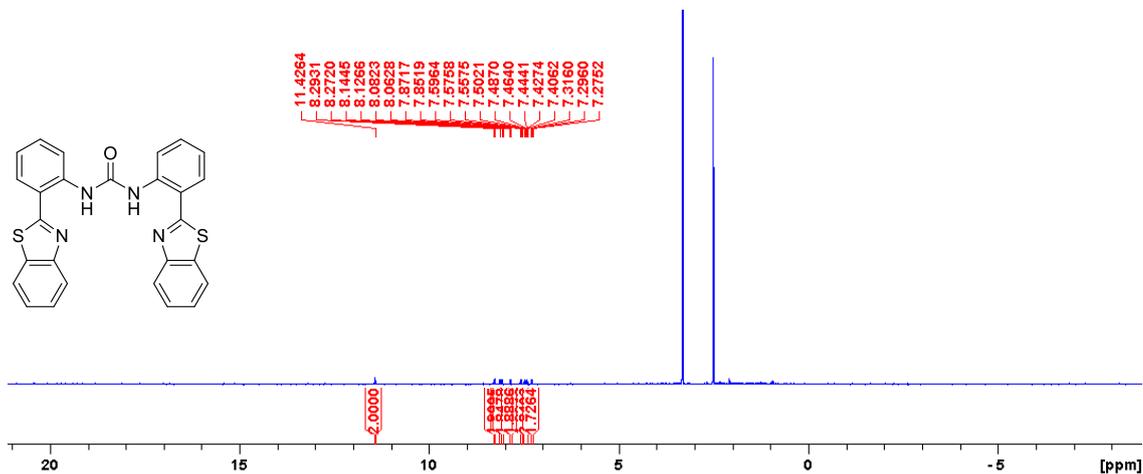
Figure 34 – ^{1}H NMR of Compound **17** in DMSO-d_6.
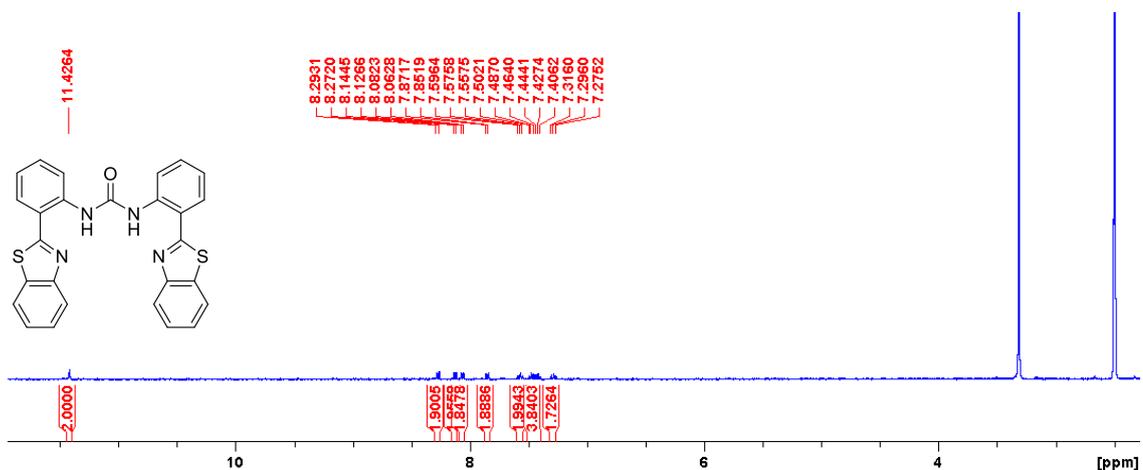
Figure 35 – Enlarged ^{1}H NMR of Compound **17** in DMSO-d_6.

8.2 ^{1}H NMR self-association studies

Table 1 – Dilution study of compound **12** in DMSO-d_6 w/ 0.5 % H_2O. Values calculated from data gathered from 2 NHs.

Compound	EK Model (M^{-1})		CoEK Model (M^{-1})		
	K_e	K_{dim}	K_e	K_{dim}	ρ
12	8.87e^{-4} (± 0.05 %)	4.43e^{-4} (± 2.63e^{-2} %)	-3.36 (± -3.27 %)	-1.68 (± -1.63 %)	0.71 (± 1.53 %)
Link for EK	http://app.supramolecular.org/bindfit/view/cf416bb3-d33d-44da-805f-406a26265789				
Link for CoEK	http://app.supramolecular.org/bindfit/view/36dfa03c-39e5-44df-8798-3b0a36fc8631				
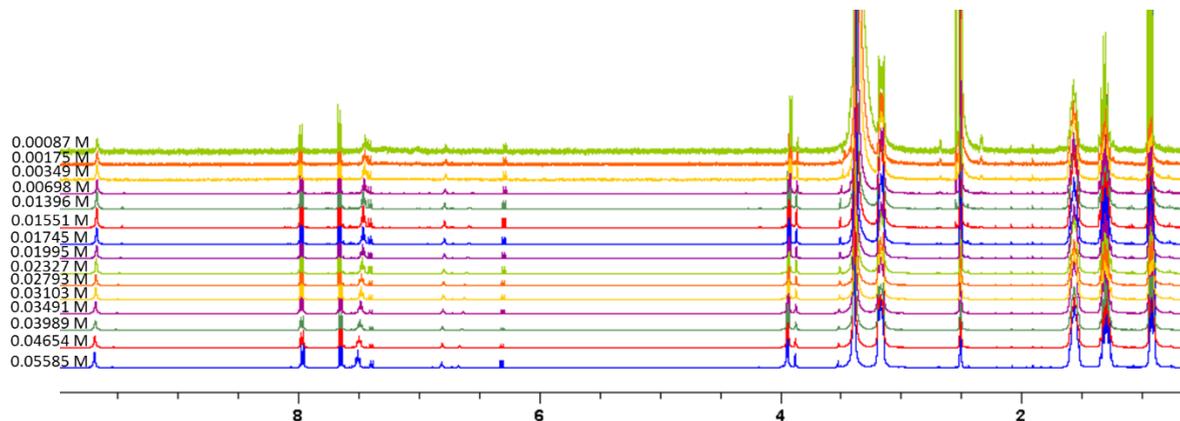
Figure 36 – ^{1}H NMR stack plot of compound **12** in a DMSO-d_6 0.5 % H$_2$O solution. Samples were prepared in series with an aliquot of the most concentrated solution undergoing serial dilution.

Table 2 – Dilution study of compound **13** in DMSO-d$_6$ w/ 0.5 % H$_2$O. Values calculated from data gathered from 2 NHs.

Compound	EK Model (M^{-1})		CoEK Model (M^{-1})		
	K$_e$	K$_{dim}$	K$_e$	K$_{dim}$	ρ
13	21.89 (± 1.56 %)	10.95 (± 0.78 %)	30.69 (± 1.77 %)	15.35 (± 0.88 %)	0.68 (± 7.27 %)
Link for EK	http://app.supramolecular.org/bindfit/view/d9c0a462-741d-4c84-b51b-1e1fc99380f9				
Link for CoEK	http://app.supramolecular.org/bindfit/view/44c7db70-8b3e-40b0-9555-9000a1b8f5c9				
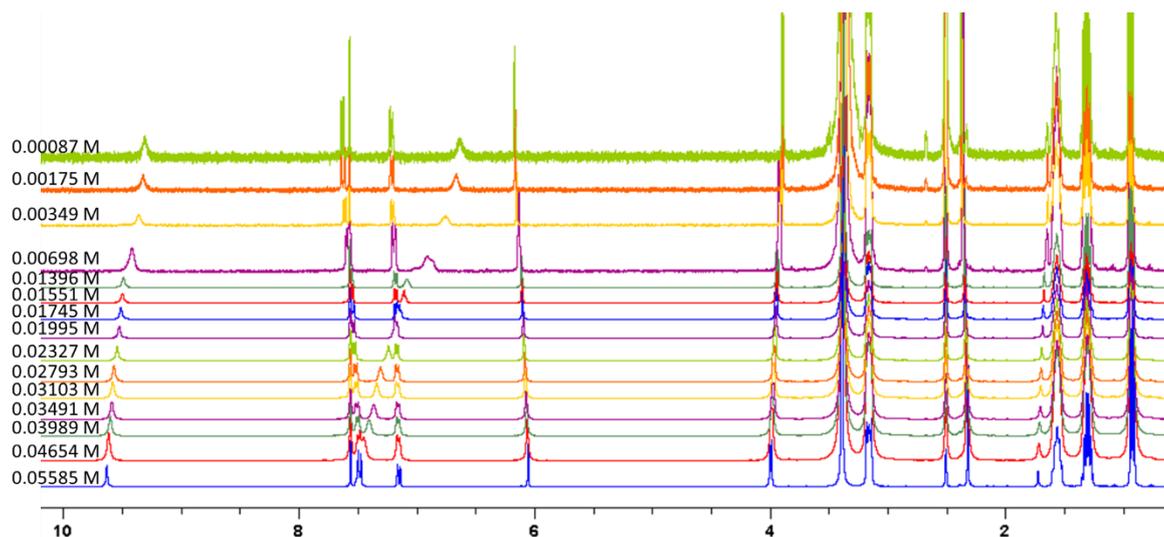
Figure 37 – ^{1}H NMR stack plot of compound **13** in a DMSO-d_6 0.5 % H$_2$O solution. Samples were prepared in series with an aliquot of the most concentrated solution undergoing serial dilution.

8.3 Fluorescent titration binding studies

Table 3 – Association constants (M^{-1}) calculated for compound **14** (host) titrated against TBA acetate (guest) in $CHCl_3$ (298 K).

Host: Guest	1: 1	1: 2		2: 1	
	K (M^{-1})	K_{11} (M^{-1})	K_{12} (M^{-1})	K_{11} (M^{-1})	K_{21} (M^{-1})
	0.015 (± 2.461 %)	-0.22 (± -32.119 %)	165182.65 (± 387.861 %)	-3.09 (± -7.463 %)	380529.91 (± 5.738 %)
Link to 1:1	http://app.supramolecular.org/bindfit/view/0ff0bee5-61b1-4303-a799-fe1b9b83a854				
Link to 1:2	http://app.supramolecular.org/bindfit/view/d111d089-264c-480c-bdf8-ddaf13ad8fb8				
Link to 2:1	http://app.supramolecular.org/bindfit/view/653d33a0-6914-44fa-a4ab-855a3a389987				

Table 4 – Association constants (M^{-1}) calculated for compound **14** (host) titrated against TBA benzoate (guest) in $CHCl_3$ (298 K).

| Host: Guest	1: 1	1: 2		2: 1	
	K (M^{-1})	K_{11} (M^{-1})	K_{12} (M^{-1})	K_{11} (M^{-1})	K_{21} (M^{-1})
	0.00547 (± 0.491 %)	1224207462269540000.00 (± 17347664665.193 %)	-136.53 (± -6.166 %)	0.06 (± 20.780 %)	343816818.1 (± 16.004 %)
Link to 1:1	http://app.supramolecular.org/bindfit/view/d9bad96b-9e12-472b-821e-be76f4ff24fd				
Link to 1:2	http://app.supramolecular.org/bindfit/view/0cb8ef81-18b5-46c8-9476-e0d598122a2f				
Link to 2:1	http://app.supramolecular.org/bindfit/view/0b7ffedf-71bc-461e-b683-7c0f36a05d37				
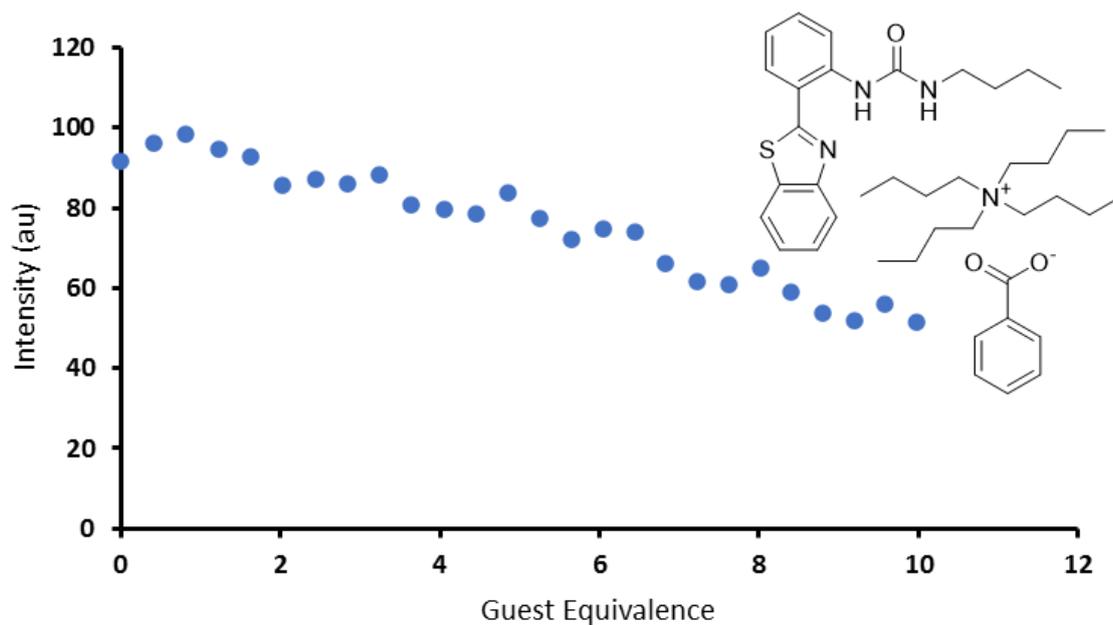
Figure 38 – A graph showing the decrease in fluorescent intensity of compound **14** (host) upon increasing concentration of TBA benzoate (guest) in CHCl$_3$ (298 K).

Table 5 – Association constants (M^{-1}) calculated for compound **14** (host) titrated against TBA chloride (guest) in CHCl$_3$ (298 K).

| Host: Guest	1: 1	1: 2		2: 1	
	K (M^{-1})	K$_{11}$ (M^{-1})	K$_{12}$ (M^{-1})	K$_{11}$ (M^{-1})	K$_{21}$ (M^{-1})
	94878.33 (± 17.630 %)	69744.14 (± 15.442 %)	32407.88 (± 38.175 %)	10834.23 (± 4.419 %)	-3949.33 (± - 1.111 %)
Link to 1:1	http://app.supramolecular.org/bindfit/view/295b503a-a41c-4df3-9d60-da6ac4d1ce23				
Link to 1:2	http://app.supramolecular.org/bindfit/view/6fc4f9d4-75a2-4d77-9550-9ebf02044c6e				
Link to 2:1	http://app.supramolecular.org/bindfit/view/de4cf5b7-9250-4f1c-adf9-9e5b1387e548				
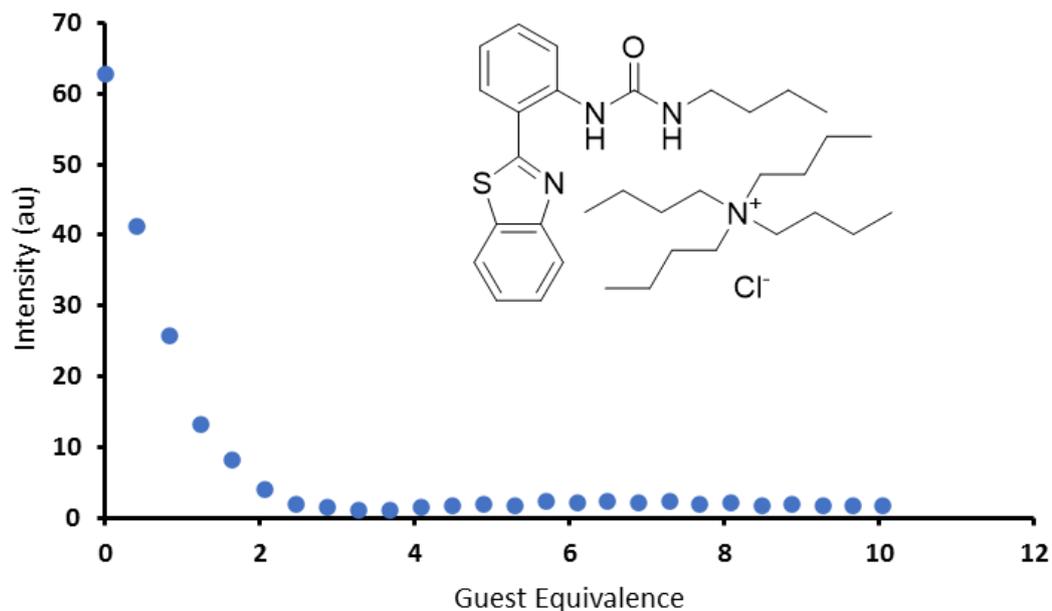
Figure 39 – A graph showing the decrease in fluorescent intensity of compound **14** (host) upon increasing concentration of TBA chloride (guest) in $CHCl_3$ (298 K).

Table 6 – Association constants (M^{-1}) calculated for compound **14** (host) titrated against TBA fluoride (guest) in $CHCl_3$ (298 K).

| Host: Guest	1: 1	1: 2		2: 1	
	K (M^{-1})	K_{11} (M^{-1})	K_{12} (M^{-1})	K_{11} (M^{-1})	K_{21} (M^{-1})
	2426.88 (± 4.660 %)	30085.63 (± 86.217 %)	4251.41 (± 11.396 %)	17073.05 (± 29.612 %)	24493.49 (± 33.039 %)
Link to 1:1	ttp://app.supramolecular.org/bindfit/view/230ce7f3-9ce4-4d74-b647-6397272900fe				
Link to 1:2	http://app.supramolecular.org/bindfit/view/c9b3595a-3e6a-4a3d-a228-6d7aa600c4af				
Link to 2:1	http://app.supramolecular.org/bindfit/view/2add63a2-157b-4880-a64b-dde13bd87023				
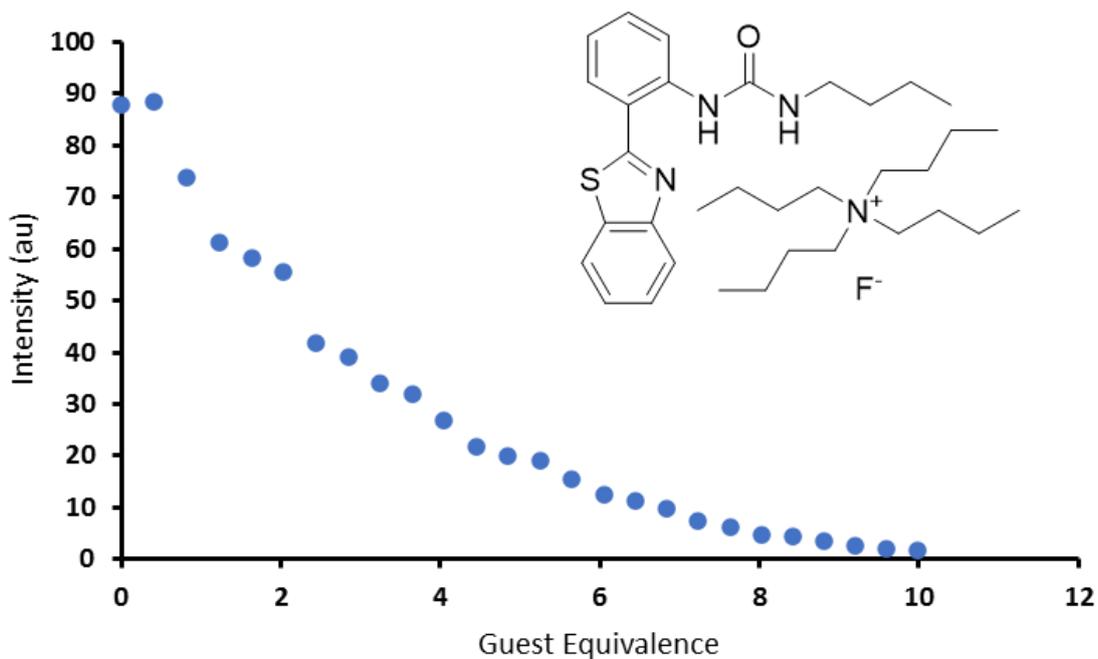
Figure 40 – A graph showing the decrease in fluorescent intensity of compound **14** (host) upon increasing concentration of TBA fluoride (guest) in CHCl$_3$ (298 K).

Table 7 – Association constants (M^{-1}) calculated for compound **14** (host) titrated against TBA hydroxide (guest) in CHCl$_3$ (298 K).

Host: Guest	1: 1	1: 2		2: 1	
	K (M^{-1})	K$_{11}$ (M^{-1})	K$_{12}$ (M^{-1})	K$_{11}$ (M^{-1})	K$_{21}$ (M^{-1})
	1544.66 (± 7.763 %)	-2047.80 (± -22.153 %)	-9844.69 (± -46.383 %)	-2006.06 (± -6.043 %)	-1441.43 (± - 2.60 %)
Link to 1:1	http://app.supramolecular.org/bindfit/view/02a3fea4-9a32-4cc7-a402-1d8ba55dc90e				
Link to 1:2	http://app.supramolecular.org/bindfit/view/aaf0a243-a394-4d52-b87e-4d60b73a1fdc				
Link to 2:1	http://app.supramolecular.org/bindfit/view/456e2438-5b62-43dc-a6f0-b01968305d8f				
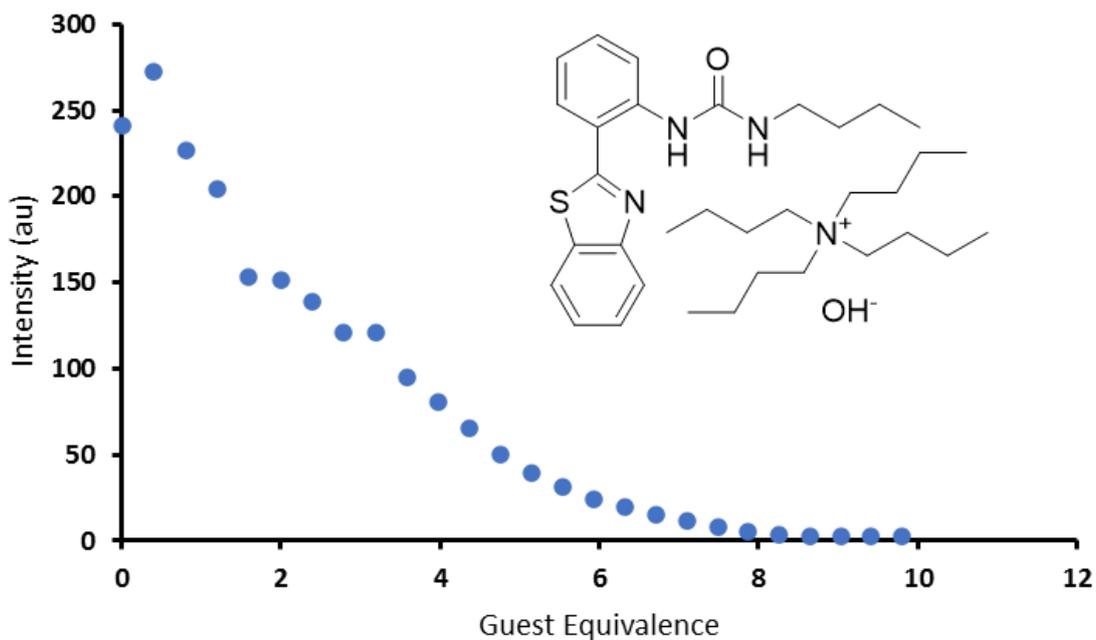
Figure 41 – A graph showing the decrease in fluorescent intensity of compound **14** (host) upon increasing concentration of TBA hydroxide (guest) in CHCl$_3$ (298 K).

Table 8 – Association constants (M^{-1}) calculated for compound **14** (host) titrated against TBA hydrogen sulphate (guest) in CHCl$_3$ (298 K).

Host: Guest	1: 1	1: 2		2: 1	
	K (M^{-1})	K$_{11}$ (M^{-1})	K$_{12}$ (M^{-1})	K$_{11}$ (M^{-1})	K$_{21}$ (M^{-1})
	15042.74 (± 10.525 %)	3266.93 (± 3.252 %)	15262.76 (± 8.485 %)	3273.53 (± 3.139 %)	-2782.41 (± - 0.887 %)
Link to 1:1	http://app.supramolecular.org/bindfit/view/5f48e23d-fed7-45fb-95c5-48f20c9296b2				
Link to 1:2	http://app.supramolecular.org/bindfit/view/22a61941-74ab-4e62-b185-a350b2aabd36				
Link to 2:1	http://app.supramolecular.org/bindfit/view/3b9bbe8c-a0bf-4110-8777-b8ddec02e782				

Table 9 – Association constants (M^{-1}) calculated for compound **14** (host) titrated against TBA phosphate monobasic (guest) in $CHCl_3$ (298 K).

| Host: Guest	1: 1	1: 2		2: 1	
	K (M^{-1})	K_{11} (M^{-1})	K_{12} (M^{-1})	K_{11} (M^{-1})	K_{21} (M^{-1})
	3087.76 (± 5.541 %)	109404.61 (± 232.056 %)	6095.32 (± 9.326 %)	12573.4 (± 8.910 %)	730.79 (± 11.081 %)
Link to 1:1	http://app.supramolecular.org/bindfit/view/239ea945-50cd-4472-9497-8f961ba68f26				
Link to 1:2	http://app.supramolecular.org/bindfit/view/d31b3c04-a7e8-4cfb-bbfd-b97c636185d1				
Link to 2:1	http://app.supramolecular.org/bindfit/view/6b2183d6-d9b1-4c86-9de5-ebaeff5314b9				
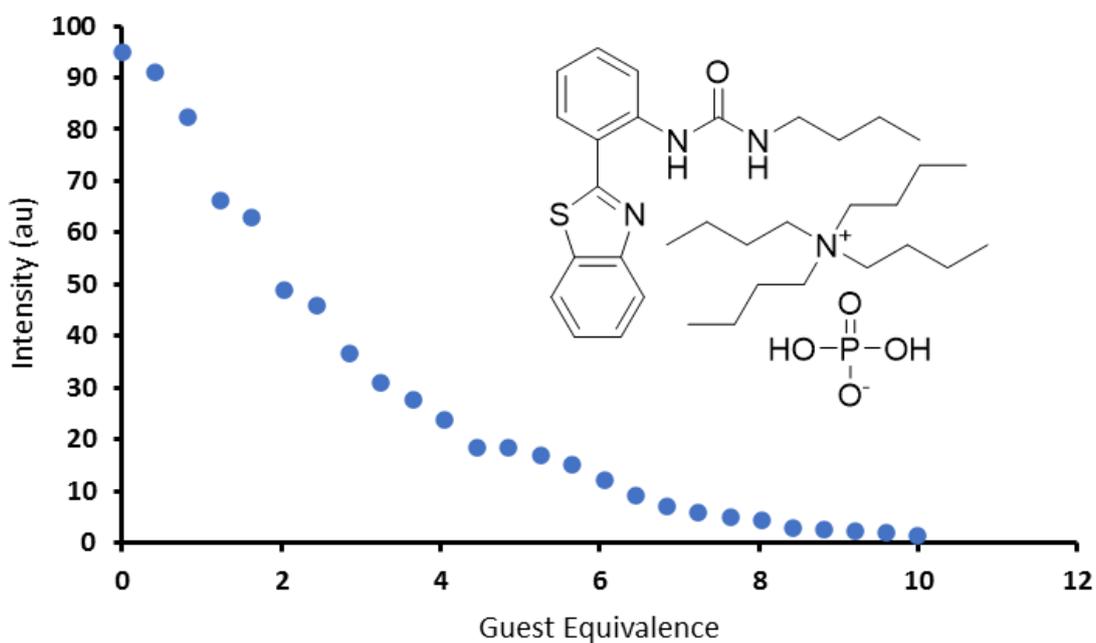
Figure 42 – A graph showing the decrease in fluorescent intensity of compound **14** (host) upon increasing concentration of TBA phosphate monobasic (guest) in $CHCl_3$ (298 K).

Table 10 – Association constants (M^{-1}) calculated for compound **14** (host) titrated against TBA sulphate (guest) in CHCl$_3$ (298 K).

| Host: Guest	1: 1	1: 2		2: 1	
	K (M^{-1})	K_{11} (M^{-1})	K_{12} (M^{-1})	K_{11} (M^{-1})	K_{21} (M^{-1})
	0.00136 (± 0.012 %)	353271643107799000.00 (±12090987986.5007 %)	-2.65 (± -3.262 %)	221.53 (± 14.928 %)	46701.17 (± 12.172 %)
Link to 1:1	http://app.supramolecular.org/bindfit/view/5ed6c22c-a540-4248-bd5e-3909099dfcef				
Link to 1:2	http://app.supramolecular.org/bindfit/view/73d3e674-d9be-490f-8c86-402911d8f5e7				
Link to 2:1	http://app.supramolecular.org/bindfit/view/7cbf5b7d-6635-4227-bc40-62f811c1d15c				
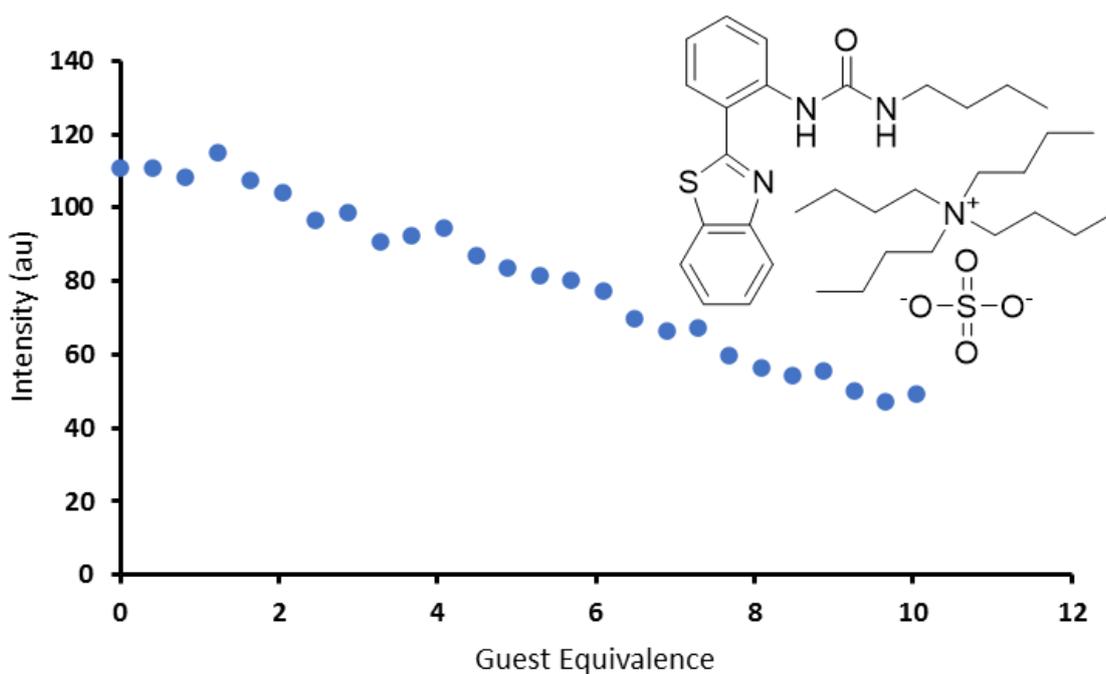
Figure 43 – A graph showing the decrease in fluorescent intensity of compound **14** (host) upon increasing concentration of TBA sulphate (guest) in CHCl$_3$ (298 K).

Table 11 – Association constants (M^{-1}) calculated for compound **15** (host) titrated against TBA acetate (guest) in $CHCl_3$ (298 K).

Host: Guest	1: 1	1: 2		2: 1	
	K (M^{-1})	K_{11} (M^{-1})	K_{12} (M^{-1})	K_{11} (M^{-1})	K_{21} (M^{-1})
	895.18 (± 39.363 %)	-1387.74 (± -6.653 %)	-364.15 (± -7.716 %)	3433.59 (± 92.901 %)	-5122.55 (± - -0.033 %)
Link to 1:1	http://app.supramolecular.org/bindfit/view/39e9780f-c5b6-4533-869d-eb7039c6e85e				
Link to 1:2	http://app.supramolecular.org/bindfit/view/9e8c6012-e30f-498f-a98f-40df615633d7				
Link to 2:1	http://app.supramolecular.org/bindfit/view/933660c3-082a-4d53-8cdf-908a640807f1				
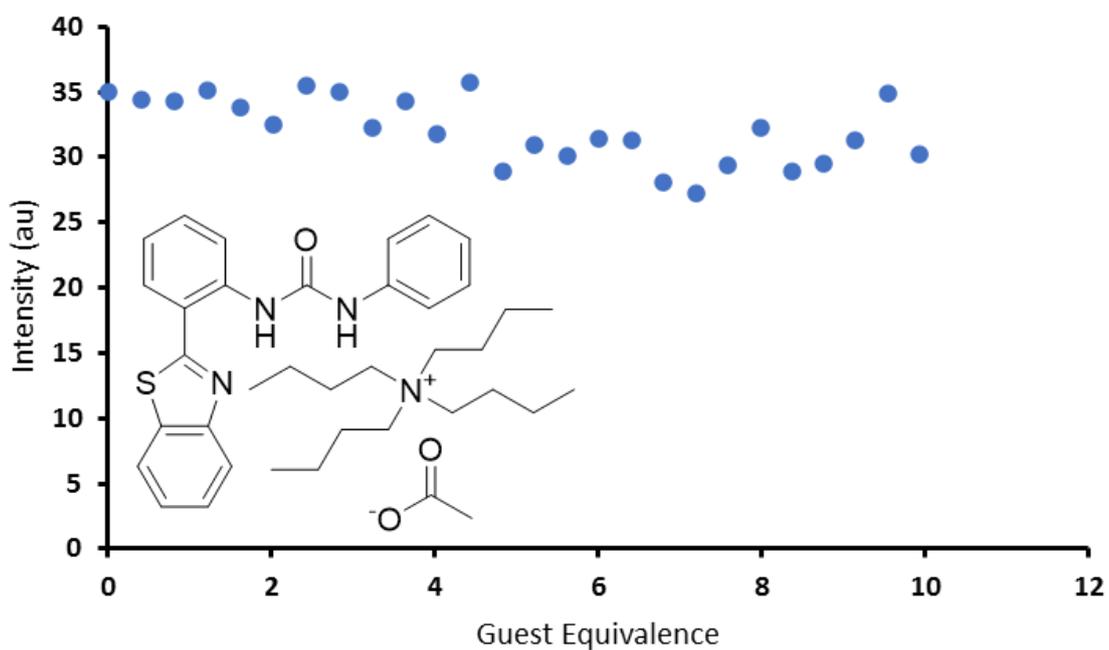
Figure 44 – A graph showing the decrease in fluorescent intensity of compound **15** (host) upon increasing concentration of TBA acetate (guest) in $CHCl_3$ (298 K).

Table 12 – Association constants (M^{-1}) calculated for compound **15** (host) titrated against TBA benzoate (guest) in CHCl$_3$ (298 K).

| Host: Guest	1: 1	1: 2		2: 1	
	K (M^{-1})	K$_{11}$ (M^{-1})	K$_{12}$ (M^{-1})	K$_{11}$ (M^{-1})	K$_{21}$ (M^{-1})
	352.09 (± 9.268 %)	-1064.49 (± -9.025 %)	-343.15 (± -10.329 %)	1441.89 (± 0.179 %)	-4959.04 (± -0.179 %)
Link to 1:1	http://app.supramolecular.org/bindfit/view/09c370ba-fd8f-4057-b053-4dbd886aec8a				
Link to 1:2	http://app.supramolecular.org/bindfit/view/15508718-cdf4-4dc4-8d54-98442a1e2105				
Link to 2:1	http://app.supramolecular.org/bindfit/view/5a6ff1b0-9eca-403c-ac76-37c1147dca82				
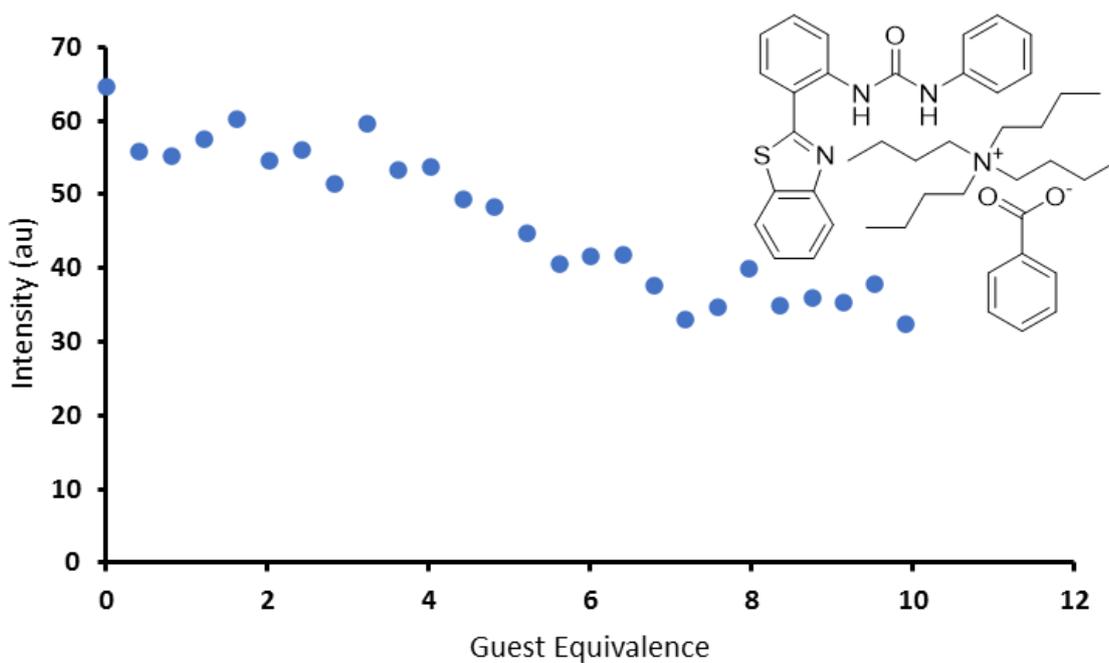
Figure 45 – A graph showing the decrease in fluorescent intensity of compound **15** (host) upon increasing concentration of TBA benzoate (guest) in CHCl$_3$ (298 K).

Table 13 – Association constants (M^{-1}) calculated for compound **15** (host) titrated against TBA chloride (guest) in $CHCl_3$ (298 K).

| Host: Guest	1: 1	1: 2		2: 1	
	K (M^{-1})	K_{11} (M^{-1})	K_{12} (M^{-1})	K_{11} (M^{-1})	K_{21} (M^{-1})
	95863.48 (± 15.389 %)	72237.79 (± 14.958 %)	3367.64 (± 52.707 %)	11578.78 (± 8.757 %)	-1905.14 (± -2.968 %)
Link to 1:1	http://app.supramolecular.org/bindfit/view/e4c63fc8-3bed-4f50-8253-3550e50c133d				
Link to 1:2	http://app.supramolecular.org/bindfit/view/ddb3f341-d9df-4726-b5aa-69bc18578411				
Link to 2:1	http://app.supramolecular.org/bindfit/view/17ef8189-1e8b-48a7-bfe6-43a2682ea8ac				
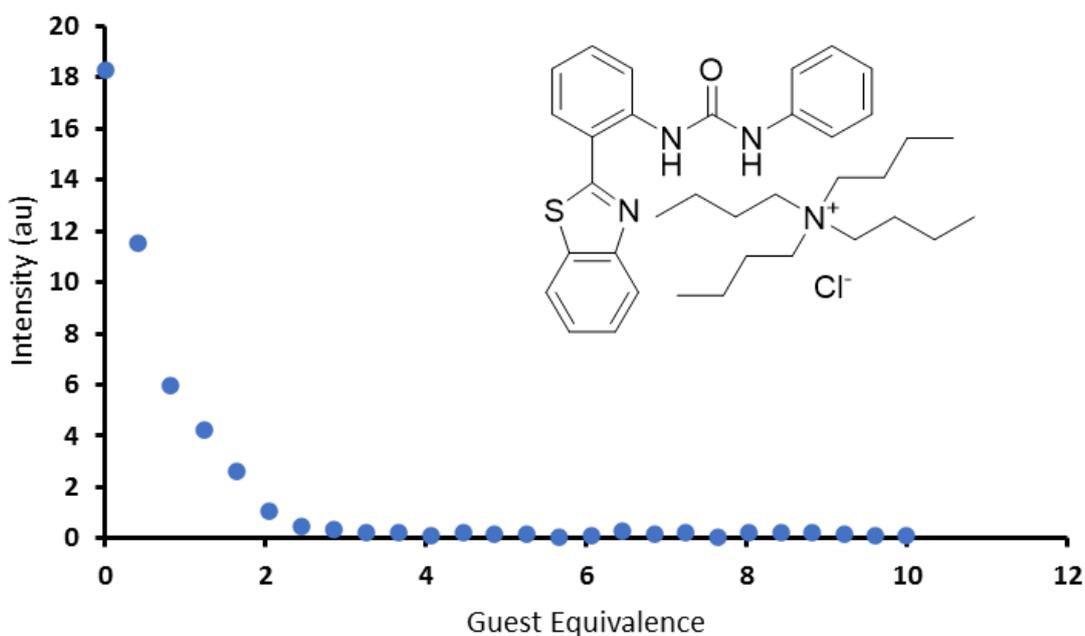
Figure 46 – A graph showing the decrease in fluorescent intensity of compound **15** (host) upon increasing concentration of TBA chloride (guest) in $CHCl_3$ (298 K).

Table 14 – Association constants (M^{-1}) calculated for compound **15** (host) titrated against TBA fluoride (guest) in CHCl$_3$ (298 K).

Host: Guest	1: 1	1: 2		2: 1	
	K (M^{-1})	K$_{11}$ (M^{-1})	K$_{12}$ (M^{-1})	K$_{11}$ (M^{-1})	K$_{21}$ (M^{-1})
	9855.59 (± 6.593 %)	5193.55 (± 4.252 %)	-137.62 (± -7.028 %)	3.45 (± 3.868 %)	2379388.45 (± 0.737 %)
Link to 1:1	http://app.supramolecular.org/bindfit/view/e99e7a6d-cc0d-4366-919b-5525605ebb0a				
Link to 1:2	http://app.supramolecular.org/bindfit/view/706974a4-b635-47b3-bbd5-8fb54da68bc8				
Link to 2:1	http://app.supramolecular.org/bindfit/view/c9bb2c54-65bb-442e-ae5a-2597de470435				

Table 15 – Association constants (M^{-1}) calculated for compound **15** (host) titrated against TBA hydroxide (guest) in CHCl$_3$ (298 K).

Host: Guest	1: 1	1: 2		2: 1	
	K (M^{-1})	K$_{11}$ (M^{-1})	K$_{12}$ (M^{-1})	K$_{11}$ (M^{-1})	K$_{21}$ (M^{-1})
	2053.74 (± 5.843 %)	875.30 (± 7.571 %)	-852.18 (± -13.511 %)	0.0274 (± 15.011 %)	60896310.08 (± 2.748 %)
Link to 1:1	http://app.supramolecular.org/bindfit/view/61f269b7-1f88-41c9-8bc4-cddf0084c81a				
Link to 1:2	http://app.supramolecular.org/bindfit/view/d02af165-397e-44a9-9c27-f05c6489695c				
Link to 2:1	http://app.supramolecular.org/bindfit/view/57eae348-01f0-4c61-894a-58586aaf1fa4				

Table 16 – Association constants (M^{-1}) calculated for compound **15** (host) titrated against TBA hydrogen sulphate (guest) in CHCl$_3$ (298 K).

| Host: Guest	1: 1	1: 2		2: 1	
	K (M^{-1})	K$_{11}$ (M^{-1})	K$_{12}$ (M^{-1})	K$_{11}$ (M^{-1})	K$_{21}$ (M^{-1})
	5596.21 (± 4.944 %)	3896.67 (± 5.677 %)	1153.24 (± 39.268 %)	956.67 (± 7.994 %)	2302.49 (± 2.739 %)
Link to 1:1	http://app.supramolecular.org/bindfit/view/99a37396-cbcd-42ac-8e6a-3fb368420715				
Link to 1:2	http://app.supramolecular.org/bindfit/view/080638dc-6821-4f9c-866b-680b63de94db				
Link to 2:1	http://app.supramolecular.org/bindfit/view/fa28dd51-7c0c-462d-9f19-e3a4c1c5e406				
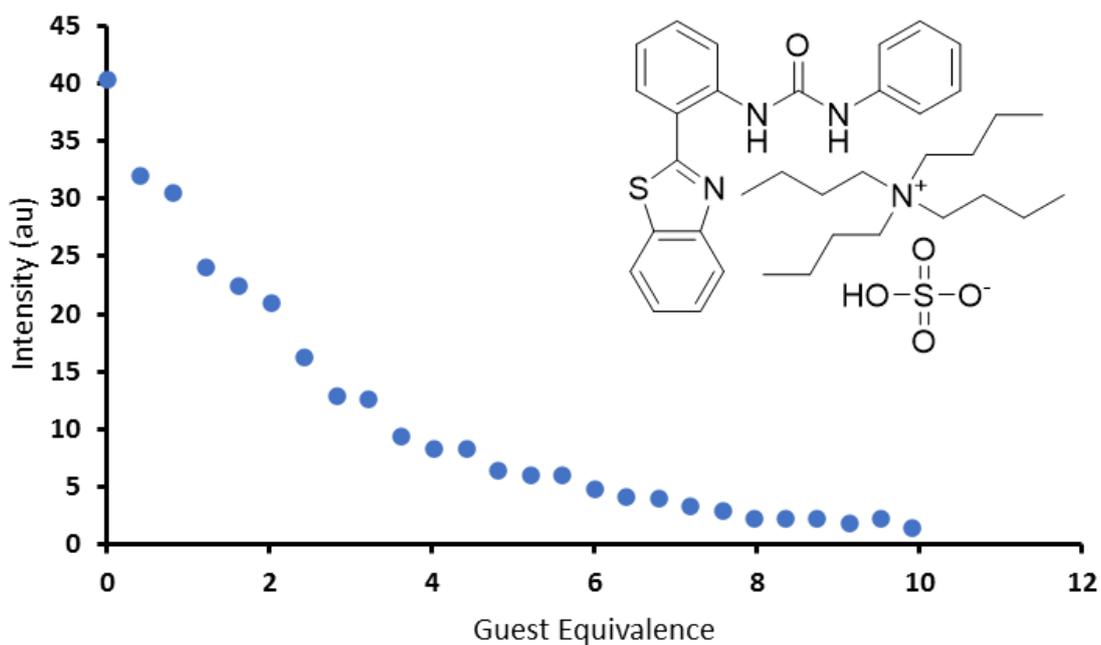
Figure 47 – A graph showing the decrease in fluorescent intensity of compound **15** (host) upon increasing concentration of TBA hydrogen sulphate (guest) in CHCl$_3$ (298 K).

Table 17 – Association constants (M^{-1}) calculated for compound **15** (host) titrated against TBA phosphate monobasic (guest) in CHCl$_3$ (298 K).

| Host: Guest	1: 1	1: 2		2: 1	
	K (M^{-1})	K_{11} (M^{-1})	K_{12} (M^{-1})	K_{11} (M^{-1})	K_{21} (M^{-1})
	428.45 (± 3.975 %)	100618420835083000.00 (± 15366953130.495 %)	558.31 (± 5218 %)	371.36 (± 71.234 %)	114437.06 (± 83.028 %)
Link to 1:1	http://app.supramolecular.org/bindfit/view/edeee61a-5754-4171-82b5-bbd1e5a489e5				
Link to 1:2	http://app.supramolecular.org/bindfit/view/c3ba235c-f169-4b21-96b9-7eb4ffb0ebf7				
Link to 2:1	http://app.supramolecular.org/bindfit/view/df247f51-a3fa-455e-8dcc-9822805c922e				
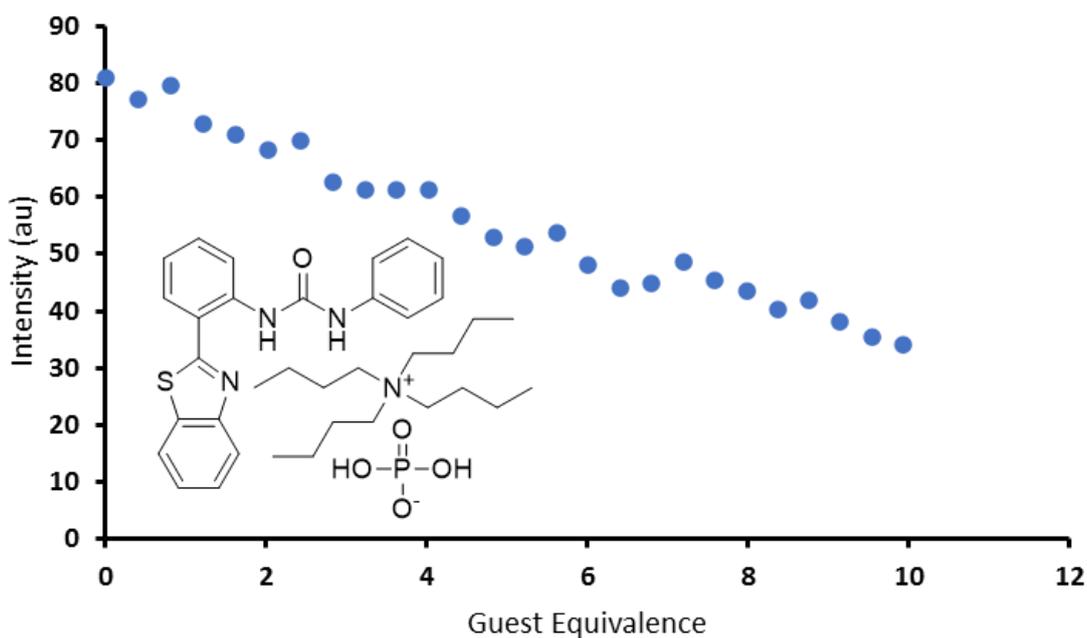
Figure 48 – A graph showing the decrease in fluorescent intensity of compound **15** (host) upon increasing concentration of TBA phosphate monobasic (guest) in CHCl$_3$ (298 K).

Table 18 – Association constants (M^{-1}) calculated for compound **15** (host) titrated against TBA sulphate (guest) in $CHCl_3$ (298 K).

Host: Guest	1: 1	1: 2		2: 1	
	K (M^{-1})	K_{11} (M^{-1})	K_{12} (M^{-1})	K_{11} (M^{-1})	K_{21} (M^{-1})
	1874.16 (± 20.378 %)	2.29869E+18 (± 22316683675 %)	-267.44 (± -13.135 %)	0.0105 (± 243.07 %)	34376544660 (± 304.078 %)
Link to 1:1	http://app.supramolecular.org/bindfit/view/fee8b310-a9a6-4c81-a03b-0245bf77f31c				
Link to 1:2	http://app.supramolecular.org/bindfit/view/9d910c53-26ce-459f-84ab-c67e354a2445				
Link to 2:1	http://app.supramolecular.org/bindfit/view/26ac0b46-cc4f-414a-ac63-462495d24b0d				
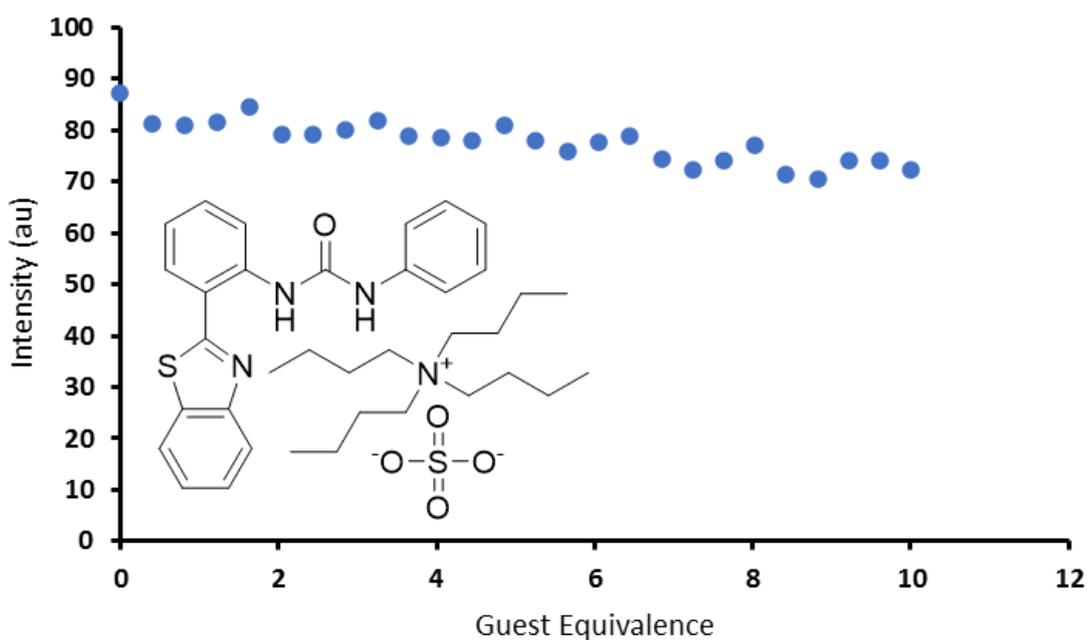
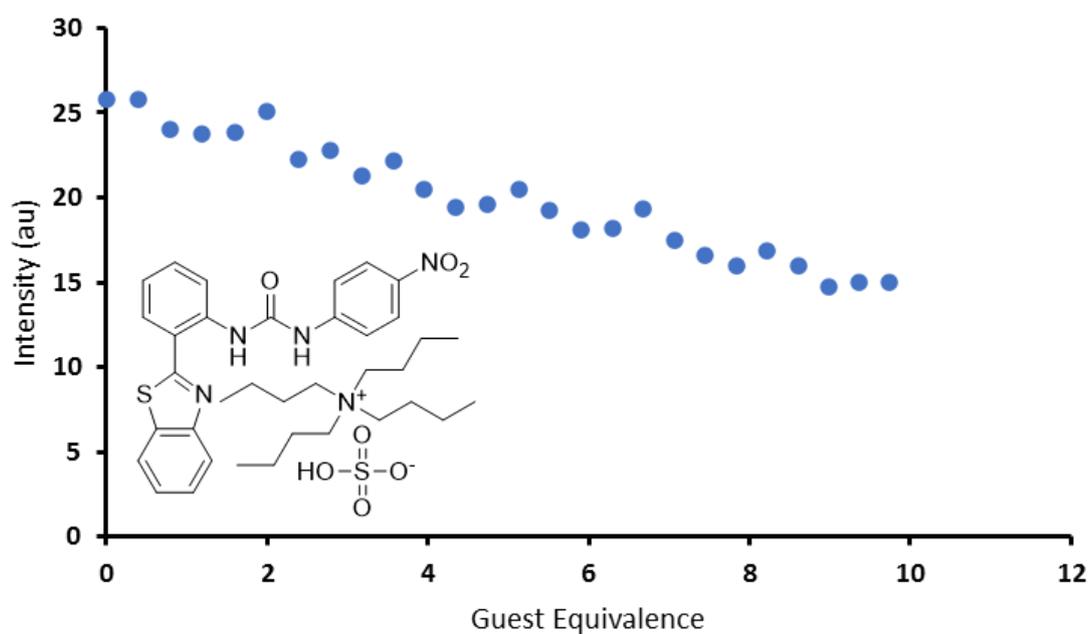Figure 49 – A graph showing the decrease in fluorescent intensity of compound **15** (host) upon increasing concentration of TBA sulphate (guest) in $CHCl_3$ (298 K).

Table 19 – Association constants (M^{-1}) calculated for compound **16** (host) titrated against TBA acetate (guest) in CHCl$_3$ (298 K).

| Host: Guest	1: 1	1: 2		2: 1	
	K (M^{-1})	K$_{11}$ (M^{-1})	K$_{12}$ (M^{-1})	K$_{11}$ (M^{-1})	K$_{21}$ (M^{-1})
	8263.55 (± 13.618 %)	0.0392 (± 5.784 %)	186491484.50 (± 7.941 %)	2828.48 (± 5.509 %)	-4409.69 (± -1.150 %)
Link to 1:1	http://app.supramolecular.org/bindfit/view/85c94164-0704-480f-aa15-047052b8576f				
Link to 1:2	http://app.supramolecular.org/bindfit/view/fb8487ea-5c6f-4929-b553-eb72d37cb2a6				
Link to 2:1	http://app.supramolecular.org/bindfit/view/d4e24062-8155-4066-8f55-6a8312ffa3c4				
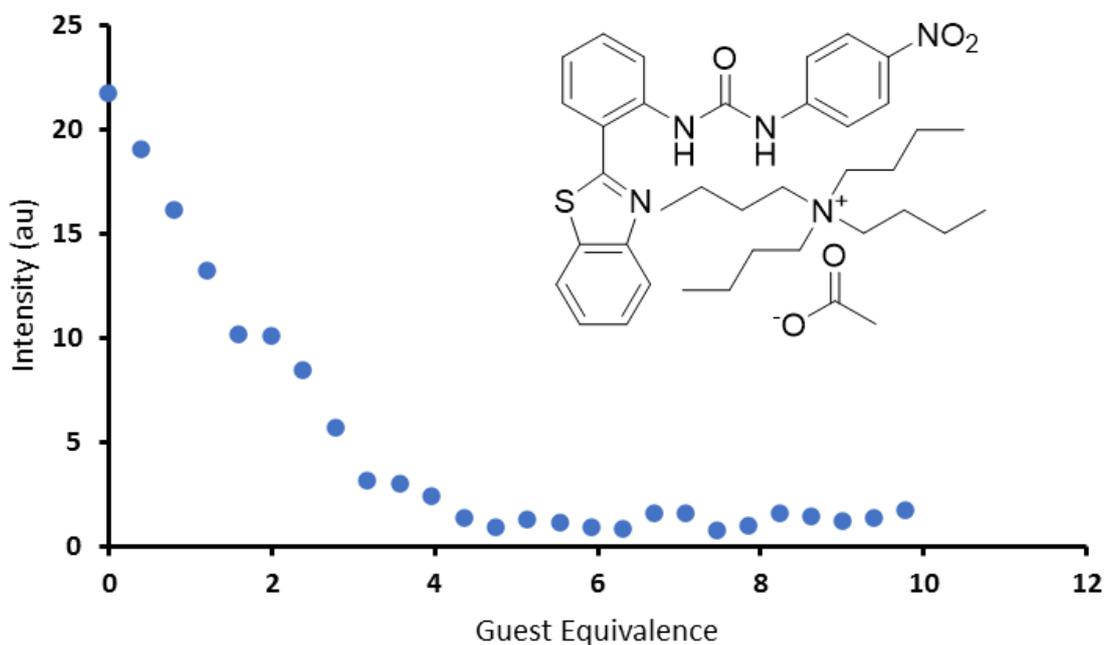
Figure 50 – A graph showing the decrease in fluorescent intensity of compound **16** (host) upon increasing concentration of TBA acetate (guest) in CHCl$_3$ (298 K).

Table 20 – Association constants (M^{-1}) calculated for compound **16** (host) titrated against TBA benzoate(guest) in $CHCl_3$ (298 K).

Host: Guest	1: 1	1: 2		2: 1	
	K (M^{-1})	K_{11} (M^{-1})	K_{12} (M^{-1})	K_{11} (M^{-1})	K_{21} (M^{-1})
	1166.91 (± 2.369 %)	319.91 (± 3.241 %)	-1600.02 (± -5.623 %)	0.19 (± 9.040 %)	4878632.27 (± 1.644 %)
Link to 1:1	http://app.supramolecular.org/bindfit/view/e14a2579-b906-4c1e-935d-8a23c8de6570				
Link to 1:2	http://app.supramolecular.org/bindfit/view/4ced9d09-8fa9-44d9-8507-644651caa597				
Link to 2:1	http://app.supramolecular.org/bindfit/view/34d99ff5-0447-4fd6-a00e-1ad69c9c51a7				

Table 21 – Association constants (M^{-1}) calculated for compound **16** (host) titrated against TBA chloride (guest) in $CHCl_3$ (298 K).

| Host: Guest	1: 1	1: 2		2: 1	
	K (M^{-1})	K_{11} (M^{-1})	K_{12} (M^{-1})	K_{11} (M^{-1})	K_{21} (M^{-1})
	73.2 (± 4.105 %)	312214073305794000.00 (± 9916484252.04800 %)	-88.5 (± -4.813 %)	0.0192 (± 171.81 %)	31924218.40 (± 475.903 %)
Link to 1:1	http://app.supramolecular.org/bindfit/view/a0437f5c-6b49-4aa5-b6df-ffc6b3a4da04				
Link to 1:2	http://app.supramolecular.org/bindfit/view/4dfa02bf-e267-45c8-bb10-ccecc21ad621				
Link to 2:1	http://app.supramolecular.org/bindfit/view/83b10ced-a326-4714-95db-4f0894d52b6b				
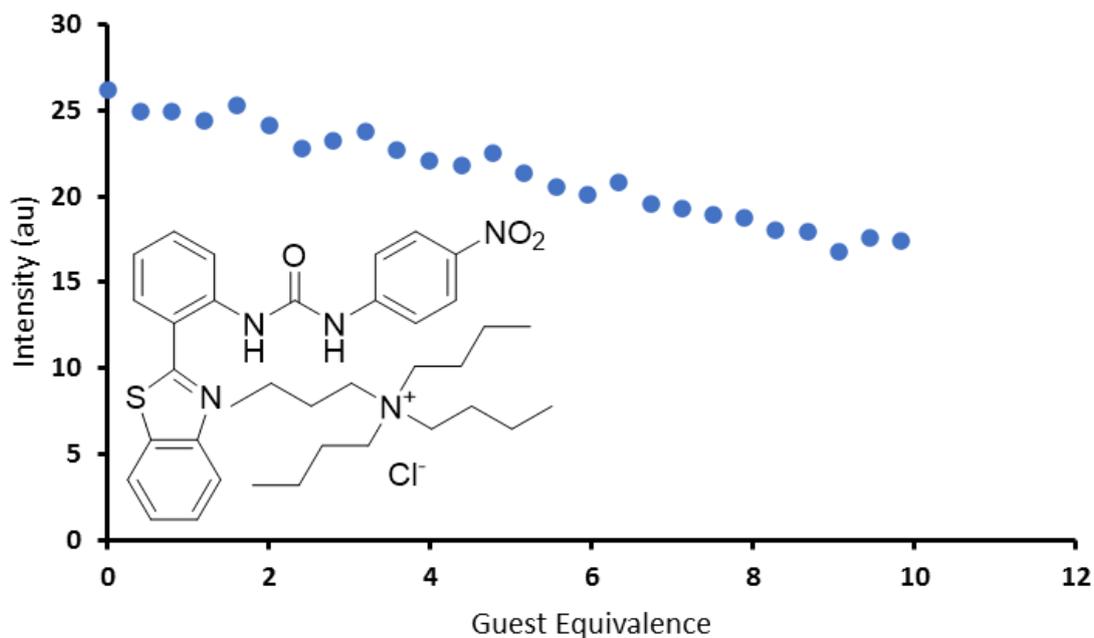
Figure 51 – A graph showing the decrease in fluorescent intensity of compound **16** (host) upon increasing concentration of TBA chloride (guest) in CHCl$_3$ (298 K).

Table 22 – Association constants (M^{-1}) calculated for compound **16** (host) titrated against TBA fluoride (guest) in CHCl$_3$ (298 K).

| Host: Guest	1: 1	1: 2		2: 1	
	K (M^{-1})	K$_{11}$ (M^{-1})	K$_{12}$ (M^{-1})	K$_{11}$ (M^{-1})	K$_{21}$ (M^{-1})
	11597.53 (± 21.347 %)	0.00685 (± 9.920 %)	2024981593 (± 13.436 %)	3747.04 (± 3.395 %)	-4832.79 (± -0.411 %)
Link to 1:1	http://app.supramolecular.org/bindfit/view/1feed665-0066-48f3-8423-d134f9bf9f8e				
Link to 1:2	http://app.supramolecular.org/bindfit/view/9be8b56d-f111-4ef0-9fd0-d41bf2ec82e3				
Link to 2:1	http://app.supramolecular.org/bindfit/view/fd71acf7-d582-4c6a-9ae1-5a6fafa22a80				
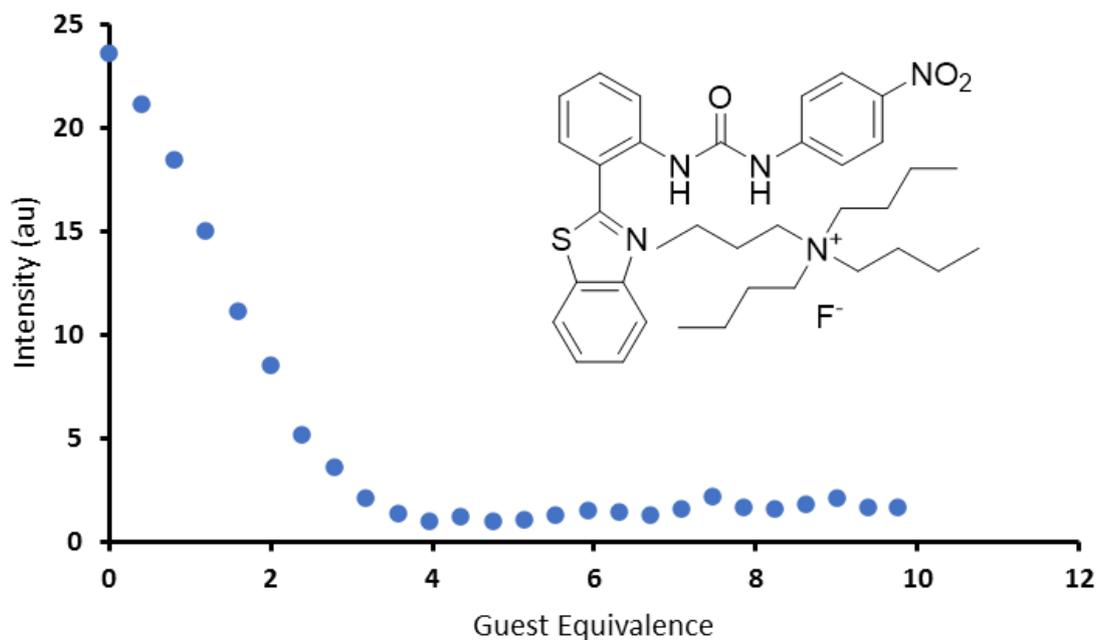
Figure 52 – A graph showing the decrease in fluorescent intensity of compound **16** (host) upon increasing concentration of TBA fluoride (guest) in $CHCl_3$ (298 K).
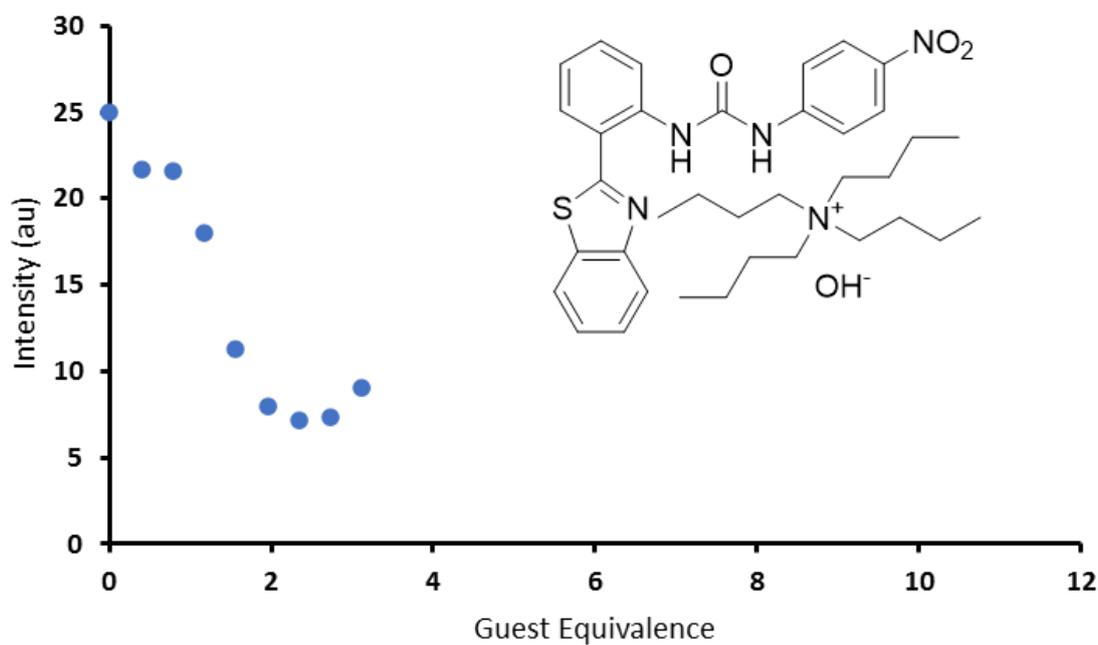
Figure 53 – A graph showing the decrease in fluorescent intensity of compound **16** (host) upon increasing concentration of TBA hydroxide (guest) in $CHCl_3$ (298 K). Partial titration due to experimental limitations.

Table 23 – Association constants (M^{-1}) calculated for compound **16** (host) titrated against TBA hydrogen sulphate (guest) in CHCl$_3$ (298 K).

| Host: Guest	1: 1	1: 2		2: 1	
	K (M^{-1})	K$_{11}$ (M^{-1})	K$_{12}$ (M^{-1})	K$_{11}$ (M^{-1})	K$_{21}$ (M^{-1})
	136.03 (± 4.901 %)	7656.39 (± 8.648 %)	237.18 (± 18.737 %)	471.54 (± 56.224 %)	4683.38 (± 70.713 %)
Link to 1:1	http://app.supramolecular.org/bindfit/view/97d2d9e8-22b3-40cd-aa44-816386d11810				
Link to 1:2	http://app.supramolecular.org/bindfit/view/9c289897-bd45-4649-ba46-cdf8d0c642f2				
Link to 2:1	http://app.supramolecular.org/bindfit/view/f30f0b2b-1079-42cb-8f39-9becfd3db084				

Figure 54 – A graph showing the decrease in fluorescent intensity of compound **16** (host) upon increasing concentration of TBA hydrogen sulphate (guest) in CHCl$_3$ (298 K).

Table 24 – Association constants (M^{-1}) calculated for compound **16** (host) titrated against TBA phosphate monobasic (guest) in CHCl₃ (298 K).

Host: Guest	1: 1	1: 2		2: 1	
	K (M^{-1})	K_{11} (M^{-1})	K_{12} (M^{-1})	K_{11} (M^{-1})	K_{21} (M^{-1})
	753.60 (± 4.565 %)	-168.63 (± -1.192 %)	1468.71 (± 1.192 %)	2027.66 (± 21.941 %)	-805.52 (± -33.181 %)
Link to 1:1	http://app.supramolecular.org/bindfit/view/2e6f6b7f-8c83-451e-85fc-d5e92121e86f				
Link to 1:2	http://app.supramolecular.org/bindfit/view/6291d893-1c7b-4ea8-9c2b-0782db59a549				
Link to 2:1	http://app.supramolecular.org/bindfit/view/113da09c-0c97-4597-a1b9-532b81f0c352				
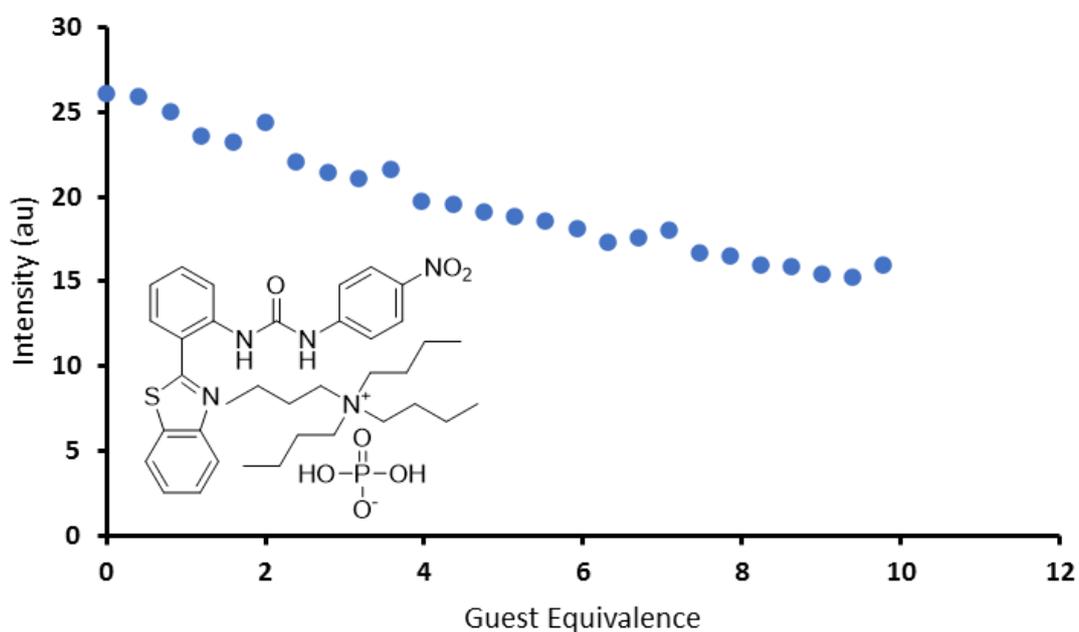
Figure 55 – A graph showing the decrease in fluorescent intensity of compound **16** (host) upon increasing concentration of TBA phosphate monobasic (guest) in CHCl₃ (298 K).

Table 25 – Association constants (M^{-1}) calculated for compound **16** (host) titrated against TBA sulphate (guest) in CHCl$_3$ (298 K).

| Host: Guest	1: 1	1: 2		2: 1	
	K (M^{-1})	K_{11} (M^{-1})	K_{12} (M^{-1})	K_{11} (M^{-1})	K_{21} (M^{-1})
	0.0109 (± 1.657 %)	0.09 (± 89.047 %)	773685.42 (± 142.675 %)	2280.28 (± 3.164 %)	-4876 (± -0.00004 %)
Link to 1:1	http://app.supramolecular.org/bindfit/view/8b7f350d-815f-4624-b2c0-edeabe99244e				
Link to 1:2	http://app.supramolecular.org/bindfit/view/82bb473f-1c79-4bbe-82f6-60a8659356d4				
Link to 2:1	http://app.supramolecular.org/bindfit/view/7e0b76fe-d281-434b-9b1b-fea56d2d6215				
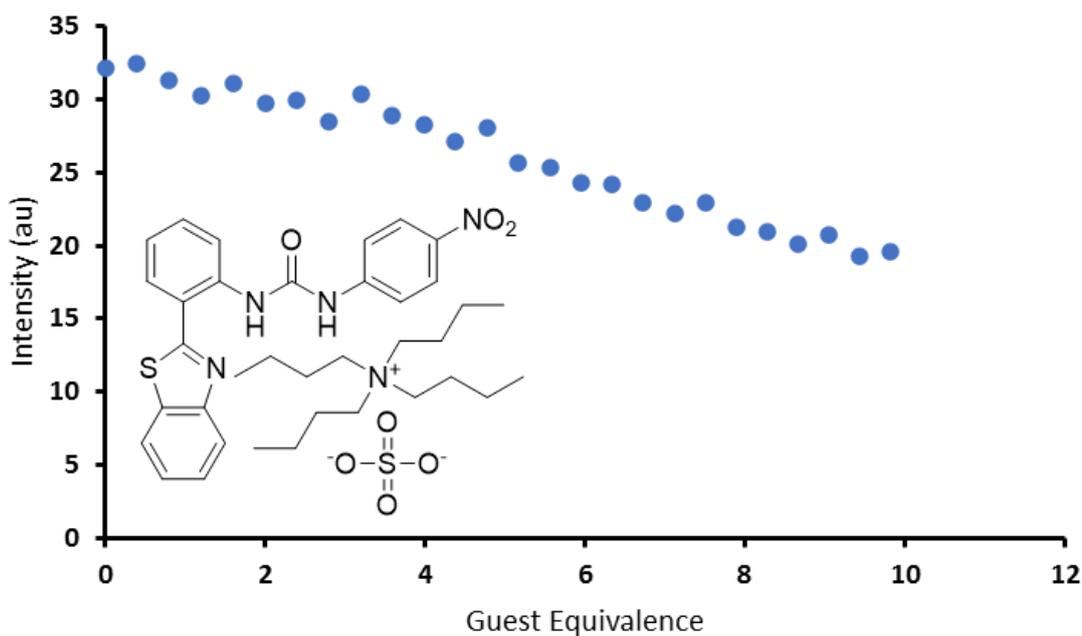
Figure 56 – A graph showing the decrease in fluorescent intensity of compound **16** (host) upon increasing concentration of TBA sulphate (guest) in CHCl$_3$ (298 K).

Table 26 – Association constants (M^{-1}) calculated for compound **17** (host) titrated against TBA acetate (guest) in CHCl$_3$ (298 K).

| Host: Guest	1: 1	1: 2		2: 1	
	K (M^{-1})	K_{11} (M^{-1})	K_{12} (M^{-1})	K_{11} (M^{-1})	K_{21} (M^{-1})
	243860.54 (± 19.191 %)	203108.18 (± 20.204 %)	4190.63 (± 63.480 %)	18905.91 (± 3.105 %)	-3363.33 (± -0.845 %)
Link to 1:1	http://app.supramolecular.org/bindfit/view/77ef616b-a9fa-44da-8d6b-07cc9da36991				
Link to 1:2	http://app.supramolecular.org/bindfit/view/b462b49b-7360-4c32-b43b-d6ae53b506ee				
Link to 2:1	http://app.supramolecular.org/bindfit/view/bc875087-c25b-4f82-95bb-c9c4fe0cf3ad				
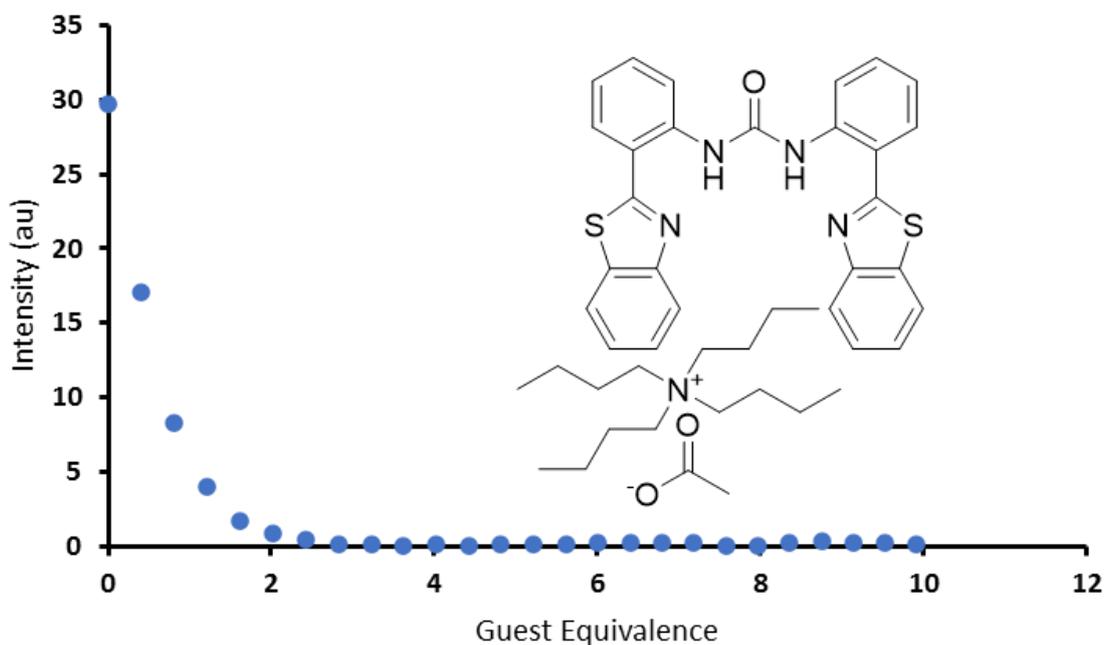
Figure 57 – A graph showing the decrease in fluorescent intensity of compound **17** (host) upon increasing concentration of TBA acetate (guest) in CHCl$_3$ (298 K).

Table 27 – Association constants (M^{-1}) calculated for compound **17** (host) titrated against TBA benzoate (guest) in $CHCl_3$ (298 K).

| Host: Guest	1: 1	1: 2		2: 1	
	K (M^{-1})	K_{11} (M^{-1})	K_{12} (M^{-1})	K_{11} (M^{-1})	K_{21} (M^{-1})
	0.0188 (± 3.890 %)	4307.67 (± 217.645 %)	759.24 (± 51.100 %)	1852.33 (± 18.810 %)	-2177.33 (± -15.340 %)
Link to 1:1	http://app.supramolecular.org/bindfit/view/1a5d89f9-924b-450e-883f-e3aebd904627				
Link to 1:2	http://app.supramolecular.org/bindfit/view/1a3b5669-5e1a-4910-99b0-336580b13c65				
Link to 2:1	http://app.supramolecular.org/bindfit/view/2b13de40-d038-432b-940b-d457ef713225				
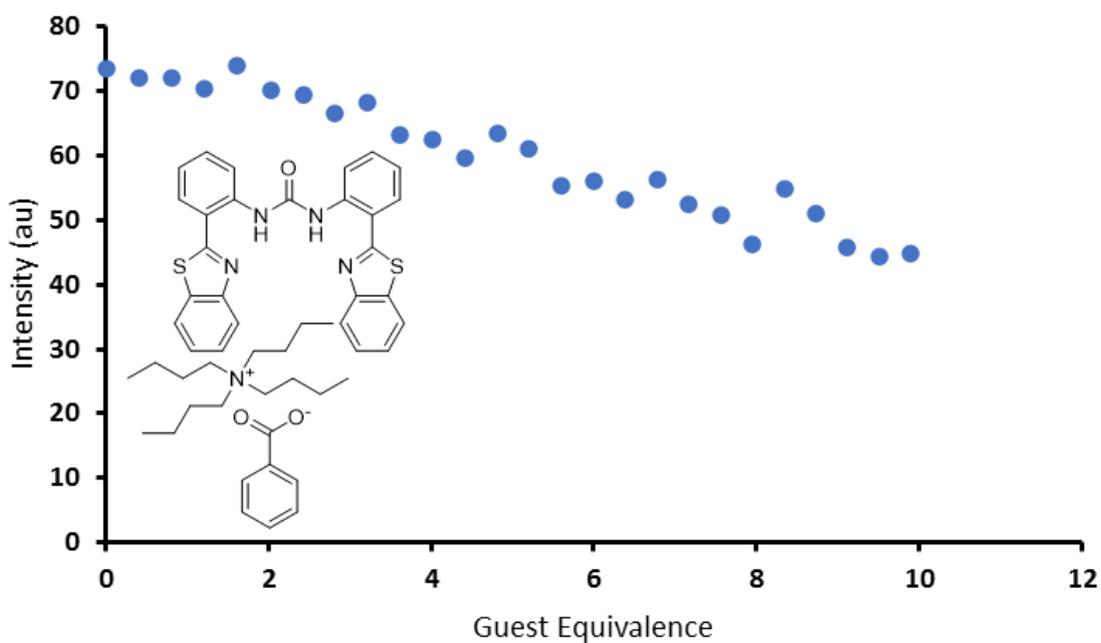
Figure 58 – A graph showing the decrease in fluorescent intensity of compound **17** (host) upon increasing concentration of TBA benzoate (guest) in $CHCl_3$ (298 K).

Table 28 – Association constants (M^{-1}) calculated for compound **17** (host) titrated against TBA chloride (guest) in CHCl$_3$ (298 K).

Host: Guest	1: 1	1: 2		2: 1	
	K (M^{-1})	K_{11} (M^{-1})	K_{12} (M^{-1})	K_{11} (M^{-1})	K_{21} (M^{-1})
	15241.79 (± 10.667 %)	9292.99 (± 18.511 %)	29606.66 (± 57.646 %)	4725.77 (± 5.399 %)	-3943.36 (± -1.692 %)
Link to 1:1	http://app.supramolecular.org/bindfit/view/1d704618-9f71-499a-89cd-f5229f4b60b1				
Link to 1:2	http://app.supramolecular.org/bindfit/view/07263213-5d8b-4032-a5a7-be090fabe2f9				
Link to 2:1	http://app.supramolecular.org/bindfit/view/278bad96-ee1f-4167-9fb8-da448b3754b5				

Table 29 – Association constants (M^{-1}) calculated for compound **17** (host) titrated against TBA fluoride (guest) in CHCl$_3$ (298 K).

Host: Guest	1: 1	1: 2		2: 1	
	K (M^{-1})	K_{11} (M^{-1})	K_{12} (M^{-1})	K_{11} (M^{-1})	K_{21} (M^{-1})
	0.0136 (± 2.343 %)	34858.08 (± 738.89 %)	217.60 (± 25.733 %)	0.06 (± 36.139 %)	428546510 (± 31.674 %)
Link to 1:1	http://app.supramolecular.org/bindfit/view/c04d9da4-203f-4975-9c50-193536f751cf				
Link to 1:2	http://app.supramolecular.org/bindfit/view/7adc9d59-eb3f-4dc3-a93f-b60107c1588b				
Link to 2:1	http://app.supramolecular.org/bindfit/view/7b11667d-c240-4274-aad7-6567fba53d9c				
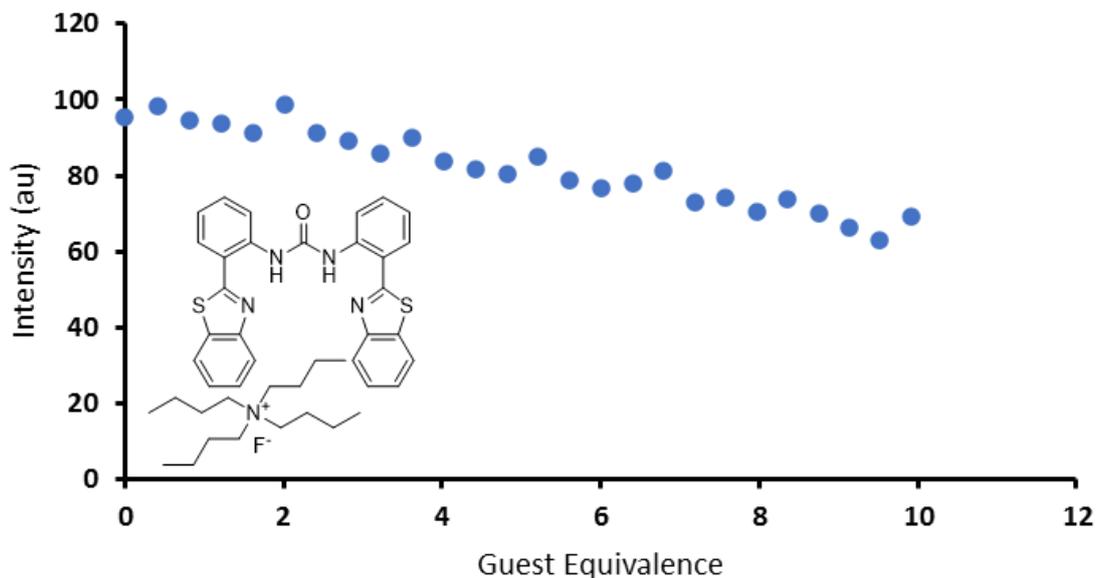
Figure 59 – A graph showing the decrease in fluorescent intensity of compound **17** (host) upon increasing concentration of TBA fluoride (guest) in CHCl$_3$ (298 K).

Table 30 – Association constants (M^{-1}) calculated for compound **17** (host) titrated against TBA hydroxide (guest) in CHCl$_3$ (298 K).

Host: Guest	1: 1	1: 2		2: 1	
	K (M^{-1})	K$_{11}$ (M^{-1})	K$_{12}$ (M^{-1})	K$_{11}$ (M^{-1})	K$_{21}$ (M^{-1})
	77551.09 (± 16.026 %)	81498.95 (± 18.880 %)	251.75 (± 276.505 %)	8195.78 (± 9.209 %)	6152.63 (± 4.157 %)
Link to 1:1	http://app.supramolecular.org/bindfit/view/9f14fc80-7b53-4263-95d9-a7fbf99614ed				
Link to 1:2	http://app.supramolecular.org/bindfit/view/aceac0a8-dc52-49a5-8304-537346c1b1aa				
Link to 2:1	http://app.supramolecular.org/bindfit/view/a4dff6c5-384b-4661-aee7-ce28eb78e8f9				
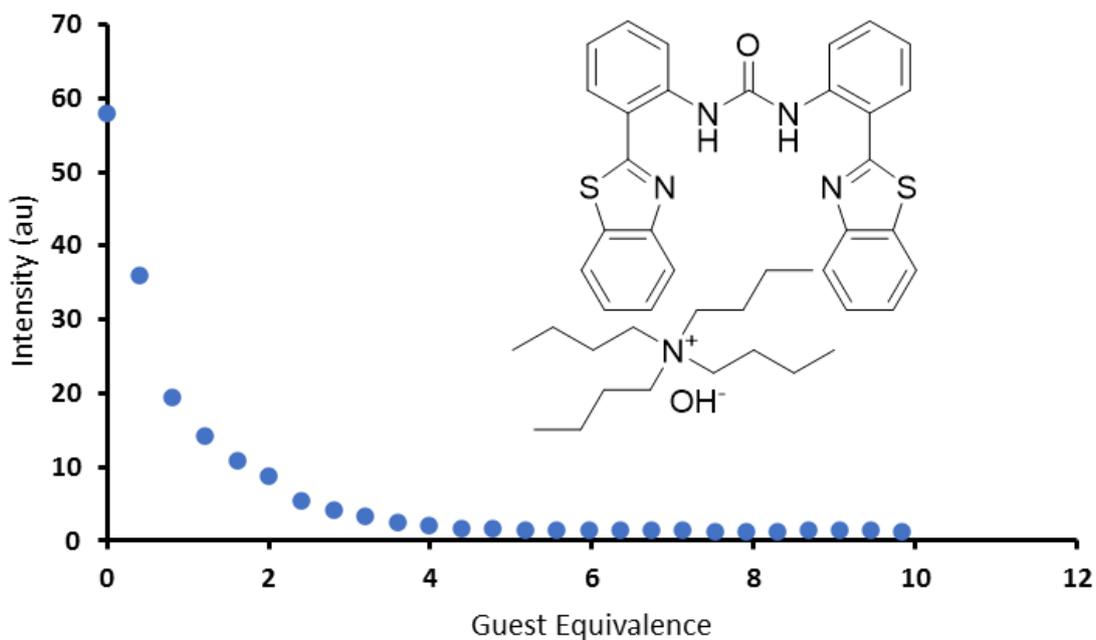
Figure 60 – A graph showing the decrease in fluorescent intensity of compound **17** (host) upon increasing concentration

of TBA hydroxide (guest) in CHCl$_3$ (298 K).

Table 31 – Association constants (M^{-1}) calculated for compound **17** (host) titrated against TBA hydrogen sulphate

(guest) in CHCl$_3$ (298 K).

Host: Guest	1: 1	1: 2		2: 1	
	K (M^{-1})	K$_{11}$ (M^{-1})	K$_{12}$ (M^{-1})	K$_{11}$ (M^{-1})	K$_{21}$ (M^{-1})
	0.00714 (± 1.233 %)	3.4692e^{+17} (±12691756379 %)	-506.96 (± -6.463 %)	-0.69 (± -45.313 %)	1559142.32 (± 35.209 %)
Link to 1:1	http://app.supramolecular.org/bindfit/view/8a67cb27-a588-4f2c-83df-7eb51a610261				
Link to 1:2	http://app.supramolecular.org/bindfit/view/d45fdc24-99bd-4b4f-8c91-73095fbe23ae				
Link to 2:1	http://app.supramolecular.org/bindfit/view/e508bc7e-5f55-45ff-a9e5-24b148c7ef38				
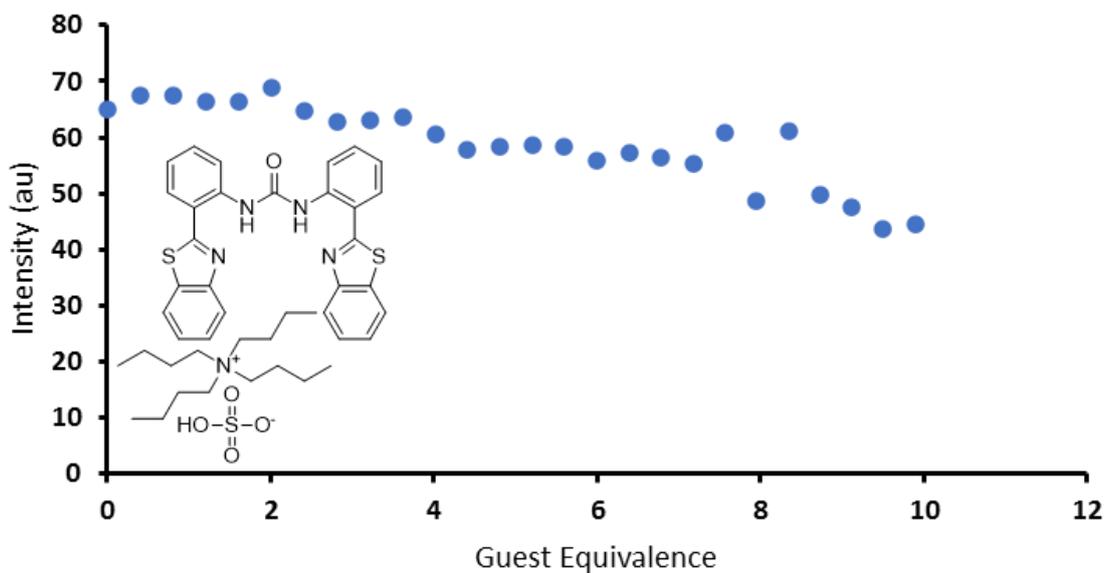
Figure 61 – A graph showing the decrease in fluorescent intensity of compound **17** (host) upon increasing concentration of TBA hydrogen sulphate (guest) in CHCl$_3$ (298 K).

Table 32 – Association constants (M^{-1}) calculated for compound **17** (host) titrated against TBA phosphate monobasic (guest) in CHCl$_3$ (298 K).

Host: Guest	1: 1	1: 2		2: 1	
	K (M^{-1})	K$_{11}$ (M^{-1})	K$_{12}$ (M^{-1})	K$_{11}$ (M^{-1})	K$_{21}$ (M^{-1})
	8816.24 (± 9.003 %)	973.44 (± 4.182 %)	43149.22 (± 16.130 %)	3026.37 (± 4.198 %)	-3793.05 (± -1.217 %)
Link to 1:1	http://app.supramolecular.org/bindfit/view/3dbcf8e6-8fb7-4682-b895-a4990810832f				
Link to 1:2	http://app.supramolecular.org/bindfit/view/77321eb2-0274-46bb-b1e9-174f61dd2804				
Link to 2:1	http://app.supramolecular.org/bindfit/view/486d8892-1d1c-4357-8266-0ce72532ec76				

Table 33 – Association constants (M^{-1}) calculated for compound **17** (host) titrated against TBA sulphate (guest) in CHCl$_3$ (298 K).

| Host: Guest	1: 1	1: 2		2: 1	
	K (M^{-1})	K$_{11}$ (M^{-1})	K$_{12}$ (M^{-1})	K$_{11}$ (M^{-1})	K$_{21}$ (M^{-1})
	15556.98 (± 9.783 %)	192788.20 (± 101.171 %)	21076.04 (± 18.802 %)	9116.08 (± 6.174 %)	-4950.07 (± -0.0002 %)
Link to 1:1	http://app.supramolecular.org/bindfit/view/a2978444-5480-4289-b832-53107c373867				
Link to 1:2	http://app.supramolecular.org/bindfit/view/af09656e-cc09-4a01-ade0-bbef3149494e				
Link to 2:1	http://app.supramolecular.org/bindfit/view/d67f5f37-1db2-47b8-9d33-abbfc25698ef				

8.4 Fluorescence titration studies
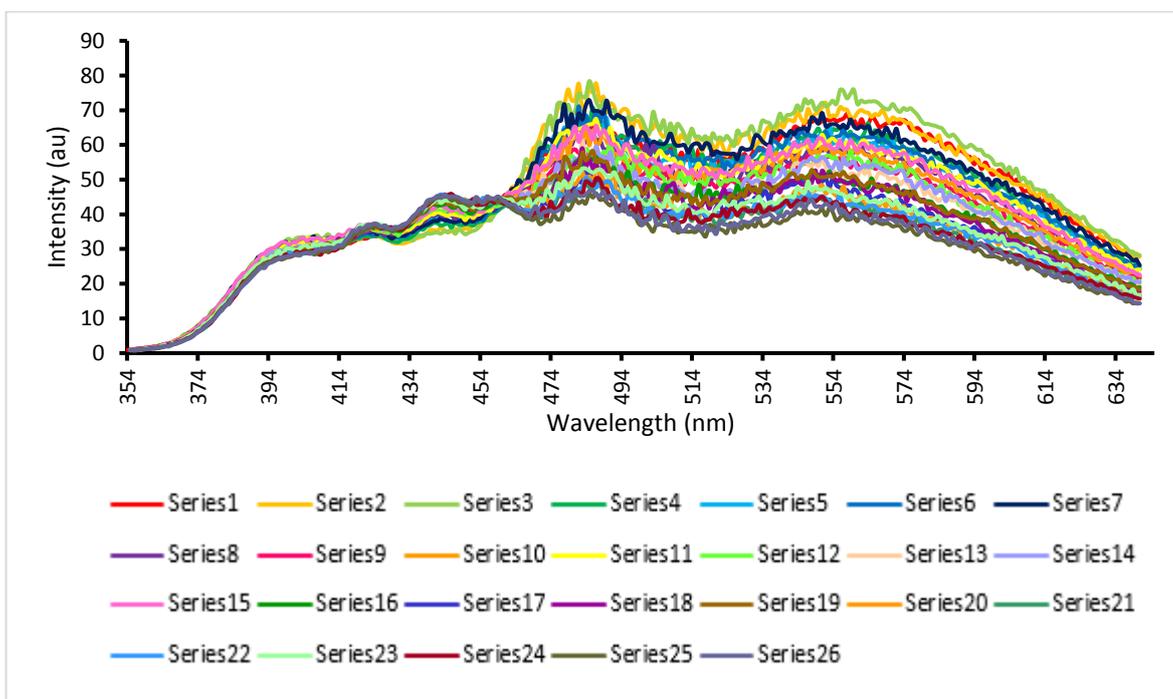
Figure 62 – A graph showing overall decrease in emission intensity of individual scans of compound **14** upon the addition of TBA acetate (guest) (series 1-26).
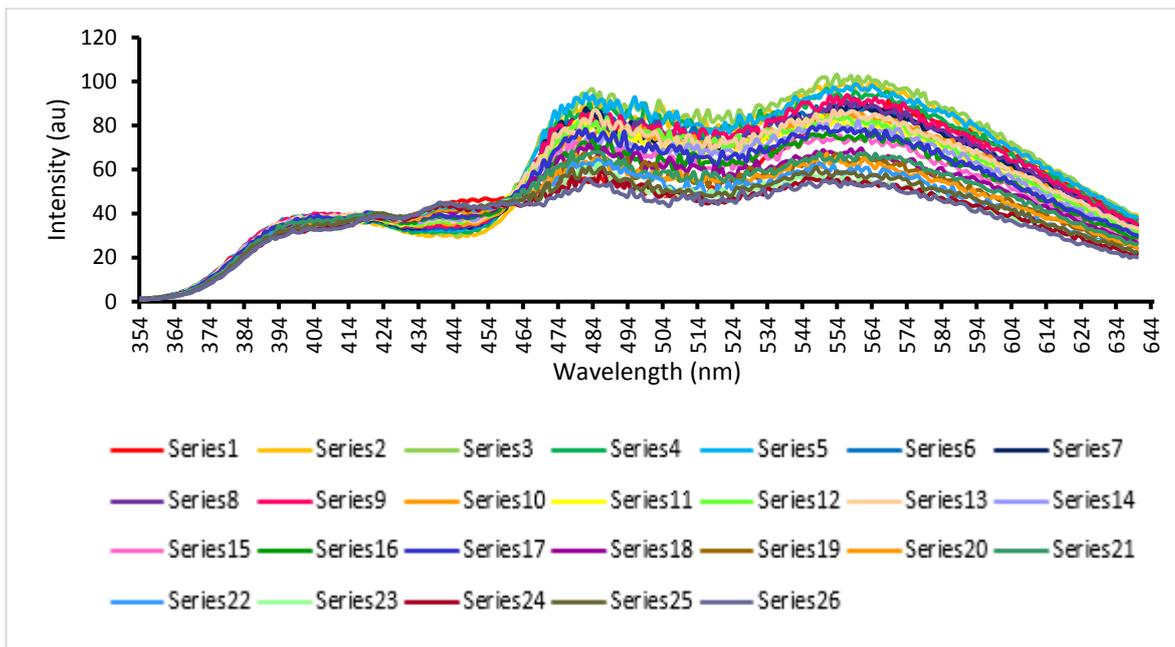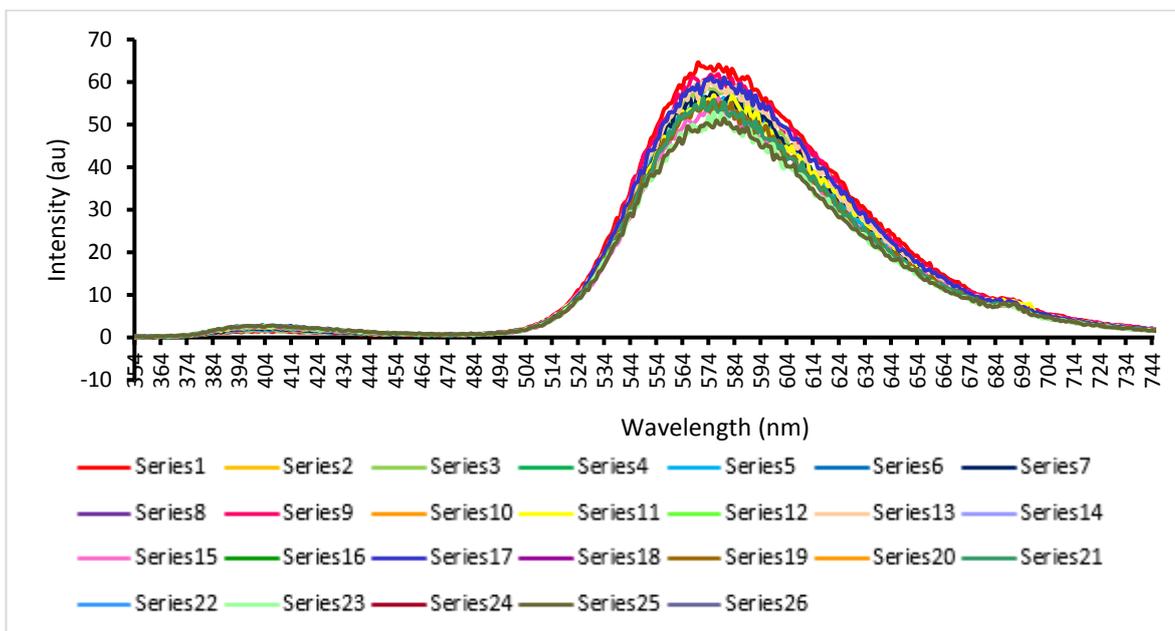
Figure 63 – A graph showing overall decrease in emission intensity of individual scans of compound **14** upon the addition of TBA benzoate (guest) (series 1-26).
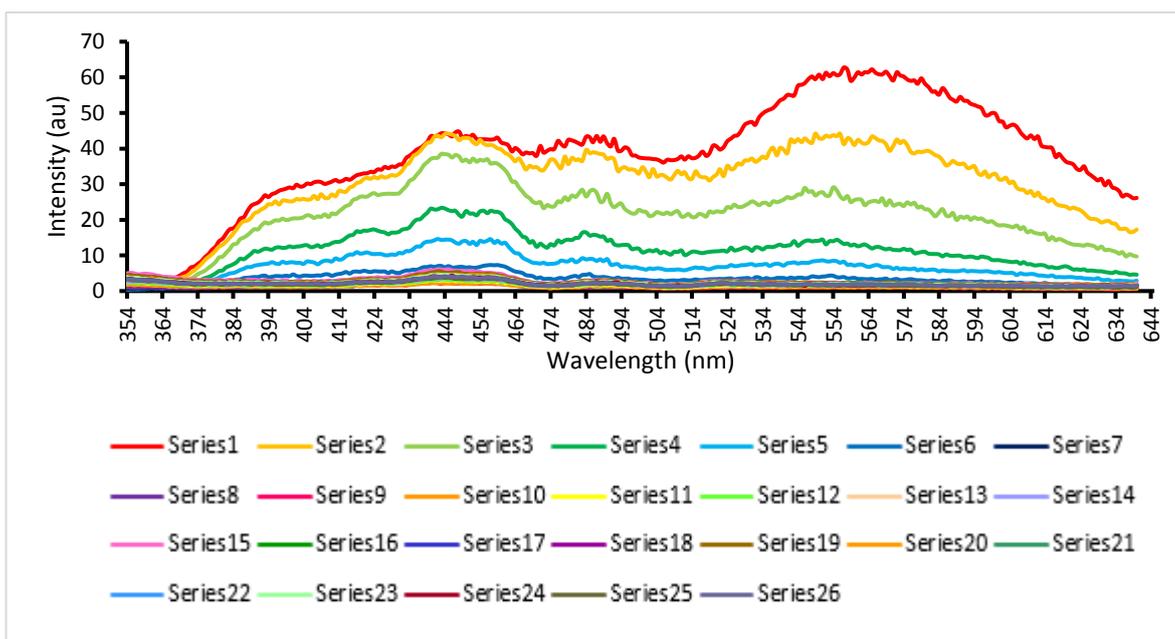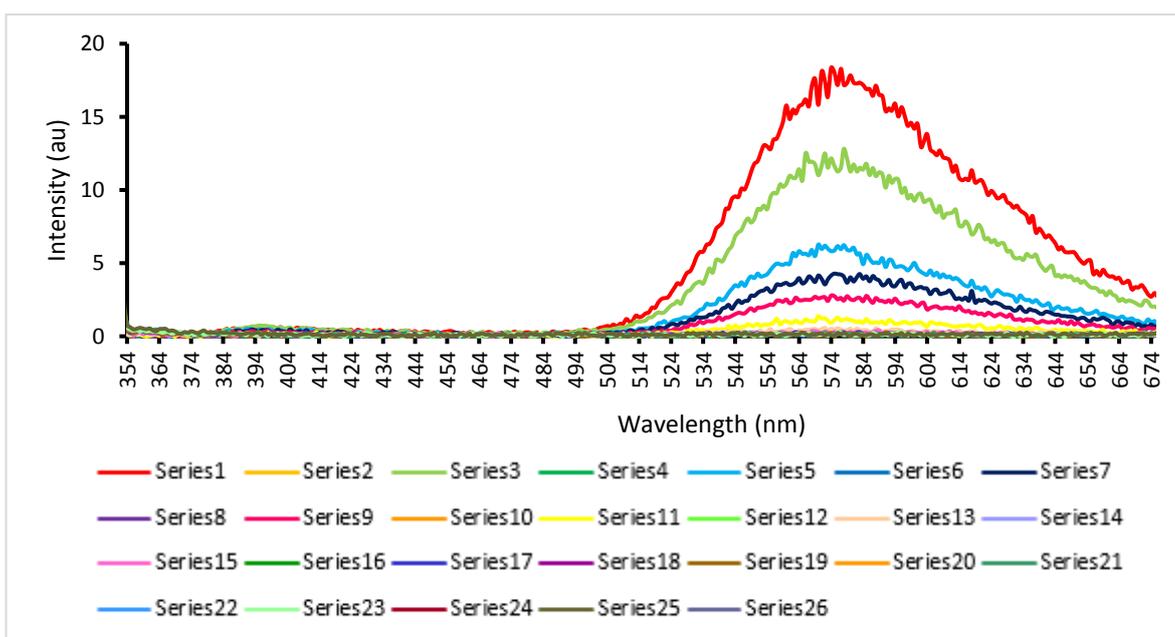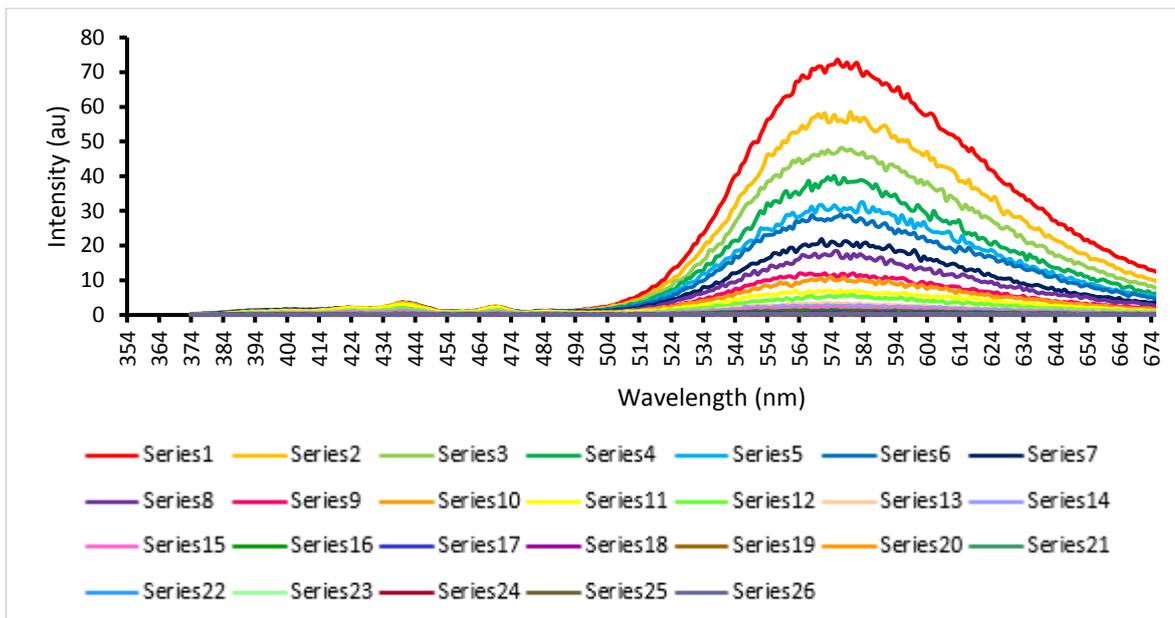

Figure 64 – A graph showing overall decrease in emission intensity of individual scans of compound **14** upon the addition of TBA chloride (guest) (series 1-26).
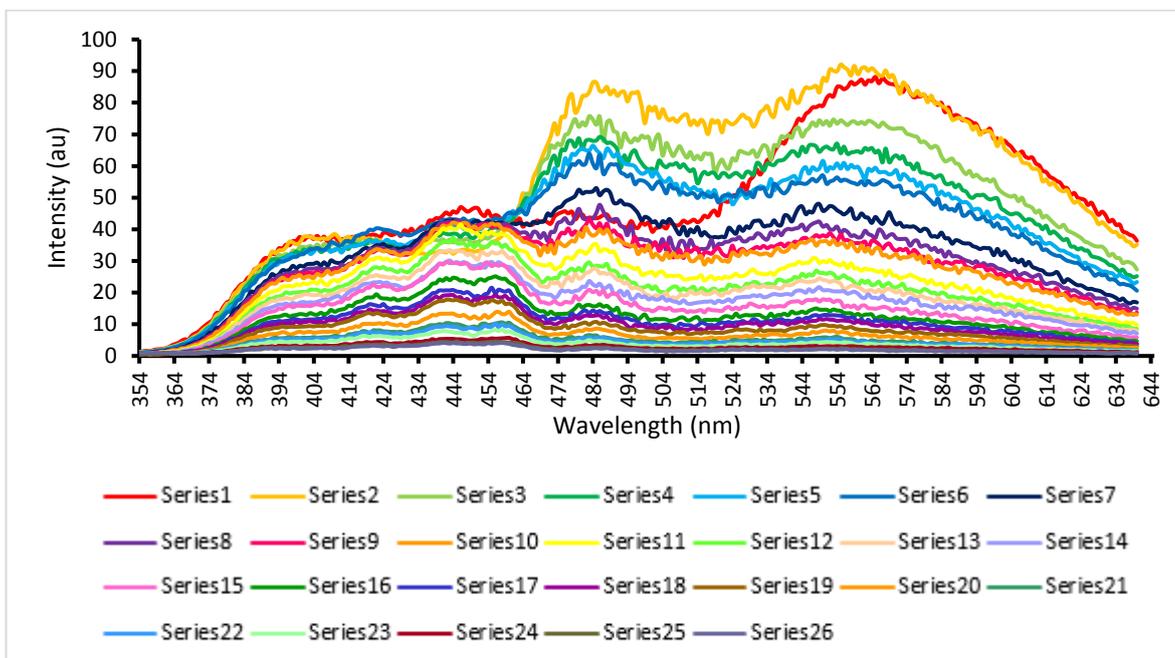
Figure 65 – A graph showing overall decrease in emission intensity of individual scans of compound **14** upon the addition of TBA fluoride (guest) (series 1-26).
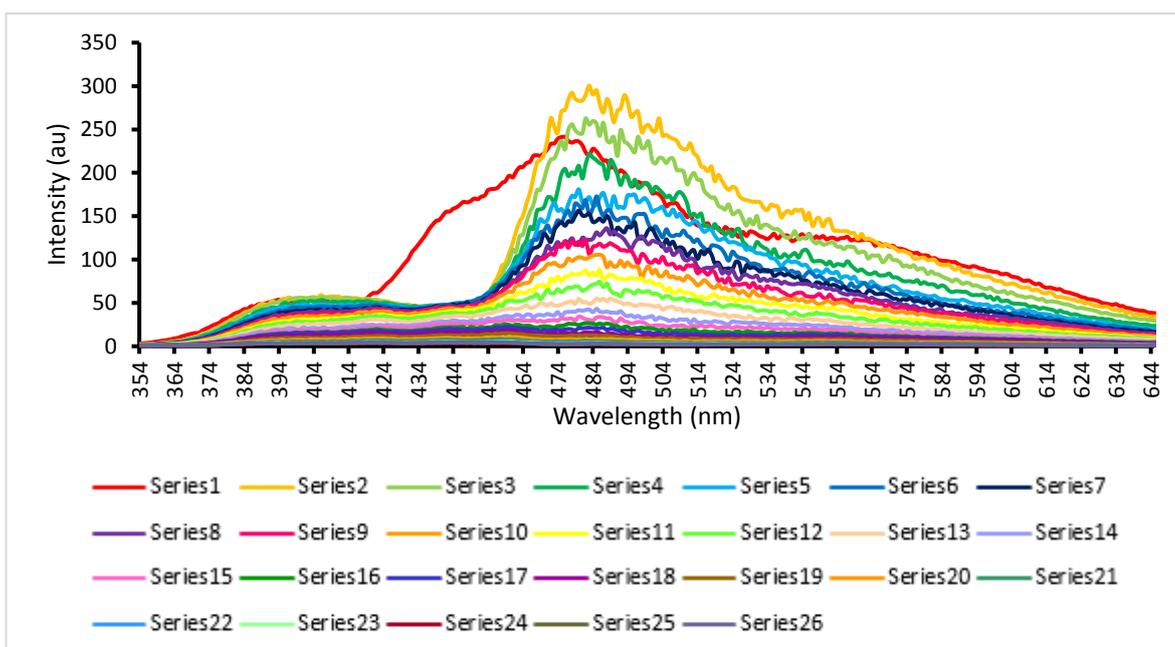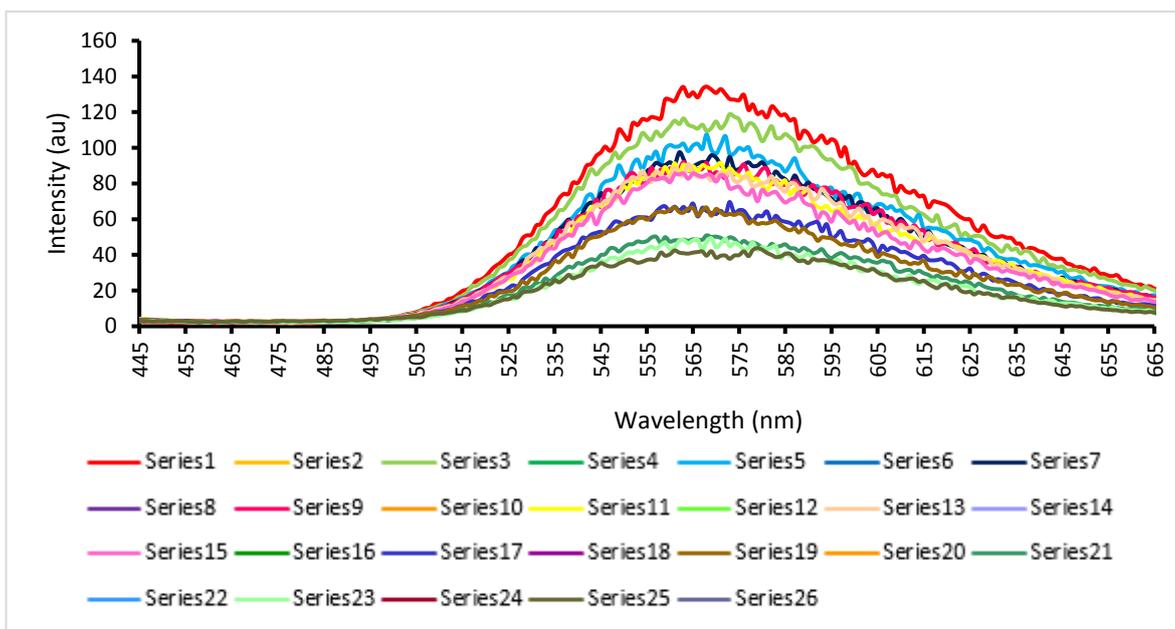

Figure 66 – A graph showing overall decrease in emission intensity of individual scans of compound **14** upon the addition of TBA hydroxide (guest) (series 1-26).
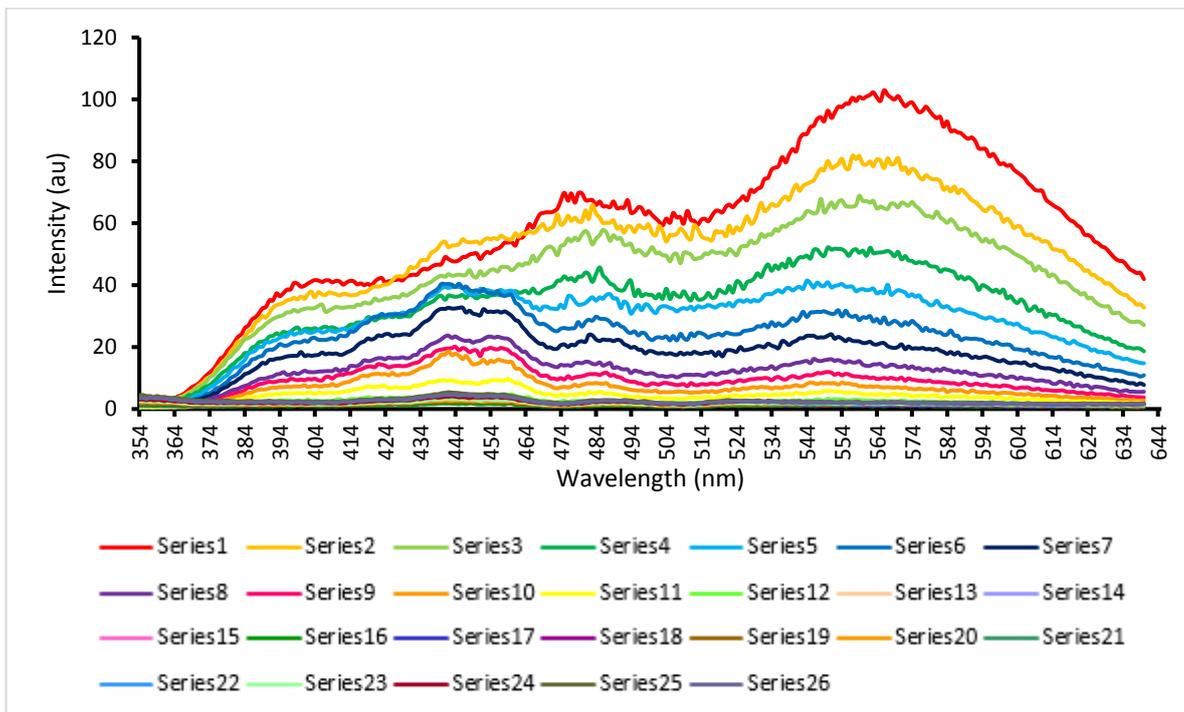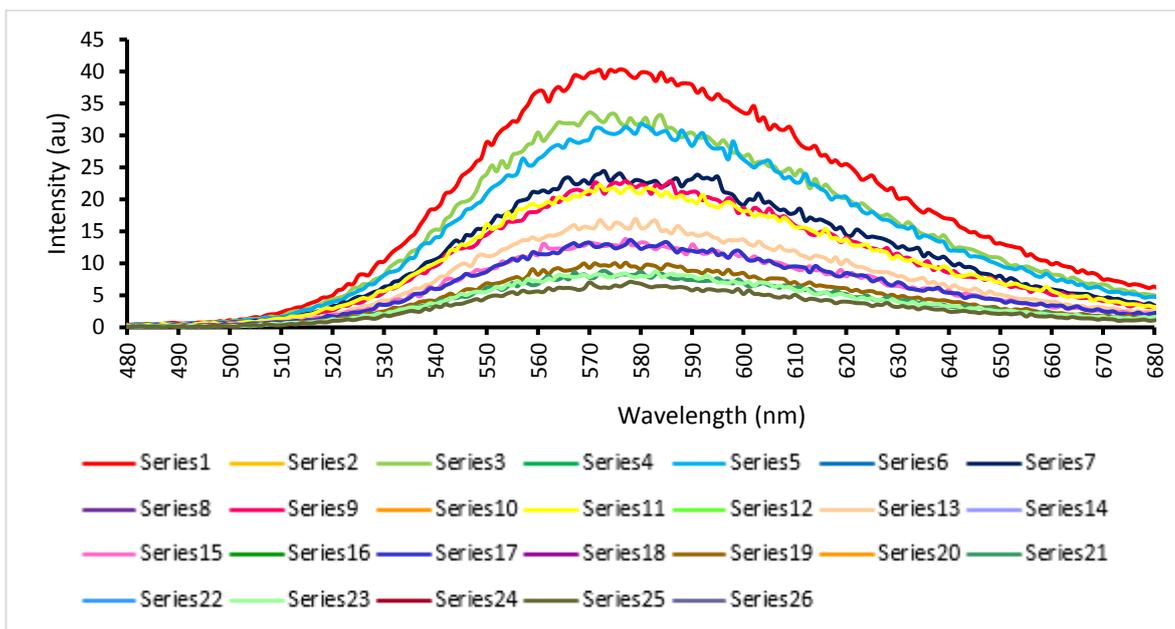
Figure 67 – A graph showing overall decrease in emission intensity of individual scans of compound **14** upon the addition of TBA hydrogen sulphate (guest) (series 1-26).
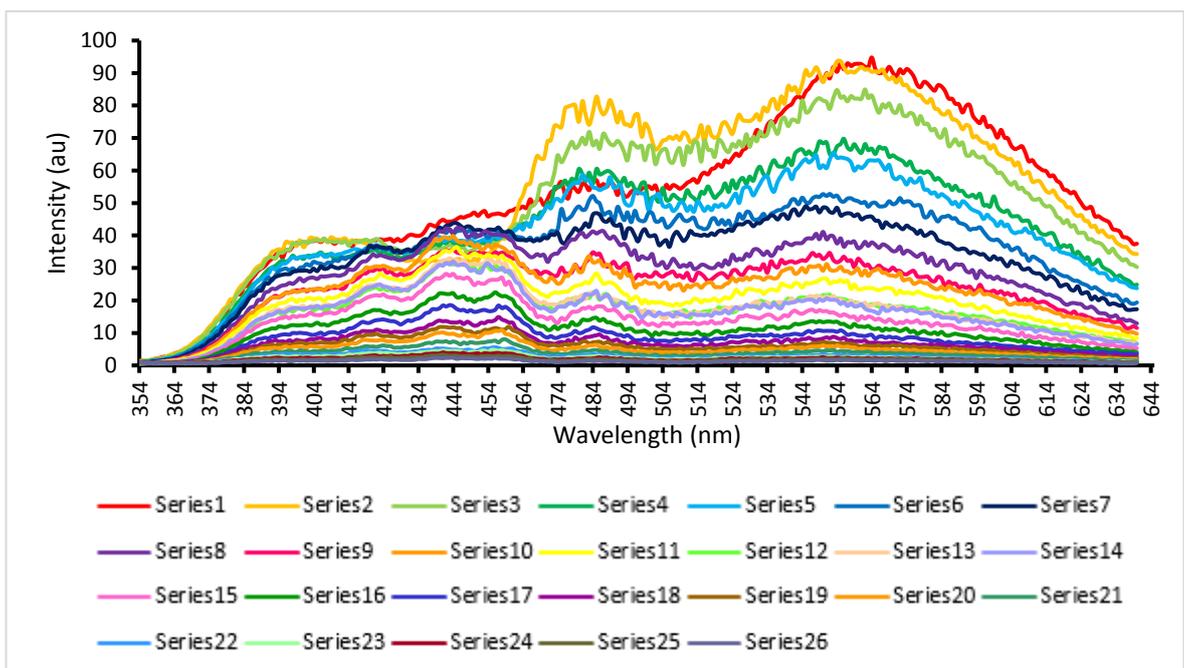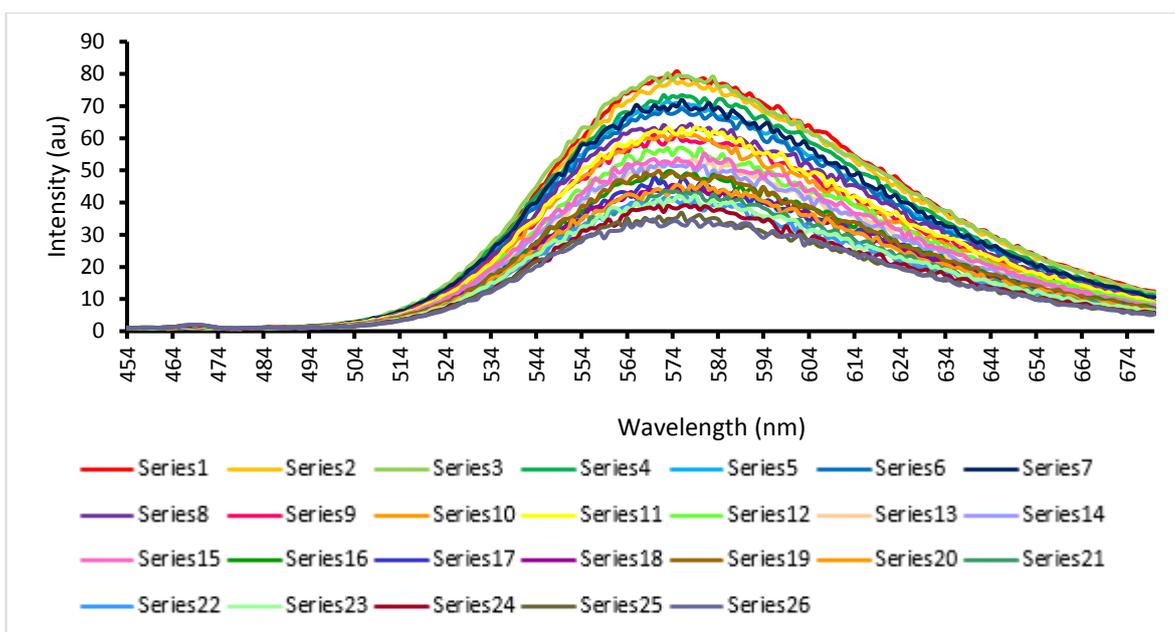

Figure 68 – A graph showing overall decrease in emission intensity of individual scans of compound **14** upon the addition of TBA phosphate monobasic (guest) (series 1-26).
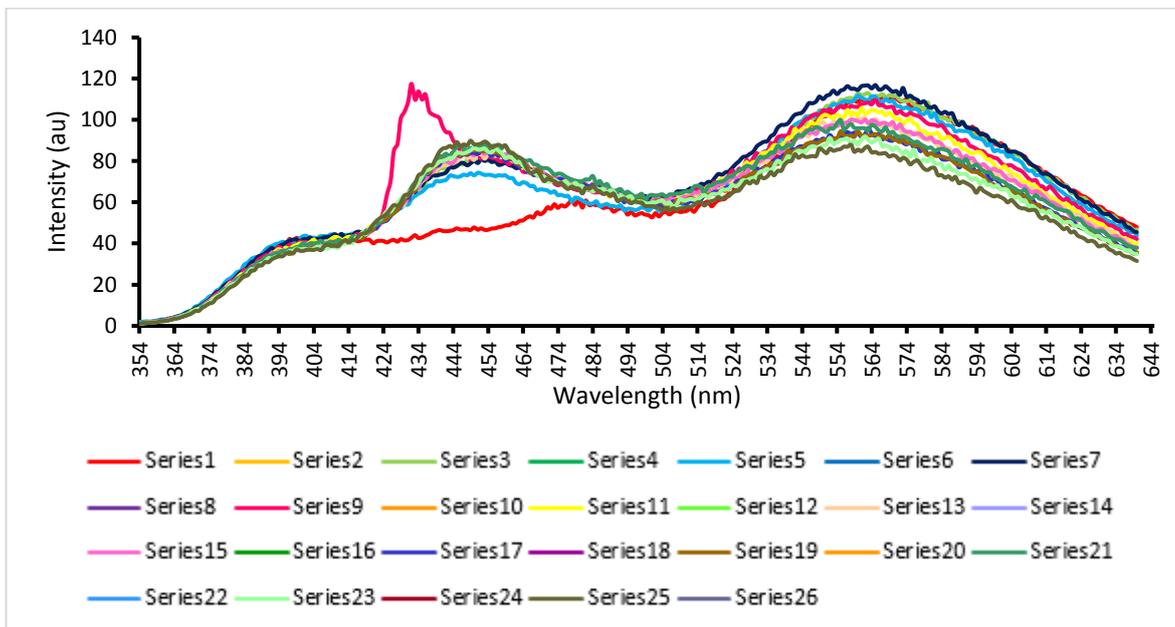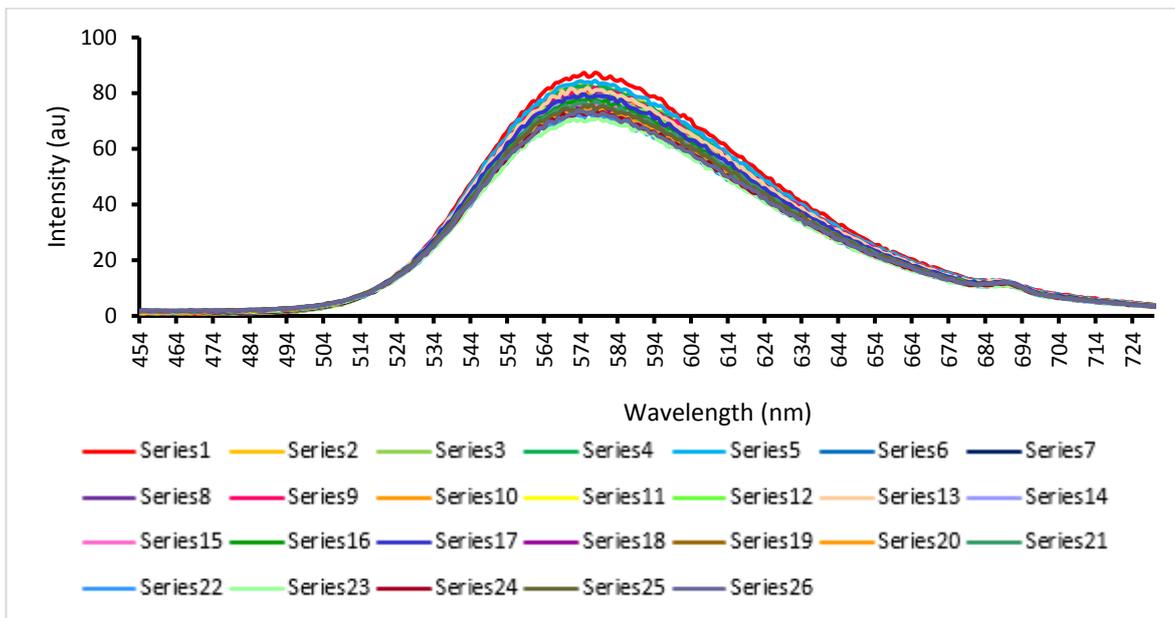
Figure 69 – A graph showing overall decrease in emission intensity of individual scans of compound **14** upon the addition of TBA sulphate (guest) (series 1-26).
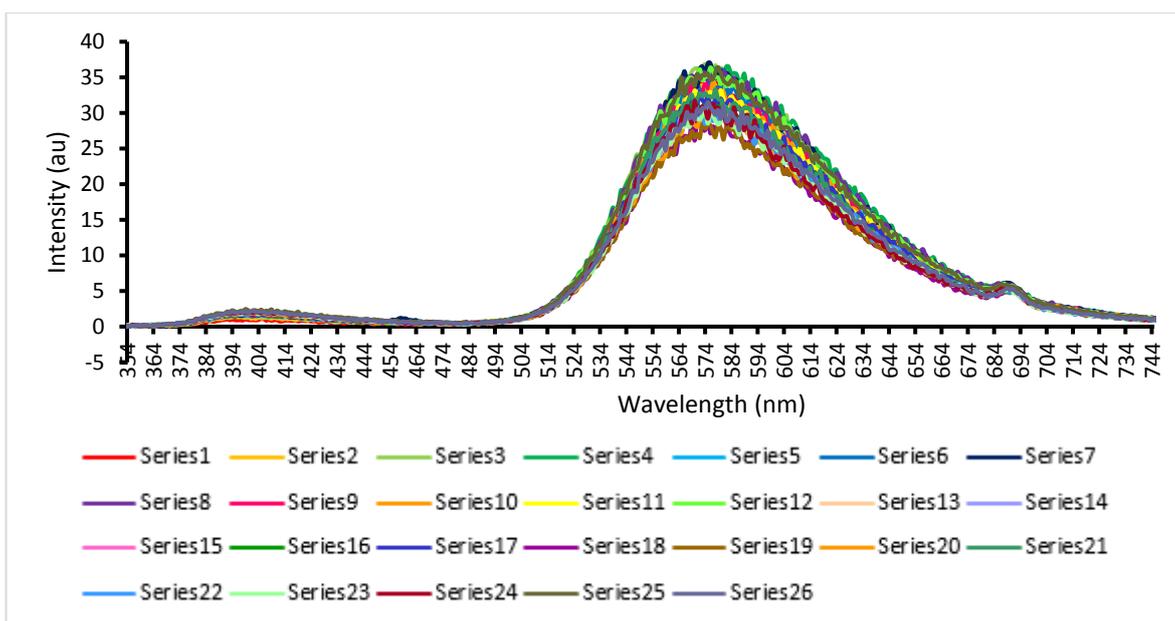
Figure 70 – A graph showing overall decrease in emission intensity of individual scans of compound **15** upon the addition of TBA acetate (guest) (series 1-26).
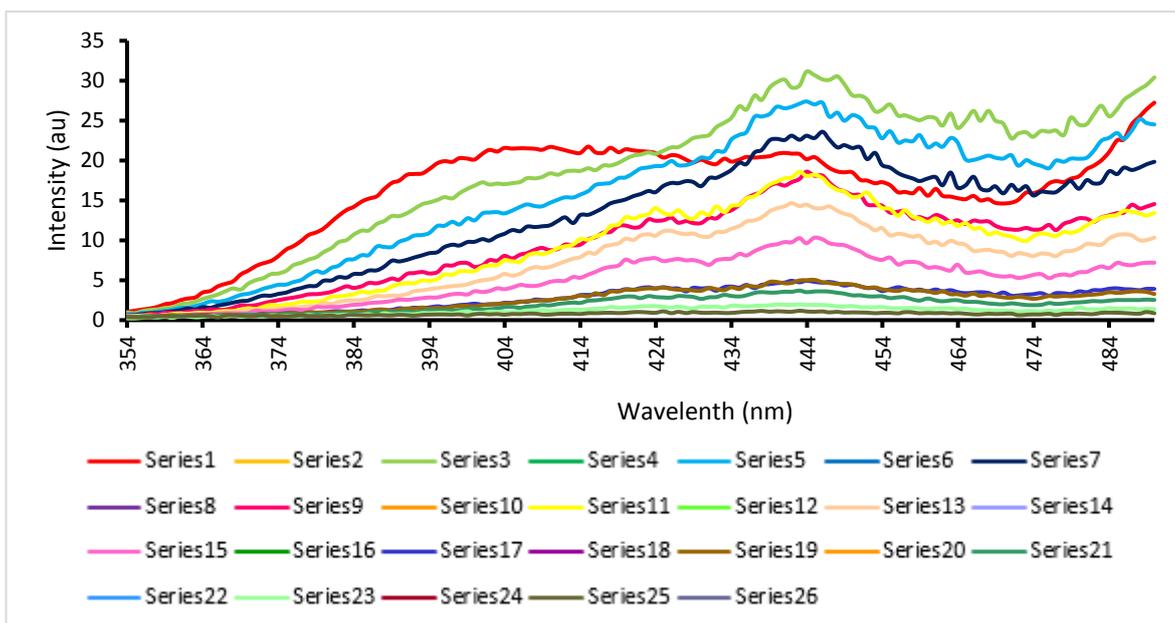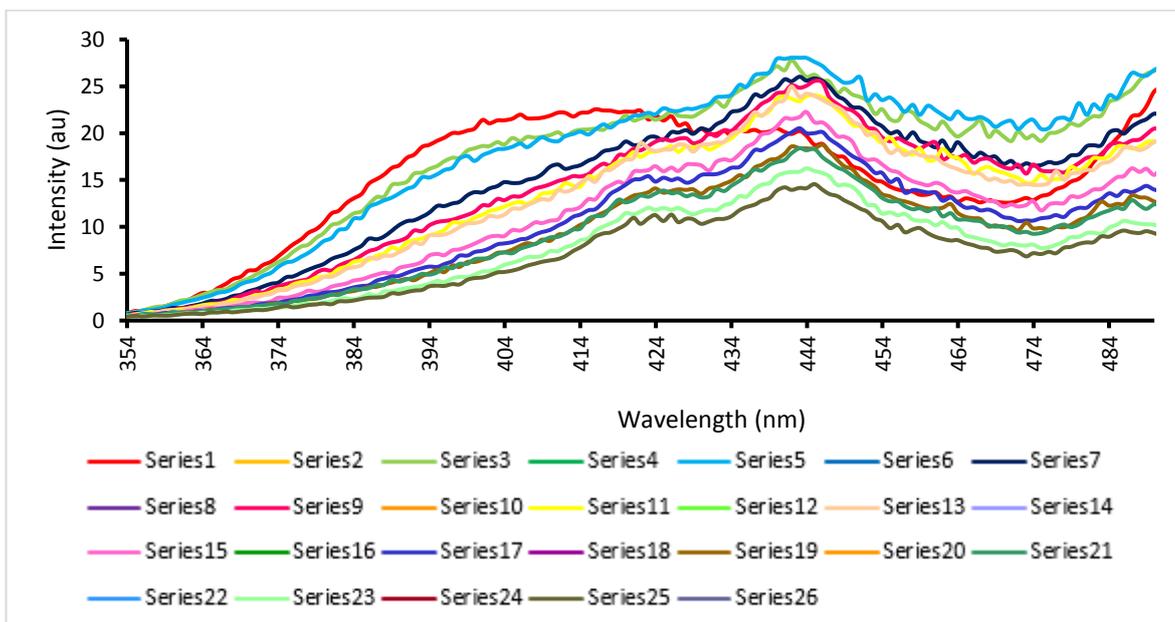
Figure 71 – A graph showing overall decrease in emission intensity of individual scans of compound **15** upon the addition of TBA benzoate (guest) (series 1-26).

Figure 72 – A graph showing overall decrease in emission intensity of individual scans of compound **15** upon the addition of TBA chloride (guest) (series 1-26).
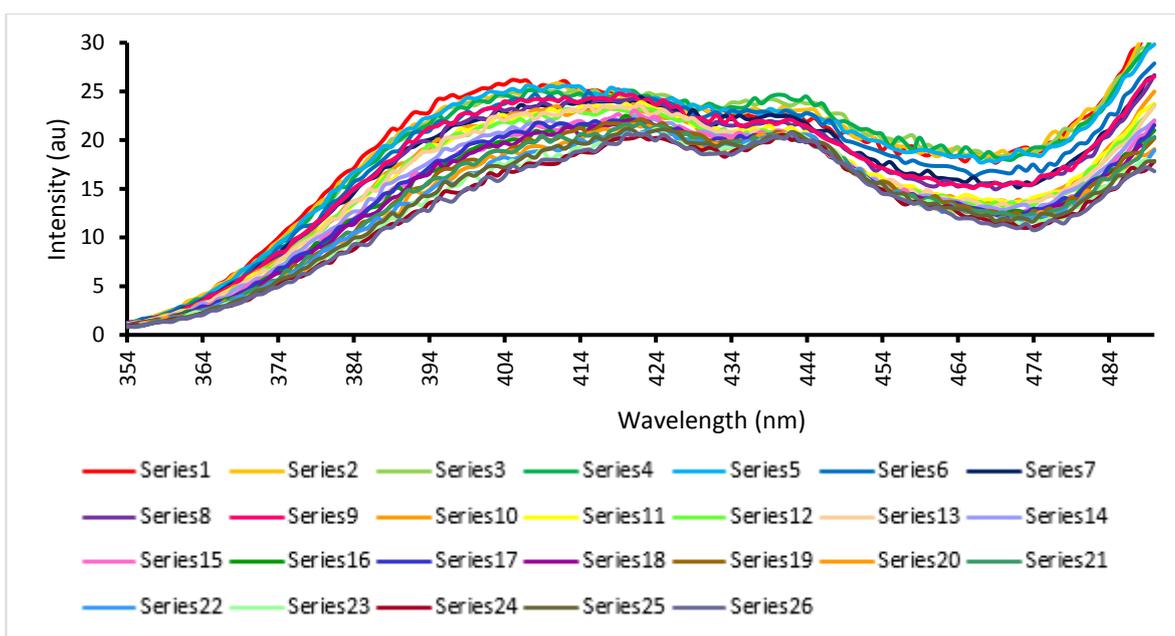
Figure 73 – A graph showing overall decrease in emission intensity of individual scans of compound **15** upon the addition of TBA fluoride (guest) (series 1-26).

Figure 74 – A graph showing overall decrease in emission intensity of individual scans of compound **15** upon the addition of TBA hydroxide (guest) (series 1-26).

Figure 75 – A graph showing overall decrease in emission intensity of individual scans of compound **15** upon the addition of TBA hydrogen sulphate (guest) (series 1-26).

Figure 76 – A graph showing overall decrease in emission intensity of individual scans of compound **15** upon the addition of TBA phosphate monobasic (guest) (series 1-26).

Figure 77 – A graph showing overall decrease in emission intensity of individual scans of compound **15** upon the addition of TBA sulphate (guest) (series 1-26).

Figure 78 – A graph showing overall decrease in emission intensity of individual scans of compound **16** upon the addition of TBA acetate (guest) (series 1-26).
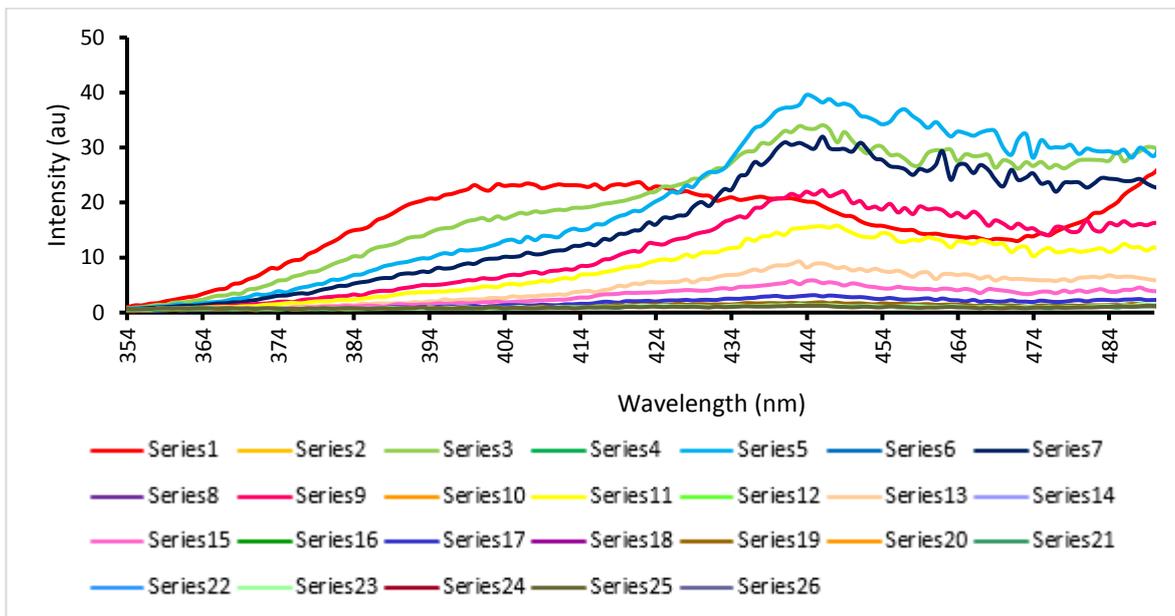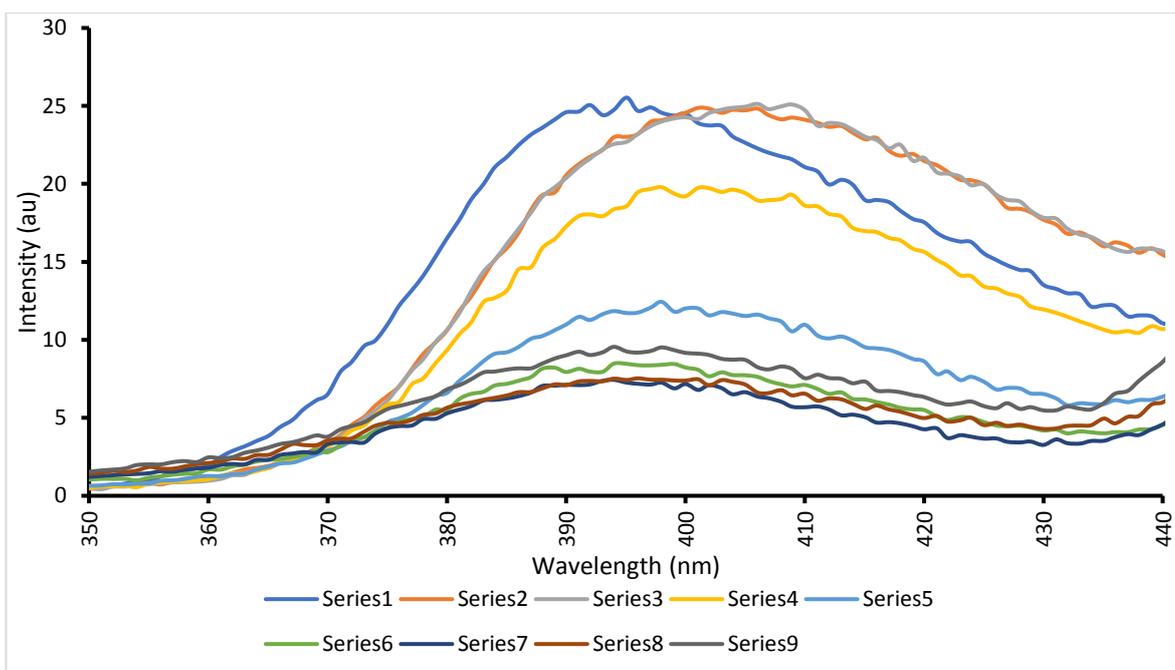
Figure 79 – A graph showing overall decrease in emission intensity of individual scans of compound **16** upon the addition of TBA benzoate (guest) (series 1-26).

Figure 80 – A graph showing overall decrease in emission intensity of individual scans of compound **16** upon the addition of TBA chloride (guest) (series 1-26).
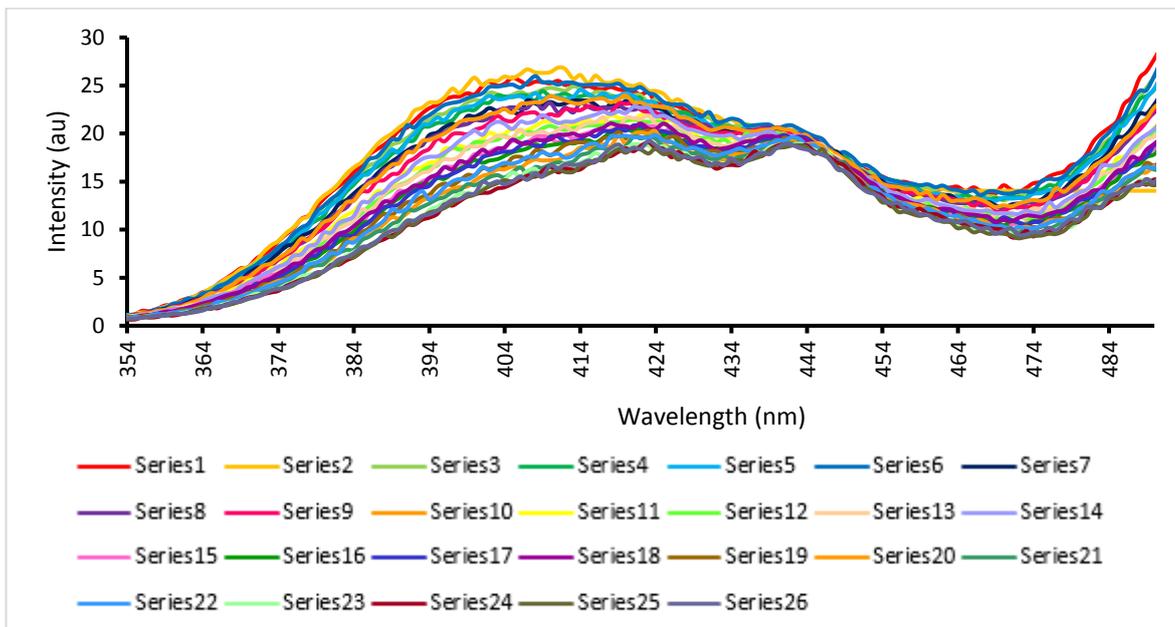
Figure 81 – A graph showing overall decrease in emission intensity of individual scans of compound **16** upon the addition of TBA fluoride (guest) (series 1-26).

Figure 82 – A graph showing overall decrease in emission intensity of individual scans of compound **16** upon the addition of TBA hydroxide (guest) (series 1-9).

Figure 83 – A graph showing overall decrease in emission intensity of individual scans of compound **16** upon the addition of TBA hydrogen sulphate (guest) (series 1-26).
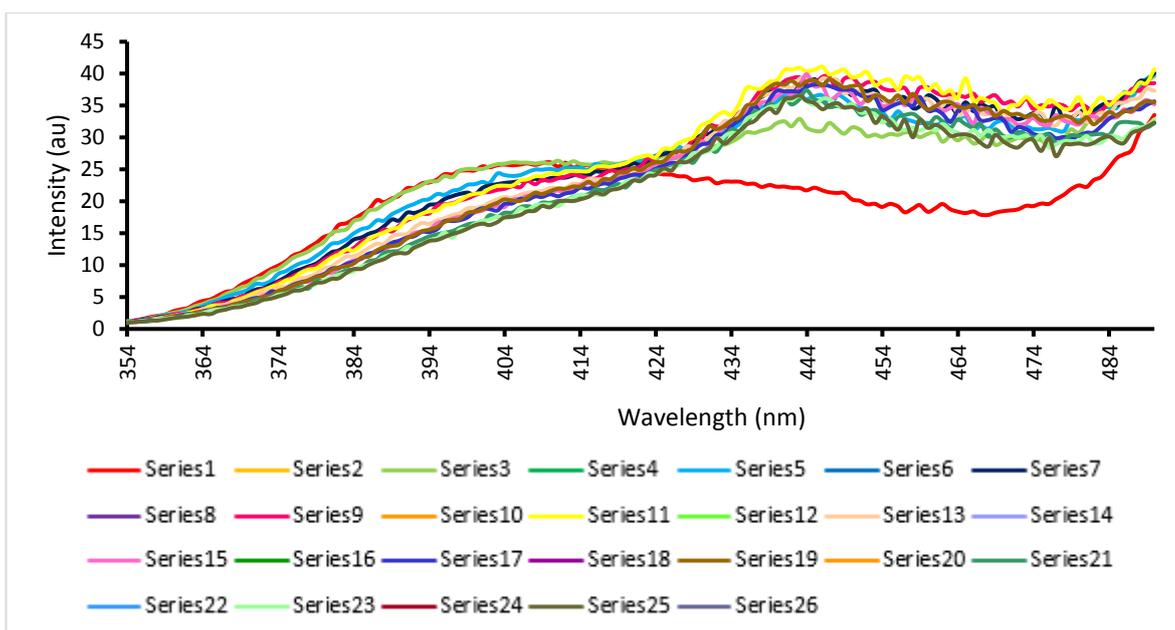

Figure 84 – A graph showing overall decrease in emission intensity of individual scans of compound **16** upon the addition of TBA phosphate monobasic (guest) (series 1-26).
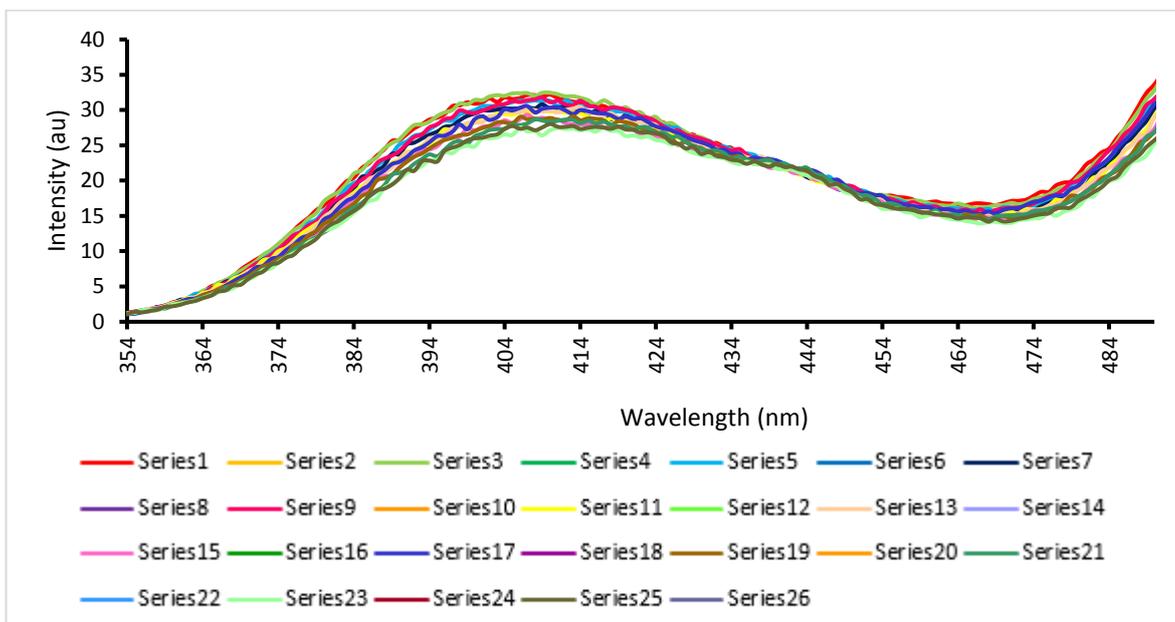
Figure 85 – A graph showing overall decrease in emission intensity of individual scans of compound **16** upon the addition of TBA sulphate (guest) (series 1-26).
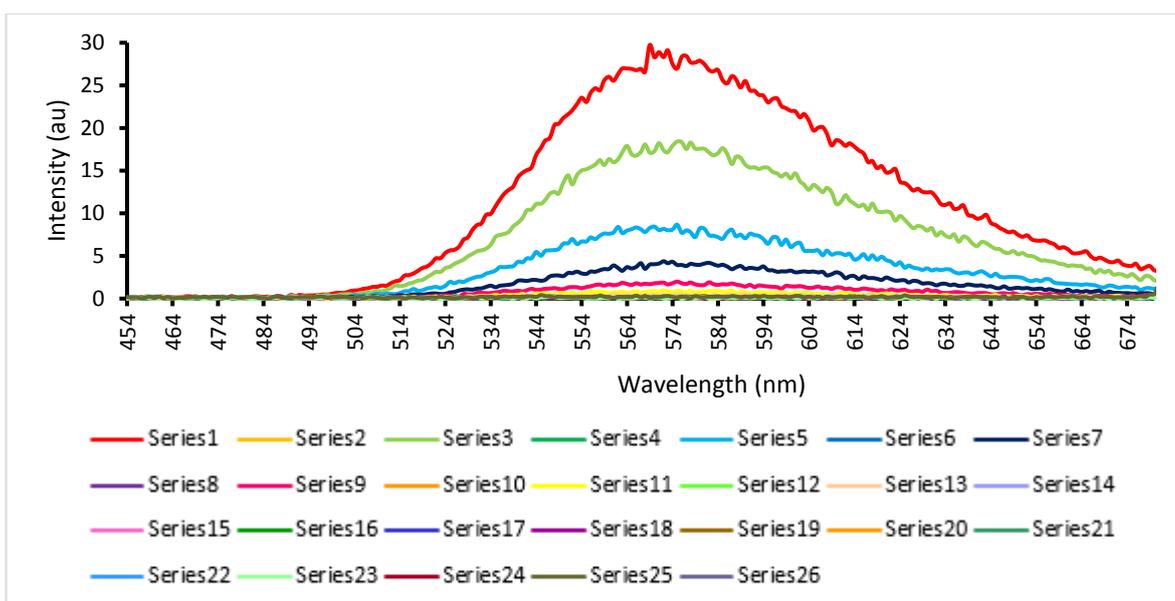

Figure 86 – A graph showing overall decrease in emission intensity of individual scans of compound **17** upon the addition of TBA acetate (guest) (series 1-26).
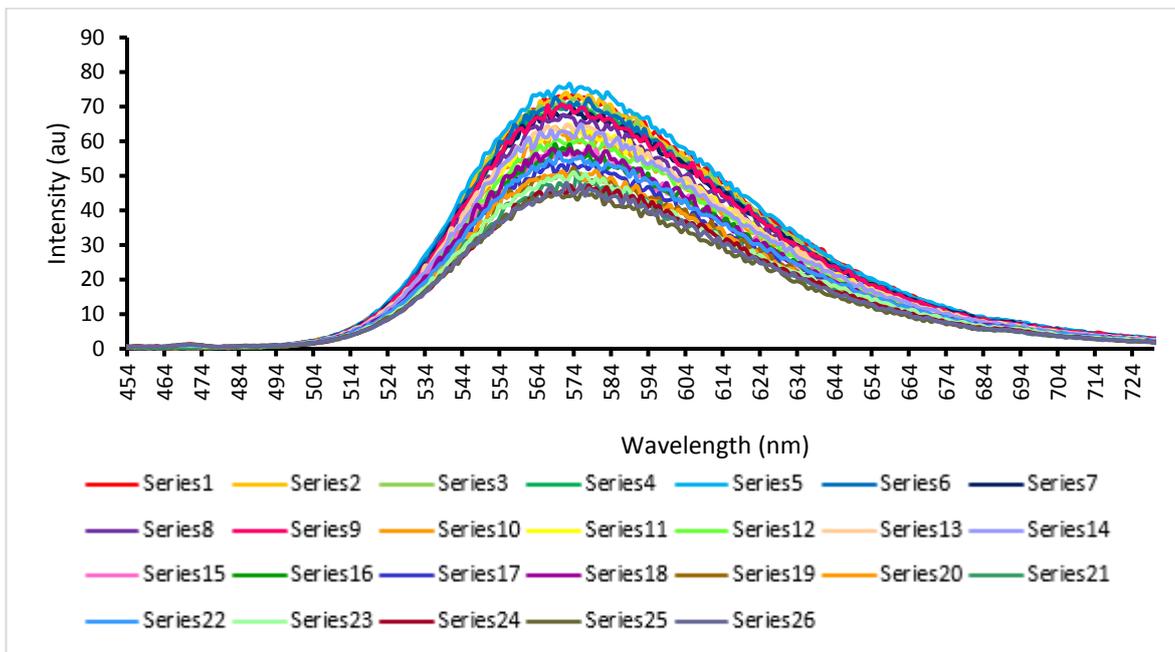
Figure 87 – A graph showing overall decrease in emission intensity of individual scans of compound **17** upon the addition of TBA benzoate (guest) (series 1-26).
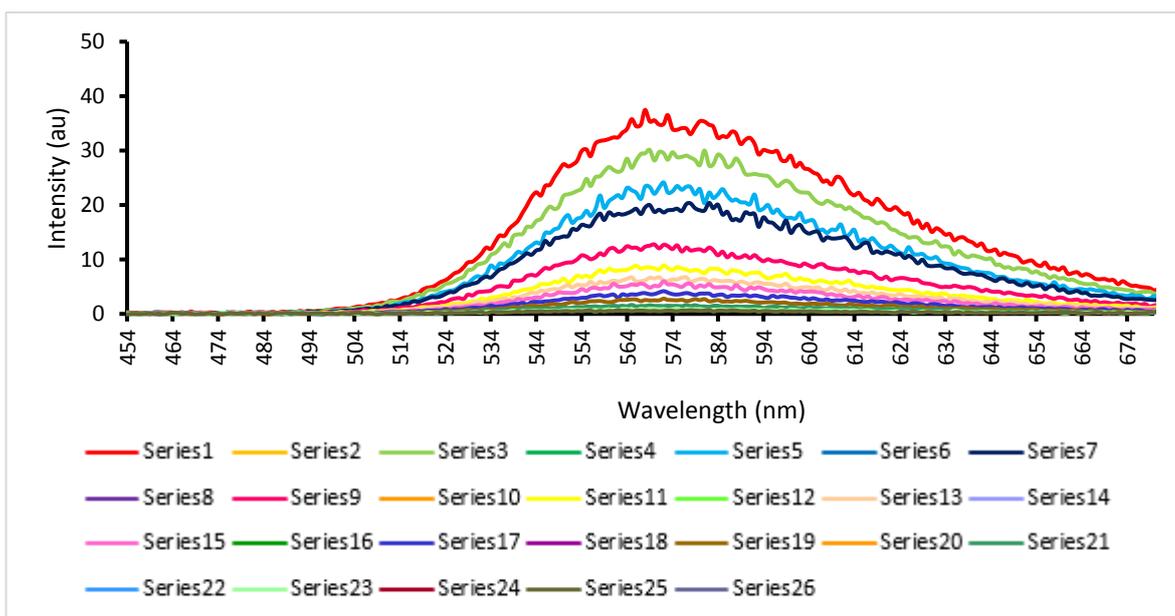

Figure 88 – A graph showing overall decrease in emission intensity of individual scans of compound **17** upon the addition of TBA chloride (guest) (series 1-26).
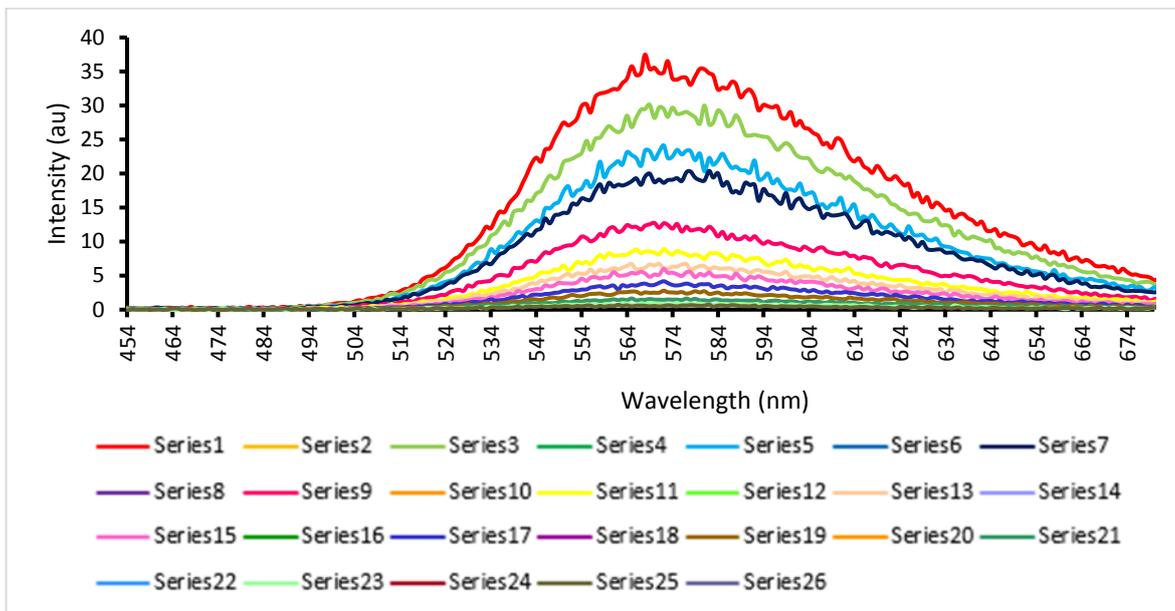
Figure 89 – A graph showing overall decrease in emission intensity of individual scans of compound **17** upon the addition of TBA fluoride (guest) (series 1-26).
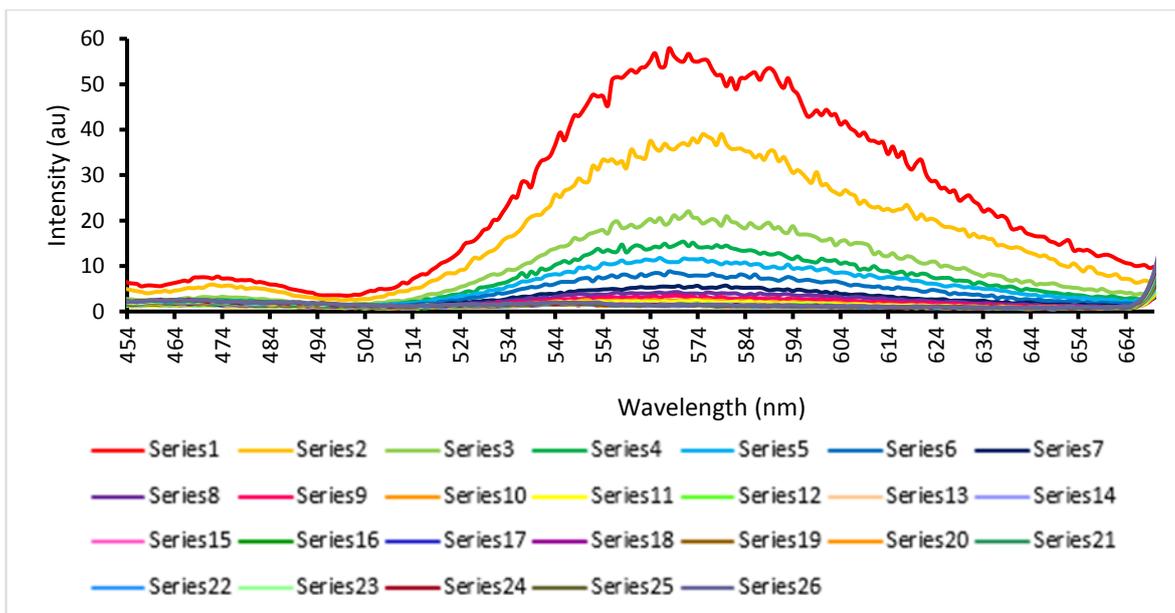

Figure 90 – A graph showing overall decrease in emission intensity of individual scans of compound **17** upon the addition of TBA hydroxide (guest) (series 1-26).
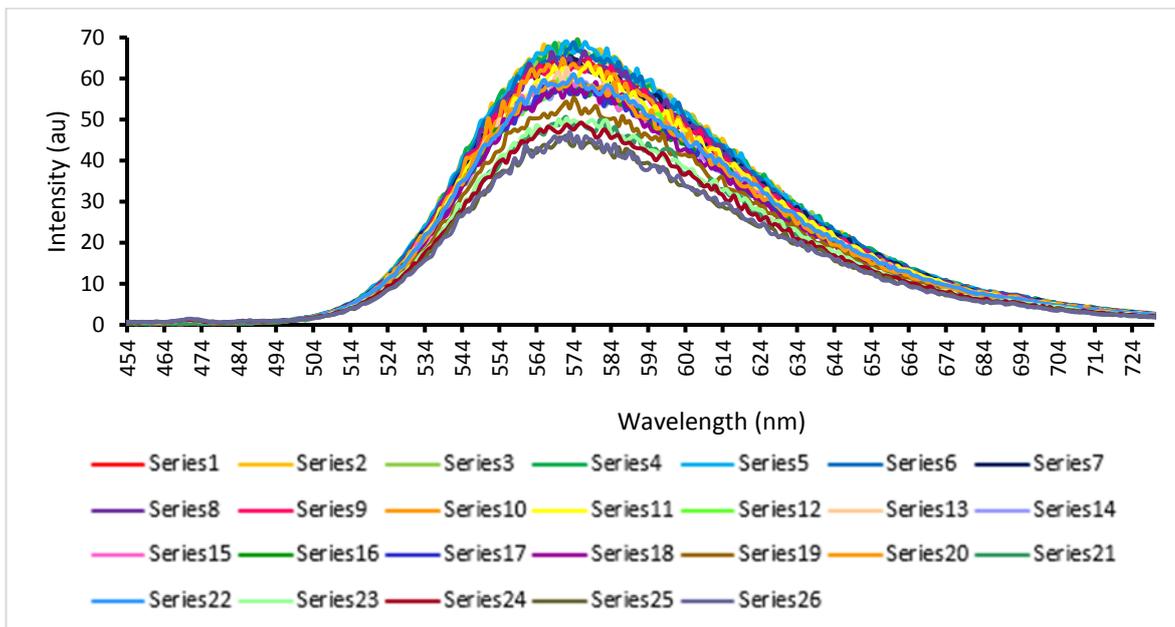
Figure 91 – A graph showing overall decrease in emission intensity of individual scans of compound **17** upon the addition of TBA hydrogen sulphate (guest) (series 1-26).
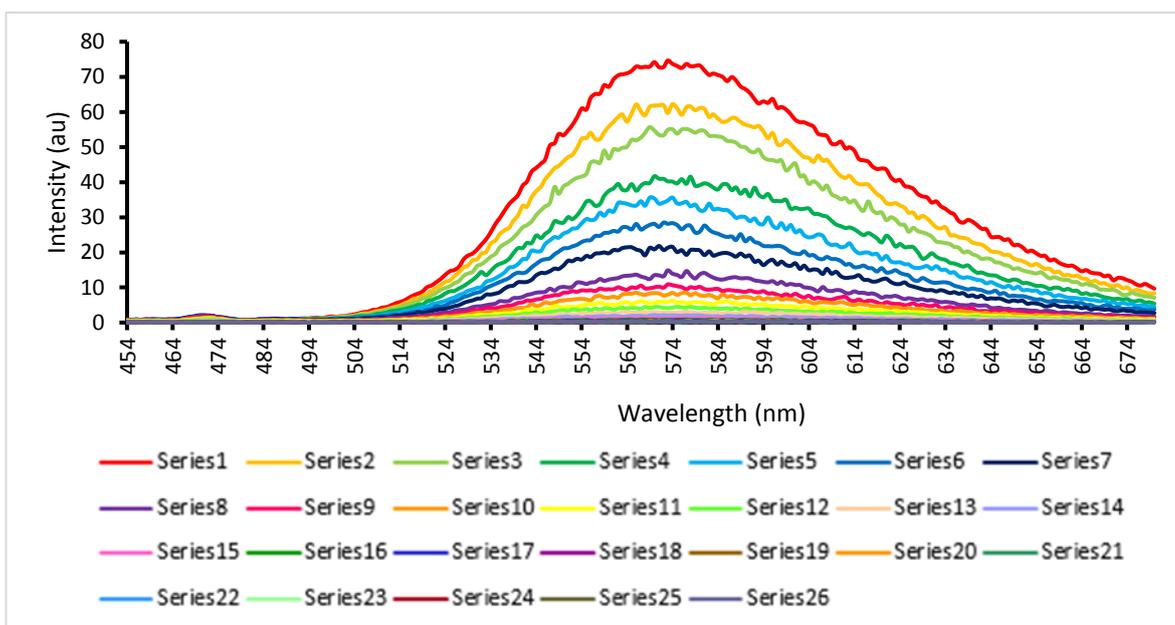

Figure 92 – A graph showing overall decrease in emission intensity of individual scans of compound **17** upon the addition of TBA phosphate monobasic (guest) (series 1-26).
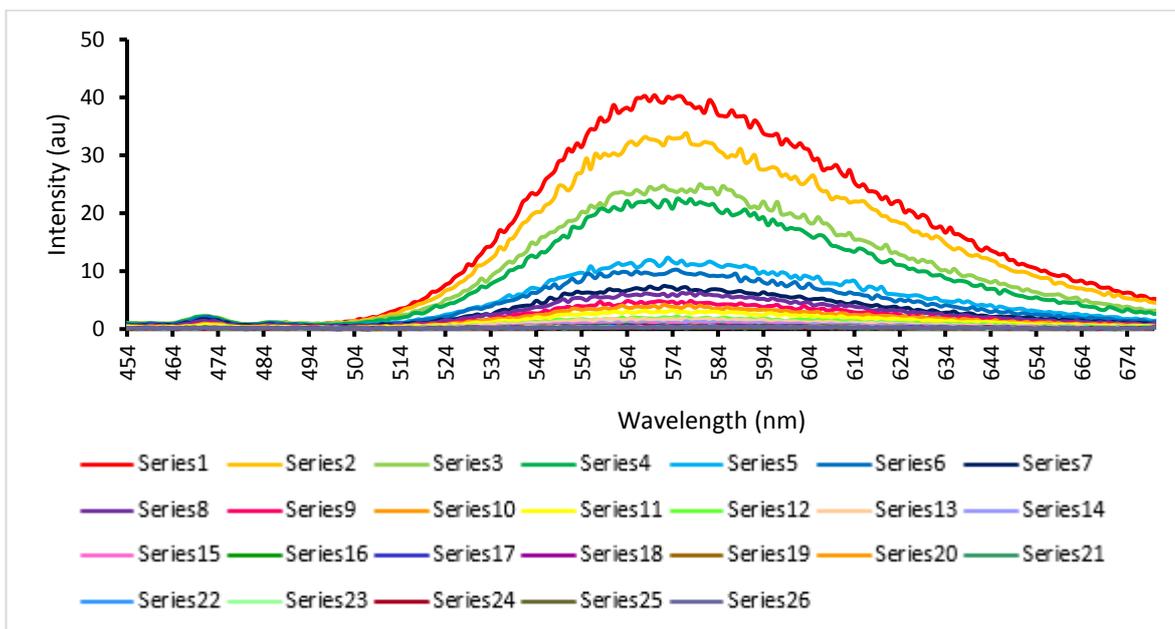
Figure 93 – A graph showing overall decrease in emission intensity of individual scans of compound **17** upon the addition

of TBA sulphate (guest) (series 1-26).

8.5 Low level in-sillico modelling

Table 34 – Electrostatic potential values calculated for E_{max} and E_{min} of compounds **12**-**17**.

Compound	E_{max} (kJ/mol)	E_{min} (kJ/mol)
12	-26.510	-699.476
13	-35.514	-699.979
14	161.777	-288.861
15	186.374	-249.312
16	228.769	-256.231
17	123.410	-236.860

8.6 DOSY

Peak name	F2 [ppm]	Io	error	D [m2/s]	error
1	9.696	1.02e+09	1.135e+05	1.83e-10	4.346e-14
2	7.972	1.64e+09	1.184e+05	1.67e-10	2.579e-14
3	7.653	1.68e+09	1.178e+05	1.66e-10	2.493e-14
4	7.510	1.44e+09	1.279e+05	1.64e-10	3.114e-14
5	3.948	3.05e+09	1.249e+05	1.63e-10	1.432e-14
6	3.172	1.10e+10	1.748e+05	1.78e-10	6.025e-15
7	1.566	1.26e+10	1.909e+05	1.75e-10	5.675e-15
8	1.303	1.62e+10	1.962e+05	1.75e-10	4.505e-15
9	0.917	2.73e+10	1.948e+05	1.75e-10	2.661e-15

Figure 94 - ^{1}H DOSY NMR of compound **12** (111.12 mM) in DMSO-d_6 conducted at 298.15 K. Anionic component is peaks 1-5, TBA counter cation is peaks 6-9. The table which represent the values for the diffusion constant for each peak used to calculate the hydrodynamic diameter (d_H) except for peak 1.

Peak name	F2 [ppm]	Io	error	D [m2/s]	error
1	9.638	1.53e+09	1.196e+05	1.44e-10	2.526e-14
2	7.569	2.37e+09	1.192e+05	1.42e-10	1.607e-14
3	7.494	3.68e+09	1.288e+05	1.42e-10	1.121e-14
4	7.158	2.34e+09	1.458e+05	1.42e-10	1.994e-14
5	6.061	2.16e+09	1.288e+05	1.42e-10	1.911e-14
6	4.001	4.04e+09	1.460e+05	1.43e-10	1.160e-14
7	3.165	1.04e+10	1.635e+05	1.78e-10	6.146e-15
8	1.565	1.22e+10	1.929e+05	1.76e-10	6.139e-15
9	1.304	1.56e+10	1.995e+05	1.76e-10	4.974e-15
10	0.928	2.55e+10	1.784e+05	1.76e-10	2.714e-15

Figure 95 - ^{1}H DOSY NMR of compound **13** (111.12 mM) in DMSO-d_6 conducted at 298.15 K. Anionic component is peaks 1-6, TBA counter cation is peaks 7-10. The table which represent the values for the diffusion constant for each peak used to calculate the hydrodynamic diameter (d_H).